Rochester Institute of Technology

RIT Digital Institutional Repository

3-26-2013

Assessing the performance of Digital Micromirror Devices for use in space-based multi-object spectrometers

Kenneth Fourspring

Assessing the Performance of Digital Micromirror Devices™ for use in
Space-Based Multi-Object Spectrometers

by

Kenneth D. Fourspring

Bachelor of Science Microelectronic Engineering
Rochester Institute of Technology

A dissertation submitted in partial fulfillment of the
requirements for the degree of Doctor of Philosophy
in the Chester F. Carlson Center for Imaging Science
in the College of Science
Rochester Institute of Technology

March 26, 2013

Signature of the Author _____

Accepted by _____
              Coordinator, Ph.D. Degree Program   Date

CHESTER F. CARLSON CENTER FOR IMAGING SCIENCE

ROCHESTER INSTITUTE OF TECHNOLOGY

ROCHESTER, NEW YORK

<u>CERTIFICATE OF APPROVAL</u>

Ph.D. DEGREE DISSERTATION

The Ph.D. Degree Dissertation of Kenneth D. Fourspring
has been examined and approved by the
dissertation committee as satisfactory for the
dissertation required for the
Ph.D. degree in Imaging Science

_____

Dr. Zoran Ninkov, Dissertation Advisor

_____

Dr. Robert Kremens

_____

Dr. Alan Raisanen

_____

Dr. Sally Heap

_____

Dr. Andrew Robinson

_____

Date

"Mirrors enable one to view the present or distant past, but the future is left to our imagination."

Assessing the Performance of Digital Micromirror Devices™ for use in Space-Based Multi-Object Spectrometers

by

Kenneth D. Fourspring

Submitted to the
Chester F. Carlson Center for Imaging Science
in partial fulfillment of the requirements
for the Doctor of Philosophy Degree
at the Rochester Institute of Technology

Abstract

A current need in space-based instrumentation is a reconfigurable slit mask. Several techniques for slit masks have been employed for ground-based astronomical spectrographs. These ground-based instruments have used large discrete components, which are impractical for remote operation in space-based deployment. The Texas Instruments' Digital Micromirror Device (DMD™) was originally conceived purely for display purposes, but is a viable candidate to be use as a slit mask in a space-based Multi-Object Spectrograph (MOS). The Integrated Circuit (IC) manufacturing industry has enabled the robust integration of both silicon transistors and Micro-Electrical Mechanical Systems (MEMS) optical components into a very reliable monolithic chip (the DMD). The focus of this work was in three areas that addressed the suitability of proposing DMDs for future space missions. The DMDs were optically characterized to assess their utility in a spectrograph. The DMDs were also cooled in a liquid nitrogen dewar to determine their minimum operating temperature. The low temperature tests indicated that the DMD operated to temperatures as low as 130 K. In addition, several DMDs were irradiated with high-energy protons at the LBNL 88″ cyclotron to determine how robust the devices were to ionizing radiation (protons). The radiation testing results indicate that DMDs would survive medium to long duration space missions with full operability. Based on preliminary tests in these three areas, the DMD should be considered as an excellent candidate for deployment in future space missions.

Acknowledgements

This is dedicated to my family and friends who were very supportive during my education at RIT.

CONTENTS

LIST OF TABLES

LIST OF EQUATIONS

LIST OF ACRONYMS

AOP Angle Of Polarization

ANSI American National Standards Institute

ARC Anti-Reflective Coating

BAO Baryon Acoustic Oscillations

BJT Bipolar Junction Transistor

CCD Charged Couple Device

CFHT Canada-France Hawaii Telescope

CMP Chemical Mechanical Polish

CPU Central Processing Unit

CMOS Complementary Metal Oxide Semiconductor

COTS Commercial Off The Shelf

CSEM Swiss Center for Electronics and Micro Technology

CTE Coefficient of Thermal Expansion

CSU Configurable Slit Unit

DDD Displacement Damage Dose

DOLP Degree of Linear Polarization

DLMM Digital Light Modulation Microscope

DLP Digital Light Processing

DMD Digital Micromirror Device

DoFP Division of Focal Plane

DOG Difference of Gaussian

DPI Dots Per Inch

DRAM Dynamic Random Access Memory

ESA European Space Agency

FEM Finite Element Model

FESEM Field Emission Scanning Electron Microscope

FITSUMMA Flexible Imaging TDI Spectrometer Utilizing MicroMirror Arrays

FOV Field Of View

FPS Frames Per Second

FWHM Full Width Half Max

Galex Galaxy Evolution Explorer

GMOS Gemini Multi-Object Spectrometer

GSD Ground Sample Distance

GSFC Goddard Space Flight Center

HgCdTe Mercury Cadmium Telluride

HST Hubble Space Telescope

ICCD Intensified Charge Coupled Device

IFU Integral Field Unit

IRMOS InfraRed Multi-Object Spectrometer

JWST James Webb Space Telescope

JDEM Joint Dark Energy Mission

LCD Liquid Crystal Display

LCOS Liquid Crystal On Silicon

LED Light Emitting Diode

LET Linear Energy Transfer

LEO Low Earth Orbit

LVDT Linear Variable Differential Transformer

LVDS Low Voltage Differential Signaling

JDEM Joint Dark Energy Mission

MEMS Micro-Electro Mechanical Systems

MGPA Micro-Grid Polarizer Array

MMA MicroMirror Array

MSA Micro-Shutter Array

MOEMS Micro-Optical-ElectroMechanical Systems

MORVS Multi-Object Radial Velocity Scanner

MOS Multi-Object Spectrometer

MSS Micromirror Self Shadowing

NASA National Aeronautics and Space Agency

NGMOS Next Generation Multi-Object Spectrometer

NGST Next Generation Space Telescope

NRC National Research Council

OPD Optical Path Difference

OTCCD Orthogonal Transfer Charged Couple Device

PCB Printed Circuit Board

PEM Photon EMission

PI Principal Investigator

POM Pool of Mirrors

RIT Rochester Institute of Technology

RITMOS Rochester Institute of Technology Multi-Object Spectrometer

RMS Root Mean Square

RTA Room Temperature Anneal

RVS Radial Velocity Scanner

SDRAM Synchronous Dynamic Random Access Memory

SPACE SPectroscopic All-sky Cosmic Explorer

SEE Single Event Effects

SEU Single Event Upset

SEM Scanning Electron Microscope

SNR Signal to Noise Ratio

SRIM Stopping Range of Ions in Matter

SLM Spatial Light Modulator

SPACE the SPectroscopic All-sky Cosmic Explorer

SPENVIS Space ENVironment Information System

TDI Time Delay Integration

TE Transverse Electric

TEC Thermo Expansion Coefficient

TI Texas Instruments

TID Total Ionizing Dose

TIR Total Internal Reflection

TRL Technology Readiness Level

TM Transverse Magnetic

TRL Technology Readiness Level

UAV Unmanned Air Vehicle

UV Ultra Violet

WFIRST Wide Field Infrared Space Telescope

WFC3 Wide Field Camera 3

WMAP Wilkinson Microwave Anisotropy Probe

XGA Extended Graphics Array

CHAPTER 1

MOTIVATION

The Joint Dark Energy Mission (JDEM) will map the expansion rate of the Universe [1]. Astrophysicists believe far away supernova are accelerating much more slowly than nearby (more recent) supernova. A fundamental question in modern physics is understanding the cause for the continued acceleration of galaxies. The light scientists view from Earth is from long ago in the past, because light travels at a finite speed (c). By measuring the spectrum of atomic absorption lines, it can be inferred that the universe is expanding at an accelerating rate. However, gravity should curb the acceleration of galaxies as the objects move further away. At the present time, the most commonly accepted theory describes the universe as a mixture of 70% dark energy, 25% dark matter and only 5% is "normal" directly observable matter (e.g. planets, stars, etcetera). A theoretical kind of fluid, quintessence (a type of dark matter), in the vacuum of space may be responsible for this discrepancy. Very high precision measurements of the Universe expansion rate are required to better understand the nature of dark energy and how it interacts with gravity. In a recent galaxy survey by NASA's Galaxy Evolution Explorer (Galex) [2], the existence of dark energy has been confirmed by two separate methods: (1) baryon acoustic oscillations (BAO) [3], which describe the distributions of galaxies in space and (2) by examining galaxy cluster formation over time. Dark energy research is in its infancy and future space missions will be developed to understand dark matter's implications on the fundamental laws of physics. These future missions require a space-based spectrograph to make more detailed measures of the Universe 's structure.

The 2010 National Research Council (NRC) Astronomy Decadal Survey specified the areas of utmost importance for space-based astronomy in the coming decade [4]. The Wide Field InfraRed Survey Telescope (WFIRST) is a mission developed to achieve the goals of JDEM. The decadal survey discusses the importance of low risk technology ready for WFIRST and a design to launch time of less than 5 years. NASA, like other government organizations, uses a measure to describe the confidence for flying electronic components in space. This scale is called Technology Readiness Level (TRL). TRL can range between 1 and 9. The list below shows a brief description of the different TRL [5].

- TRL1-2 Basic technology research
- TRL3-4 Research to prove feasibility
- TRL5 Technology development
- TRL6 Technology demonstration

- TRL7 System and subsystem development
- TRL8-9 Systems test and launch

Many of NASA's research programs invest money to raise the TRL of emerging technologies. WFIRST is projected to launch after 2020, but this will likely be delayed as James Webb Space Telescope (JWST) is now projected to launch in 2018. However, the present time is appropriate to test new components for this mission and other smaller explorer class missions. WFIRST is a 1.5 m telescope that will use a spectrometer to measure redshift of low-Z shift galaxies [1]. The H-Alpha emission line (nominally 6562.8 Å) is used as a reference to measure the radial velocity (redshift of galaxies). Mapping the galaxies' structure is fundamental to understanding properties of dark matter. This measurement process must be done in parallel to perform these measurements for millions of galaxies. A multi-object spectrometer (MOS) provides a logical way to parallelize these measurements. JWST is the successor to the very successful Hubble Space Telescope (HST). The technical development and cost problems with the JWST have delayed its launch time and time again. The low risk approach chosen for WFIRST is a consequence of the massive technology development that took place for JWST. JWST has a multi-object Near InfraRed Spectrometer (NIRSpec) [6]. The instrument uses a micro-shutter array (MSA) to define the slits for the spectrometer. With considerable financial investment, NASA Goddard Space Flight Center (NGSFC) built MSAs from the ground up. MSAs have major limitations due to their cost and cosmetic quality (high number of defect pixels). Additionally, the MSA development and construction was done exclusively for JWST, with no plan for additional production. In order to negate the complexity and financial investment of building a space-based MOS, a slit-less low risk approach was chosen for WFIRST.

The baseline spectra measurement technique for WFIRST is slit-less spectroscopy utilizing a prism or grism to disperse the light for all objects simultaneously [7]. For WFIRST, astronomers desire a spectrometer with Hubble's Wide Field Camera 3 (WFC3) spectral coverage. WFC3 uses HgCdTe (Mercury Cadmium Telluride) detectors sensitive from 0.6 µm to 1.8 µm. The advantages of MOS over slit-less spectroscopy are many. The slit-less technique is applicable to astronomy because stellar sources are sparsely positioned in the telescope field of view. Despite this general principle, across all science frames spectral overlap and multiple source confusion will be major issues. Additionally, the Zodical dust backscatters sunlight into the telescope aperture. In a slit-less spectrometer, the background signal from the Zodiacal light is collected from the whole telescope field of view. If a MOS slit spectrometer is used instead, only the light from the object of interest and the zodiacal light along the slit's line of sight is imaged onto the detector. Therefore, slit-less spectroscopy has on the order of 1000 times (or N - the number of spectral channels) higher background noise than a comparable MOS slit spectrometer. A slit-less spectrograph certainly limits the science that can be done.

Previous ground-based approaches to build MOS are simply not feasible in space. There are several limitations that make the past ground-based instruments not practical for deployment in space. The WIYN-Hydra instrument is a MOS system that positions fibers into the focal plane of a telescope [8]. The Hydra instrument is quite slow at repositioning optical fibers into its focal plane and takes approximately one hour for this process. The apparatus required to position fibers into the focal plane array is impractical also because of its size, maintenance, and reliability. Another ground-based instrument, GMOS uses machined slit mask plates [9]. During the first observation period, the targets of interest are selected. The slit mask is then machined at another facility and then returned to the instrument for a second observing run. It is not possible to machine plates for each science frame in space. Weight is one of the biggest limitations

for space-based instruments. The mass sent into space directly correlates to cost. Therefore, space-based instrumentation must be compact, lightweight and efficiently designed.

A potential candidate to fulfill the slit mask requirement is the Texas Instruments (TI) Digital Micromirror Device (DMD). The DMD will be discussed further in Chapter 2. Two ground-based MOS instruments utilizing DMD slit masks have already been constructed: (RITMOS - RIT multi-object spectrometer [10] and IRMOS InfraRed Multi-Object Spectrometer [11]). IRMOS and RITMOS were both much significantly more compact than other MOS instruments, but were optically limited because the primitive DMDs had very low contrast. A newer generation of DMDs will be examined as part of this work. Utilizing a commercial off the shelf (COTS) part such as the DMD, will equate to cost savings, higher quality science data and decreased mission preparation time. Chapter 2 will further discuss the history that has brought the field to its current state.

Several experiments were completed to access the ability of DMDs™ to operate in the space-based instrument. These initial tests were performed to determine if DMDs are a suitable candidate for a space-based scientific instruments and are summarized below.

1.1 Optical Tests

The contrast of a DMD™, when used as a slit mast in a MOS is investigated. Previous modeling and measurements have only evaluated the DMD™ as utilized in a digital projector. Optical measurements will assess the following characteristics of the DMD:

- The effect of mirror size and tilt angle on contrast
- The effect of sub-pixel illumination
- The contrast of a DMD™
- How illumination wavelength affects the contrast
- Optical characteristics of the package design
- UV reflectivity

1.2 Environmental Tests

The expansion of the Universe red-shifts the visible light of stars and galaxies to the infrared. In order to use a DMD in an infrared spectrograph, the DMD must be cooled to reduce its thermal emission and preserve the low background required in a spectrograph. In 2004, micromirrors were investigated as a possibility for the MOS on JWST (at this time the telescope was called Next Generation Space Telescope (NGST) [12] [13]. Micromirrors were not chosen for this mission, because they were difficult to model optically, and their cryogenic tests had not been completed. JWST will operate at $L2$ [14]. Due to limited knowledge about DMDs operation in low temperatures, the low temperature operation of DMDs was investigated (Chapter 5):

1.3 Radiation Tests

A DMD™ must be able to withstand the cumulative dose of radiation over the duration of a space mission. The European Space Agency (ESA), in collaboration with European research institutes, has performed

cooled testing and gamma radiation testing on DMDs in preparation for the EUCLID mission [15], but no proton irradiation tests have been completed on DMDs. The DMD was proposed to fly in the Euclid Mission [16], but was cut due to financial constraints. DMDs were stated to have a gamma radiation tolerance of approximately 15 krad. In the current work, proton radiation tests were performed on 3 new DMD™ XGA (Extended Graphics Array) 13.68 µm pitch devices (Chapter 4).

1.4   Objective

The goal of this work was to determine if DMDs could operate effectively in a space-based spectrograph. Three of the main uncertainties related to their: optical characteristics, low temperature operation and radiation hardness are examined in detail.

CHAPTER 2

2.1 Prolegomenon

Mirrors have been in existence for centuries, allowing humans to modulate light to suit their needs. Over time, these needs have continuously evolved. With sight being our most predominant sense, mirrors enable us to magnify the world around us. According to historians, the first mirrors were developed around 6000 B.C. by the Egyptians [18]. The Egyptians polished bronze and copper to construct the first man-made reflective surface. The ancients viewed their image through this "looking glass." A history book from the 12th century Chiliades suggests that the almighty Archimedes was able to burn ships from afar by focusing the suns rays using polished metal mirrors. This burning mirror would be useless at noon, on a cloudy day, or at night. This myth is one of the first demonstrations illustrating the power of reflective optics, even if it was just a psychological weapon.

2.1.1 Mirrors and Electronic Imaging in Astronomy

By investigating the cosmos deeper than ever before, polished mirrors continue to modulate light to suit the desires of both scientists and casual observers alike. To this end, massive telescopes have been built to bring far away galaxies, planets, quasars and stars closer to our vision. These advanced optical systems fuel our desire to build more efficient instrumentation to provide astrophysicists with new answers that have plagued other scientists for decades. Early astronomers were quite content with sketching star fields onto paper because they were busy understanding the dynamics of our solar system and understanding the difference between stellar objects and the motion of the planetary bodies. Later, advances with silver-halide coated glass plates were used to record images similar to black and white film cameras. To understand a star's chemical composition, the spectrum must be examined by quantitatively measuring molecular emission and absorption lines. This additional information can give information about how the star was born and determine the spectral classification of the star. Further information can be inferred after the stars MK-spectral classification type is known. MK-classification can determine whether the star is a viable

Figure 2.1: Sketch of Archimedes Burning Mirror [17].

candidate for planets. Today, examining exoplanets and studying the dark matter of the universe compels us to build more advanced instrumentation.

Electronic imaging and Charged Coupled Devices (CCDs) have slowly found their way into astronomy. It was by no means an easy journey. The invention of the transistor in 1945 has lead to great monolithic integration of transistors in silicon foundries. Soon, dozens of transistors became integrated on single silicon substrates and Moore predicted that the number of transistors on a silicon chip would double every 18 months [19]. This is now called Moore's Law. Moore made this famous projection in 1965, which has subsequently been the law semiconductor manufacturers must follow even to this day to remain profitable. It is amazing to think that this prediction was made when only a single level of metal interconnects were common. Today it is common for central processing units (CPUs) to have 8 or more metal interconnect levels. From the silicon processing technology, CCDs were conceived. They were originally designed as a memory storage device. Early CCDs were not cosmetically perfect and primarily limited by:

- The low area coverage in comparison to plates.
- The poor spectral coverage (especially in the ultra-violet).
- The readout noise dominated when they were used in spectrometers.
- The charge transfer characteristics, which limited the detector area and also the lowest measurable signal.
- The uniformity of pixel response in large format sizes.
- The numerous hot and stuck pixels.
- The small format sizes available.

Most modern CCDs have evolved to overcome these shortcomings. The microelectronics industry has brought a considerable benefits to the astronomical community, but their most important endowment is the drastic improvement in silicon growth, processing, and low defect wafers. Modern electronic detectors have greatly enhanced the astronomical data acquisition process. The amount of data and knowledge

acquired since the advent of the CCD is astounding. This same technology that brought the CCD to the spotlight is currently delivering another modern electronic device, namely arrays of mirrors.

2.2 Introduction to MEMS

Micro-Electrical Mechanical Systems (MEMS) are devices created by micro-machining common semiconductor fabrication materials. These devices contain at least one moving part. MEMS devices are tiny mechanical devices fabricated with existing semiconductor fabrication techniques that integrate electrical interconnects and drive electronics into a single package. MEMS usually consist of an actuator, either electrostatic or thermally actuated, and a membrane or structure that physically moves. MEMS are the solution for miniaturizing bulky discrete sensors. Currently available MEMS sensors include: accelerometers, gyroscopes, humidity sensors, and temperature sensors. The field is multi-disciplinary and combines the fields of electronics, mechanical engineering, physics, fluid mechanics and chemistry. Two physical methods are utilized to translate individual MEMS components on silicon substrates: thermal actuation and electrostatic actuation. Each method involves transferring one form of energy into motion. Thermally actuated MEMS devices make use of bimetallic actuation. A bimetallic actuator operates by putting two dissimilar metals together. Each metal has a slightly different thermal expansion coefficients (TEC) or coefficient of thermal expansion (CTE). As current passes through an on-chip heating element (usually a diffused resistor), the metals heats up. As one material expands more quickly, the two layers begin to contract. Once the potential is removed and the materials cool to ambient, they return to their equilibrium position. The other principle method to actuate MEMS objects is by means of electrostatic attraction. When a charge difference is placed across an electrode pair, an attraction force is induced. If these electrodes are attached to a free-standing structure, then this force is into motion. DMDs (manufactured by TI) operate by electro-static attraction.

Care must be taken in the design process so that arcing or contact of the electrodes does not occur. If two electrodes contact each other the high current that travels through them can cause the two electrodes to permanently bond and burn out their control electronics. Also, the surface properties of thin-films dramatically affect MEMS performance. Thin-film formation process parameters can be optimized to manufacture stress-free films or intrinsically stressed films. Intrinsic stress is created by lattice mismatch between two adjacent material layers. Thin-film stress falls into one of two categories: compressive and tensile. A tensile stressed film deposited on a wafer will cause the wafer to bow up (bowl shaped) because the film has smaller lattice spacing than the substrate. A compressive film conversely causes the wafer to bow down (hill shaped). Some of the important parameters are deposition pressure, voltages, temperature, and film thickness. Thin-films can also be deposited by several techniques such as evaporation, chemical vapor deposition, or sputtering, and each of these techniques has their advantages with regard to the mechanical and electrical properties of the thin film. The amount of stress is proportional to the film thickness. Very thick films are very challenging to engineer and it is possible for them to crack a substrate if enough stress during the deposition process is formed. Contaminates can also change the film properties and cause a change in stress. Controlling these intrinsic film properties are extremely important for building high quality thermally actuated optical MEMS. Packaging these devices is a very important aspect of building them to ensure long lifetime and operation. Moisture and other contaminates must not contaminate the surfaces of these devices. MEMS require electronics to control their motion and often times these drive electronics can be integrated with the MEMS structure. The mature silicon foundries were an excellent choice for
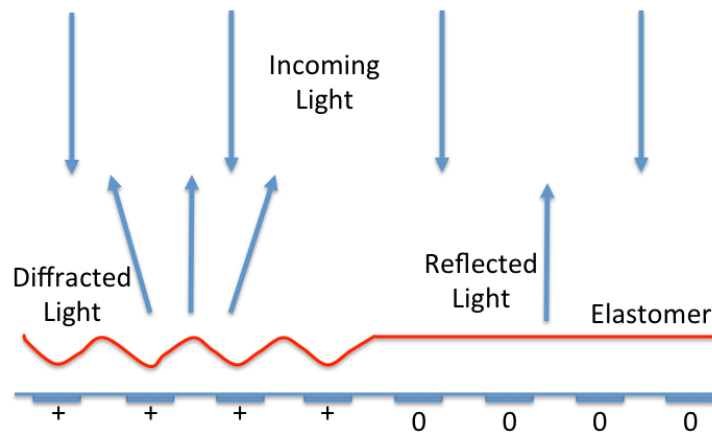
Figure 2.2: Actively addressed eidophor light modulator [20]. Pixels on the left show a charge placed on the electrode. Light is diffracted out of the projection aperture.

adapting this technology. The most exciting and recent advancement in MEMS is the addition of optical MEMS.

2.2.1   Electrostatically Actuated Optical MEMS

Micro-Optical-Electro-Mechanical (MOEM) devices have been around since the late $1930's$. The first example of a MOEM was the eidophor. This device operated by utilizing electrostatically actuated phase gratings. An elastomer membrane material was placed to diffract light. Figure 2.2 shows the concept of how an actively addressed device operates. Initially, the eidophor was addressed by a scanning electron beam, but subsequent attempts used a locally addressed electrode to electro-statically modulate individual pixels. A reflective thin oil film sat atop the electrode array. To activate the pixel, a charge was placed on the electrode, and consequently the light was diffracted out of the projection aperture [20]. This is the first known example of a modern spatial light modulator. It was not free from problems. At the time, it was difficult to find materials that could be modulated repeatedly without failing. Until recently, the technology did not exist to manufacture dense actively controlled electrode arrays.

2.3   The Digital Micromirror Device

A miniaturized array of mirrors has been under development at TI for approximately twenty years. TI began working on the spatial light modulator (SLM) designs in 1977. The technology was originally labeled as a Deformable Mirror Device (DMD) [21]. The original device was designed to perform phase modulation of wavefront, by actively addressing an elastomeric material with an array of electrodes. Work on this type of technology is still underway primarily for wavefront correction in adaptive optics systems by commercial vendors such as Boston Micro-machines [22]. The DMD structure and optical characteristics have drastically improved since its inception. The digital version of the design (amplitude only modulation) was first constructed in 1987. The DMD requires an electrical bit stream as an input and outputs an optical bit stream. The Digital Micromirror Device (DMD) has a bi-stable design. Each mirror would be tilted either $\pm 10°$ or $\pm 12°$ depending on the specific model. Amplitude only modulation is possible with the digital
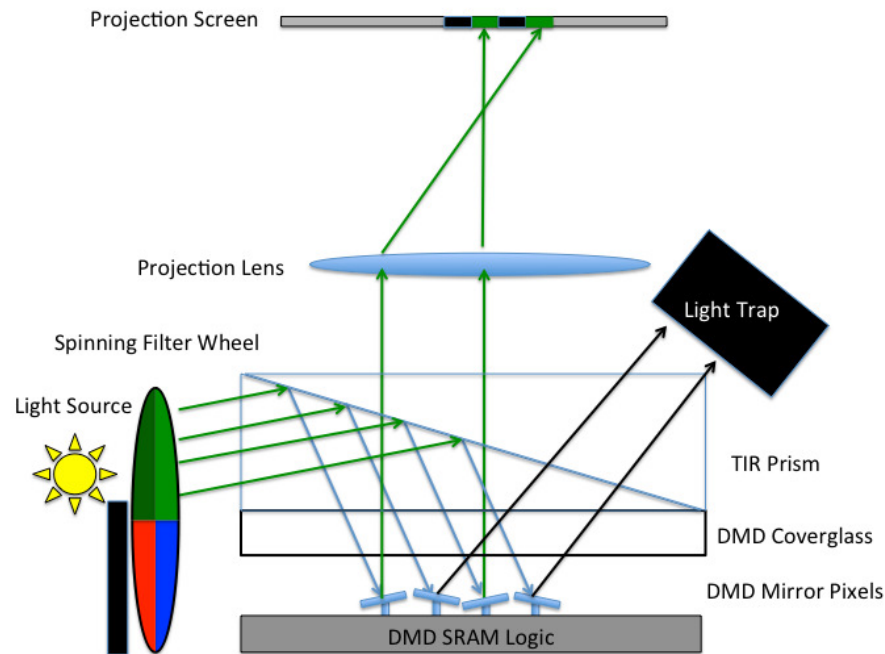
Figure 2.3: DMD projector consists of several components. First a white light source is used in combination with a filter wheel. In pico projectors, the source and filter-wheel has been replaced with three switchable colored Light Emitting Diodes (LEDs). Colored light enters a Total Internal Reflection (TIR) prism. Light intersects the cut in the prism at an incident angle greater than the critical angle, so the light is totally internally reflected. Then light is then directed through the DMD cover-glass to the DMD mirrors. This is where the optical switching occurs. Mirrors 1 (the left most mirror) and 3 are on and directing green light towards the projection optic and screen. Light is not internally reflected here because the light angle of incidence is less than the critical angle. Off mirrors project no light towards the screen and show up dark. Light from these mirrors instead travels to a light trap. Note: this drawling is not to scale.

micromirror device. The digital device operates with a much larger swing angle at much lower voltages than the analogue device, which required much larger voltage levels to operate. In 1993, the first commercially available MEMS based SLM was available from TI. Figure 2.4 shows a Scanning Electron Microscope (SEM) image of this type of mirror. This mirror structure had a contrast ratio of 50 : 1. This technology was finally commercialized in 1996 under the name Digital Light Processing (DLP™). By 2002, over 1.5 million projection displays had shipped with this technology [23].

2.3.1 DMD Display Technology

DMDs were manufactured to primarily be used in digital televisions and projectors [24]. DMDs convert an electrical data stream into a digital optical stream. This TI technology is broadly referred to as DLP™. This technology is ideal for showing digital videos. An example digital projector is illustrated in Figure 2.3. A tungsten filament light or light emitting diode LED, uniformly illuminate the DMD. A filter wheel is placed in the optical path to modulate the color of light illuminating the DMD. Additional optics are present to collimate and make the light uniform prior to illuminating the DMD and are not shown. A Total Internal Reflection (TIR) prism is used to fold the light path, and make the DMD light engine significantly more compact. The memory cell below each individual micromirror determines what the state of each DMD mirror in the array. The light is either reflected out the projection optics to a screen, or instead

reflected to a light trap. When the mirror is tipped away from the projection optics a dark spot is imaged onto the projection screen. Individual micromirrors are either landed in their "ON" position or their "OFF" position. The mirrors cannot be tipped to an arbitrary analogue position between these two stable positions. However when charge is removed from either of the control electrodes the mirrors rest in their flat state. By limiting the DMD to two states of operation, feedback electronics are not required greatly simplifying the MEMS structure.

DMDs in projectors can utilize very fast binary frame rates (up to 22,000 Frames Per Second (FPS) for the full array). By modulating individual mirrors very rapidly, the display system can produce black, white and all gray levels in between [25]. The DMDs are refreshed many times a second with different duty cycles to create various brightness levels. The integration time of the human visual system (0.1 seconds or 10 Hz [26]) is long relative to the period of a single DMD mirror oscillation. This allows for color information to be added by means of a rotating color wheel, or alternatively by employing three DMDs (one for each color) and a color combing prism. DMDs cannot be run significantly faster than this, because the time it takes for an individual mirror to land is on the order of 10 μs. For more details on the electrical method to land a micromirror refer to Appendix B. In addition, the projector electronics enable the performing of phased resets on portions of the DMD chip simultaneously, so that groups of DMD rows can be individually reset. A fair amount of psychophysical studies and visual perception experiments have been conducted to build single chip DLP™ displays that exhibit very minimal artifacts in the human visual system [27] [28] [29].

The television market has been saturated with thin low cost Liquid Crystal Displays (LCD) and plasma displays. DMD rear-projection televisions could not be manufactured as thin as comparable LCD televisions, so the primary market for DMDs is currently limited to digital projection. Competing technologies such as Sony's Liquid Crystal on Silicon (LCOS) have had reliability problems. Many studies have been done to evaluate the long-term reliability and stability of DMDs in digital projectors with favorable results [30]. The projector application uses the DMD switchable mirror to direct the light from a lamp source to either a projection lens or a light trap. The various intensities across the imaging field are produced by pulse width modulation of individual mirror. The need for a digital operation was seen as advantageous in many respects. DMDs can also be used in a three dimensional volumetric display [31], and more recently in $3 - D$ projectors. Currently TI's pico projectors are becoming more common, and may eventually be integrated into consumer smart phones.

2.3.2   DMD Device Mirror Structure

In 1996, the basic mirror functional components are illustrated in Figure 2.4 (Top Right). This design was known as the "hidden hinge" design, because the hinge is now located below the optical surface. The mirrors have hinges at the corners and tip 45° relative to the complete DMD array orientation. Electrodes are positioned below the mirror, which are the mechanism to actuate the mirror. This type of DMD shown is Figure 2.4 (Top Right) was a 17 μm pitch device with 1 μm gaps between mirrors. The devices were available in an 848 × 600 format. These mirrors tipped ±10° relative to the optical axis. This MEMS super-structure evolved into the second-generation hidden hinge DMD (Figure 2.4 Bottom Left). Additionally, spring legs were added to minimize mirror stiction to the substrate (Figure 2.5). These legs also prevented the mirror from shorting to the electrode. The spring tips are are always at the same electrical potential as
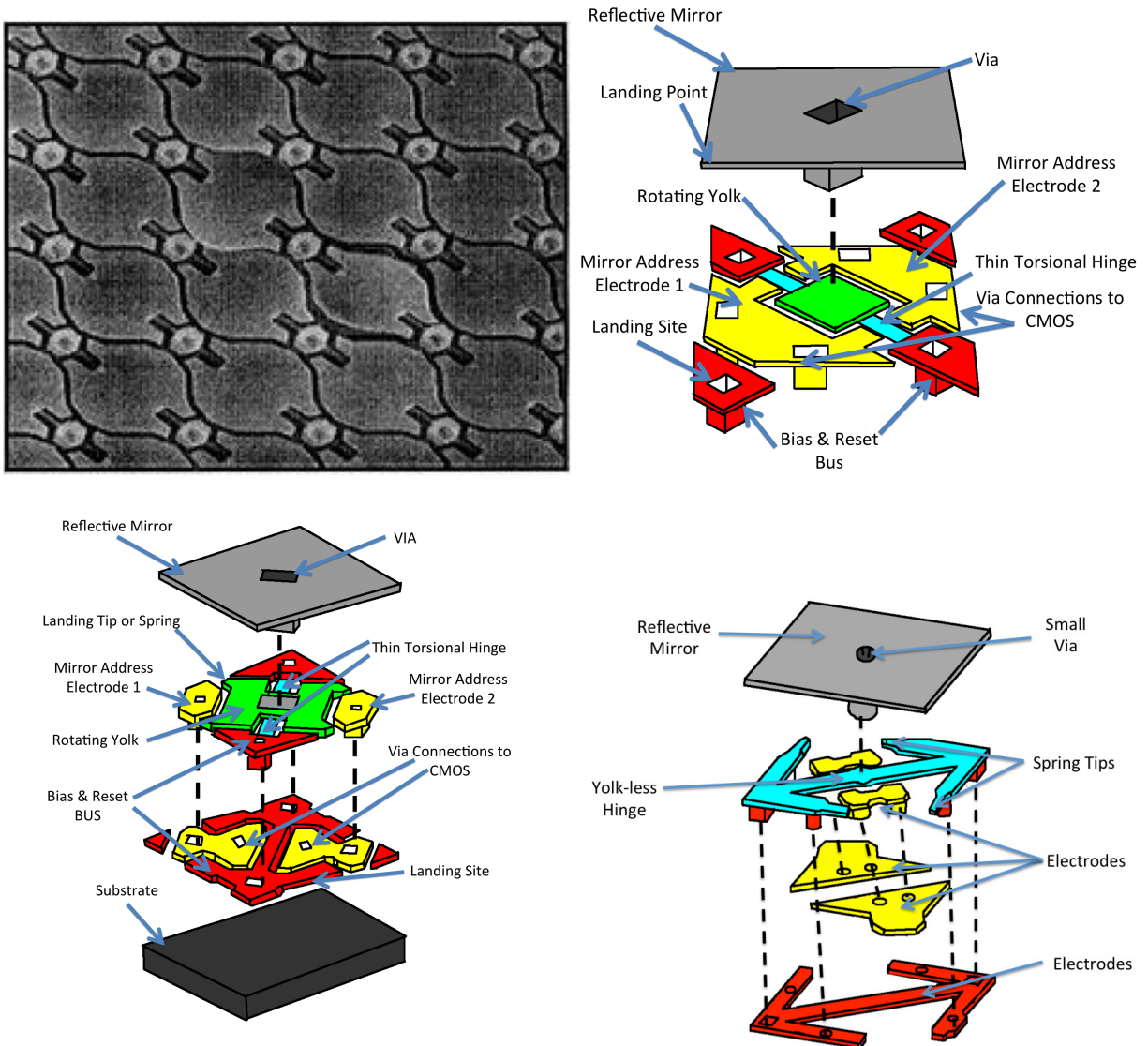
Figure 2.4: (Upper Left) First DMD array (1993) [32] was imaged with a SEM. (Upper Right) Hidden hinge DMD design is shown here [33]. Red region is the reset bus and the yellow are the electrodes which are attached to the CMOS logic below. Substrate is not shown [32]. This mirror stops on the mirror corner. (Lower Left) Extrapolated pixel shows the different components of a superstructure. Reflective mirror surface is shown on top. Aqua colored regions are the thin torsional hinge that allows the mirror structure to rotate on the yolk [34]. Mirror is electrically connected to the bias and reset bus (shown in red), hence the reason the landing top rests on the bias bus. Mirror address electrodes are colored in yellow. CMOS below on the substrate ensures these two electrodes are always opposite in charge (there is a logical inverter connected to the two connections). (Lower Right) Newest scalable "fast track mirror" used for the 13.68 µm, 10.8 µm and 7.6 µm pixel DMDs [35] is shown here. Note: the substrate is not shown.
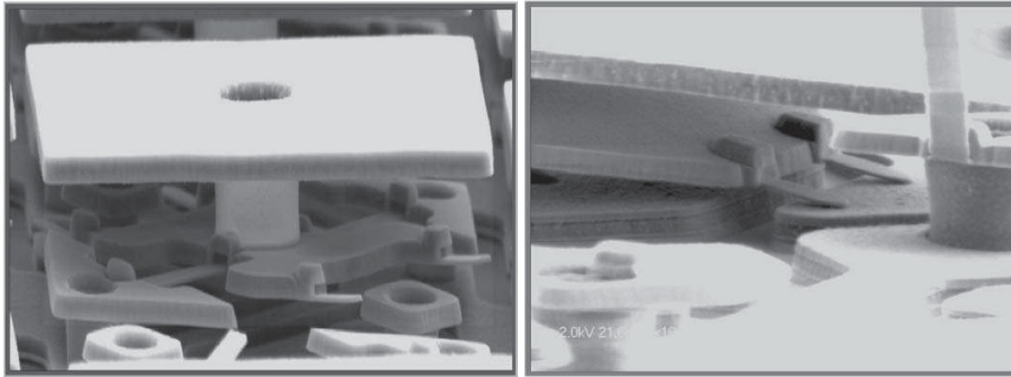
Figure 2.5: Spring tips shown on a DMD prevent stiction on a DMD. These tips are fabricated with same metal the torsional hinge [20].

the mirror. The yoke is the portion of the super-structure that supports the aluminum mirror and hinge assembly.

2.3.3   Fast Track Pixel Design

TI released a computer controlled electronic prototyping board to drive DMDs called the Discovery Kit, which allowed end users to incorporate DMDs into their novel optical systems. The first DMD discovery 1100 kit was available with a single 0.7" diagonal 1024×768 DMD. These DMDs had $\pm 12°$ tip angles, and this chip had 64 single-ended data-inputs. Next, came the DMD Discovery 3000 kit. In this design, TI switched over to a Low Voltage Differential Signaling (LVDS) double-ended-input to load data into the integrated DMD memory . The current discovery design is the Discovery 4100 kit. This new discovery kit speeds up mirror reset times, and also allows a user to run a 0.95" $1080p$ DMD. Two types DMDs are examined in this thesis. The optical characterization was completed on the generation of DMD shown in Figure 2.4 (Upper Right). The DMD characterized in the remainder of this thesis is a $13.68\,\mu$m XGA 4000 fast track DMD.

The fast track "super-structure" is somewhat different than previous designs because its structure is scalable to smaller pixel sizes. The largest revision over previous designs is that the hinge is the last deposited metal layer before the mirror and the mirrors' very yolk and via have consequentially decreased in size. The moving mass of the mirror was significantly reduced. This reduced the DMD switching time. As a result, the mirrors' natural frequency increased and enabled them to operate at appreciably higher frame rates, due to the decreased force required to land the mirrors. The fast track pixel design is illustrated in Figure 2.4 (bottom right). Recently, TI has released a series of smaller format, decreased pitch mirror arrays for mobile projectors ($7.6\,\mu$m mirrors with formats of 320×240 (half VGA) or 640×480 (VGA)). TI would like to dominate the cellphone projector market. Many different DMD formants have been released to projector manufactures from standard resolution VGA to the wide screen high definition ($480i$, $480p$, $720i$, $720p$, $1080i$, and $1080p$).

Specialty chips are manufactured for large format digital cinema projection. Several select cinema projector manufacturers (Christie and Barco) sell DLP cinema projectors utilizing DMD Cinema chips (2048×1080 $13.68\,\mu$m format sizes). In 2011, TI released the Enhanced $4k$ Cinema (1.38" diagonal) DMD. These chips have a slightly larger die size (the 2048×1080 have a 1.2" diagonal), but have $4\times$ the number of

pixels. The pixels are 7.6 µm in size, and it appears TI uses the same pixel structure from the pico projectors for the Enhanced 4*K* Cinema Chips. The optical effects associated with this will be discussed in greater detail in Chapter 3. Most projector companies such as Christie are building projectors that can be upgraded from the 2*K* chip to the 4*K* chip [36]. Scientific applications are limited to utilizing the pixel pitch and chip formats currently available from TI. It is not practical to have TI to build a custom format device for the astronomical application of multi-object spectroscopy.

2.4 Fabrication Procedure

The backend process for fabricating TI's DMD is shown in Figure 2.6. The "backend process" refers to post transistor level, this is the term used in the microprocessor industry for the many subsequent metal interconnect layers. The MEMS portion of the DMD is commonly referred to as the DMD "super-structure." The process starts by patterning the metal 3 layer. The previous two metal layers are used for the SRAM memory, one for the bit lines and one for the word lines. Metal 3 will act as the electrode layer to provide the electrostatic force required to direct the mirror. A sacrificial layer is then spin coated on the device and patterned. Holes are patterned in this layer to form posts to support the mirror superstructure. A thin 600 Å metal layer is then deposited for the hinges. A layer of insulator is deposited. Another layer of metal is deposited to form the yoke [37]. Then sequentially both the hinge and yolk parts are patterned and etched. Another spacer layer is deposited and the aluminum layer is sputter deposited to form the mirrors. The mirrors are etched and then the sacrificial layers are removed to form the mirror superstructure. This process has changed slightly in newer mirror generations.

2.4.1 Window Coatings and Protection

TI engineers have performed reliability testing of these devices and have found a correlation with UV irradiation. Therefore, TI has integrated additional filters in the window and projector systems to filter light below 400 nm. This UV inducted damage is one of the main reasons these devices has not been overly successful at replacing deep UV lithography reticles. High energy UV light from 248 nm lasers or 193 nm ArF lasers can cause the DMD to degrade over time. However, it is important to note, that the flux level in lithography systems is very large, much greater than would ever occur during an UV astronomy mission. Additional coatings on the packaged layer can be optimized to control what wavelengths are reflected from the device. The telecommunications industry has pushed the need for DMD's optimized for use in the 1 µm to 2 µm range. Changes in the processing include changes in window transmission and tilt-angle optimization to maximize diffraction efficiency at 1.55 µm, the most efficient wavelength to transmit signals over long distance fiber-optic networks. Systems optimized for the far infrared region of the spectrum (greater than 2.5 µm) become impractical due to package window transmission cutoff and increased diffraction from the mirrors.

2.5 Other Applications for DMDs

Many scientific applications for DMD have been developed over the last 20 years including: infrared scene projectors [38], single pixel cameras [39], and semiconductor lithography re-programmable masks [40].
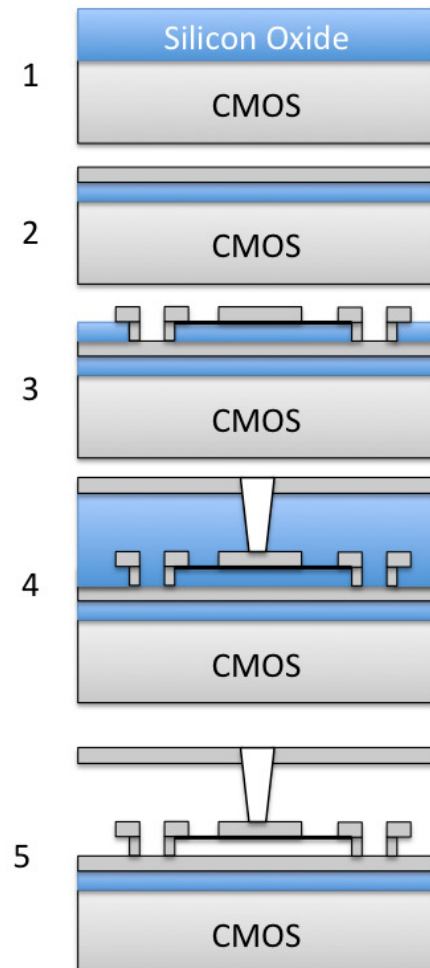
Figure 2.6: Fabrication process for the DMD superstructure is shown here. (1) First, the CMOS memory circuit is built using conventional semiconductor processing. (2) Next, a chemical mechanical polish (CMP) is done to make a flat surface to start building the mechanical portion of the chip. At this point in the process there is a fair amount of topology on the chips surface. The remaining oxide layer is the roughened surface, which acts as a dark oxide layer newer DMD devices which have the "DarkOx" technology. The CMP ensures there are no topology issues when making the hinge structure. Next, aluminum is deposited and the electrodes are etched. (3) Now the organic sacrificial layer is pattered and deposited. Next the hinge and yolk metal are deposited using an oxide mask and an etch stop. (4) Second sacrificial layer is deposited and pattered. Aluminum mirror surface is deposited using another oxide mask. (5) Wafer is partially sawed to minimize the particulate contamination that can occur after the mirrors are etched. Sacrificial layers are then chemically plasma etched away. Passivation step is then performed which prevents the mirrors from sticking. Wafers then go to electrical test, are extracted and bonded to individual ceramic packages. An additional plasma clean is done with a passivation. Devices are then packaged with a sealed window and a burn in is one on the devices.

Digital photo-printing is another application for DMDs. The DMD is used to print full color images at greater than 300 Dots Per Inch (DPI) with greater than 12 bits of dynamic exposure range. One of the first commercial systems for DMDs was an airline ticket printer. Semiconductor reticle manufacturing is a very expensive process, therefore using a DMD as a reconfigurable reticle pattern is attractive proposition. TI is currently researching DMDs optimized for the near UV (350 nm to 450 nm) spectral region. More recently, Printed Circuit Board (PCB) manufacturers use DMD projection systems to define the inter connect patterns. On a similar front, DMDs can be used for $3 - D$ rapid prototyping. The communications industry has switch networks used to multiplex signals between various fiber-optic lines. The wavelength of interest is generally 1550 nm due to the efficient transmission and low dispersion of fibers at this wavelength. A DMD was used as a add-drop filter in a dense wavelength division multiplexer [41]. It was seen that this DMD based multiplexer has low cross talk, sometimes even better than the signals of much more costly systems. The DMD also has the advantage of opening up a much greater switching potential, because previous switches were often one-dimensional arrays. By illuminating a DMD with four different light sources and by modulating each region at a different frequency, a time domain representation of the signals can be obtained [42]. Another more recent use for a DMD device is to act as an optical tweezer [43] to use the forces of laser radiation to manipulate nanometer scale particles [44].

Another use of DMDs is as a programmable light source engine. A company, OneLight, now builds programmable light source [35] using DMDs. They disperse a white light source over a DMD. The row direction controls the intensity of a given wavelength bin, and the column direction represents the wavelength. When this light is remixed, any arbitrary spectrum over the wavelength output of the light source can be generated on the fly. This type of light source can be extremely useful in optics laboratories for spectrometer calibration. One notable application of a DMD is for a confocal microscope design [45]. Generally, with conventional microscope illumination the diameter of the illumination aperture is controlled through means of a mechanical iris. In a DMD based confocal microscope, the DMD is used to dynamically change the shape or scan points within the aperture. The DMD is used to make a dynamic optical system capable of rapidly modulating between dark-field and light-field microscopy. A modified design has recently been used to measure sub-cellular texture [46]. This technique uses a variable diameter iris as a Fourier filter in a dark-field microscope. After using the DMD to implement $2 - D$ Gabor-like filters, the specimen particle roundness and size could readily be measured. The new confocal microscope system can be used to examine changes in the sample. Other microscopy technologies such as Scanning Electron Microscopy (SEM) have sufficient resolution to characterize these samples, but are impractical for examining living biological samples. Another novel microscope design uses the DMD to modulate the illumination pattern in the spatial domain, but also in a temporal domain to examine phosphorescence of various materials. This new class of microscopes is referred to as a DLMM (Digital Light Modulation Microscope). The rapid switching time by the DMD enables short high-speed light pulses to illuminate portions of the sample specimen [47]. This new microscopy technique allows the detailed examination of cellular oxygen uptake rate and will greatly help improve the understanding of the metabolic responses of living cells to oxygen. A material, Porphyrins, is used to phosphoresce and allow scientists to see active regions of the cellular structure. Phosphorescence is when a material will absorb the higher energy photons and release lower energy photons. This is a novel imaging technique, because the higher energy photons are emitted by the microscope illumination system and the secondary lower energy photons are viewed after being emitted by the phosphor
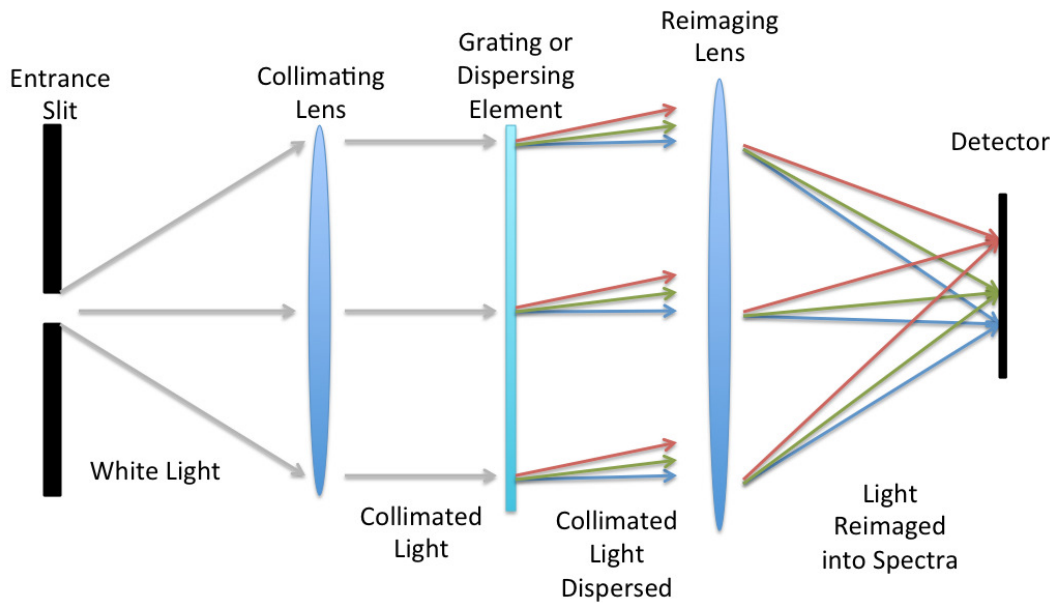
Figure 2.7:   Spectrometer is composed of an entrance slit, collimating optic, a dispersing element, a re-imaging lens, and a detector. Note: the fore-optics (that image an object onto the entrance slit) are not shown.

material. Many cutting edge microscopes use a functionalized phosphor coated sample and a centroiding technique to greatly enhance resolution.

There are many diverse applications and uses for arrays of small mirrors in optical systems, and all of these applications have one thing in common: the DMD. The DMD by its nature of being incredibly compact, and rapidly reconfigurable has enabled a highly reliable method to spatially and temporarily modulate light fields. This thesis works towards examining its use in Multi-Object Spectrometers.

2.6   Spatially Resolved Spectral Imaging

A spectrometer is merely a special kind of instrument that disperses light into its spectral components. Figure 2.7 illustrates how a simple spectrometer works. A spectrometer in its simplest form is composed of an entrance slit, which is used to spatially filter the input object. White light is imaged into the spectrometer entrance slit. The light from the slit is then collimated. This can be accomplished by putting the slit at the focal length of the lens. After the collimating lens, a grating, prism, grism, or another dispersing element is placed into the path. The light is now dispersed into its spectral components. The light is then re-imaged onto a detector. There are many variations on spectrometers, but this represents the simplest scenario. Often times, spectrometers are built with reflective optics so that they can operate over a broad wavelength range. All transmissive optics exhibit chromatic dispersion (wavelength dependent change in the index of refraction). Also, if a grating is employed in a spectrometer, there needs to be order sorting filters in the optical path, because usually only one diffraction order is used to collect spectra. As further sections will discuss, an individual DMD mirror can be used as the entrance slit in the spectrometer. One common metric in spectrometers is the resolving power (Equation 2.1) determined by the ratio of the central wavelength (λ) to the measurable change in wavelength ($\sigma\lambda$). This describes the quality of the spectrometer as a filter. Also, in spectrometers the rejection ratio is the measure of light in the passband over that of light that

makes though the filter outside the passband. A Multi-Object Spectrometer (MOS), can be though of as many individual point spectrometers operating in parallel. Generally, MOS systems are used to coarsely sample the Field-Of-View (FOV). MOS differ from imaging spectrometers, in the sense that most imaging spectrometers are line scanner systems that utilize the platform motion to collect spectra in the along track direction.

$$RP = Q = \frac{\lambda}{\delta\lambda} = \frac{\sigma}{\delta\sigma} \tag{2.1}$$

Astronomers are interested in collecting full spectral information at many spatial locations within the telescope FOV. Conventionally, astronomers use a single slit to examine one object or target at a time. As telescopes become larger, more efficient instrumentation should be used to make the most of the expensive telescope time. A MOS has the ability to select multiple objects within a FOV, thus greatly increasing the data collection efficiency process. Both MOS systems and IFU's collect spectra information from a given scene of interest. MOS systems generally have a larger FOV with sparsely populated slits. Alternatively, an IFU is used to examine extended objects over a smaller field of view but with higher spatial sampling. While the methods in which these two types of systems collect spectral information vary, discussions of both instrument types are included for completeness. Several conventional IFU's and MOS instruments are discussed in the following sections. Collecting hyperspectral information about a scene is very important in both astronomy and remote sensing applications. In astronomy, the multiplexing advantage of a MOS is key for building efficient instrumentation for the next generation large-scale stellar and galaxy surveys.

2.6.1 TIGER and PUMA

The Canada-France Hawaii Telescope (CFHT) is the home to the first multi-object spectrograph. The TIGER instrument involves an enlarger coupled to the telescope focal plane. A spatially filtering micro-lens array was placed in the path. The micro-lens array was rotated slightly so that spectra would not overlay. This light was then collimated, pass through a grism, and then re-imaged onto a CCD. In this instrument, the micro-lens array performs the spatial sampling in the field. The micro-lens array was chosen so that adjacent spectra wouldn't overlap and so that there was separation in the cross dispersion direction between adjacent objects. This instrument's multiplexing advantage on a large 3.6 m telescope was limited by the fact that the micro-lens array was not reconfigurable on-the-fly.

2.6.2 WIYN Hydra and Fiber Based Spectrometers

At the Wisconsin Indiana Yale NOAO (National Optical Astronomy Observatory) (WIYN) located on Kitt Peak, Arizona a clever instrument was developed that robotically positioned fibers into the integral field unit (IFU) at the telescope's focal plane [8]. The instrument, HYDRA, can house 288 fibers and position them into place with xyz positioning robots. Two sets of 96 fibers are installed within each science cable, one set of 2 arc second fibers optimized for the red and one set of 3 arc second fibers optimized for the blue. This instrument was originally tested on the Mayall 4 m telescope and then permanently moved to WIYN (See Figure 2.8).

A prototype IFU array spectrometer (called DensePak) was composed of 91 fibers in a 7×13 rectangle. These fibers were quite large (310 μm), which corresponded to about 3 arc seconds on the sky. These fibers were then fed to a bench top spectrograph (Hydra). An Intensified Charged Couple Device (ICCD) was used to align the fibers in the scene. The throughput of this type of spectrometer was $3 - 7\%$ across the visible region of the spectrum [48]. Other subsequent fiber instruments have been developed such as SparesePak [49]. These types of instruments perform well, however there are issues with centroiding stars into the fiber. This system is very slow between changing targets, and a great deal of light is lost because the fiber fill factor is not 100%, which also means that it is difficult to get spectra of adjacent objects.

Fibers are an appropriate method to couple light from a focal plane to a spectrometer, but have several disadvantages. The coupling efficiently is not optimum for stars and also the exit focal ratio is usually reduced the lights passage through the fiber. For example, if a telescope operates at $f/8$ the resulting output cone from the fiber is approximately a $f/16$ beam. Also there is a huge variance of the throughput of a fiber depending on where the star is positioned relative to the center of the fiber. Therefore it is very important to centroid the fiber and star accordingly. A new type of square clad fiber may solve some of these issues, but also at the expense of greater light loss [50].

2.6.3 GMOS

Another ground-based MOS is the Gemini's GMOS instrument [9]. This instrument uses a machined plate to create many slits that can then be utilized in the MOS. An initial observation with the telescope is performed with the FOV, and the positions for science objects are recorded. The instrument was designed to maintain image quality over the 5.5 arc minute FOV. A significant amount of research has gone into making cleaner slits (slits with perfectly planar edges) by using different material types for the manufacturing of the slit mask and different cutting techniques. While it is advantageous to have the ability to form slits anywhere in the focal plane (alternatively a DMD can only create discrete slits where the DMD mirrors are positioned in a rectangular grid), there are a lot of problems with this approach. Edge smoothness, edge parallelism, limited material thickness, sag under gravity, opaqueness over 3000 Å to 25 000 Å, low reflectance, stable, corrosion resistant, and low CTE are the requirements for the slits in GMOS. Only one metal material met these strict requirements, invar, but other materials such as graphite and carbon fiber were investigated for use as the slit material. Unidirectional carbon fiber sheet of 190 μm thickness was used to make the masks, because it has the highest specific stiffness and lowest CTE. An 18 Watt Nd:YAG laser system was used to cut the holes in the carbon fiber sheet. A mask handling system was developed to move these masks in and out of the IFU. The masks on average take less than one hour to fabricate [52]. However due to manufacturing time constrains, initial observations are completed on the first night and science observations with the new slit mask are completed on a subsequent night.

2.6.4 DEIMOS

DEep Imaging Multi-Object Spectrograph (DEIMOS) was built at the Lick Observatory [53]. It has a high spectral resolution and range 5000 Å and $R = 6000$. The instrument can be run in several different modes, long slit spectroscopy, up to 100 targets per mask, or 1000 point sources with narrow band filters. It has a large $8k \times 8k$ detector array. The slit masks holes in DEIMOS are fabricated from thin sheets of aluminum,
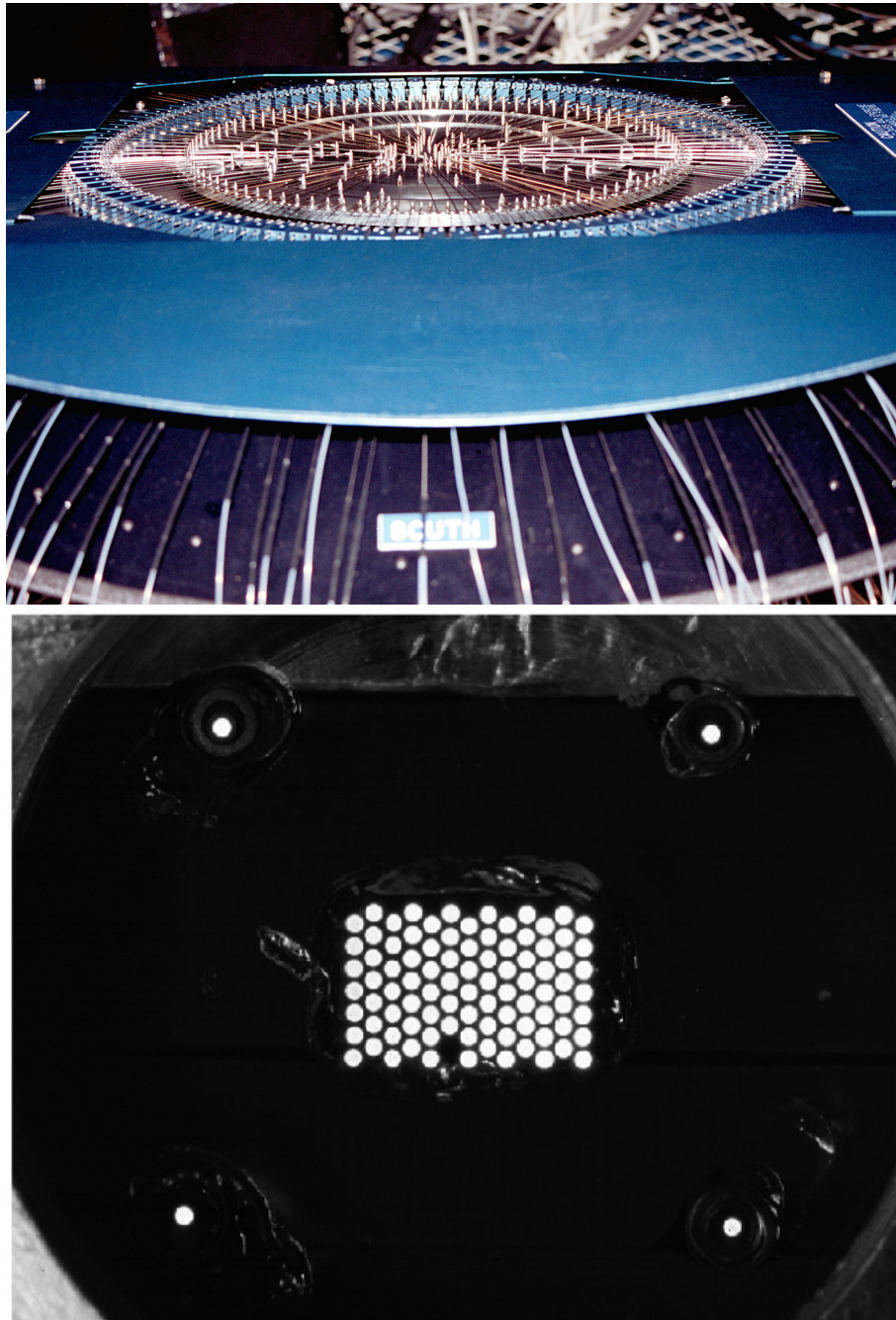
Figure 2.8: Hydra fiber positioning instrument mounted on the Mayall 4 m telescope (Top) [51]. (Bottom) DensePak IFU instrument [48].
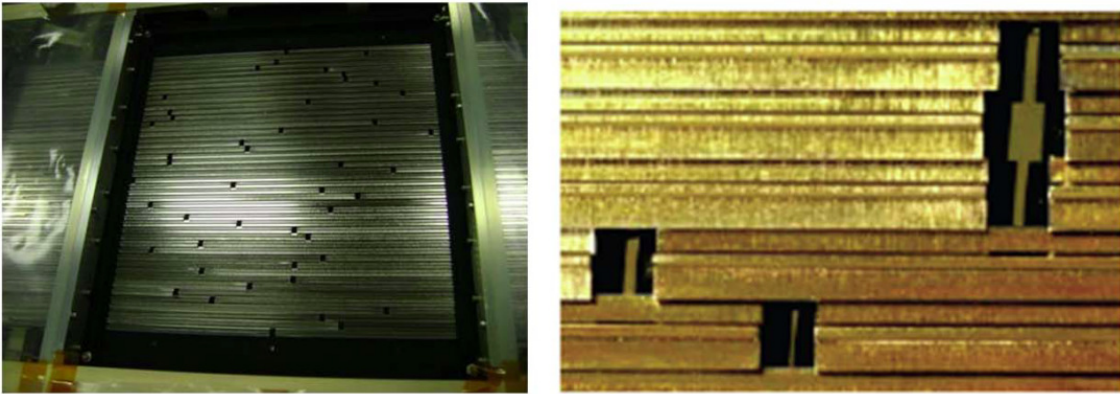
Figure 2.9: (Left) Complete Configurable Slit Unit (CSU). (Right) Magnified image showing close up of the slits [54].

which sit in a cassette (which can hold up to 11). An arm positions the slit masts onto a curved form that deforms the slit mask to approximate the curved form.

2.6.5   Multi-Object Spectrometer For Infra-Red Exploration (MOSFIRE)

A new MOS system is being built for the Cassegrain focus of the 10 m Keck 1 Observatory [54]. The design of the instrument allows operation from $0.97 - 2.45\,\mu m$ over a $6.14' \times 6.14'$ FOV. The slit width is 0.7″ and the instrument has a resolving power of $R = 3000$. This instrument does not use a DMD for the spatial light modulator; instead 46 slits can be formed by using the cryogenic Configurable Slit Unit (CSU) (See Figure 2.9). The slits are defined by moving bars laterally from both sides of the focal plane. The advantage of this system over one that uses punch plates is that the slits can be reconfigured in 5 minutes without thermally cycling the instrument (i.e. warming it to room temperature). This system was developed by ESA as one of the candidates for the slit masks on James Web Space telescope by the Swiss Center for Electronics and Micro Technology (CSEM). The CSU has two main components an indexing frame and a support frame. The indexing stage utilizes a voice coil actuator (similar to the type of mechanism that moves a speaker) to move each of the bars incrementally. A Linear Variable Differential Transformer (LVDT) is used to track the position of each of the bars. A brake and ratcheting setup is to move bars either in pairs or individually. In addition, the bars can be aligned to create longer slits. This CSU was build with off-the-shelf components. The instrument used a H2-RG $2k \times 2k$ HgCdTe from Teledyne Imaging Sensors with SIDECAR ASIC electronics. Figure 2.10 shows the size of this instrument. The instrument has very high throughput in each of the bands (30%). This instrument was extremely large and the cost to build optics and mechanics to support this large mechanism makes this kind of instrument unpractical to many smaller observatories.

2.6.6   James Web Space Telescope (JWST)

In 1990, Hubble Space Telescope (HST) was launched by National Aeronautics and Space Administration (NASA). In the mid $1990's$, NASA was already working towards the Next Generation Space Telescope (NGST). This project became the James Webb Space Telescope (JWST) after the design was selected for this telescope. During this period, NASA was looking for a way to build a space-borne MOS.
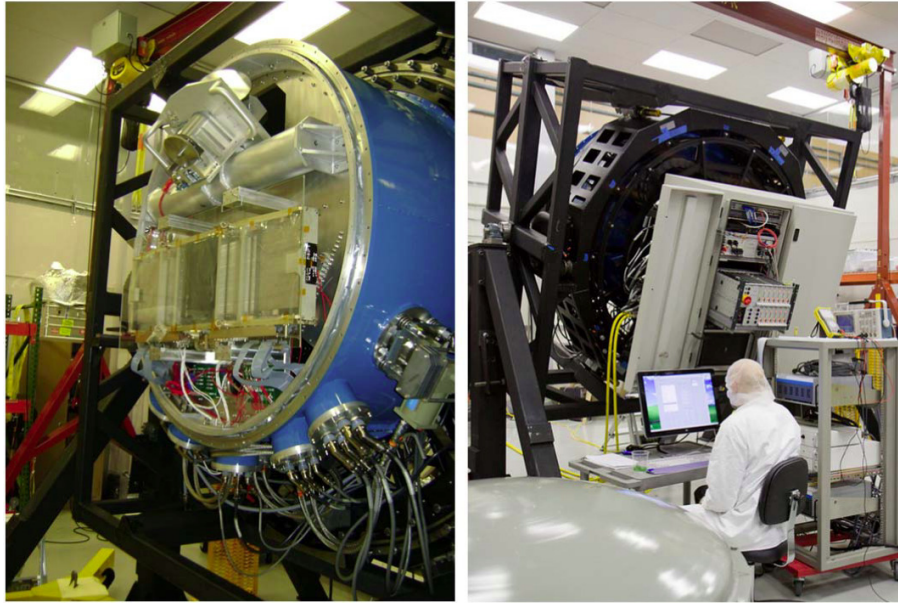
Figure 2.10: (Left) Front of the MOSFIRE instrument shows the CSU. (Right) Instrument electronics and the backside of the MOSFIRE instrument [54].

The Near Infrared Spectrograph (NIRSpec) in JWST is composed of Micro-Shutter Arrays (MSA) [55]. NASA chose to develop a custom-built solution for JWST rather than using commercial off-the-shelf device. The development of the MSA at GSFC was a remarkable endeavor to take on. The devices perform as expected, however the MSA cosmetic quality is rather disappointing. The contrast of these devices is greater than $100,000 : 1$. It was measured by simply taking an extended $f/12$ source and illumining several micro-shutters. The ratio of the open shutter intensity to that of the close shutter intensity was the contrast ratio. The operating environment of JWST makes the shutter design quite complicated. The requirement for NIRSpec is to have the shutters operate at 37 K. Stiction and mechanical effects are very challenging issues for any MEMS component operating at 37 K. In addition, building electronics to operate at this temperature was also a challenge. The space qualification of the MSA is an appropriate example of the requirements for a MEMS device to be ready for space flight. It has to be shown to have the optical characteristics to complete the mission goals. It also has to be able to operate at the temperature of the spacecraft or the temperature required to not contribute to the infrared background. The MEMs device also has to operate reliably in a radiation environment.

2.7 DMD Based Spectrometers

2.7.1 A Novel DMD Spectrograph

In 1995, a group at the department of chemistry at the University of Florida used TI's DMD mirrors to evaluate using a DMD array in visible spectrometer [56]. These mirrors were $19 \times 19\,\mu m$. This array was a linear array of micromirrors 2×840 mirrors. The light from a grating was focused onto this micromirror array. The spectrum was measured by stepping through the mirrors and sending one wavelength of light to a photo-diode at a time. A great deal of scatter was present in all of the measurements (typically 8 times the signal level) and the cause of this serious scattered light was determined to be caused by the

DMD light shield. The measured spectral resolution was 11.5 nm, when theoretically it should have been less than 1.0 nm. The light shield was not removable from this model, and therefore limited the amount of useful information that could be obtained from this linear DMD chip. This light shield was improved in subsequent designs, as the fill factor is greater. Transmittance curves were generated by sequentially stepping through two different mirror pairs. Overall it was determined that with an improved DMD chip a UV-Visible spectrometer should be possible with a spectral resolution of less than 1 nm This spectrometer, even with very limited performance, paved the way for future spectrometer designs incorporating TI's mirror technology.

2.7.2   Rochester Institute of Technology Mulit-Object Spectrograph (RITMOS)

The concept to use a 2-dimensional array of micromirorrs as a multi-object spectrograph originated at RIT. Initial measurements to assess the utility of DMDs for use as a slit mask in astronomy were very encouraging. This led to the development of RITMOS (Rochester Institute of Technology Multi Object Spectrometer). Central to RITMOS operation is a DMD that permits the spatial selection of targets and the acquisition of many spectra simultaneously. The focal plane of the telescope at which RITMOS is to be used was re-imaged using relay optics operating at $f/8.5$ onto a DMD. The target selection process occurs at this intermediate focal plane (the DMD). An Offner relay with two fold mirrors re-images the DMD onto a peltier cooled CCD that records the image. The light not deflected into to the imaging channel instead is reflected into the RITMOS spectral channel. In the spectral channel, the light travels through a collimator operating at $f/7.62$, through a stop, and then is dispersed by a $1200\frac{l}{mm}$ grating. This light is then re-imaged using $f/3.35$ optics onto a second CCD that records the spectra. A spectrum can be determined for each of the slit positions selected by the DMD. The spectral side of the RITMOS was designed to operate from 390 nm to 490 nm with a spectral resolution of 0.703 Å for a two mirror wide slit [10]. A simple transmission grating spectrometer was constructed to transmit both the zero order and first diffraction order to a CCD imager [57]. Figure 2.11 shows the basic configuration for the MOS system. The DMD works effectively as an imaging coronograph to selectively block out elements of the astronomical field. The rejected light can be used for a number of purposes including to record a broadband image as to allow for confirmation of motion or simply recording the complement of the spectrally analyzed channel. Other advantages using a DMD at an intermediate focal plane include increased well depth, by selectively masking out brighter regions of an image after long exposure times. DMDs mirrors for astronomical spectrometers are kept in a fixed mirror position for an extended period of time. At this time, TI only sold electronics that cycled DMDs at 60 Hz for video applications. A special electronics system had to be designed to latch the mirrors for an extended time.

2.7.3   IRMOS

As part of a feasibility study for JWST, (at the time referred to as NGST) a MOS using MicroMirror Arrays (MMA) was developed by Space Telescope Science Institute and NASA Goddard Space Flight Center (GSFC). This instrument was called IRMOS [11]. The arrays to be used were the same 17 μm DMDs that were incorporated into RITMOS. These DMDs were produced in the late 1990$'s$ by Texas Instruments (TI). A Rochester based company Rochester Microsystems designed and built a special set of electronics that were used for both RITMOS and IRMOS. TI didn't have discovery kits available at this time, because they
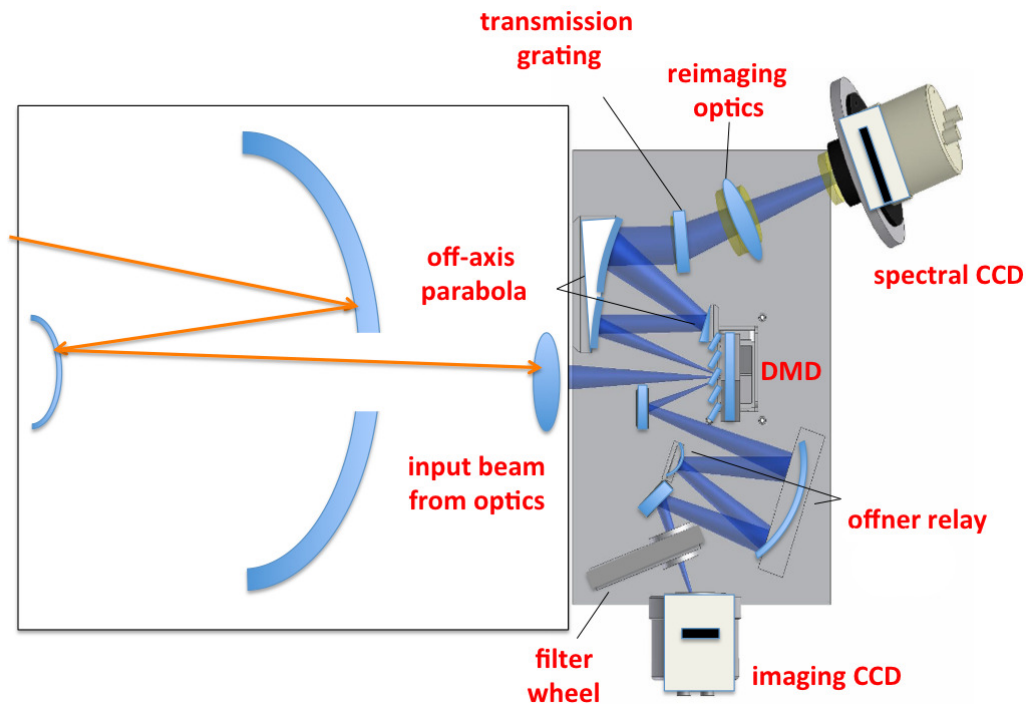
Figure 2.11: RITMOS optical path is shown here. There are optical channels in this instrument: an imaging channel and a spectral channel.

were interested in protecting their technology and limiting its utility to the projector and rear projection television market. The IRMOS instrument was an infrared version of RITMOS that used a complex optical design, and only one channel on the DMD. A cryogenic dewar surrounded the DMD and optical system, the instrument operated at $-40\,^{\circ}$C. IRMOS currently resides at the Kitt Peak National Observatory. IRMOS operates in the J (1.25 µm), H (1.65 µm), and K bands at spectral resolutions of 300, 1000, and 3000 correspondingly. IRMOS utilized the DMD in the projector configuration (DMD illuminated 20° off axis).

2.7.4 EUCLID (Formerly SPACE)

The Euclid mission is sponsored by the European Space Agency (ESA). Euclid started as the Spectroscopic All-sky Cosmic Explorer (SPACE) [58]. Its primary goal is to build a three dimensional evolutionary map of the universe by taking near-infrared spectra by measuring redshifts from $0 < z < 2$. TI's Cinema DMDs were proposed to be flown in EUCLID as the slit mask in the MOS. Cinema DMD chips are very costly and difficult to obtain, even directly from TI. Four separate DMDs were proposed to simultaneously take spectra over a wide FOV. Initial gamma-radiation tests of the DMDs have been completed by ESA (European Space Agency) for this mission. Several devices were illuminated with gamma-radiation and the DMDs functioned properly up to a dose of 20 krads. Proton and heavy-ion testing were not completed. These devices have been shown to operate to $-40\,^{\circ}$C and thus are candidates for use in a cooled infrared instrument [59]. Other than these very limited results, no additional details have been released on space qualifying the Cinema DMDs.
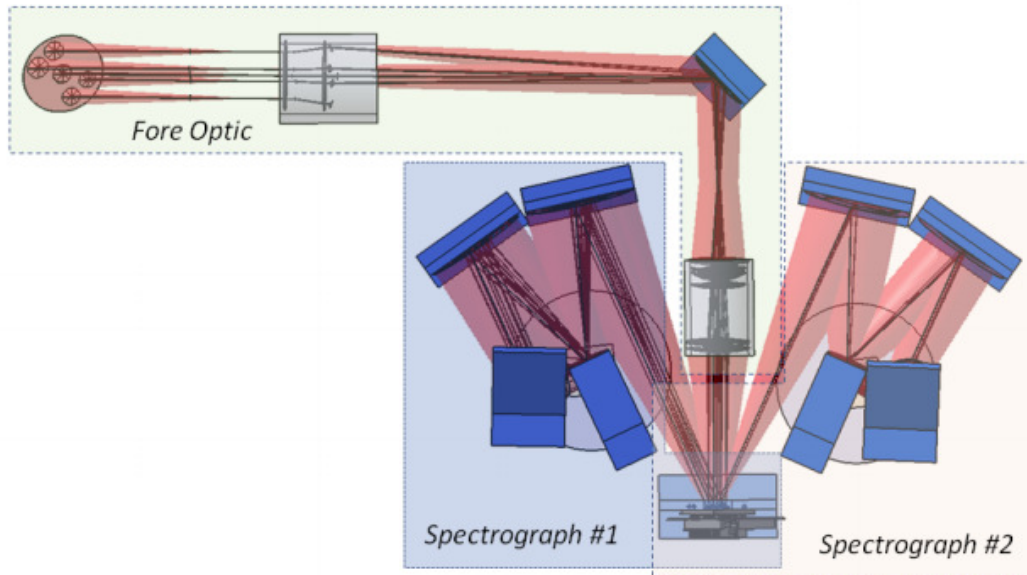
Figure 2.12: BATMAN optical design is shown here. Two-symmetric channels are illuminated by a set of fore-optics illuminating the DMD at normal incidence [60]. This design is similar to RITMOS.

2.7.5   BATMAN

One of the most exciting DMD instruments under development is the BATMAN instrument. The DMD Cinema chips that were slated for the EUCLID mission are now being used in this ground-based spectrograph. This instrument will be a demonstrator instrument on the Galileo telescope [60]. BATMAN is a spectrograph similar to RITMOS. A set of fore-optics illuminate the DMD at normal incidence. The two channels are symmetric and the DMD is rotated 45° relative to the z axis of the focal plane to make the two arms lie on the same plane. It is a visible instrument designed to operate from 400 nm to 800 nm. The instrument is supposed to have a 4.5 × 4.5 arch minute FOV with a $f/4$ beam illuminating the DMD with a pate scale of 0.2 arc seconds per micromirror. It is designed to have a spectral resolution grater than 250. Figure 2.12 shows the optical path of the instrument. The optical bench prototype instrument (ROBIN) has been built and testing is underway [61] [62].

2.7.6   Technology Readiness Level (TRL)

The DMD is a natural candidate for use in a space based MOS. At the inception of this study, the DMD was rated at a TRL level 3. Contrast measurements, proton radiation testing, low temperature performance (cooled to below −40°C) had not been completed. The DMD is highly reliable as commercial SLM, but has not been qualified for space. In order to raise the DMD's TRL, the current thesis examines three areas: (1) the optical characteristics of the DMD (2) the functionality of DMDs when operating cold (3) the DMD lifetime and failure mechanism in the proton environment. The following chapters will examine these issues in detail.

2.8 Summary

Recently there has been interest in using multi-object spectrometers in applications beyond the field of astronomy [63]. A feasibility study has been initiated at RIT to generate an end-to-end model of a vehicle tracking system and determine expected performance when using the RITMOS instrument. To achieve this DIRSIG [64], a software package developed at RIT was used to generate synthetic Earth scenes. This package is capable of generating hyperspectral image cubes of synthetic scene data and can propagate this radiation to the aperture of a sensor. This software model was used to generate synthetic input imagery. This input data is then convolved with the system parameters of RITMOS to determine expected performance. Characterizing RITMOS optical properties are essential to building back-end models and making sensor performance predictions. In particular, no information was available on the scattering properties of the DMD when used at a focal plane of an optical system to describe the aggregate light adjacent micromirrors scatter into a target's spectrum. This parameter is key to determining signal-to-noise and threshold detection limits. To quantify this parameter, an apparatus was assembled to measure the stray light function for a single micromirror. This is discussed in Chapter 3.

CHAPTER 3

DMD OPTICAL CHARACTERIZATION

The DMD is a remarkable MOEMS. Its unique design creates some distinctive optical characteristics. These will be discussed in the following sections. First, some of the implications of utilizing an DMD in a optical system are discussed, such as multiple ways to orient the DMD within the optical system, the effects of a tilted focal plane, and diffraction properties of the DMD. These have important implications for designing an optical system that uses a DMD, whether it is a projector, a MOS, or another novel optical system. Secondly, a description of the building of a spot-scan system to understand the effects of illumining only part of a DMD mirror will be presented. The spot scans not only helped to build a sub-mirror reflectivity model, but also enabled the contrast of individual mirrors to be determined. Third, optical effects associated with the DMD packaging and the reflectivity of the aluminum alloy used to make the DMD mirrors is discussed. Through examining the DMD optical characteristics, more efficient scientific instrumentation can be built in the future.

3.1 DMD Optical Effects

Scattering by rough surfaces can be a significant source of stray light. There are two general regimes for scatter from rough surfaces. Scattering by object size on the order of the wavelength of light used is referred to as Mie scattering [67], and scattering by particles much smaller than the wavelength of light is referred to as Raleigh scattering [68]. In a DMD, the inherent aluminum surface roughness would result in Raleigh scatter, which contributes to the diffuse scatter component. This type of scatter is wavelength dependent, because the surface roughness remains constant while the illumination wavelength changes.

3.1.1 The Multiple Optical Configurations of a DMD

DMDs can be illuminated in ether normal to the DMD as was done in RITMOS, or at 20° off-axis, as in digital projectors. The illumination angle of incidence with the DMD array determines the location of the secondary focal plane in a MOS. Figure 3.1 shows two such configurations. The configuration used in the IRMOS instrument and all digital projectors is to illuminate the DMD 20° off-axis along the diagonal of

the DMD chip for a 10° tip angle DMD (or 24° if the DMD tilt angle is 12°). The angle of incidence with an "*on*" pixel is 10° and the light is reflected out normal to the DMD chip. The "*off*" state mirror pixels are illuminated at an angle of incidence of 30° so the light is reflected to 40° normal from the chip. It is also important to note that when the DMD is operated, there is a set of mirrors surrounding the active array (called the Pool of Mirrors (POM)) that are always in the "off" position. The purpose of these mirrors in a digital projector is to provide a dark border region that is always dark. Field stop is etched on the inner glass layer. The position of this field stop is slightly asymmetric, to block light at the edge of the DMD from entering the projection optics. The alternate configuration (Figure 3.1 bottom) utilized in the RITMOS instrument is the illumination normal to the DMD. This means that the angle of incidence with an individual mirror is 10°. The individual mirrors tip about the pixel diagonal, so this is 10° tilt about the *XY* axis.

3.1.2   Tiled Focal Plane (Scheimpflug Principle)

When the DMD is illuminated on-axis, such as in RITMOS, the re-imaged focal plane must be tilted to match the DMD image position. Figure 3.2 shows a tilted object plane being imaged onto a tilted focal plane. This concept is referred to as the Scheimpflug principle [66]. The object plane is at the $2f$ point for this lens. Three points are imaged using the ray-tracing package FRED [65]. FRED is a non-sequential ray-tracing program. This relationship between a tilted object plane and a tilted image plane is related by equation 3.1. f is the focal length of the lens being used, and s_0 is the object distance s_i is the image distance. Also, the optics must be designed to keep illumination constant across the DMD, which can be quite challenging design problem. If the illumination variation is not minimized in instrument design, then this effect can be mitigated by performing flat fields with the instrument prior to observing. The tilted focal plane tollerancing becomes an issue with fast (large aperture) systems, because they have a smaller depth of field. However, when using a DMD the telescope focal plane is must be re-imaged on to a secondary tilted focal plane.

$$\frac{1}{f} = \frac{1}{s_0} + \frac{1}{s_i} \tag{3.1}$$

$$\Delta phase_{\texttt{max}} = \frac{2\sqrt{2}M_W \sin(\theta_{tilt})}{\lambda} \tag{3.2}$$

Across an individual mirror, there is a phase shift that is related to the width of the mirror and the mirror tip angle (Equation 3.2). This phase effect can be mitigated by minifying the image of the micromirror onto the re-imaged focal plane. This is also normally done so as to match larger mirror pitch DMDs to smaller pixel sizes on commercial image sensors. The equation for longitudinal magnification is shown in Equation 3.3.

$$M_L = -\frac{f^2}{x_0^2} \tag{3.3}$$

Projector Configuration Tilt =10 Deg.

Cover Glass

Air In Package

Substrate

RITMOS Configuration Tilt =10 Deg.

Cover Glass

Air In Package

Substrate
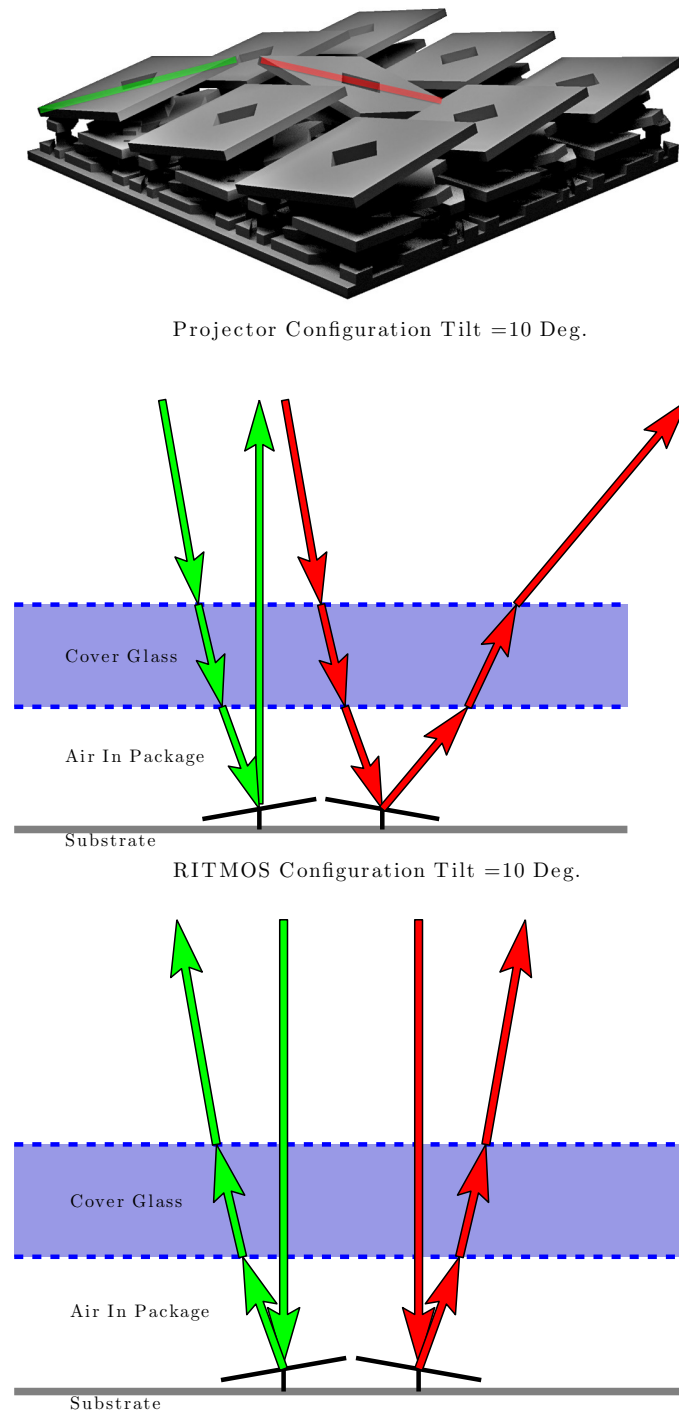
Figure 3.1: (Top) 3-dimensional CAD drawling of TI 10° DMD. Two red lines show the cross section of two pixels, which are shown in the following illustrations. (Middle) Left most pixel is tilted 10° to the left and the right mirror is tilted 10° to the right. This configuration used in digital projectors and the IRMOS instrument. (Bottom) Configuration used in the RITMOS instrument. In this configuration, the device is illuminated from above and the light is reflected 20° off axis symmetrically.
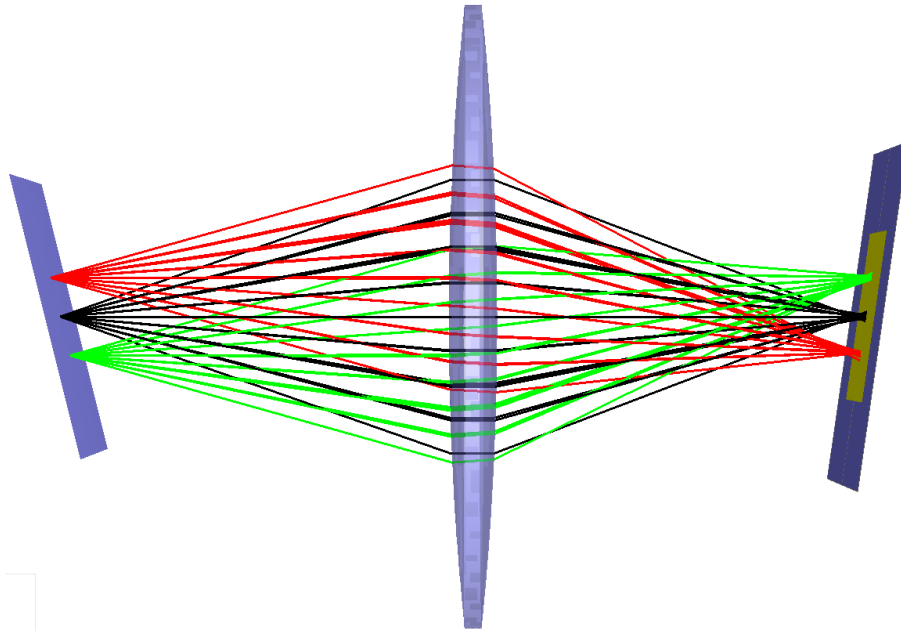
Figure 3.2: Scheimpflug principle is illustrated here. Tilted object plane (left) is imaged as a tilted image plane. This is a consequence when utilizing a DMD because it must be either be illuminated off-axis or re-imaged off-axis.
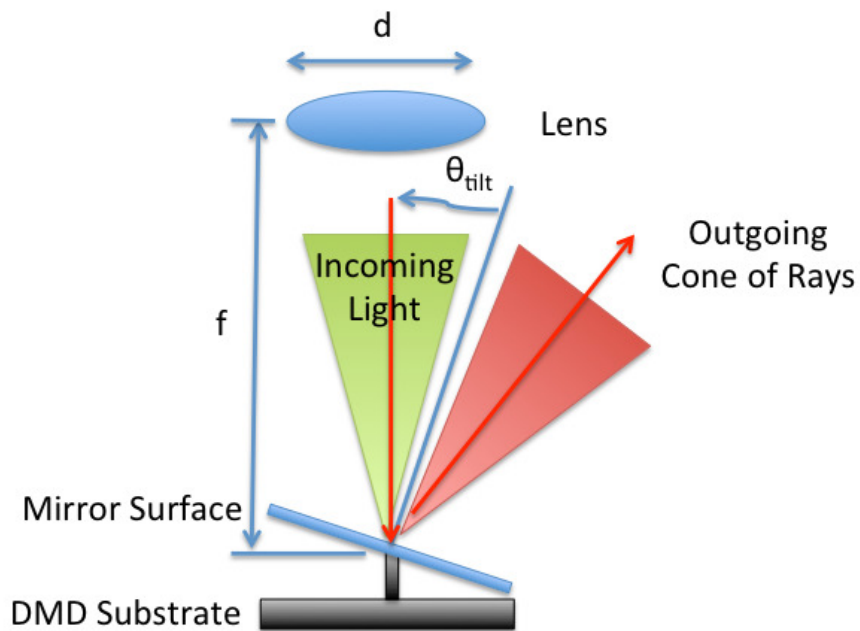
Figure 3.3: Incoming beam can be separated from the outgoing beam when the f/# is larger than that specified by Equation 3.4.

3.1.3 Beam (Cone) Separation

A fundamental limit to the size of the $f/\#$ illuminating a DMD, is determined by the DMD tip angle. The DMD must be able to separate the incoming and outgoing cone of light. Figure 3.3 illustrates this limitation for a single mirror, and Equation 3.4 shows the mathematical formulation of this limitation. For a single mirror, the most important parameter is the tilt angle (θ_{tilt}). The illumination $f/\#$ limitation becomes larger as the DMD format size increases, because the separation criteria must exist over the whole FOV.

$$f/\#_{lim} = \frac{1}{2tan(\theta_{tilt})} \tag{3.4}$$

3.1.4 Slit Diffraction Effects

A DMD is a complex array of rapidly reconfigurable slits. The pitch of the mirrors contributes to the diffraction efficiency of these DMDs. Equation 3.5 shows that the far-field (Fraunhofer) diffraction pattern can be modeled as a $sinc^2$ function for a single slit (Equation 3.5). A plot of the diffraction pattern for 4 different slit sizes is shown in Figure 3.4. Slits of width 100 μm are shown as a reference for JWST (This is the size of the MSAs). It can be seen that as the slit size decrease a larger optics is needed to collect all of the diffracted light from the slit. However, there is a fundamental limitation in the $f/\#$ that can illuminate or subsequently re-image a DMD. To make more efficient optical systems, it is therefore important to use fast enough optics to collect sufficient light for the reconstruction process, or to use larger slits, so that a majority of the light isn't diffracted outside the spectrometer. A 7.6 μm slit is also shown, because the size of the mirrors on TI's Pico projectors. If the pitch continues to be reduced by TI, it will limit the DMD contrast, and make them less useful for scientific instrumentation.

$$I = I_0 sinc^2 \left(\frac{a\pi sin(\theta)}{\lambda} \right) \tag{3.5}$$

The diffraction efficiency is closely related to the single slit diffraction pattern. The diffraction pattern for a single slit diffraction is highly dependent on the wavelength and pitch (a as shown in equation 3.5). When the collection aperture re-imaging the DMD is small, the diffraction efficiency drops. Figure 3.5 shows the diffraction efficiency for several different focal ratios, $f/3$ being the fastest optical system shown.

3.1.5 Mirror Structure and Hinge Orientation

The DMD mirror surface is constructed with aluminum. Each mirrors tips about the diagonal on a torsional hinge located below the reflective mirror structure. By making the mirrors tip about their diagonal, the TI engineers were were able to obtain significantly higher contrast ratios. This can be easily understood using Fourier optics. The mirrors edges produce a great deal of diffracted light. Because the mirrors tip about the diagonal, the diffracted light from the "off" state mirrors is diffracted outside of the projection aperture. Figure 3.6 illustrates this concept. Because the mirror tips about the vertical axis the output aperture must be either on the left or right side. The edges of the pixels are aligned with the hinge in this hypothetical example. The diffracted orders are strongest along the mirrors edges. In the middle portion of Figure 3.6,
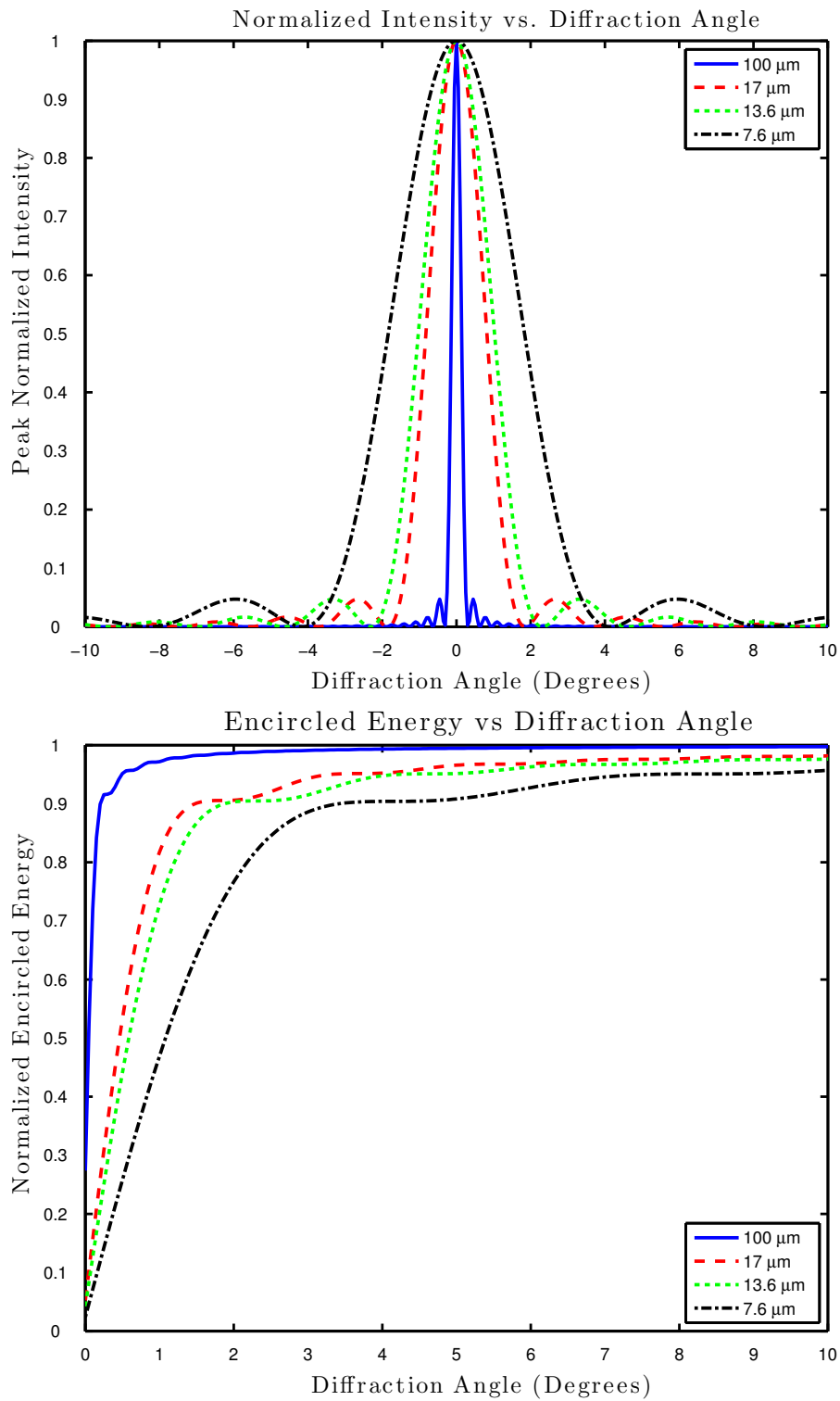
Figure 3.4: (Top) Fraunhofer diffraction pattern from a single slit for 550 nm light. (Bottom) Normalized encircled energy .
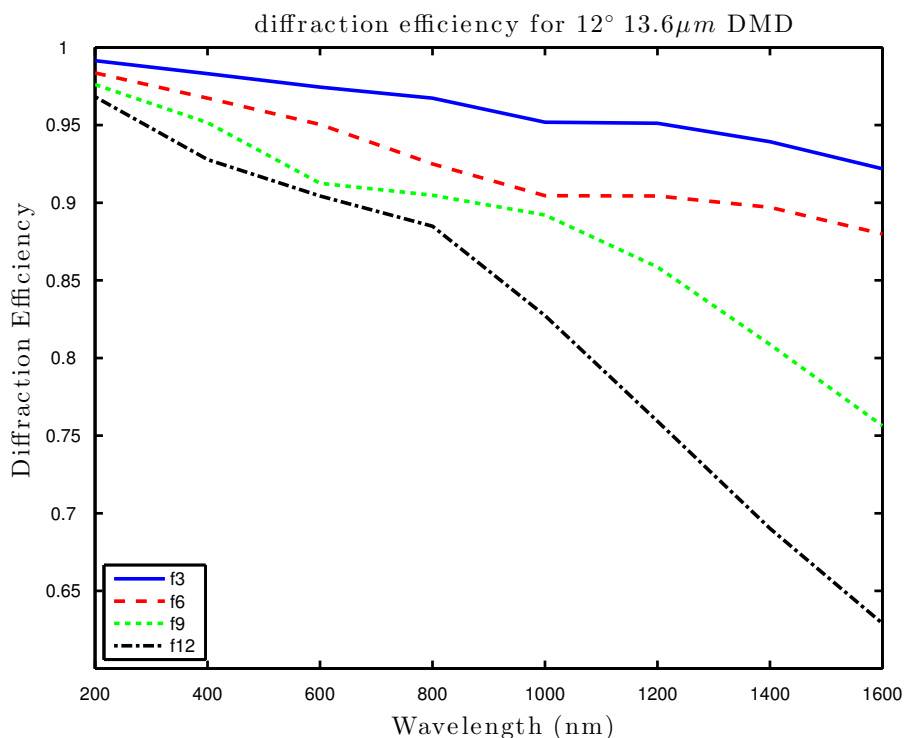
Figure 3.5: Diffraction efficiency as a function of wavelength for various focal ratios.

the pixel has been rotated $45°$, but the hinge is still orientated along the vertical. In this example, the mirror edges are not in the same axis as the hinge. The diffracted light from the mirrors edges would no longer be reflected to either of the apertures. The bottom image has the output apertures superimposed above the diffraction pattern. Since the majority of the diffracted energy gets diffracted out of either output aperture, much higher contrast can be achieved. In short, the diffracted light from the edges of the off state mirrors does not enter the projection aperture.

3.2 DMD Intra-pixel Sensitivity Variations (Spot Scan)

Due to the geometric effects in a DMD, there are intra-pixel reflectance variations across an individual mirror. The goal of this section is to illustrate the magnitude of this effect and create a reflectivity model. The spot scan experiment involved creating an experimental apparatus to collect data to determine what the scattered light. Several different version of the experimental apparatus were investigated prior to settling on the final design. The experimental setup consisted of several different components and each was individually optimized. The experimental setup involved selecting an appropriate source of photons. Next, these photons had to be collected by an optical element and focused down to a point that could be imaged on to the micromirror array. This light was reflected off the DMD and was collected by another optical element, which focused the light onto a detector. The DMD was translated across the optical spot, rather than moving the slot lens or pinhole. This way same spot illuminated each position in the DMD.

An experimental apparatus was realized to measure stray light for a DMD as used in the RITMOS instrument. A novel scanner was designed to project a sub-mirror sized spot onto the DMD. The DMD under test is shown in Figure 3.8. The main sources scattered light from a DMD mirror are:
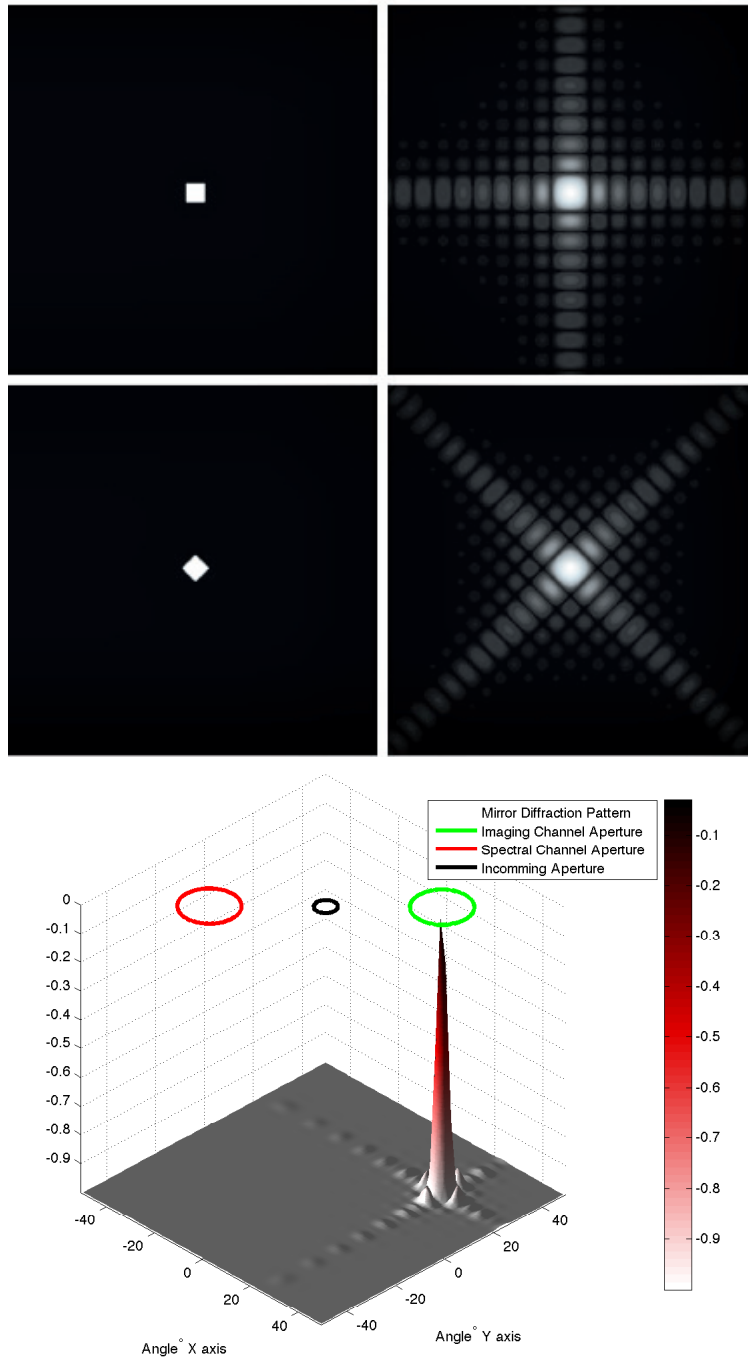
Figure 3.6: (Upper Left) Single DMD mirror with a tilt axis along the vertical direction. (Upper Right) FFT of the DMD on the left. (Middle Left) Single DMD mirror with the tilt axis along the diagonal, the array is rotated, so that the hinge is shown along the image vertical. (Middle Right) FFT of the image on the left. (Bottom) FFT of the rotated diagonal aperture is plotted with two apertures superimposed above the angular space.
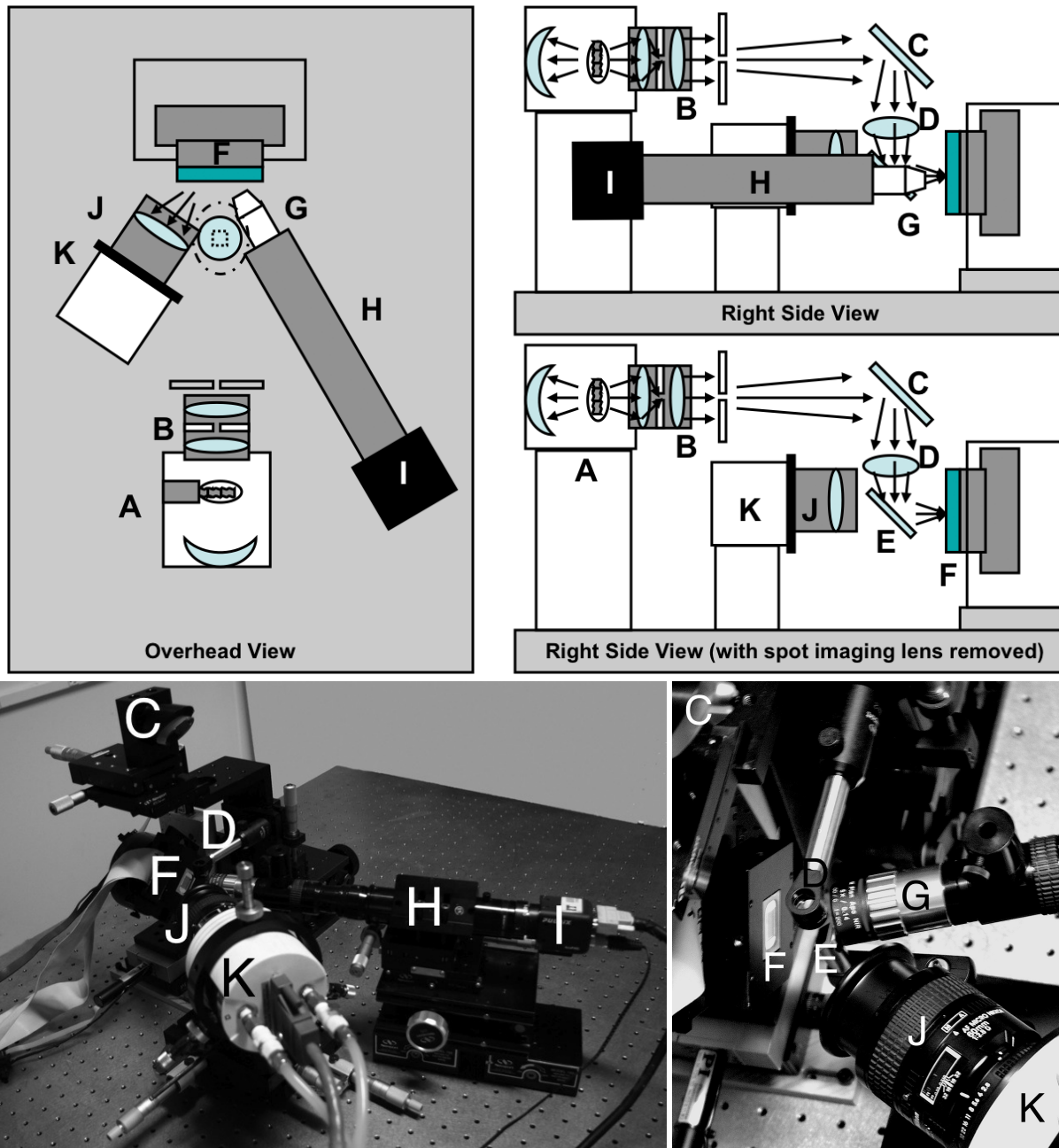
Figure 3.7: Experimental setup showing the source and the scatter measurement system. (Top) Images shows a sketch of the system A. is the Oriel Q series light source. B. Oriel collimator assembly. C. is the first fold mirror in the periscope system. D. is the Thorlabs spot projection lens. E. is the second fold mirror in the periscope system. F. is the DMD assembly mounted to a rotation stage. G. is the Mitutoyo microscope objective. H. Is the Navitar lens tube. I is the spot-imaging camera. J. is the Nikon macro lens. K. is the Scatter-collecting camera. (Bottom) Two photographs were taken to show the laboratory setup.
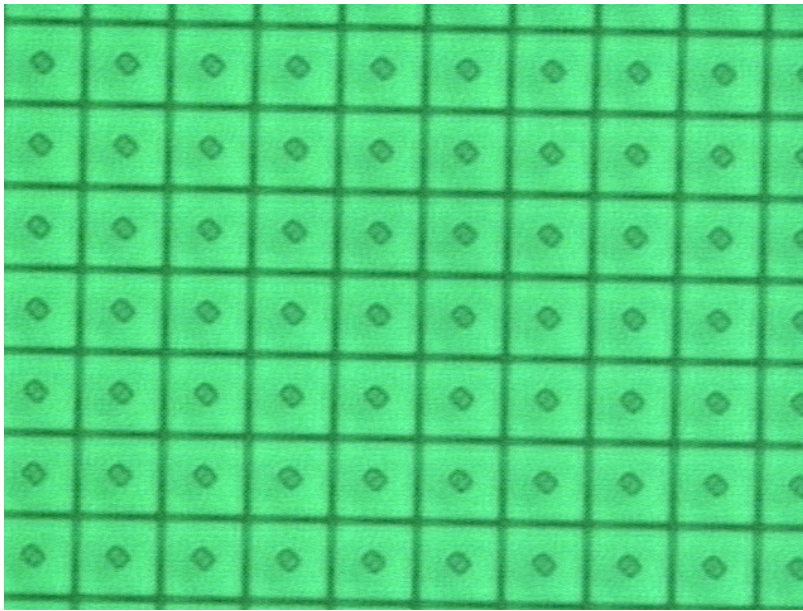
Figure 3.8: RITMOS DMD was placed under a microscope for inspection. Notice the large via structure and relatively large gaps between mirrors.

- the via located in the center of the mirror
- the edges of the mirror
- multiple scatter events that occur underneath the mirror that propagate into the field of view of the detector
- the protective window that is placed above the DMD in the optical path (an external source of scatter).

3.2.1   Light Source

A laser was initially thought to be an ideal light source, because of its high power and the availability of optimized optics. A HeNe laser was initially used as a light source. A Keplerian style beam expander was built and the light was focused onto the DMD array. A screen was placed approximately a meter away from the DMD. An image of the screen was then taken using a digital camera. It was determined that it would be very difficult to use a laser source due to speckle patterns caused by random interference of the beam with itself (Figure 3.9). Figure 3.9 also illustrates an x-shaped pattern surrounding the central lobe. This stray light is due to light scattering off the edges of a mirror. In view of these problems a tungsten filament source was chosen that has a wider spectral output and can be easily filtered so as to examine the scattered light with wavelength.

An Oriel Q-series tungsten filament source was used with a $f/1.0$ collimator lens assembly (*PN*#60076). This housing also contained a rear reflector to refocus the light, improving throughput. A 25 µm pinhole was then used to further spatially filter the light source. An optically stabilized power supply provided power to the 100 W bulb, which was the maximum rated power for this particular light source enclosure. The filament was aligned to the collimator by putting a laser through the collimator lens (Figure 3.11). Additionally, an enclosure was built on top of the light source collimator assembly so that light from the heat vents would not reach the micromirror array. Care was taken to make the enclosure large enough so that the there was enough room for the lamp to cool sufficiently. Before taking any measurements, the light
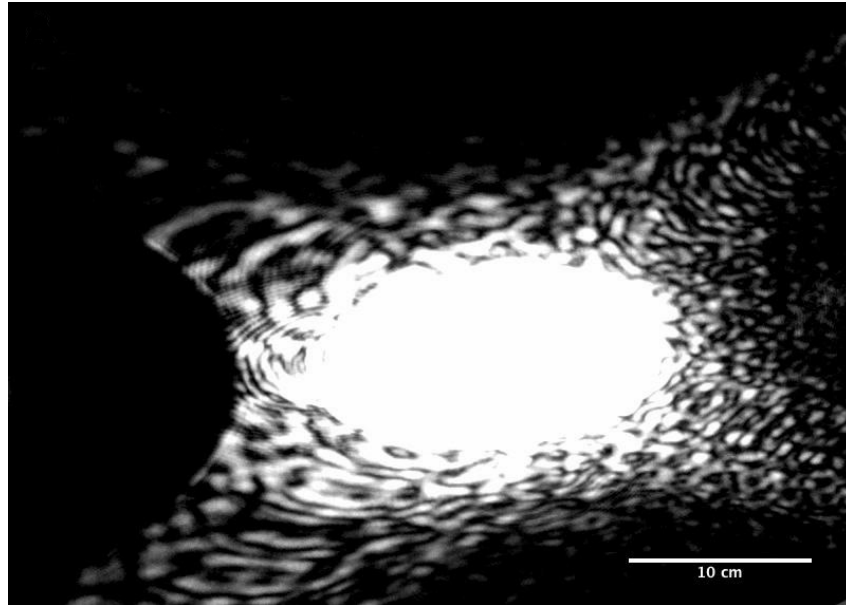
Figure 3.9: Laser source was focused through a lens onto a micromirror array. Speckle pattern was then reflected onto a screen and imaged.
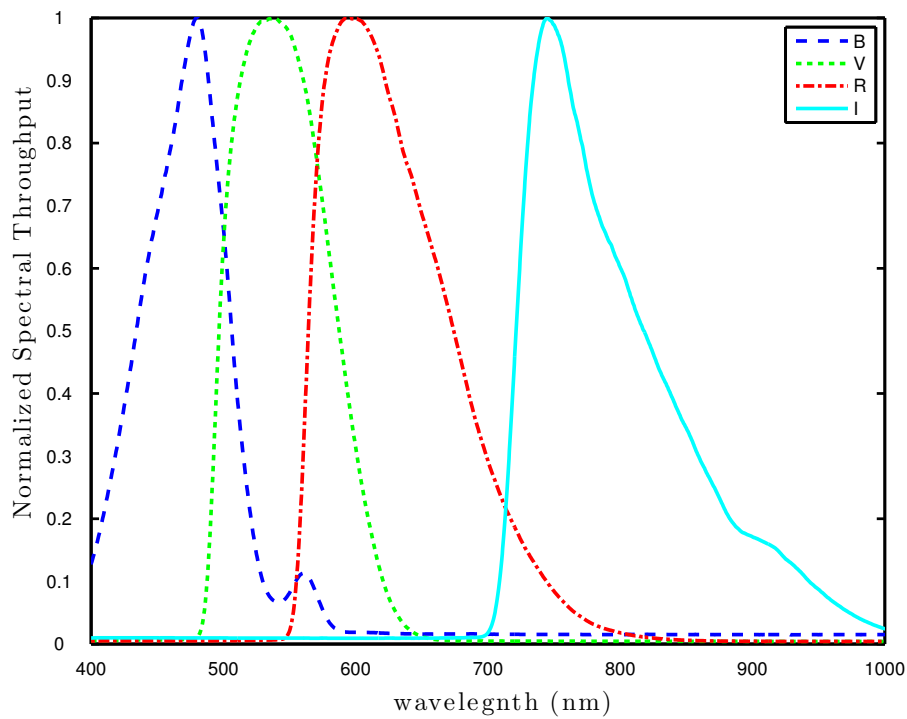
Figure 3.10: Throughput of the B, V, R, and I Bessell filters is convolved with the output white light spectrum and is shown here. This data was measured by using a Ocean Optics USB2000 spectrometer.
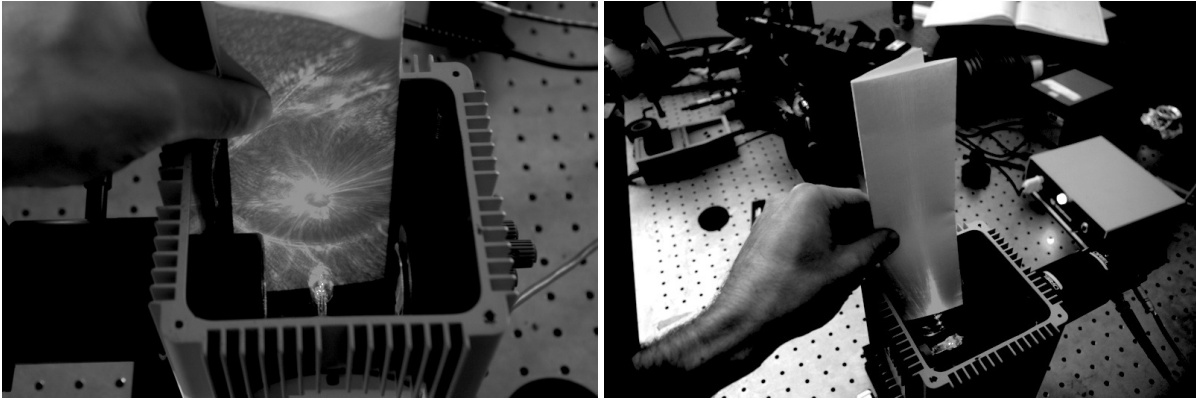
Figure 3.11: Oriel Q-series light source's filament was aligned with a laser by projecting the laser backwards through the collimator system. Using the scattered light from the filament, it was determined that the filament was aligned to the center of the collimating lens.

source was turned on for a period of time (approximately 1 hour) and allowed to thermally stabilize. The light source was rated to have an *RMS* stability of 0.5%. Figure 3.10 shows the spectral throughput of the Bessell spectral filters placed in the beam path to permit the measurement of scattered light at different wavelengths [69].

3.2.2   Spot-Projection Lens

Next, an optical system was designed to take the light from the light source and project it onto the DMD, just as a star would be imaged. A minification factor of 5 (a 5 µm diameter spot) illuminated the DMD. Moving further away from the DMD does not create a smaller spot due to the diffraction limit of the spot-projecting lens. The lens used to project the spot was a Thorlabs AC254-075-A-ML $f/6.0$ achromat made from BK7 and SF5. It was essentially a diffraction limited optic, and its $f/\#$ was close to that of the RITMOS relay optics. The expected spot size was modeled using the OSLO package [70]. The lens model was imported into OSLO and the lens was verified to be diffraction limited (Figure 3.12) at the wavelengths of interest. The spot size calculated by OSLO was compared to the diffraction limited spot size modeled by a circular aperture and the squared magnitude of J1 Bessel function. The relative aperture size of the spot-projection lens was the limiting factor for creating a smaller spot.

3.2.3   Spot-Imaging Camera

In order to image the illumination spot and determine its sub-mirror position on the micromirror array a microscope re-imaging system was used. A Mitutoyo 0.14 NA 5× NIR Infinity corrected microscope objective was used to image the spot. The lens tube used was a Navitar zoom 6000 series coupled to a Prosilica GC-1380 camera with a $\frac{2}{3}''$ sensor array. This camera enabled one to focus the spot onto the DMD and determine the relative position of the spot on the DMD. The total system magnification ranged from 3.48× to 22.86×. The microscope had a working distance of approximately 34 µm and a resolving power of 2 µm.
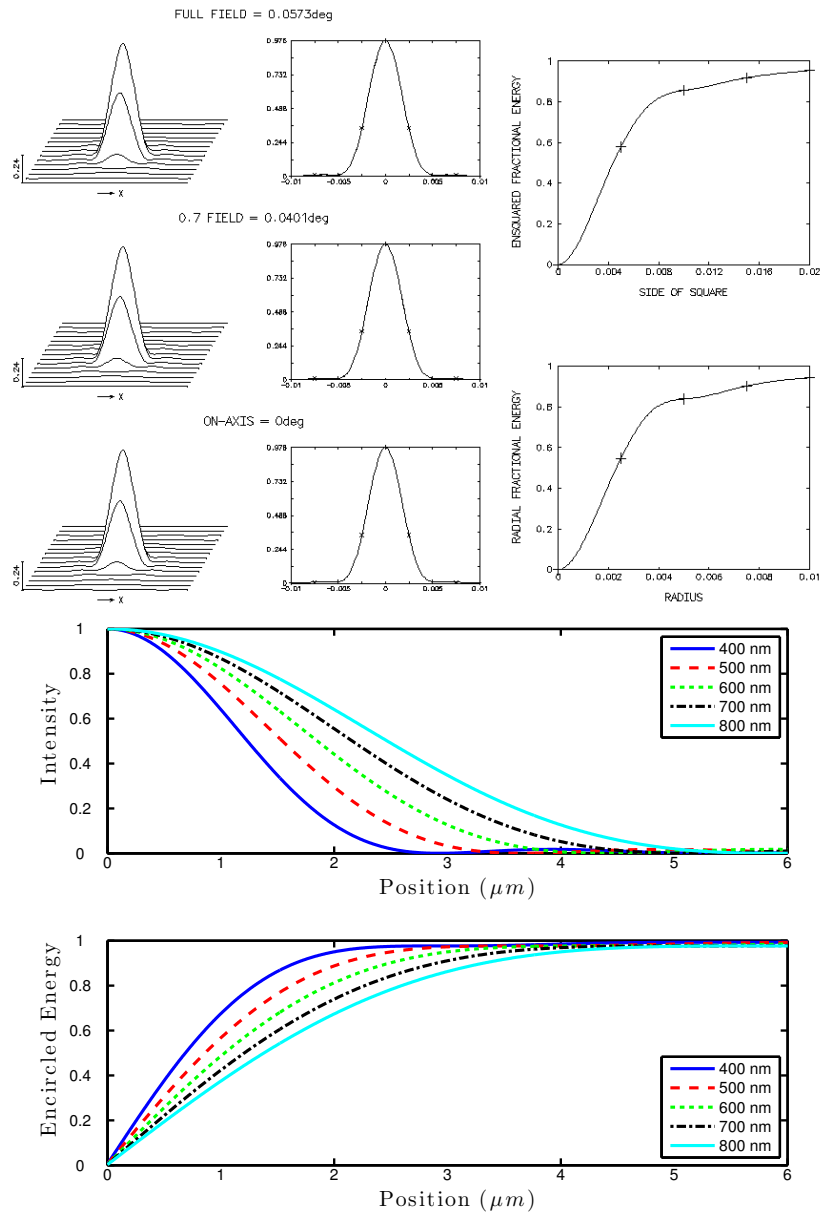
Figure 3.12: (Top) Point Spread Function of the Lens used to create the sub-mirror sized spot. (Bottom) Calculated diffraction limited spot size as a function of wavelength for the Thorlabs $AC254 - 075 - A - ML$.

3.2.4   Stage Selection

Next, a method was required to move the spot across the micromirror. A two axis DC motor Physiks Instrumente stage was used as the raster scan stage to move the mirrors across the spot. The DMD was translated, rather than moving the spot projection lens and light source. The stage has a resolution of 0.06 µm and a repeatability of 2 µm. This resolution was sufficient for examining micromirrors. The acceleration, ramp rates, and velocity were optimized to give the best stage repeatability results.

3.2.5   Scatter-Collecting Camera

To collect the scattered light, a camera with a large dynamic range was required. Also, a macro lens was required so that enough light could be collected and focused onto the sensor. A cooled Photometrics CE-350 CCD camera was chosen to collect the scattered light. This scatter-collecting camera utilized a back-thinned SITe SI502AB backside illuminated CCD. The CCD had an RMS read noise of approximately 8 electrons and a full well capacity of approximately 300, 000 electrons, so it was very suitable for performing low light level scatter measurements. The macro lens used to capture the stray light was a Micro-Nikkor 60 mm f/2.8. It had a 39.7° FOV and was operated at a 1:1 magnification. The reflected light was collected at f/11, to enable the shutter to be open for a longer period of time and minimize the effect of shutter jitter.

3.2.6   Additions to the Experimental Setup

Several additional items were included in the final experimental setup. To enable viewing of the spot at the specular angle, a fold mirror periscope system was developed. This enabled the spot to be projected onto the DMD by the spot projection lens and simultaneously imaged by the microscope objective. A fold mirror system was prototyped in the ray-tracing package FRED to determine the size of the fold mirrors required, and to ensure that all of the proper working distances would be maintained (Figure 3.7). Figure 3.7 shows two views of the experimental apparatus. A half-silvered mirror and an Ocean Optics USB2000 spectrometer were also added after the filter wheel and pinhole to monitor light source power. All of the elements of the apparatus are labeled in Figure 3.7 as follows:

- A. the Oriel Q-series light source,
- B. the Oriel collimator assembly and pinhole,
- C. the first fold mirror in the periscope system,
- D. the Thorlabs spot projection lens,
- E. the second fold mirror in the periscope system,
- F. the DMD assembly mounted to a rotation stage,
- G. the Mitutoyo microscope objective,
- H. the Navitar lens tube,
- I. the spot-imaging camera,
- J. the Nikon macro lens,
- K. the scatter-collecting camera.
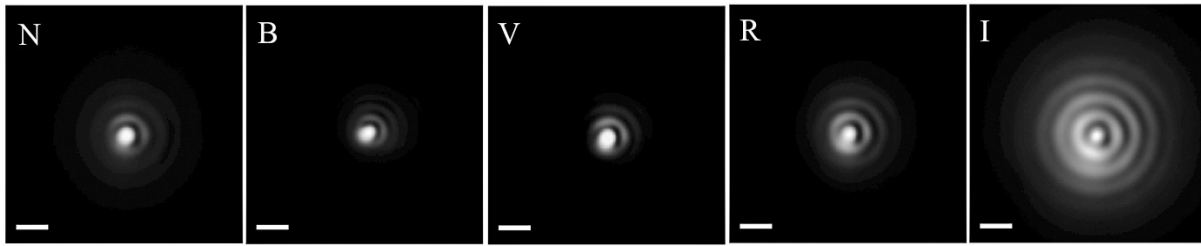
Figure 3.13: Spot size imaged by the spot-imaging camera directly (not reflected off DMD mirrors). Scale bar is 10 µm in size. N image is with a blank bice of glass in the beam. B, V, R, I represent the Bessel filters.

3.2.7 Spot Size Validation

Figure 3.13 show images of the spot that were taken by turning the spot-imaging camera directly at the spot. Additionally a DMD window was placed in the beam to examine the increase in spot size. By adding the window to the path the spherical aberration increased, the resulting spot images had greater counts in their Airy wings, but still sufficient energy in their central bright region to perform scattered light measurements with this apparatus.

3.2.8 Focusing and Aligning the Optical Components

A HeNe laser was used to coarsely align all optical components. However, a more accurate procedure had to be performed to focus the two cameras and spot-projection lens onto the DMD. To align the spot-imaging camera, the pinhole was removed from the light source, so that a large flood illumination was focused onto the DMD. This made it possible to use short integration times with the spot-imaging camera. After this, the spot-imaging camera was translated so that the large spot was centered in the FOV of the array. A histogram was used to aid in finding and focusing the spot. All of the mirrors were then turned toward the spot-imaging camera. The camera was then focused so that the relative edge response was greatest in the center of the FOV of the spot camera. The relative edge response was calculated by applying an edge detector to the image, setting a threshold and grouping several sets of columns on the image. The columns with the highest relative edge response were in the best focus. Since this camera was imaging at 20° off axis and the microscope had a large numerical aperture, it had a very limited depth of field (about $14\mu m$). Due to this constraint, it was very important to obtain the best possible focus of the projected spot in the center of the field of view.

To focus the spot onto the mirrors, the DMD was not powered and the mirrors consequently moved to their flat state. An iris was used to stop down the beam at the pinhole location. The focus was adjusted on the spot projection lens while monitoring the continuous video feed of the spot-imaging camera. After the approximate focus was found the iris was replaced with a pinhole. Next the spot-projection lens' micrometer position was recorded and a pseudo-random spot scan was performed to randomly step the stage in x and y. The stage was stepped in a random fashion to avoid the problem of having the spot illuminating the region between two mirrors or within the via. These images were averaged together so that all of the non-uniformities of the DMD were averaged out. This process was repeated through focus of the spot projection lens. At each focus position the FWHM was found for the spot and this value was recorded. The FWHM size was then plotted versus focus position and a minimum was identified. This was found to be the best method of minimizing the spot size on the DMD (Figure 3.14). The procedure to focus the scatter-collecting camera was very similar to the procedure for focusing the microscope lens.
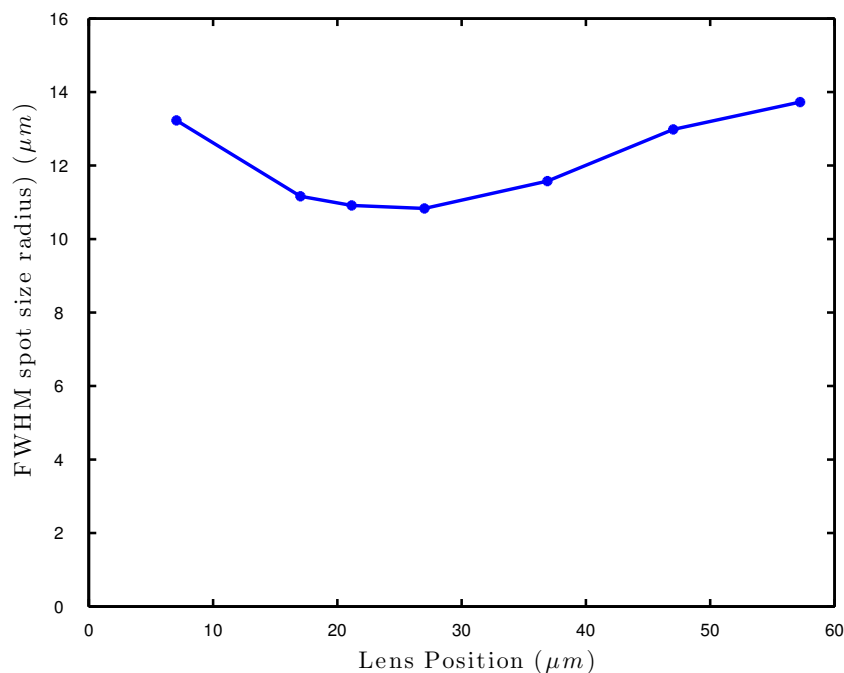
Figure 3.14: (a) FWHM radius size as a function of focal position of the spot-projecting lens.

3.2.9   Data Collection

A raster scan was conducted across the micromirror array by translating the DMD beneath the projected spot. Scanning was always performed in a single direction to minimize stage hysteresis. The scanning region was 68 µm by 40 µm, with 140 individual data locations. Four different mirror orientations or cases were examined as shown in Figure 3.15. The spot-imaging camera observed the inverse slit that the scatter camera recorded.

The motion order was very important for collecting co-aligned scatter data. The mirrors were moved to their four orientations (Figure 3.15) in each stage position. Images were obtained from both cameras simultaneously in each case. The spot-imaging camera was used to determine the current position and the scatter camera to collect the radiometric data. Several frames were co-added on the spot-imaging camera to improve the signal to noise of the recorded image. Exposure times were set by moving to the nominal location in the center of the mirror and choosing an exposure time that was approximately 75% of the camera's full well capacity. Data was taken with each of the spectral filters at each of the spectral filters at each stage position. As the filter wheel was large, and the table was floating this caused the optical table to vibrate. A period of 30 seconds was sufficient to allow the table oscillations to damp out. The completely automated scan took approximately 1 week of time in the laboratory to fully scan 1 individual mirror.

An automated method determined which DMD micromirror was being illuminated. This enabled the four different mask patterns to be generated automatically. The automated method first stepped through the rows on the DMD to find the highest change in flux on the scatter-collecting camera. The process was repeated for the DMD columns within the previously found row. Once the DMD row and column were found, the slit or mask patterns were programmed into the DMD controller. The spot was then centered by viewing the image on the spot-imaging camera. To improve SNR on the pixels receiving lower flux, the scatter-collecting camera was binned into 3×3 pixels around the maximum pixel. When the system was
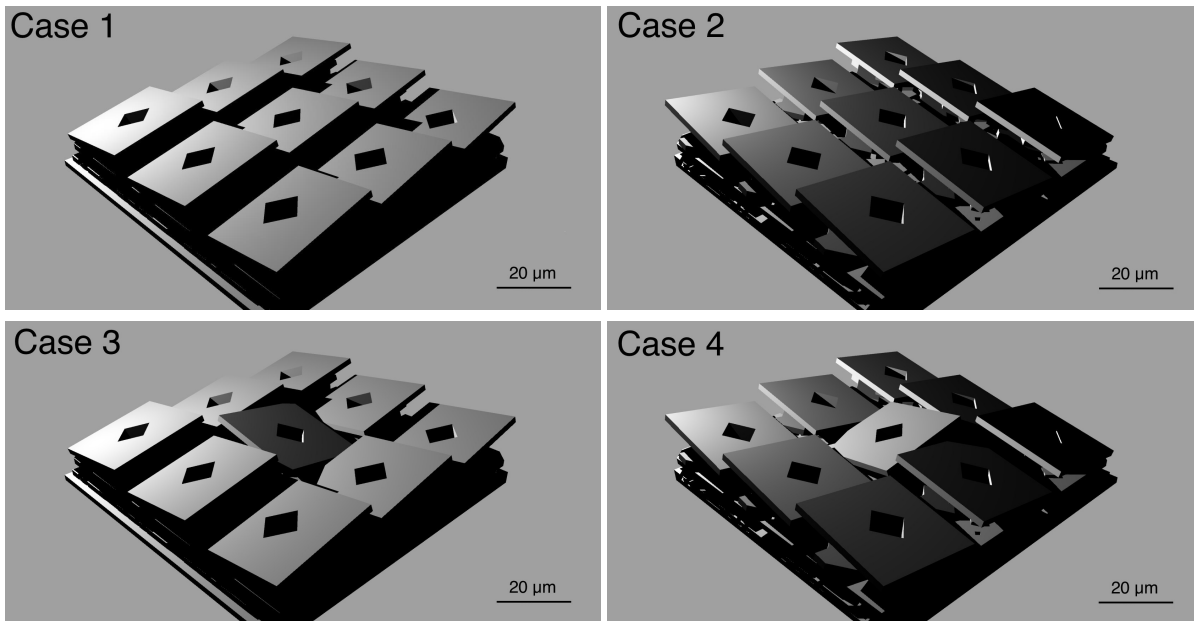
Figure 3.15: Rhino software package [71] was used to generate the above renderings of four different mask patterns. Scatter camera would be positioned above and to the left of the micromirror and the spot-imaging camera would be positioned to the right side. Note only 3×3 mirrors are shown here for each case, not the complete 848×600 DMD array.

aligned properly, the majority of the light illuminated a single detector element on the scatter-collecting camera. During the initial data collection an extraneous noise was seen in the CCD measurements. This noise source was eventually eliminated and more details can be found in Appendix A.

3.2.10   Data Analysis

Two important parameters are required to characterize scatter in DMD: I_R and I_S. I_R is the reflected light from a single micromirror and I_S is the scattered light by the surrounding micromirror array. To determine the difference in reflectivity as a function of sub-mirror position, the following equations were derived from the four mirror states as shown in Figure 3.15:

- Case 1. All of the mirrors are facing the scatter-collecting camera, so the light recorded by the scattering camera is the sum of the reflected light from the center mirror, the reflected light from the adjacent mirrors and the scattered light from all mirrors (Equation 3.6).

- Case 2. All of the mirrors are pointing away from the scatter-collecting camera, so only the scattered light is collected by the scatter-collecting camera (Equation 3.7).

- Case 3. One mirror is turned away from the scatter-collecting camera. Therefore the camera collects the reflected light from the adjacent mirrors and the scattered light from the central mirror (Equation 3.8).

- Case 4. Only the central mirror is facing the scatter collection camera. Therefore the camera records the reflected light from this single mirror plus the scattered light from all mirrors (Equation 3.9).

$$Case_1 = I_R + I_{RA} + I_S \tag{3.6}$$

$$Case_2 = I_S \tag{3.7}$$

$$Case_3 = I_{RA} + I_S \tag{3.8}$$

$$Case_4 = I_R + I_S \tag{3.9}$$

$$Contrast = \frac{I_R}{I_S} \tag{3.10}$$

The unprocessed data can be seen in Figure 3.16. General insight was gathered from the raw data. Case 1 shows the maxim response was obtained on a periodic structure with the same pitch as the micromirror array. This indicates that the spot was likely much smaller than a single micromirror element. Case 2 shows the scattered light. The scattered light was much brighter around the edges of the pixel. Note that the pitch of the peaks for case 2 is doubled suggesting greater scatter at the edges of individual micromirrors. These equations were solved to find the I_R and I_S at each position. To achieve this, a matrix was set up and a Gaussian elimination method was used to back out the reflectance and stray light values. After these were determined, a ratio can be taken to determine the ratio of reflected light to the ratio of stray or scattered light at each position within a DMD mirror. Figure 3.17 shows the resulting data at three different spectral bandpasses as defined by the Bessell [69] filters whose transmission are seen in Figure 3.10. The orientation of the mirrors was obvious when viewing the contour plot. These initial measurements indicate there is a variation in scatter with spot position on the individual DMD mirror (Figure 3.17).

Additionally, the scatter data were viewed as a function of distance from the center pixel on the scatter CCD array (see Figure 3.18). These results will be further interpreted to determine the degree of spectral contamination by adjacent mirrors as a function of wavelength. When the illuminating spot is in the center of the micromirror, higher reflectance values are measured at the center pixel on the scatter-collecting camera. There is less scattered light (I_S) at distances further from the center pixel on the scatter-collecting camera when the spot illuminated the center of the pixel. The edge measurements have lower I_R values and also change less as a function of distance. This indicates that when the illuminating spot is closer to a mirror's edge, more scattered light (I_S) occurs. There are not only intensity differences between the mirror's values, but additionally differences in shape of the curves. In the future, images will be co-added to help boost the signal of the pixels at greater distances from the center pixel.

The spot scan analysis was processed by subtracting the co-averaged dark frame from each image taken in each of the filter and DMD mirror states. A 40×40 sub-array was recorded to reduce the time required to download a camera image. The maximum value from each scatter-collecting CCD image was found. Then these values were then recorded for each spot position to build up a 25×25 scan position image. These scan images cover a spatial area of 50×50 μm, so several DMD mirrors are seen in each image. In the blue,
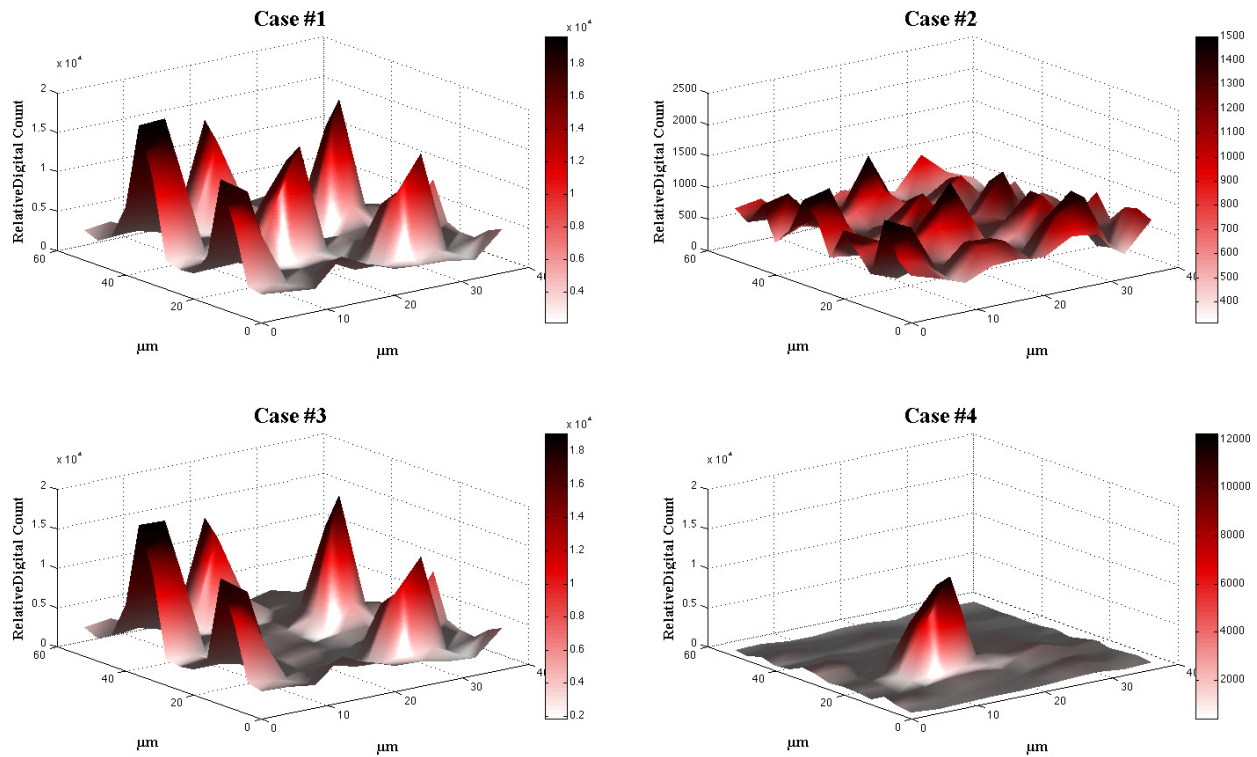
Figure 3.16: Raw case data for the four micromirror mask positions are shown above with the Bessell V filter. Note the difference in scale for case 2.
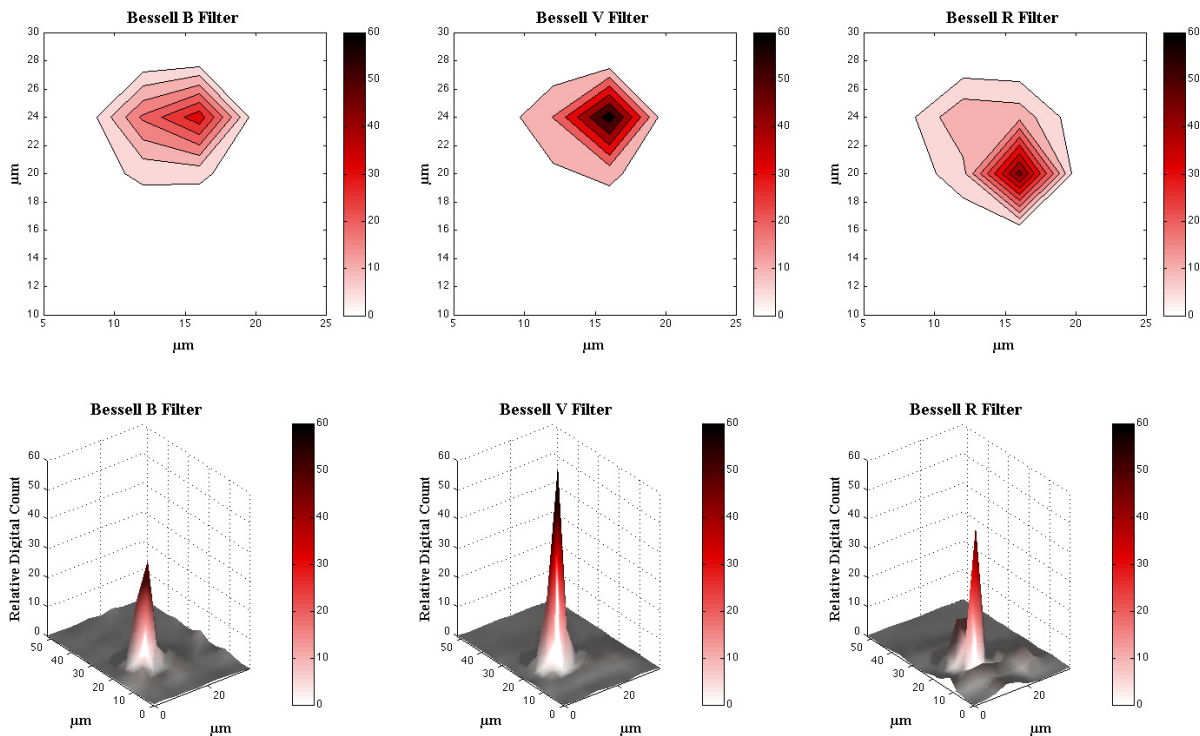
Figure 3.17: This shows the results of applying equations 3.6, 3.7, 3.8 and 3.9. Equation 3.10 was then applied to all of the data points and the contrast ratio results are plotted here. The data on the top and bottom plots are the same, just two different methods to visualize the information.
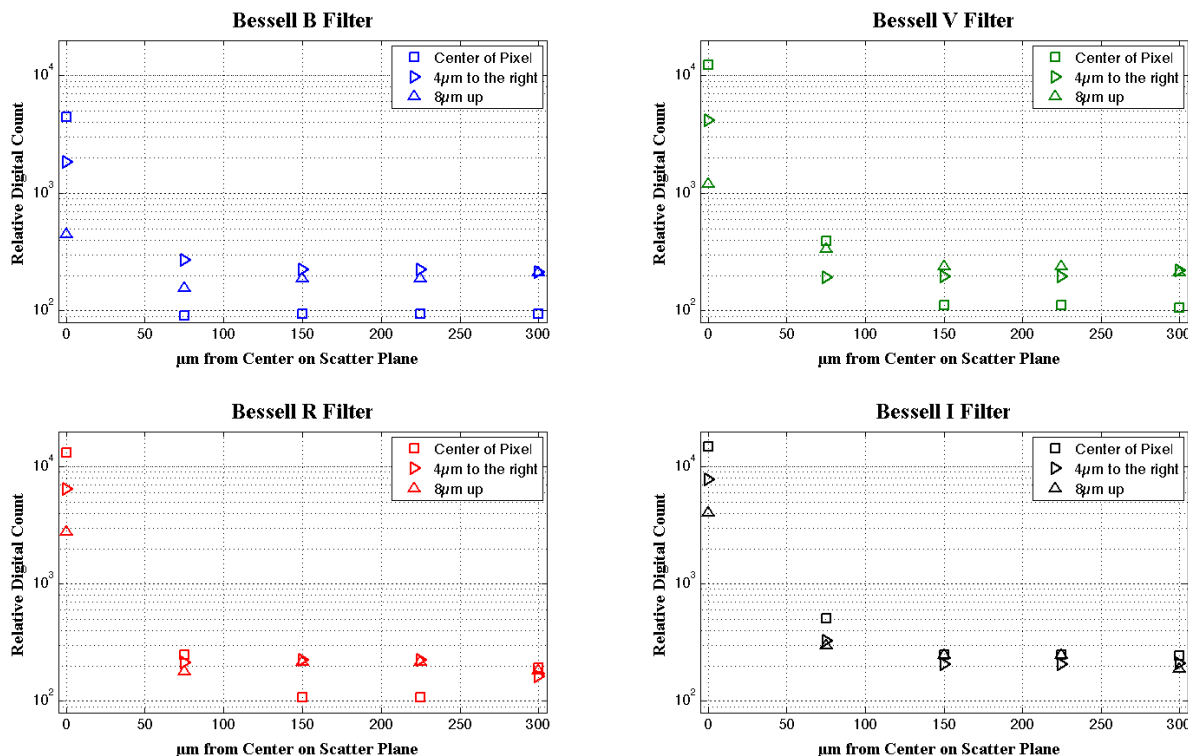
Figure 3.18: A cross-section of the spot is shown when illuminating the DMD at different locations within a single mirror. Each data point represent one of scatter-collecting CCD camera's pixel value. The four plots show when different color filters were placed in the beam.

Table 3.1: The maximum integrated contrast values for each spectral filter.

B	273
V	305
R	318
I	106
N	287

there appears to be a lower fill factor. This is because the parts of the mirror near the edges are curved up and reflect less light to the scatter-collecting camera. The images (Figure 3.19) for case one show structure that is periodic at the same pitch of the micromirrors. Case 2 all of the mirrors are turned away, showing scattered light from all of the mirrors. There is a great deal of scattered light at the edges of the mirrors and in the central region of each mirror near the via. Case 3 shows the absence of one mirror and case 4 shows the reflected and scattered light for a single micromirror. There is a square region missing in each of the spot scans (the mirror via), and it is also apparent that the scattered light is wavelength dependent. From these plots one can derive the reflected light and scattered light for a single micromirror (Equation 3.10). By solving for the I_R and I_S the contrast value (Contrast = $\frac{I_R}{I_S}$) for each position in the micromirror can be determined. Integrating these values over a complete micromirror can gives a single mirror contrast ratio analogous to a SNR. This is the maximum contrast ratio possible from a DMD based MOS instrument with this generation of DMD and is shown in Table 3.1.
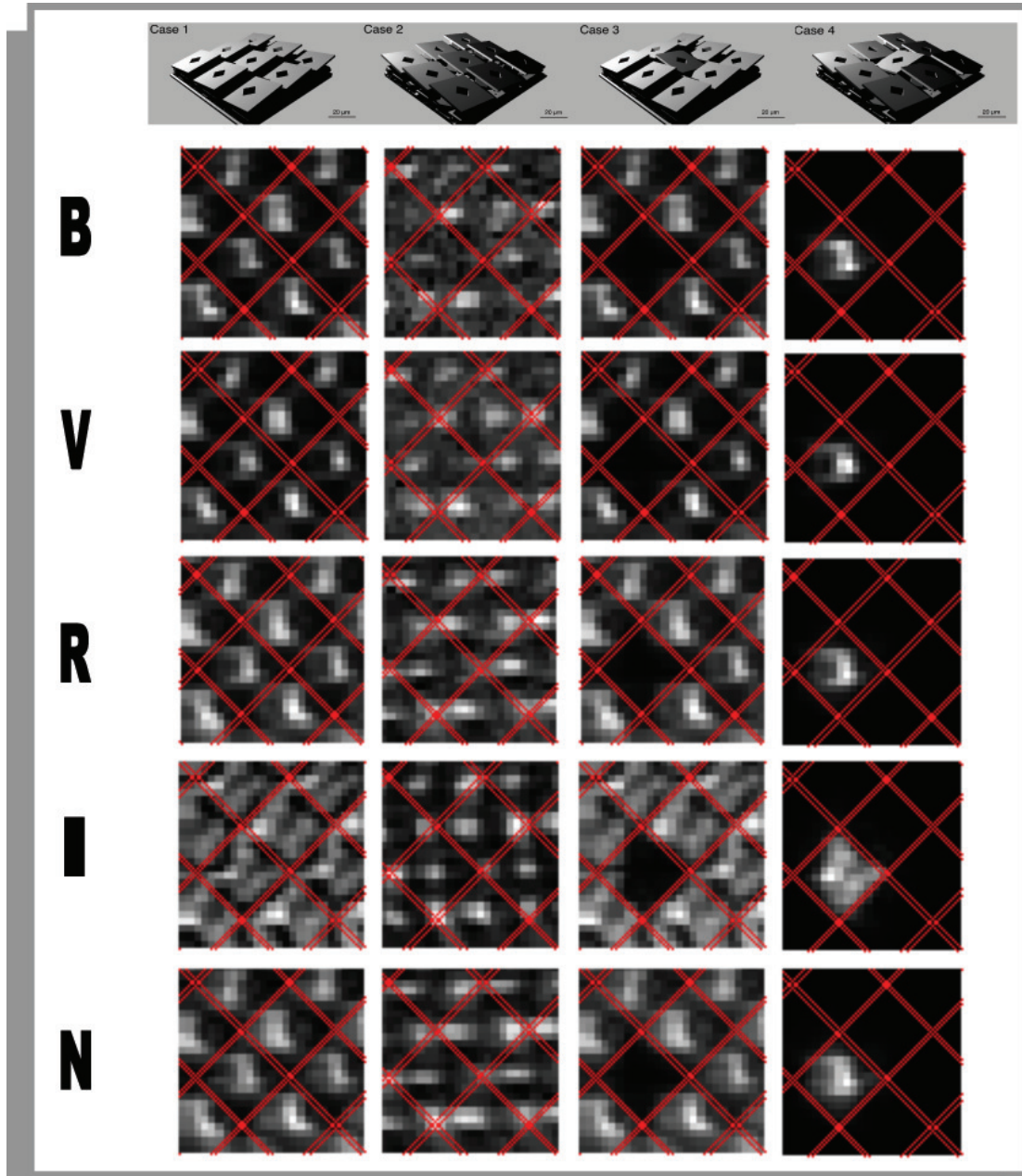
Figure 3.19: In the top boxes, the four mirror slit patterns are shown. Central mirror pictured in each of the slit patterns is the mirror under test. Remaining mirrors in the array are set to the same state as all of the outside mirrors. Case 1, all mirrors are positioned toward the scatter-collecting camera, Case 2 all mirrors are placed away from the scatter-collecting camera. Case 3 one mirror is turned away from the scatter-collecting camera. Case 4 only one mirror is turned towards the scatter-collecting camera. The labeling along the vertical axis indicated the different filter used in each of the four mirror cases.

3.2.11 Mirror Curvature

Flatness and surface roughness are two of the key parameters, which determine the amount of scattered light. The DMD mirrors are made in a semiconductor process, and thin film properties become very important. The DMDs are packaged at TI with a transparent window ahead of the DMD for protection. The window was removed from a non-functioning DMD of the same model as the DMD under test. A Veeco Wyko NT9000 white light interferometer was used to examine the surface relief of these mirrors. These interferometer measurements enabled the mirror curvature to be extracted. Figure 3.20 shows the variation in mirror height measured. It can be seen that the mirror edge is 0.25 µm higher than the region around the via at the mirror center. Also the height profile is symmetric around the mirror and not aligned with the axis that the mirrors tip on. Our initial thought was that this might be the result of the mirrors hitting a hard stop when they are tilted. However, this is not the case as the stop is not located at the mirror edge but rather closer to the underlying hinge structure in this generation of DMDs. Knowing the mirrors are 16 µm across, this implies that the radius of mirror curvature is approximately 257 µm. Also notice that there appears to be a square region in each of the mirrors which is flat. This is likely the same square pattern that was seen in the spot scan data, which for the B,V, and R filtered data. Figure 3.20 was also rotated so that the mirrors would be the same orientation as the other measurements presented in this paper.

An alternative approach to characterize the mirror flatness was also investigated. Using case 4 from each of the scans in each of the scatter camera images, the row and column centroid are computed. At each location in the scan, the spot motion across the scatter-collecting CCD was plotted as shown by the arrows in Figure 3.21 and 3.22. This method of plotting the data enabled one to view where the spot was being imaged on the scatter-collecting camera (Figure 3.21). Two cut-lines were made through this plot, one in the vertical direction and one in the horizontal direction. The vertical cut-line should be flat if there is no mirror curvature, because this is the direction parallel to the hinge, which is flat relative to the DMD substrate. The mirrors only tip across the row direction in the scan, so a dip in the plot should be seen there. In Figure 3.21, there is curvature in both the x and y direction for the blue case. Figure 3.22 shows the same data plotted for the I filter. It can be seen that there is very little curvature in the vertical cut-line. This is likely due to the fact that the spot is bigger in the I band and therefore the curvature is averaged out.

3.2.12 Micromirror Self-Shadowing (MSS)

Micromirror self shadowing, is the change in illumination caused when part of the incident beam of light is blocked by the edge of an adjacent mirror. Therefore, a fraction of the reflected cone of light is also blocked by the adjacent mirror. The self-shadowing does not become an important factor until illumination angles become faster than $f/3$ for the $10°$ tip DMD. Since the spot projection lens only illuminates the mirrors at $f/7$ and the RITMOS relay optics only illuminate the mirrors at $f/8$ MSS is not a significant factor for these experiments.

3.3 Software Modeling

The experimental apparatus as described earlier was modeled in the FRED software package. An image of the experimental apparatus rendered in FRED is shown in Figure 3.23. The fold mirror setup was prototyped in FRED prior to building it to ensure that there would not be any vignetting of the scatter-collecting
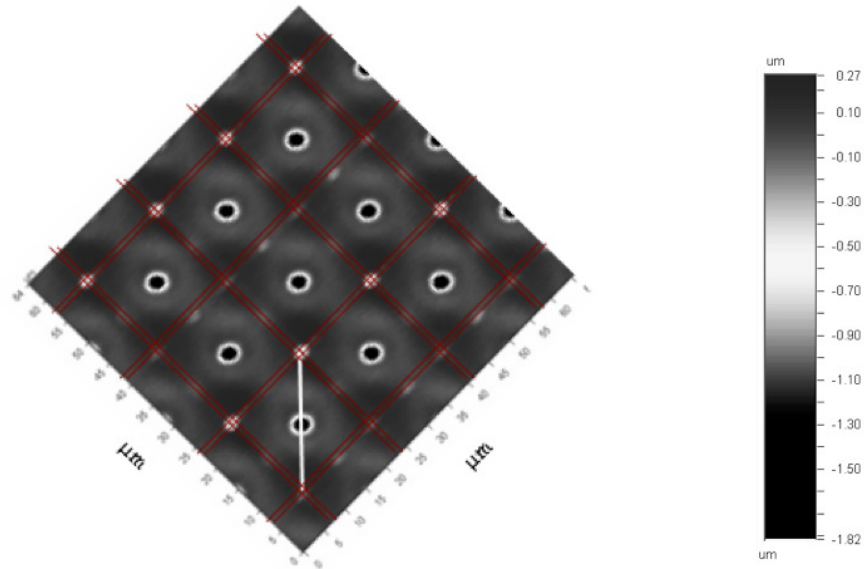
Figure 3.20: The image above is a interferometric surface height map of a 3×3 mirrors on a section of a DMD. The mirror edges are outlined. The orientation of the hinge is also outlined in a white overlay. The mirrors bow up $0.25\,\mu m$ around the edge.
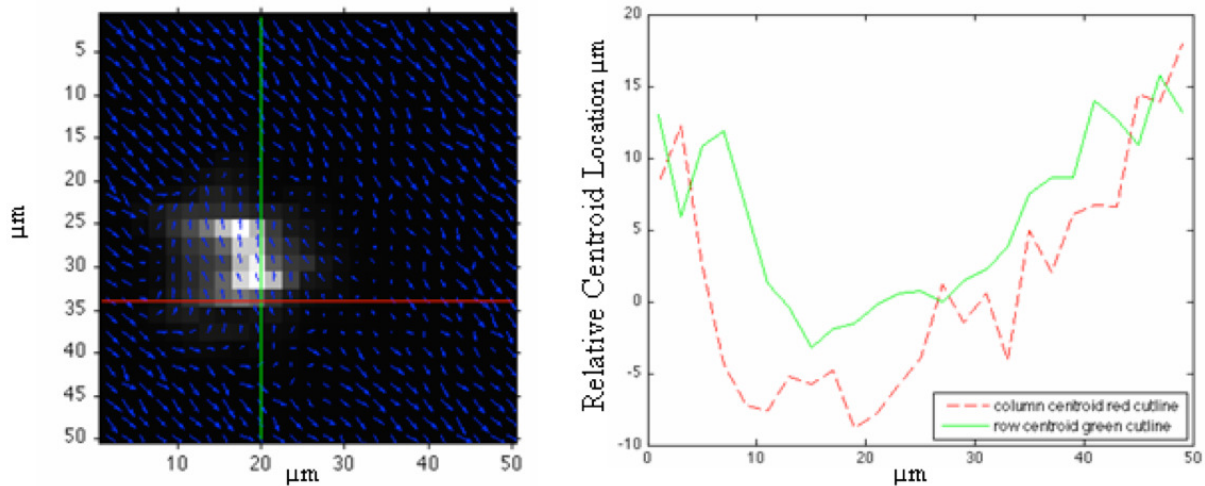
Figure 3.21: (Left) Case 4 overlaid by a vector plot. Arrows indicate the direction that the centroid translates on the CCD during the spot scan. (Right) Two different cut-lines through the spot scan data are shown here. This data was obtained using the B filter.
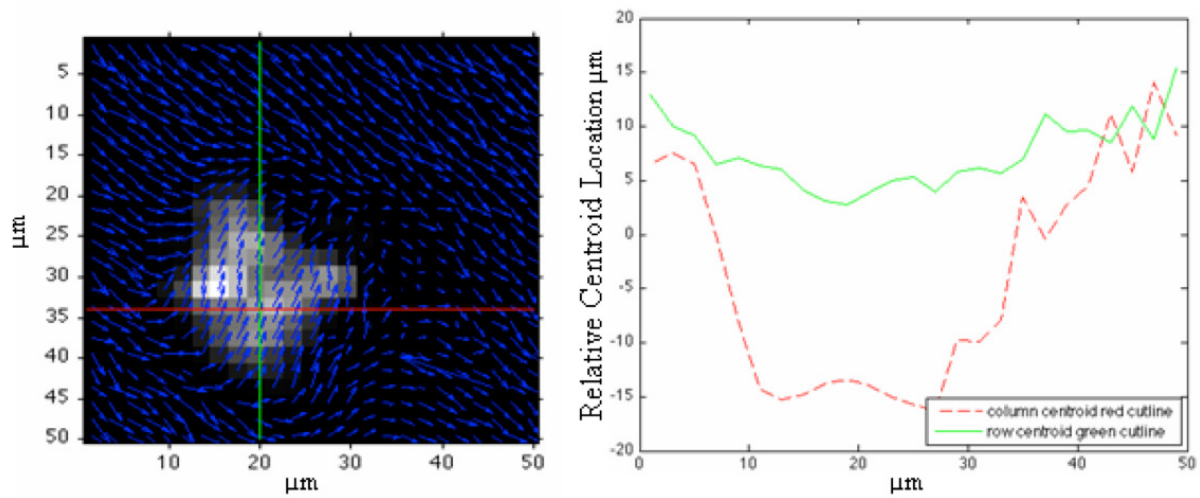
Figure 3.22: The left plot shows the vector plot of the centroid motion during the scan. This data is shown for the I filter.
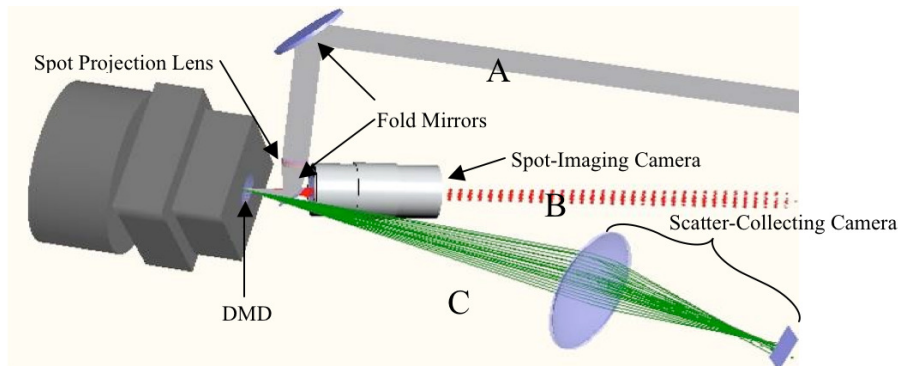
Figure 3.23: Experimental apparatus shown in the FRED software package. (A) Rays show the incoming wavefront. (B) Rays show the light reflecting from micromirrors towards the spot-imaging camera. (C) Rays show the light being reflected into the scatter-collecting camera..

camera system. The fold mirror system was used rather than a direct illumination path, because it was not possible to illuminate the mirrors and image them at the proper $\pm 20°$ with both camera systems. Partial vignetting of the spot-imaging system occurred, but since this system was only used for determining where the spot was, (no radiometric scatter measurements were derived from this system) this was not an issue.

3.3.1   External Stray Light Paths in DMDs

While taking the experimental measurements, an additional stray light path was discovered as shown in Figure 3.24 A. Depending on the wavelength of illumination, a ghost image was observed approximately 1800 µm away from the specular reflection of the micromirror. Assuming that the glass thickness is 2500 µm the ghost image was predicted in the vicinity of this location. Figure 3.25 shows the additional stray light paths possible in a DMD as utilized in a spectrometer. This scatter path was not a significant problem in the typical DMD projector application, because this would occur with the pixel in the off state. This becomes an important parameter in both the spectral and imaging channel of the RITMOS. For the spectral channel, it poses a different problem. Since the location of the slit or micromirror determines the center of the spectrum, this ghost image will essentially be a second slit in a different row. This effect causes
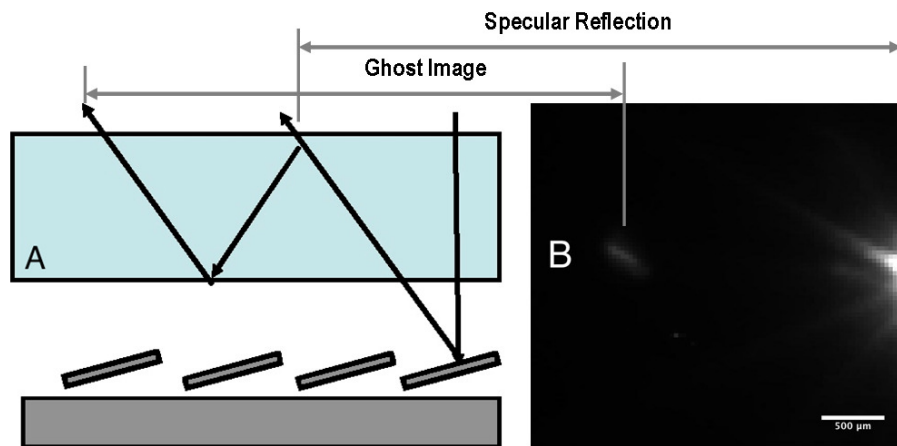
Figure 3.24: An important scatter path is shown here which is caused by multiple reflections within the cover glass window. (a) Is a sketch that illustrates the light bouncing off of the mirror, going through the first interface of the glass, but then being internally reflected by the glass. The light is then internally reflected again. (b) An image from the scatter-collecting camera showing the ghost image.

low-level spectral contamination. Further optical modeling suggests that this was primarily a function of the wavelength region the window's anti-reflection coating was optimized for. Producing a high-quality anti-reflection coating optimized for the spectral region of the MOS is very important.

3.3.2 Shift-Variant Spatial Reflectivity Model

After performing these spot scan measurements, a model was generated to simulate the reflectivity as a function of spatial position across the mirror. The results shown in Figure 3.19 were normalized and a function was parameterized for each wavelength (filter). Equation 3.11 shows the different parameters used for modeling the shift variant reflectivity. The sub-mirror position orientation has a value of $(0,0)$ in the pixel center. Seven parameters are used to fit a function to each filter at the each wavelength a spot scan was completed for. A larger Gaussian is used to model the pixel edges. A smaller Gaussian is used to model the loss at the mirror via. These two are differenced. This model is a Difference Of Gaussians (DOG), with an additional background term and a scaling term (reflectivity coefficient). This model does not account for any stray light effects from the window. An input scene could be digitally simulated with this model the spatial reflectivity variations of the DMD. Figure 3.26 shows the model for a group of 5×5 micromirrors.

$$R_{(\lambda)}(x_p, y_p) = A_{4(\lambda)} \times \left(A_{1(\lambda)} gaus(x_p, y_p, \sigma_{1(\lambda)}) - A_{2(\lambda)} gaus(x_p, y_p, \sigma_{2(\lambda)}) + bkg_{(\lambda)} \right) \tag{3.11}$$

3.3.3 DMD Aluminum Reflectivity

The bulk reflectivity of the DMD mirror aluminum is an important parameter for planning any space mission, as end-to-end system throughput of critical importance.
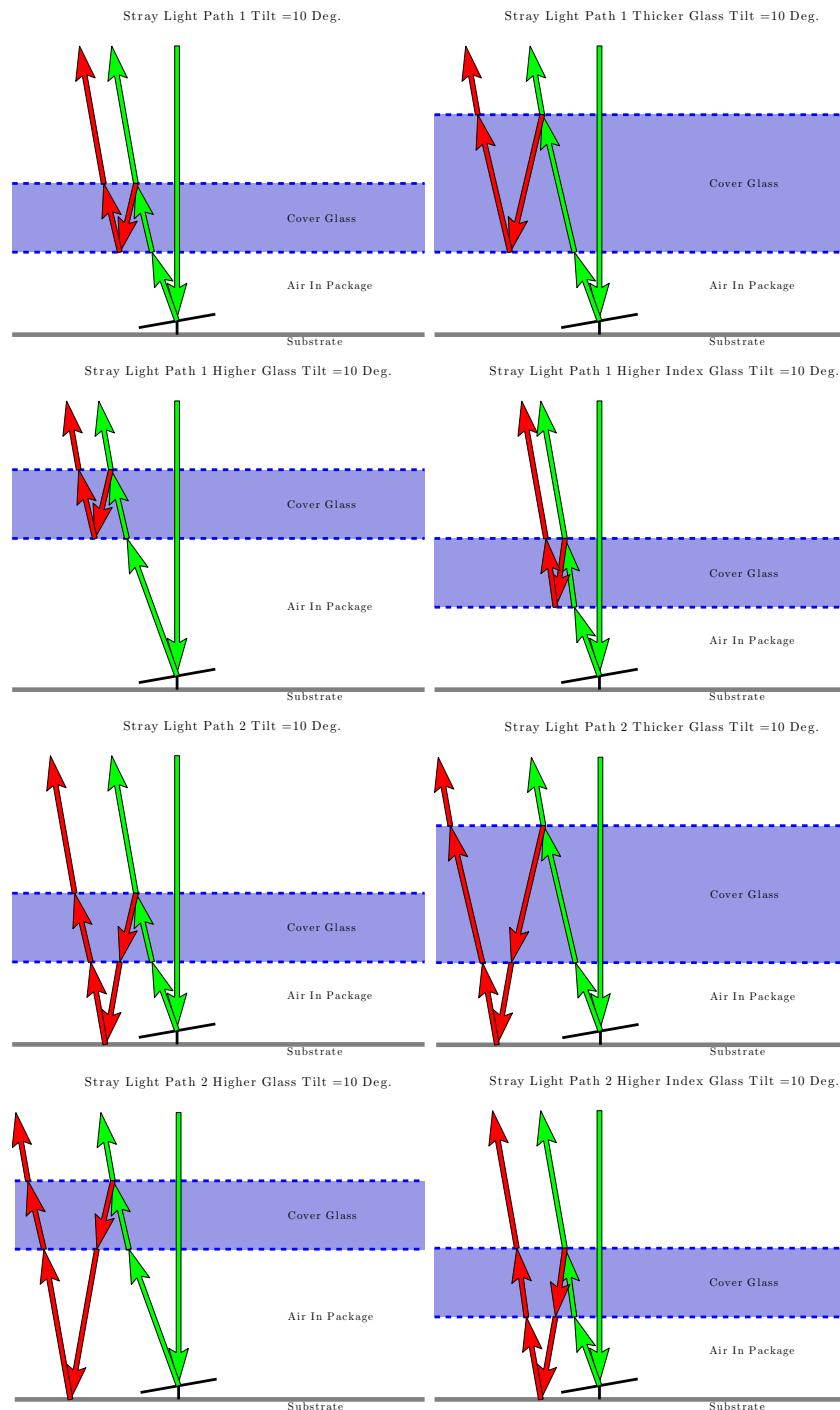
Figure 3.25: Stray light paths as used in RITMOS. Top two figures show that a ghost image can be created by a double reflection on the window glass. Second set of figures show that the window height above the DMD also determines how close the ghost image occurs to the regular image. Next set shows what happens if a reflection from the window reflects from the substrate and back out. Final set show the distance from the array to window is important.
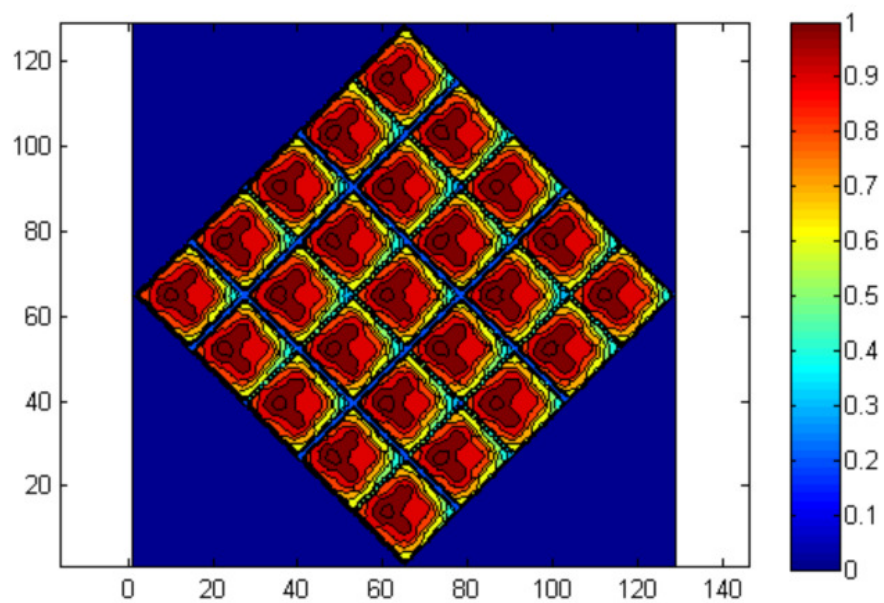
Figure 3.26: Matlab micromirror model illustrating the shift variant reflectance function (Equation 3.11).
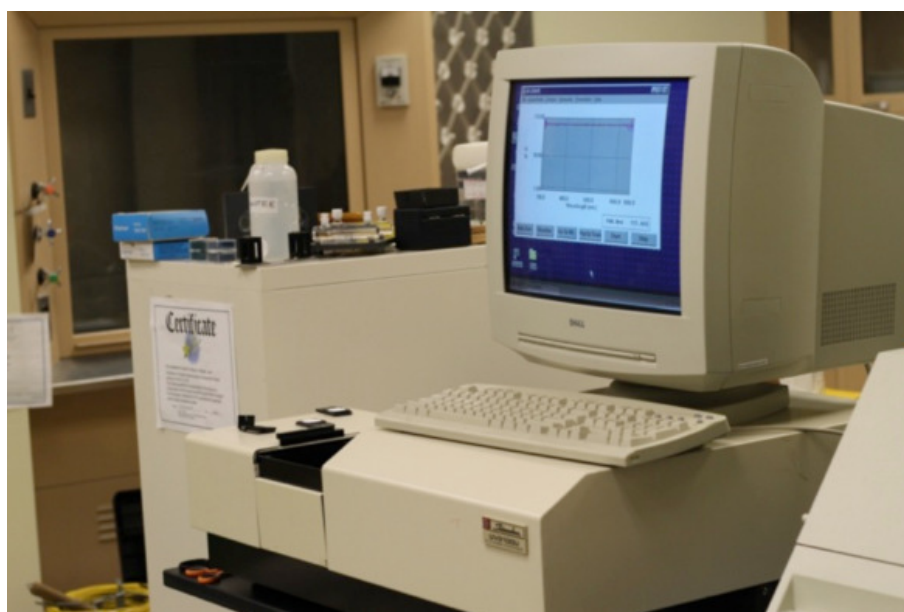
Figure 3.27: Shimadzu UV-VIS spectrophotometer was used for the reflectivity measurments.

Table 3.2: The fitted shift variant reflection model parameters

Filter	B	V	R	I	Parameter Description
A_1	0.98	0.98	0.98	0.75	Magnitude of Outer Envelope
σ_1	3.5	2.5	2.5	7	Spread of first Gaussian
A_2	0.01	0.01	0.05	0.35	Magnitude of Second Gaussian (via)
σ_2	0.49	0.49	0.49	3.5	Spread of Second Gaussian
A_3	0	0	0.15	0.35	Tilt Coefficient
A_4	1	1	1	1	Reflectivity Coefficient
Bkg	0.03	0.03	0.05	0.1	Background Term
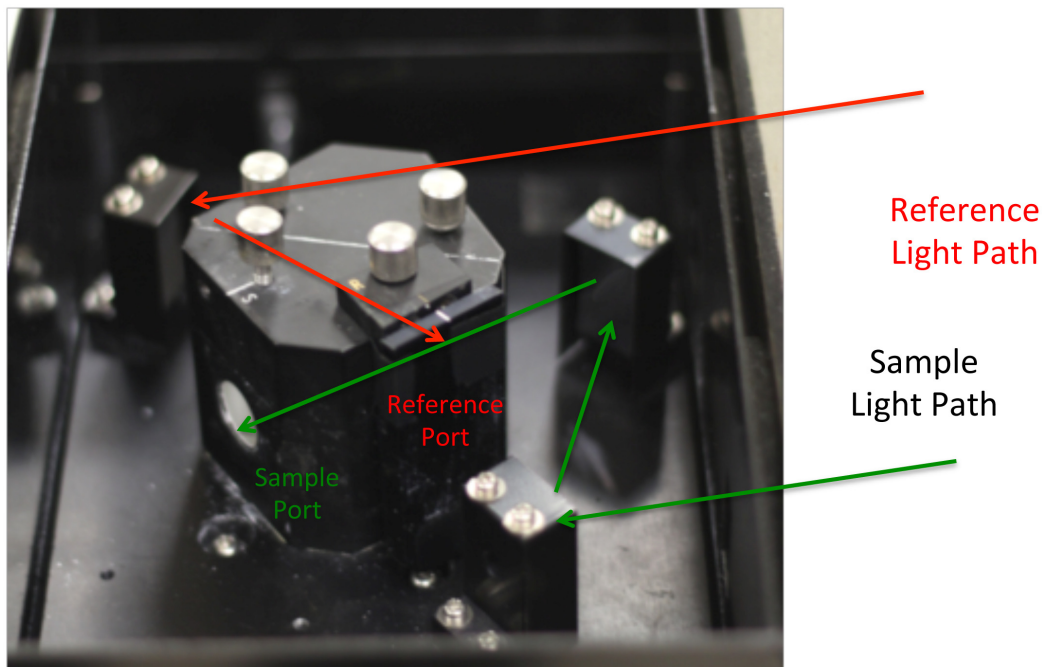
Figure 3.28: Shimadzu UV-VIS spectrophotometer double-pass module was used for the reflectivity measurements.

3.3.4   Reflectivity Experiment

A Shimadzu UV-VIS spectrophotometer (model UV-VIS 2100) was used to measure the reflectivity of an 848×600 17 μm pitch DMD. A diffuse reflectance double pass integrating sphere module (Figure 3.28) was placed in the spectrophotometer (shown in Figure 3.27). This spectrophotometer was calibrated using two barium sulfate samples. A reference barium sulfate was kept in the reference beam at all times. A baseline scan was performed with two identical barium sulfate samples to remove instrumental differences between the sample and reference light path. The measurements were made over the wavelength range 200 nm to 900 nm. The integrating sphere has a built-in illumination angle of $8°$, inferring the DMD is illuminated at $8°$ off-axis and the specular reflection surface impinges onto the inside surface of the integrating sphere. The DMD that was used for these measurements is shown in Figure 3.29.

3.3.5   Measurement Results

After the instrument was calibrated, the DMD reflectivity was measured. Since the barium sulfate was used to normalize the instrument, the reflectivity measurements of the DMD are referenced to the known
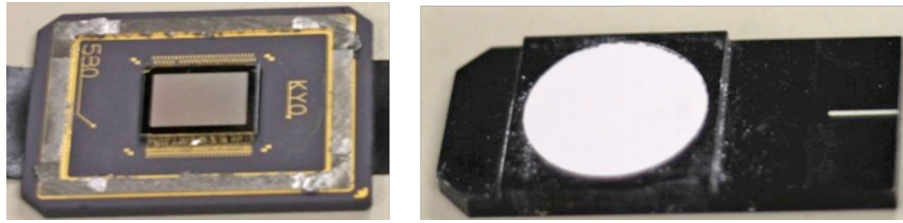
Figure 3.29: (Left) unpackaged DMD (Right) barium sulfate sample.

barium sulfate reflectivity. The reflectivity curve for barium sulfate [72] is plotted in Figure 3.30 (blue line). A multiplication factor was used to match the raw instrument to this known curve for barium sulfate. This same multiplication factor was then used to convert the raw measured DMD reflectance (red curve) to an absolute reflectance (green curve).

A TI datasheet [73] shows the aluminum alloy reflectivity measurements (Figure 3.30 (gray line)) between 300 nm and 700 nm. A previous graduate student (Lance Barron) in the Microelectronics program at RIT completed a Masters thesis [74] on the spectral reflectivity of aluminum alloys (he in now employed at TI) and TI has filed a patent [75] that references his work. Figure 3.30 (orange line) shows the sputtered deposited aluminum film reflectivity from 250 nm to 1050 nm (from Barrons Thesis).

The general shape of the reflectance curve matches Barron's values for pure aluminum quite well. However, the measured data indicates a lower reflectivity than the TI measured value at 300 nm. This is likely due to the fact that, this sample of mirrors was open to air for approximately 1 year, and there were several damaged mirrors as a result of the window removal process. The spectrometer used becomes relatively noisy for measurements below about 220 nm. Additionally at 360 nm the spectrophotometer switches between a deuterium and tungsten light source, so there is a slight discontinuity in the curve at this wavelength.

The measured DMD reflectivity was very sensitive to the mounting location within the integration sphere. It was critical that the specular reflection from a majority of the mirrors be orientated into the integrating sphere. These reflectance measurements slightly underestimate the DMD reflectivity, because some of the second bounce light is absorbed around the DMD periphery masked region (this should be a small effect) rather than being reflected back into the integrating sphere. These measurements were made on an older generation of mirrors, and its optical properties are likely not as good as the newer DMD that would be used in a future space instrument. The edges of the newer DMDs are different than this measured DMD.

A final factor that needs to be accounted for is the losses attributable to light falling in the gap between the individual DMD mirrors and in the central hole. The mirrors are 16 µm square with a 2 µm central hole and are on a pitch of 17 µm. Therefore the geometric ratio of the aluminum reflecting area to the total pixel area is $\frac{16\times16^2\times2}{17\times17} = 0.87\%$. In order to compare the measured DMD reflectance to a continuous film of aluminum this loss mechanism must be accounted for by multiplying the measured DMD reflectance by $\frac{1}{0.87} = 1.15$. Clearly multiply the green curve by 1.15 would indicate a much high reflectance than aluminum which is unphysical. The likely issue is that not all the light that falls in the gap or hole is absorbed and therefore multiplying by 1.15 overestimates the loss. There was no straightforward independent means to estimate this factor and it might range anywhere between 1 and 1.15. If the green curve in Figure 3.30 is matched to TI reported reflectance, this factor would be about 1.04. The systematic uncertainties associated with this experiments are on the order of $\pm5\%$.
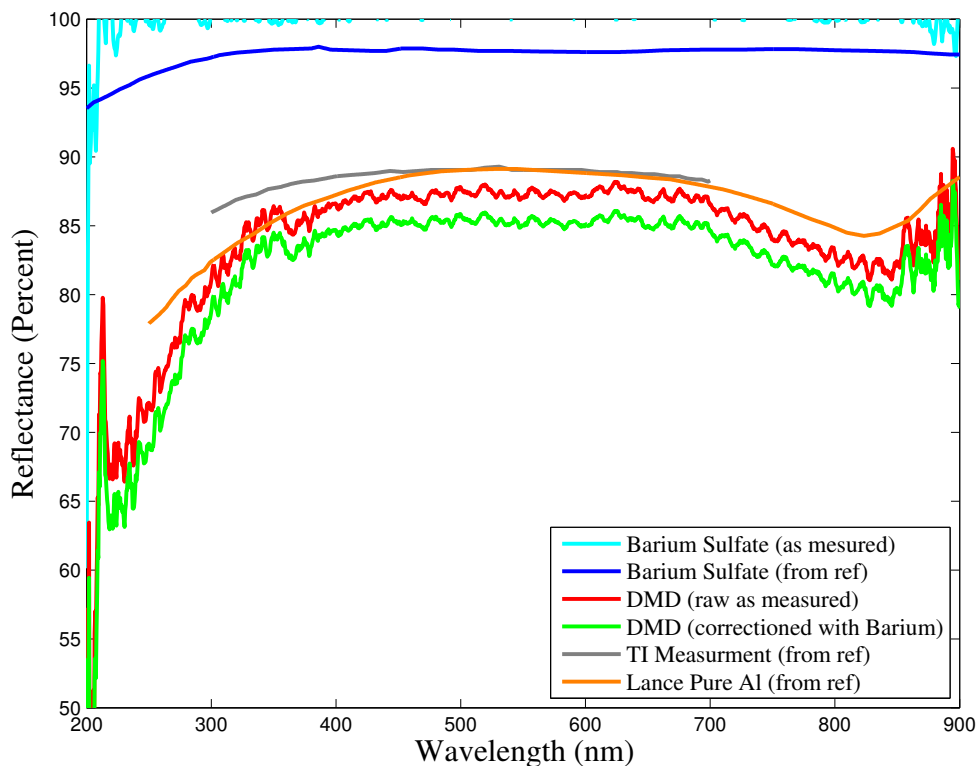
Figure 3.30: The measured DMD reflectivity versus wavelength is illustrated here.

Based on the measurements performed, the DMD likely has a reflectance of approximately 65% at 200 nm and of approximately 82% at 300 nm. At wavelengths longer than 300 nm the reflectivity appears to follow that of pure aluminum (the alloy is probably a 1% silicon and 0.2% titanium alloy based on a TI patent [76].

$$E_\lambda = FF \times DE_\lambda \times R_\lambda \times DC \times WT_\lambda^2 \tag{3.12}$$

3.3.6   Total DMD Optical Efficiency

There are many parameters, which contribute to the DMDs optical throughput. Equation 3.12 shows the effect of various parameters and Table 3.3 using both measured parameters and in the near-infrared values from literature to predict DMD efficiency with a "TYPE - A" package and borosilicate window. FF is the DMD fill factor, which can be calculated by taking the total pitch area and determining the active portion of this region. The mirror gaps and via are subtracted to get the fill factor. The Diffraction Efficiency (DE) is determined by assuming an $f/3$ optical system is used to collect the diffracted light from the DMD. A $f/3$ system is the fastest system one could design a spectrometer. The encircled energy over this aperture relative to the complete encircled energy determine the diffraction efficiency. R is simply the reflectivity, which is a function of wavelength and is measured above. DC is the duty-cycle, and in the case of an astronomical spectrograph it would always be 1 (100%) because the mirrors are always in one position and not oscillating. WT is the Window transmission. The WT is squared, because the DMD requires the light

Table 3.3: DMD efficiency Parameter values for a 13.68 μm DMD.

Wavelength (nm)	Fill Factor	Diffraction Efficiency	Reflectivity	Duty Cycle	Window Transmission	Efficiency	Efficiency without Window
200	0.91	0.99	0.65	1.00	0.00	0.00	0.58
300	0.91	0.99	0.77	1.00	0.60	0.25	0.69
400	0.91	0.97	0.85	1.00	0.80	0.48	0.75
500	0.91	0.97	0.85	1.00	0.95	0.68	0.75
600	0.91	0.95	0.85	1.00	0.96	0.68	0.73
700	0.91	0.95	0.85	1.00	0.98	0.70	0.73
800	0.91	0.95	0.82	1.00	0.90	0.57	0.71
900	0.91	0.95	0.85	1.00	0.85	0.53	0.73
1000	0.91	0.94	0.95	1.00	0.78	0.49	0.81
1100	0.91	0.94	0.95	1.00	0.77	0.48	0.81
1200	0.91	0.93	0.95	1.00	0.70	0.39	0.80
1300	0.91	0.93	0.95	1.00	0.67	0.36	0.80
1400	0.91	0.93	0.95	1.00	0.65	0.34	0.80
1500	0.91	0.92	0.95	1.00	0.65	0.34	0.79
1600	0.91	0.92	0.95	1.00	0.65	0.34	0.79

pass through the window twice. Table 3.3 shows that a significant portion of the loss in a DMD is a result of the window transmission.

3.4   Summary

Several methods have been developed to experimentally measure the stray light from a DMD used at the focal plane of a MOS. The contrast ratios are generally lower than the ratios given in the projector applications due to differences illumination angle. A reflectivity model was developed to mathematically describe the sub-mirror shift variant reflectivity. Also, an important stray light path was found due to the inner reflection at the window surface. One method to mitigate the stray light ghost image is to incorporate an index-matched prism (with a corresponding index-matched adhesive) as used in digital projectors. There are other advantages to prism based systems such as making the system fold much more quickly rather than relying on the air gap to separate the ingoing and out going beams.

The reflectivity between 200 nm and 900 nm of a bare 17 μm pitch TI DMD was measured. The device measured had been unpackaged, meaning that the protective window and frame were removed. Thus the reflectivity reported is for the intrinsic MEMS DMD aluminum alloy itself. The device used for the measurements had been unpackaged approximately a year prior to these measurements and had been stored in a laboratory environment exposed to the atmosphere. It was found that the DMD has a reflectivity of approximately 65% at 200 nm rising to 83% at 300 nm.

Many factors contribute to the overall DMD optical efficiency, but one of the limiting ones for an astronomical spectrograph is the protective window. When using a DMD it is important to optimize all aspects of the optical system to account for the DMD.

There are several other important areas that need to be tested with regard to the DMDs performance. One is related to how the backfilled gas affects the measured spectrum. When the DMD is placed in a vacuum, is there a significant path length of helium in the package to create Helium 1 lines in the measured spectrum of a black body source? The second issue is that of electro-luminescence or glow from the DMD

circuitry beneath the mirrors. This is referred to as PEM (Photon EMission in silicon) [77] in the literature. Some work was done to investigate the electro-luminescence, using an available Platinum Silicide Infrared Camera and InGaAs camera, but neither camera systems were sensitive enough to detect thermal glow from the 1024×768 XGA 13.68 μm XGA 12° DMD. It was beyond the scope of this work to investigate these two phenomenon in more detail.

CHAPTER 4

PROTON RADIATION TESTING

There are many unique challenges associated with building electronics for long-term operation in space. This chapter examines the space radiation environment, radiation test procedures developed for DMDs, and prediction of DMD lifetime. It is through these preliminary tests that further MEMS radiation test procedures can be developed for future space missions.

4.1   Space Radiation Environment

The radiation environment found in space is tremendously different than that found at Earth's surface. The Earth's atmosphere and magnetic field protects us from the extreme conditions in space. Our atmosphere is a great shield, which allows much simpler electronics design for terrestrial electronic systems. Radiation hardening a spacecraft's electronics is key for its long-term survival and operation. Spacecraft and high altitude aircraft have to employ radiation-hardened electronics. For such aircraft and satellites alike, all electronic components must be tested for the specific space environment that they will be deployed in. The Van Allan radiation belt contains ionizing radiation with electrons (energies up to 10 MeV and protons (energies up to 100 MeV). Cosmic rays are also a significant source of radiation in the space environment, which is composed of protons, electrons, gamma-rays, x-rays and heavy-ions. The Sun is the primary source of proton radiation in the space environment. Therefore, electronic devices are tested to understand how long they can operate in a radiation environment and predict mission lifetime. In spacecraft, it is not practical to shield against all kinds or energies of radiation, due to the weight of the required shielding. The radiation environment also changes drastically depending on the satellite orbit. For example, the radiation environment in Low Earth Orbit (LEO) is much different than the environment at a geosynchronous orbit.

There are four main classifications of radiation tests that can be performed on the ground: gamma, proton, neutron and heavy-ion testing. Gamma radiation is present in both the space environment and is also created upon nuclear detonation. The gamma rays can create secondary electrons after passing though a target material. These secondary particles can also be damaging to electronics. Gamma-rays are extremely penetrating, and can easily pass through a significant amount of shielding. Proton testing involves accelerating protons and then irradiating an electronic device. Proton has both ionizing and non-

ionizing damage components. Heavy-ions are composed of significantly more massive ions where $Z > 1$ (e.g. more massive elements than hydrogen), and they can cause considerable damage to electronic devices.

4.1.1   Radiation Effects

Proton testing often involves irradiating electronic parts of interest and assessing both ionizing and non-ionizing damage. The effect of proton radiation on an electronic component can be cumulative or transient in nature. Cumulative effects are associated with the Total Ionizing Dose (TID). Conversely, one kind of transient phenomenon is known as Single Event Effects (SEE). There are many different classifications of SEE's, but one of particular interest is Single Event Upsets (SEU). A SEU is a type of soft error, which occurs when an energetic particle passes close to a sensitive node of a memory element, resulting in a flipped bit. The difference between radiation-hardened parts and standard parts can be quite significant in terms of both design and expected lifetime in a radiation environment. Certain electronic components are built radiation-hardened by design. For example, radiation hard parts are generally not processed with hydrogen, have no field-oxide layers near sensitive portions of the chip, and most avoid high-temperature processing.

4.1.2   Favored Orbit

The spacecraft orbit or location has a large factor in a mission's radiation budget. A favorable orbit for future astronomy missions is the second Lagrangian point (L2). Past missions have already flown to L2. These include the Wilkinson Microwave Anisotropy Probe (WMAP) [78], Herschel [79] and Plank. The L2 orbit is shown in Figure 4.1. In any two-body system, there are several saddle points where there is zero net gravitational force. The L2 saddle point is located away from the sun, and 1.5 million km from the earth. L2 is an unstable saddle point, meaning that some fuel is required to keep a spacecraft in orbit. For comparison, the Moon's orbit is $383,000$ km from Earth. The orbit has several obvious advantages for a space telescope mission. Its radiation environment is typically outside the Van Allen radiation belts, so the important types of radiation to consider are limited to cosmic rays and solar protons. However to reach L2, the spacecraft must pass through the Van Allen belts several times depending on the orbital transfer method used. In addition, the spacecraft temperature in this location is very stable. Scattered light from either the Earth or moon is significantly lower at this location. For the DMD to be used at L2, proton testing is the most relevant radiation test procedure. Proton irradiation is very applicable to this orbit, because the solar wind is composed primarily of high-energy protons. The number of solar protons depends greatly on sun's solar 11-year solar cycle. There will be a significant variation during a 5-year mission depending on this solar cycle.

4.1.3   Radiation Tolerant Slit-Mask (Motivation)

The current ground-based approach to MOS generally uses one of two approaches to separate targets of interest: fibers (e.g. Hydra[8]) or masks (e.g. GMOS [9]) as discussed previously in Chapter 2. While the MSA are already locked in as the method of spectroscopy in JWST, a future mission could be more suited to use DMDs as a slit mask in a space-based MOS. The Ground based instruments (RITMOS [10], IRMOS [11] and more recently BATMAN [60]) all illustrate the DMDs potential on the ground. These systems proved
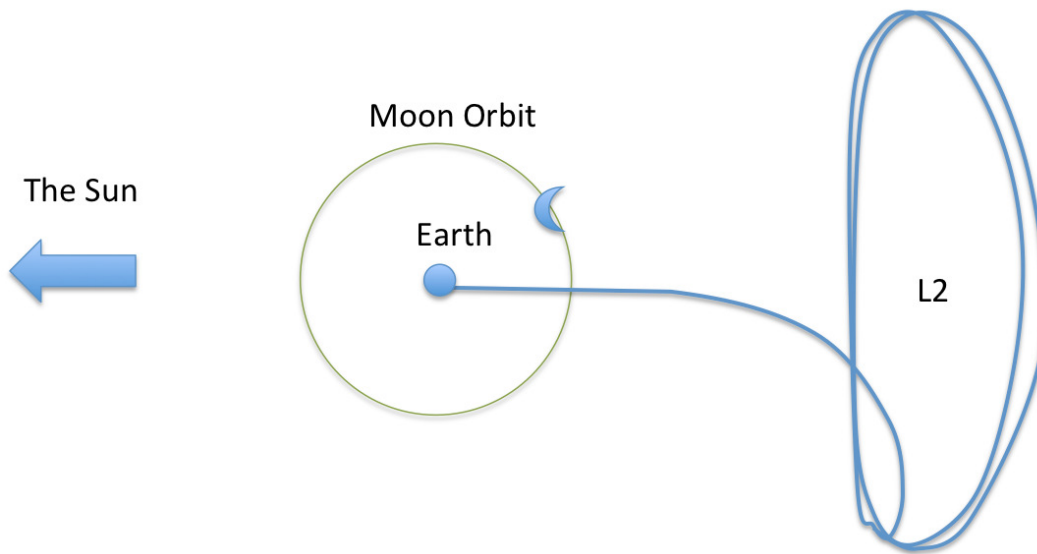
Figure 4.1: The L2 orbit is far outside the lunar orbit and has a 180 day period. The orbit always resides at the anti-Sun position.

to be useful MOS instruments and are precursors for future space experiments [80]. However, one of the outstanding uncertainties is the radiation tolerance of the DMD.

The James Webb Space Telescope (JWST) includes a multi-object Near InfraRed Spectrometer (NIRSpec) [6] as a primary instrument. The instrument uses a Micro-Shutter Array (MSA) to define the slits for the spectrometer. The JWST MSA uses $100 \times 200\,\mu m$ shutters and was custom built at the NASA Goddard Space Flight Center (GSFC). These MSAs have limitations due to the high number of defective shutters and small format sizes (365×171). There is great interest to find alternative technologies to make programmable slits for future space missions. The Commercial Off The Shelf (COTS) Digital Micromirror Device (DMD) is a logical candidate to fulfill this role. DMDs are readily available with 100% operability and large format (up to 4000×2000 elements). The mirrors' aluminum surface provides a broad spectral reflectivity. These COTS low cost mirrors are integrated with CMOS circuitry to allow spatial mirror patterns to be uploaded easily.

4.1.4   Previous Radiation Testing

The DMD is being considered as a new technology to be used in space, but has never been fully characterized or qualified for use in a radiation environment. Previously as part of the ESA qualification for the EUCLID Mission, gamma radiation testing was performed on DMDs with a cumulative gamma dose of $10 - 15$ krad-Si [81]. These results reported some failure modes at this dose. Unfortunately, the DMD and its drive electronics were both irradiated during this test. It is not possible to unambiguously distinguish whether the DMD or drive electronics was the source of the degraded performance in these tests. Although gamma testing is representative of an electron environment, the proton environment is more of a concern for a spacecraft operating at the second Lagrange point (L2). By analogy with CMOS imagers, protons can compromise on-chip readout electronics by charging gate oxides. MEMS components are becoming more commonly used in spacecraft, but radiation testing of these devices is still a young field in its infancy [82]. This chapter reports on the first completed proton testing of a DMD.

No previous proton irradiation tests on DMDs have been completed. As part of the Euclid mission, proton tests were planned, but the beam-line malfunctioned before any significant dose irradiated the DMDs. Ideally, these the DMDs should be tested cold in a dewar, but as a preliminary test, the devices were irradiated at room temperature. The test apparatus was simplified drastically without the requirement of a liquid nitrogen dewar. By testing the DMDs warm, this will give the most optimistic operational results for the devices. Total Ionizing Dose (TID) effects will be investigated. The DMDs will remain in their permanently sealed hermetic package during the test procedure because it is not practical to test unpackaged DMDs. The devices come prepackaged in this protective seal directly from TI in order to isolate them from dust and moisture. The inherent shielding in the DMD package is favorable from a flight perspective, but it is unfavorable from a radiation testing perspective. Proton energies incident on the device window less than 30 MeV tend to deposit most of their energy within the glass window and therefore would not be useful. Proton energies greater than 10 MeV at the device are useful for examining TID in silicon. Figure 4.3 shows the fluence of 100 mil equivalent aluminum shielded protons for a 5-year mission at L2. Providing accurate dosimetry behind the window in the packaged DMD is essential to accurately determine the dose absorbed by the electrically active silicon in the DMD.

4.2   Radiation Units and Dosimetry

There are many different units to quantify radiological measures. Linear energy transfer (LET) is an important parameter for characterizing ionizing particle energy loss in matter and is closely related to the ion stopping range. The units for LET are $\frac{MeVcm^2}{mg}$. It is the energy loss of a particles and is also related to the energy absorbed by the medium. A "rad" is defined as 100 ergs of energy absorbed by 1 gram of material. Equation 4.1 is from Bethe's formula. In this equation v is the velocity of the particle, e is the charge of the electron, Z is the atomic number. This gives energy lost per unit length via ionization or electronic stopping power. There are many different forms of this energy loss equation depending on the fidelity of the model and number of correction factors (NZB is a correction factor for protons). Bethe's formula can be used to calculate the LET (equation 4.2). Equation 4.3 shows that with LET, proton fluence and a unit conversion factor the absorbed dose in krad's can be computed. The *krad* is the commonly used unit by space electronics radiation effects groups to characterize the dose absorbed in a device.

$$\frac{dE}{dx} = \frac{4\pi Z^2 e^4 Z^2}{m_o v^2} NZB(m_o, v, I) \tag{4.1}$$

$$LET = \frac{1}{\rho} \frac{dE}{dx} \tag{4.2}$$

$$X(krad) = LET\left(\frac{MeVcm^2}{mg}\right) \times fluence\left(\frac{1}{cm^2}\right) \times \left[1.60 \times 10^{-8}\left(\frac{mgkrad}{MeV}\right)\right] \tag{4.3}$$
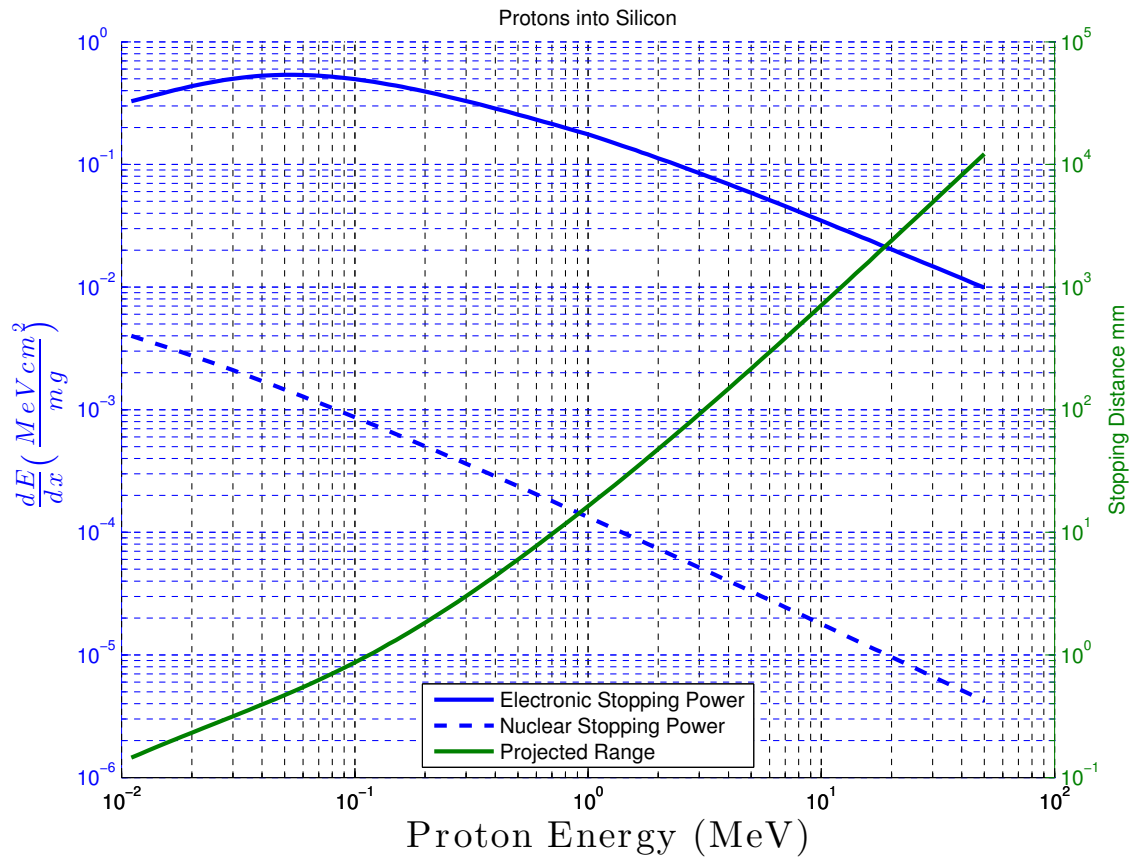
Figure 4.2: Three curves are shown on this plot. Both blue curves are energy loss in the target material. The Electronic stopping power also called Linear Energy Transfer (LET) is the mechanism for energy deposited in the silicon. The right axis (green curve) shows the projected range of silicon as a function of energy level in silicon.
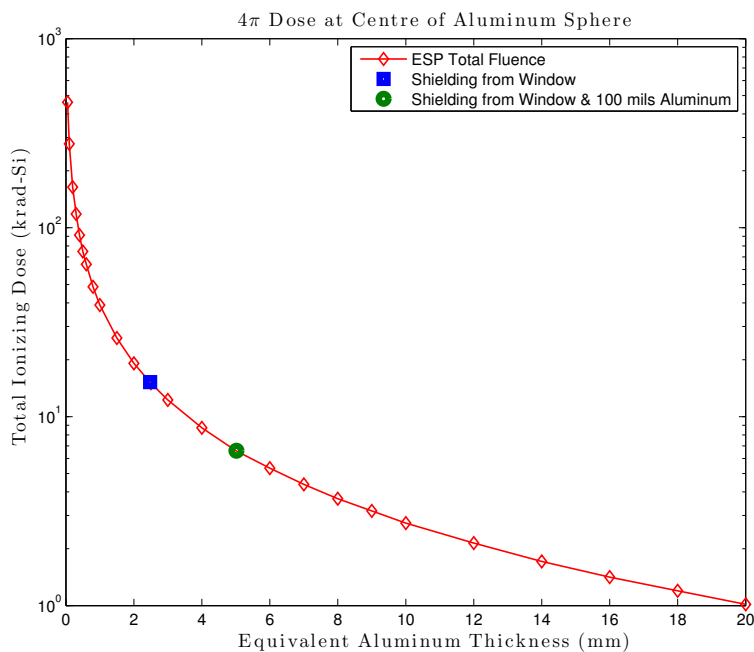
Figure 4.3: Total dose of Solar protons in Si after a 5-year mission at L2 (modeled by SPENVIS). 2.47 mm of aluminum shielding corresponds to the shielding provided by the package. Additionally, 100 mil of equivalent aluminum shielding is shown.
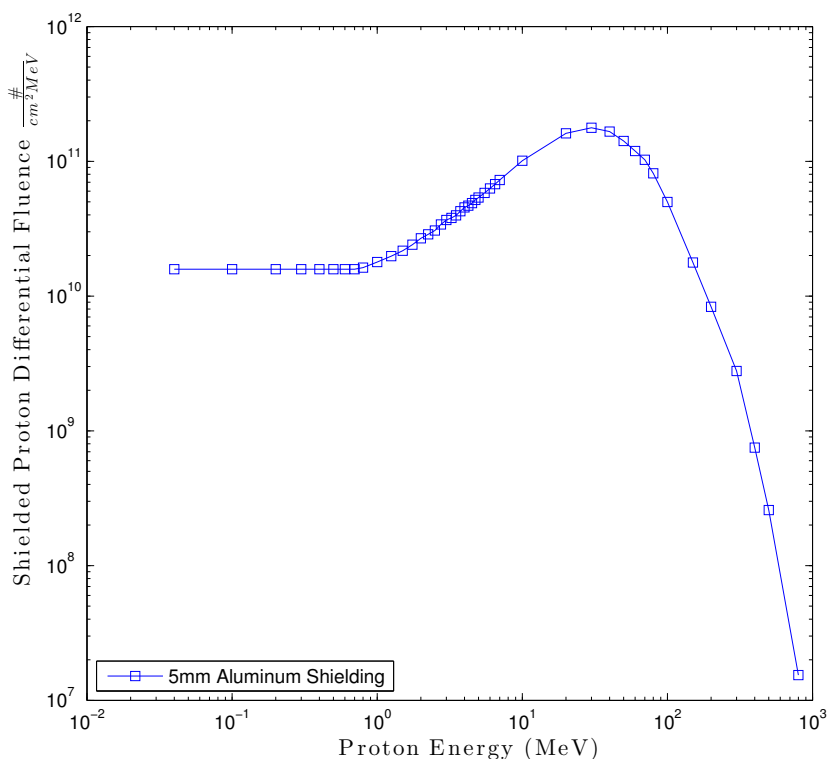
Figure 4.4: Proton fluence as a function of energy at L2. Calculated using the ESP solar proton model using a total shielding thickness of 5mm equivalent aluminum.

4.2.1   Radiation Modeling

The purpose of proton testing the DMD is to evaluate how it would function at L2. The L2 orbit is generally outside the boundary of the Van-Allen Radiation belts (except during large solar events), so the radiation species are primarily composed of solar protons. Cosmic rays (composed of primarily of protons) also account for a smaller portion of the radiation exposure at L2. The the Sun's eleven-year cycle plays a role in a mission's radiation budget. The proton spectrum at L2 was modeled using the SPENVIS (Space ENVironment Information System) software package [83]. The Emission of Solar Proton Model [84] (ESP) was used to predict the long-term solar particle fluence for a 5-year mission at L2 assuming a 95% confidence level. Figure 4.3 shows the shielded proton fluence for a 5-year mission at L2 starting in 2020 using the "SHIELD-DOSE2" model. For a 3 mm thick borosilicate window, the shielding provided by the glass is 2.47 mm of equivalent aluminum. The ratio of borosilicate's density $\left(2.33\frac{g}{cm^3}\right)$ to aluminum's density $\left(2.70\frac{g}{cm^3}\right)$ was used to calculate this equivalent thickness. The lower section and sides of the DMD offer additional shielding beyond that of the window. As shown in Figure 4.3, the expected dose at the DMD silicon with just the window as shielding is predicted to be 15 krad. A common value used for the typical level of spacecraft shielding is 100 mils = 2.54 mm of equivalent aluminum [85]. Assuming this additional shielding, the expected dose at the DMD silicon would be 6.6 krad for a 5-year L2 mission. As will be discussed in Section 4.3.3, the DMDs were irradiated to a dose of 40 krad. The range of proton energies (i.e. $35 - 50\,\text{MeV}$) used in the irradiation test undertaken in this work was chosen to be near the peak proton fluence (see Figure 4.4) at L2.

The DMDs were proton tested with their packaging intact, as this is the most likely scenario for deployment in space. Any material (e.g. the DMD window) in the proton beam results in interactions that degrade the beam energy and fluence; however, testing the packaged DMD eliminates the possibility of moisture or particle induced mirror failure. This means that the protons must be accelerated with sufficient energy to pass through the DMD window and interact electrically with the DMD silicon to obtain meaningful results.

The proton flux incident on the DMD window was measured using an ionization chamber. The software package SRIM (Stopping Range of Ions in Matter) [86] was used to model the beam energy at the DMD silicon after passage through the window. A simple model stack was set up in SRIM. The first compound layer was borosilicate glass (3 mm thick). Next a thin 0.5 mm layer of nitrogen gas was added. Then finally a thick 12 mm layer of silicon was used. The projected range was found for each of the energy levels used in the DMD irradiation (34 MeV, 44.2 MeV, 49.9 MeV). SRIM was then used to find the same energy protons that would deposit the ions at the same depth in just the silicon (the borosilicate glass and nitrogen were removed from the film stack). After this energy was determined, it was assumed that this would be the energy impinging on the DMD silicon. The results of this modeling are shown in Table 4.1: which lists the input beam energy, modeled energy at the device and corresponding dose conversion factor (CF). The dose conversion factor (CF) using the lower energy LET (Linear Energy Transfer) was used to calculate the dose deposited in the device behind the window. A dose measured incident on the window is then multiplied by the CF to obtain the dose at the DMD silicon behind the window. After the protons pass through the window they have a lower energy, and therefore deposit a greater dose due to the larger LET ($\frac{dE}{dx}$). For example, a 1 krad dose of 34.0 MeV protons incident on the package, corresponds to a 1.4 krad dose of 21.0 MeV protons at the silicon.

Table 4.1: Beam Energy, LET and Dose Correction Factors (CF) from SRIM model

Beam Energy (MeV)			LET $\frac{dE}{dx}$		CF
At Window	At Mirror	$\Delta Energy$	In Window	In Silicon	
34.0	21.0	13.0	0.0134	0.0189	1.409
44.2	34.5	9.7	0.0109	0.0132	1.214
49.9	40.9	9.0	0.0100	0.0116	1.158

4.3 Experiment

The experiment was run using the following strategy. Three DMDs were irradiated (Serial numbers 140508, 140507, and 140106) using a different proton energy for each device, 34.0 MeV, 44.2 MeV and 49.9 MeV. We will refer in the rest of this chapter to the beam energy on the DMD after the window's absorption, i.e. 21.0 MeV, 34.5 MeV, and 40.9 MeV respectively. The absorbed dose (i.e. the total "irradiation" time of the DMD in the beam) was increased in steps of 2 krad or more. This step in dosage is the equivalent dose obtained after 2 years at L2 (assuming a 6.6 krad total dose). The functionality of the DMDs was examined during the intervals between each irradiation step by exercising the DMD with a series of patterns. The irradiation sequences are described in Sections 4.3.3, 4.3.3, and 4.3.3. The measures of the DMD post-irradiation operability are described in Sections 4.4 and 4.4.3.

4.3.1   Proton Irradiation Facility

To undertake proton testing of DMDs, 48 hours of beam time were allocated at the Lawrence Berkley National Laboratory (LBNL) 88″ cyclotron. The testing was completed in cave $4A$ where the beam-line provided protons with energies between 35.0 MeV and 49.9 MeV. Electronic attenuators allowed control of the beam to a desired flux rate. Only three beam energies were utilized because the facility required a change time of 5 to 8 hours. A considerable amount of the time between irradiation increments was required to complete the optical characterization of the DMD.

Figure 4.5: Parts of the experimental apparatus are as follows: (A) is the proton beam-line exit port, (B) ionization chamber, (C) aluminum aperture plate, (D) high-speed CCD camera, (E) a macro lens, (F) LED light source, (G) kinematic mount, (H) 0.75″ aluminum shielding for the drive electronics, and (I) test DMD.

4.3.2   Irradiation Test Setup

Figure 4.5 shows the beam-line experiment. The protons from the cyclotron exit the port labeled as (A). The ionization chamber (B) is located after the beam exit port. A 2″ aluminum aperture plate (C) is employed to collimate the proton beam as the DMD (I) under test has a 0.7″ diagonal. This aperture size is sufficient to permit the entire DMD active area and package to be uniformly irradiated. The DMD drive electronics (Discovery 4000 Kit) is shielded using 0.75″ aluminum plate (H) and therefore is not irradiated. This allows us to evaluate the true radiation tolerance of the DMD itself. The DMD was placed as close as possible to the beam exit port, but with sufficient room to insert the camera test fixture. To limit systematic uncertainties and facilitate comparison between subsequent irradiation runs, the DMD is not removed from the test bench or un-powered for the duration of the test procedures. After each irradiation step, a CCD camera (D) and 50 mm C-mount lens (E) is placed in the beam-line looking at the DMD. The camera mount had two stages: z (along the optical axis) and x (along lateral DMD direction), mounted to focus the camera. The coarse positioning in the vertical direction was completed by having the DMD on a lab jack stage. This allows the DMD to be re-imaged onto the camera. A kinematic magnetic mount (G) serves as the repeatable mounting fixture for this camera and light source (F). The lens aperture is set to $f/4$ for the duration of the
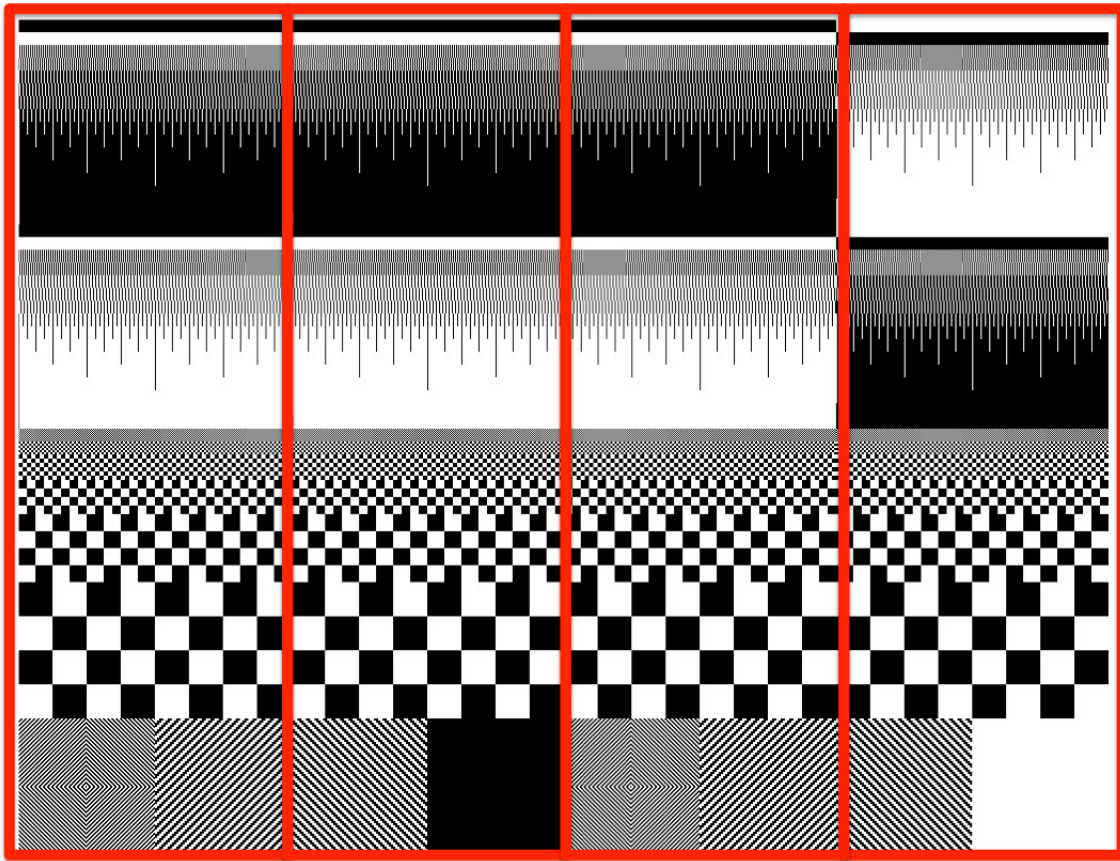
Figure 4.6: First DMD pattern sequence for the optical test. The DMD was divided into four distinct sections as highlighted by the red sections. Leftmost 256 columns were kept in the same position (same mirror tilt angle) for each irradiation step. Rightmost 256 columns were set to a 50% duty cycle in which the mirrors were switched for each irradiation step. Middle two sets of 256 columns in between were set to other duty cycles between the two extremes. Figure 4.7 shows five such frames from this mirror pattern sequence. same sequence for each

experimental data collection. An LED light source is used to uniformly illuminate the active area of the DMD during the imaging process.

Three DMDs were powered on and latched during the irradiation tests. The testing for each of these DMDs at the 3 beam energies was repeated until the DMD showed an appreciable degree of failure. The run logs for each DMD are shown in Appendix Tables C.1, C.2, C.3. Each DMD was finally exposed to greater than the 30 krad silicon dose. Each table shows the exposure number, the average flux, fluence, integrated fluence, and integrated dose in krad. The quoted dose is not adjusted for the proton beam degradation through the DMD borosilicate window, but instead it is representative of the dose at the window surface. Because lower energy protons deposit more dose, (lower energy protons have a higher interaction cross section), the dose behind the DMD at the silicon was slightly higher for all devices tested. Table 4.1 shows the correction factors for this dose differential.

Zone 1 => fixed 100%
Zone 2 => period = 4 => 3 the same, 1 flip => 75%
Zone 3 => period = 3 => 2 the same, 1 flip => 66%
Zone 4 => period = 2 => flips every run =>50%
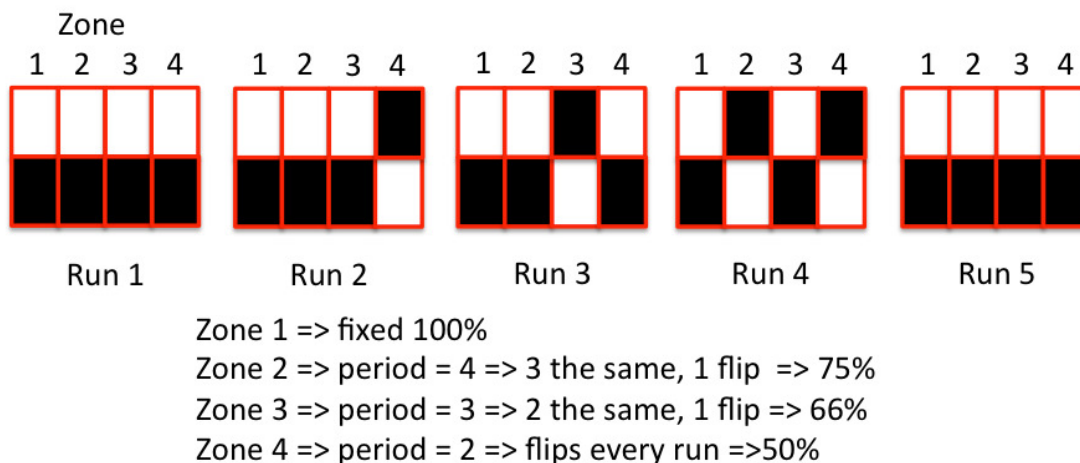
Figure 4.7: Five sequential DMD run patterns are shown here. Each zone is composed of 248 columns of DMD mirrors. For run 1 the top half of the DMD mirrors are on, and the bottom half are off. During run 2, the mirrors are flipped in zone four. Next, for run 3, the mirrors in zone three are flipped. This sequence continues for each irradiation step. This set of patterns is used to investigate the mirrors duty-cycle during proton irradiation. For the zones 1 to 4, the duty-cycles tested were 100%, 75%, 66%, and 50%. Mirrors in zone 1 were in the same position for each irradiation. Mirrors in zone 4 alternated positions every other irradiation step.
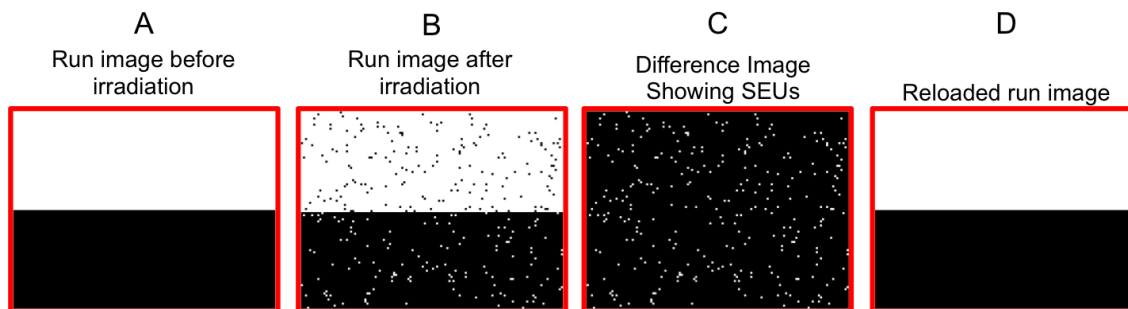
Figure 4.8: (A) Run pattern was loaded into the DMD prior to the proton irradiation and an image was captured with the camera. (B) Image was captured with the CCD camera after irradiation. Mirrors that flipped during the irradiation look dark in the top half of the array and bright in the bottom half to the array in this example. (C) $|A - B|$ shows the locations of all of the flipped mirrors in the irradiation. (D) The same run pattern was reloaded into the DMD to ensure all mirrors went back to their programmed state.

4.3.3   Irradiation Sequence

Energy #1 (Beam - 34.0 MeV **Device -** 21.0 MeV**) DMD serial number 140508.**

The initial set of tests was conducted with the beam energy tuned to 34 MeV. Prior to irradiating devices, the beam had to be optimized for uniformity across the beam aperture. Gafcrhomic *RTAQ*2 [87] film recorded the beam uniformity. The film was scanned using an on-site densitometer. This process was repeated until the beam was adjusted to be within the desired uniformity (approximately 1% uniformity across the DMD).

Prior to traveling to LBNL, the top kovar metal frame with window was removed from four surplus DMDs. This process is illustrated in Figure 4.9. The bottom portion of the package with the DMD silicon was discarded. These four sets of window frames were used to determine if the glass transmission changed after proton irradiation. One of the DMD window frames was then irradiated with 34 MeV protons to a dose

of 20 krad with the beam incident normal to the window. The window transmittance results are shown in Figure 4.14, and the results are presented in Section 4.4.1. The windows were irradiated with Gafchromic film in front of the window and behind the window. However due to time restrictions, a characteristic curve was not completed for the films at each energy. The Gafchromic film is composed of five different layers, a yellow polyester, a pressure sensitive adhesive, and active layer, a surface layer, and a while polyester layer. The film was then scanned into a Labview software program that looked at the density of hits per area. Each hit on the film correspond to a proton passing through. The more protons that pass through the film, the darker the film became. The film was darkened more with lower energy protons. A dose of 0.1 krad was sufficient to expose the film. The across beam uniformity was better than a few percent for all 3 energies. Therefore, it was not possible to directly measure the energy behind the DMD window. The energy has not been measured at the beam-line exit since the machine was commissioned in the 1960$'s$. In the near future, an electron cusp detector will be available for performing such measurements.
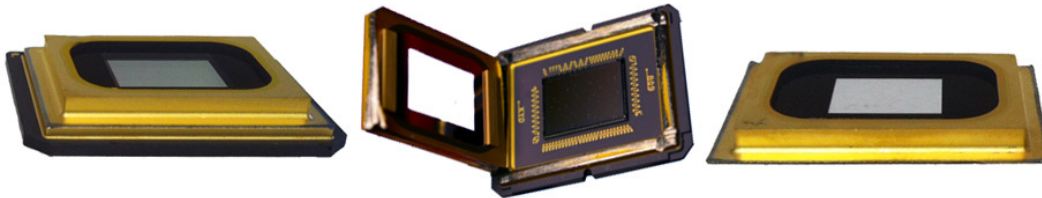
Figure 4.9: (Left) Original DMD package. (Middle) Kovar metal frame and window are in the process of being removed from the DMD package. (Right) Kovar frame and window are separated from the the DMD package.

After the first window frame had been irradiated, a powered and biased DMD was tested at 34 MeV (21 MeV incident at the silicon). All of the DMDs were irradiated with the proton beam incident normal to the window. Before irradiation, the baseline DMD functionality was validated using an optical test procedure as is described in Section 4.3.4. The DMD run 1 pattern was loaded into the DMD. Next, the full surface of the DMD was irradiated to 2 krad incident. The optical test procedure (Section 4.3.4) was then performed. For each run, the loaded run pattern (Figure 4.7) was modified to test the influence of duty-cycle. This was repeated until run 10, where each run corresponded to an additional 2 krad incident dose. After run 10 the irradiation dose step was increased to 5 krad incident, and three additional runs were performed. The 34.0 MeV run log is shown in Table C.1.

Energy #2 (Beam - 44.2 MeV **Silicon -** 34.5 MeV**) DMD serial number** 140507**.**

Next, the beam energy was tuned to 44.2 MeV. The same beam uniformity measurements were taken with the Gafchromic film. The second DMD window was placed in the beam, irradiated to 20 krad and then removed. The second DMD was then placed in the beam-line after A pre-irradiation optical scan was completed. A run pattern (Figure 4.7) was then loaded into the DMD. The DMD was irradiated to a 4 krad incident dose, and a post-irradiation optical test was completed (Section 4.3.4). The modified run image for run 2 was then loaded into the DMD. This procedure was repeated until run 6 at which time the irradiation dose increment was changed to 5 krad incident. The 44.2 MeV run log is shown in Appendix Table C.2. After the final irradiation increment and prior to the removal of this DMD from the beam-line, an unknown but substantial proton dose irradiated this device due to a beam-line control malfunction.
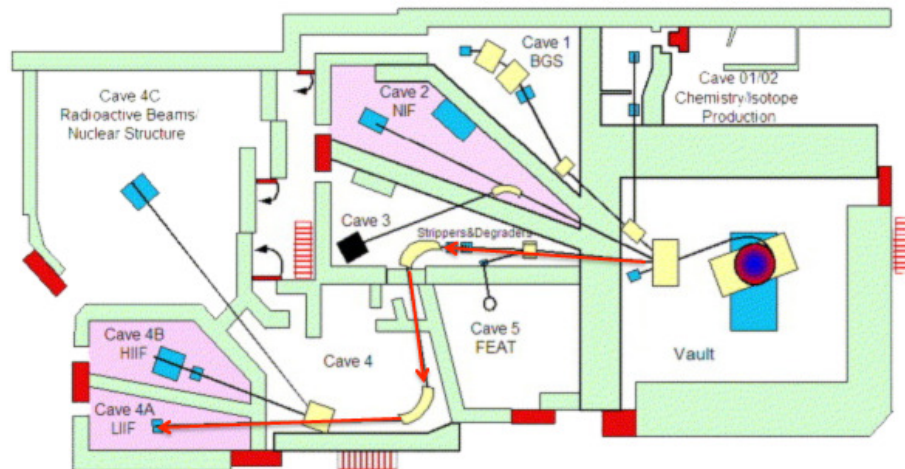
Figure 4.10: 88" cyclotron is shown here. DMD testing was completed in Cave 4 A. Red arrows illustrate the beam path our protons take out the cyclotron.

Energy #3 **(Beam -** 49.3 MeV **Silicon -** 40.9 MeV**) DMD serial number** 140106**.**

To test the final device, the beam was tuned to 49.3 MeV. At the highest energies the operators of the LBNL had more difficulty tuning the cyclotron, and it therefore involved the longest downtime. The third window was irradiated to a dose of 20 krad. The optical pre-irradiation test was done on the third DMD. The run pattern (Figure 4.7) was loaded into the DMD. It was irradiated to a 4 krad incident dose. The optical test procedure was then repeated on this DMD at each irradiation step. The incremental doses were kept constant at 4 krad until run 6, at which point the step size was changed to 5 krad incident. The 49.3 MeV run log is shown in Appendix Table C.3.

4.3.4   Optical Test Procedure

The goal of the optical test procedure was to determine which mirrors in the DMD array remained fully functional at increasing dose levels. Operational mirrors were defined as mirrors that would flip to both stable states. Non-functional mirrors were either stuck in one position, or failed to flip towards the CCD camera. Mirrors that stick would be permanently attached to the substrate in either the "on" position or the "off" position. Mirrors that fail to flip are mirrors in the central neutral position due to, e.g. a broken hinge or electrodes that fail to load the proper voltages. The optical test procedure for the DMD had two sets of patterns. One set of "run" patterns was sent to the DMD for use during the proton irradiation (Figure 4.7). A second set of "test" patterns (Figure 4.6) was used to check the functionality of each individual mirror after irradiation.

 An automated Matlab script was written to upload each DMD pattern and take a corresponding image. A total of 305 frames were taken for each test run. The purpose of the first set of run patterns was to have the mirrors latched in one of the two stable positions during the proton irradiation, much like they would be held in a MOS in orbit. It was of interest to determine if any mirrors flipped during the irradiation, so a simple procedure was devised. The run pattern was loaded into the DMD and an image was taken with the CCD camera. After the DMD was irradiated, a second image was taken. By subtracting these two images, the mirrors that flipped during the irradiation were detected. Next, the same run pattern was reloaded and another image was taken. This procedure is illustrated in Figure 4.8. The second image was used to verify
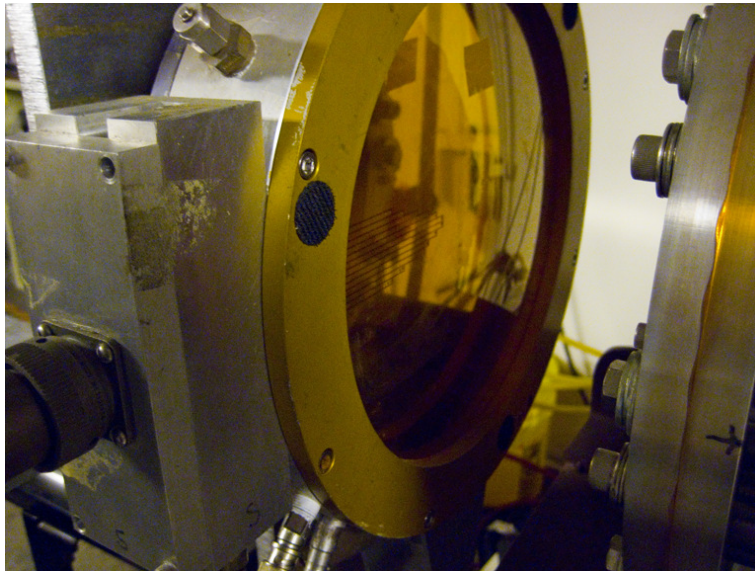
Figure 4.11: Ionization chamber at LBNL is shown here. A second set of electrodes going to the various rings can be seen on the left side extending into the center of the ionization chamber. These are generally aluminized Mylar coated films for each of the two parallel pates. The very sensitive ammeter is used to measure the current through, and this has been previously calibrated to the number of protons that hit the ionization chamber.

that flipped mirrors would return to their programmed state after reloading the DMD memory. The run pattern was divided the DMD into four duty-cycle zones. Each zone was composed of 256 columns on the DMD. Duty-cycle is defined as the percent of time a given mirror is in one state during the irradiations versus the opposite state. To determine if the mirrors' duty-cycle was a significant parameter, the run pattern was changed between subsequent irradiation steps. In zone one, the mirrors were kept in the same state for all irradiation steps. The zone four mirrors changed position at each subsequent irradiation step. For the zones one to four, the duty-cycles tested were 100%, 75%, 66%, and 50%. The test pattern was latched and held for the duration of one irradiation.

After the run pattern images were taken, a separate set of "test" patterns (Figure 4.12) was sent to the DMD. The first DMD test pattern had all of the mirrors along the perimeter orientated towards the CCD camera. An image was then taken with the CCD camera. This enabled the calibration of spatial correspondence between mirrors and CCD pixels. The DMD test pattern was then broken up into 10×10 blocks. A single DMD mirror, from each 10×10 block, faced the camera. This 10×10 blocking was repeated across the entire DMD. The CCD camera captured a series of 100 test patterns, so that each individual mirror in the DMD faced the CCD camera in exactly one image. These "test" frames were then repeated at two longer exposure times. This procedure was repeated at each irradiation step. This same testing procedure was performed at each of the three energies. The images were post-processed and truth maps were constructed after the testing was completed.

The light source was sufficient for the first round of testing, but was not as stable over time. There was a significant decrease in brightness as the batteries drained. If a subsequent test were completed on DMDs an optically stabilized source would be utilized instead. The camera exposure time was adjusted to compensate for the source instability during the optical tests. The camera lens aperture was set to $f/4$ for all of the experimental data collection. Additionally uniform ally illuminating the DMD and getting a better
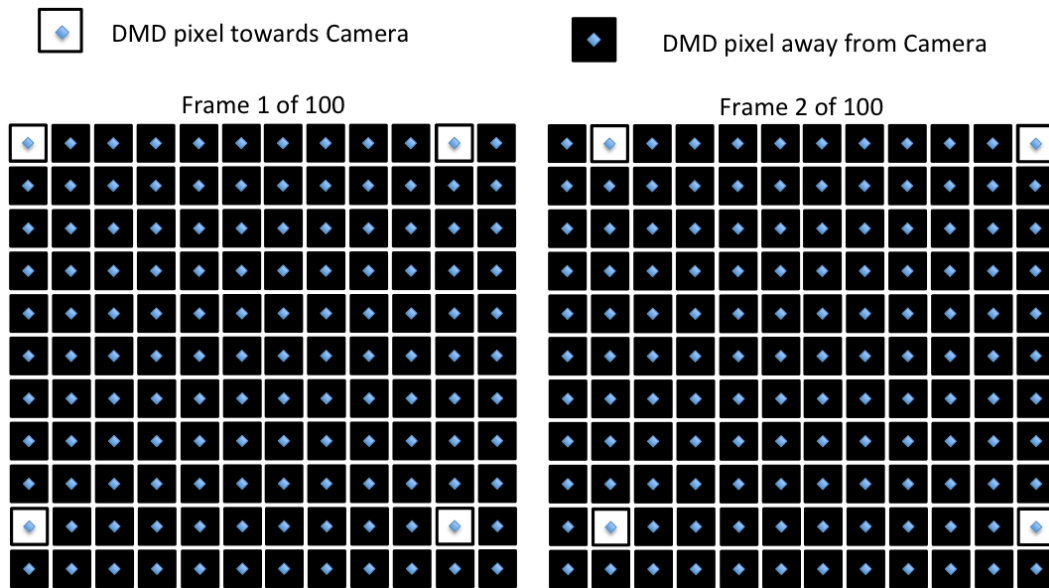
Figure 4.12: Two adjacent test patterns for the DMD optical "test" patterns. Black pixels are not facing the camera, and the white pixels are facing the camera (i.e. directing light in the direction of the camera). Re-imaging optics limited the experiment to a 10×10 sub array to be tested.

MTF macro lens that to re-image the DMD would greatly reduce the data reduction complexity. Doing both of these tasks requires an optimized optical system for analysis of the DMD through its cover-glass.

4.4   Results (Device Performance Post Irradiation)

There are many different reasons why individual pixels could no longer function properly after being irradiated. The purpose of this section is to examine the physical effects that occur as a result of performing the radiation tests on the devices. During the post irradiation test, the DMD Discovery 4000 electronics failed. The problem with these drive electronics is likely independent of the radiation testing. The 4000 series board was buggy from the beginning, and TI made changes and quickly phased it out of its catalog. An updated replacement Discovery 4100 kit was ordered to complete the post-irradiation testing.

The package did become activated during the irradiations, and the devices had to remain at LBNL until they cooled down to less than background levels. Because it was predicted that the DMDs would become activated, a General Employee Radiological Training (GERT) and Radiological Worker training (RW) were completed on-site prior to the handling of irradiated and radioactive devices. The results of the optical tests at each irradiation step are shown in Figure 4.18. The percentages of operational mirrors are shown as a function of proton dose. At all three tested energies, the DMDs withstood a TID of approximately 30 krad. After the irradiation procedure at each energy was completed, the mirrors were exercised using an alternating checkerboard pattern for several thousand cycles. Since the DMDs can flip mirrors at 20 kHz this operation requires a fraction of a second. For the DMD irradiated with 21.0 MeV protons, 90% of the mirrors immediately recovered any defective mirrors. Exercising was not as effective for the 49.9 MeV irradiated device. The results of exercising the DMD after 34.5 MeV protons are ambiguous because of the substantially large dose this DMD received after a beam-line malfunction. The same three DMDs were then tested again after a six-month room temperature anneal. Most of the mirrors fully recovered after this
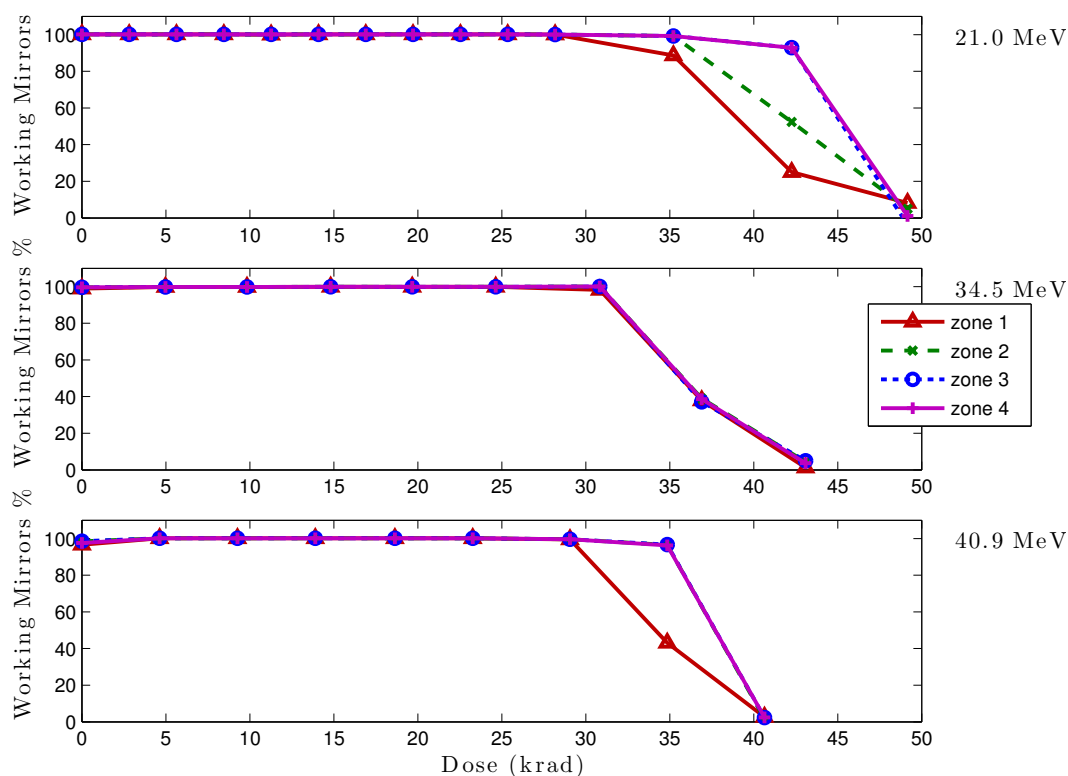
Figure 4.13: Percentage of working mirrors is plotted versus proton dose in krad. Note, the 34.5 MeV device was irradiated to an additional unknown dosage level after the last data point.

anneal (Table 4.2). It is likely that an accelerated anneal could be done at elevated temperatures with similar results that was not something that was attempted as part of this work.

4.4.1 Post-Irradiation Window Transmittance Loss

After irradiating the window frames to 20 krad, they became activated, and remained at Lawrence Berkley National Labs (LBNL) for several weeks until their activity level as measured with a Geiger counter returned to background level. After the windows were returned to RIT, their transmittance and that of an un-irradiated control window frame were measured on Shimadzu Spectro-Photometer 2100-UV. Figure 4.14 shows the transmittance measurements before and after irradiation. A loss of $1 - 3\%$ in the range $3,500\text{Å}-9,000\text{Å}$, and a loss up to 10% at $3,000\text{Å}$ can be seen after the irradiation. The windows were then re-measured on a separate instrument, a J.A. Whoollam VASE (Variable Angle Spectroscopic Ellipsometer) to validate these results. It is well known that borosilicate glass will yellow after being exposed to high-energy protons [88] [89] and our results all illustrate this effect. The peak in the curve at 300 nm is an actual transmission peak of combination of the glass and AR coating. These results are for a single-pass measurement, so the total loss of transmittance in the MOS application would be the square of this value. An alternative window material such as magnesium fluoride, which does not yellow as readily, could be used in the DMD package. However, the coefficient of thermal expansion (CTE) of the borosilicate window is best matched to the entire DMD package.

Table 4.2: The post-exposure DMD operability is shown here. The "after irradiation" column shows the number of working mirrors after the specified dose. The mirrors were exercised and the number of working mirrors was tabulated in the "after exercising" column. Finally after the DMDs returned to RIT and it had been 6 months since irradiating them, they were tested again "after 6 month room temperature anneal". Exercising was beneficial for the mirrors at the lowest energy 21.0 MeV. The * indicates no data. Room Temperature Annel (RTA)

21.0 MeV	After 49 krad Irradiation	After Exercising	After 6 Month RTA
Zone 1	5.0%	26.7%	99.98%
Zone 2	2.9%	86.9%	100%
Zone 3	0.0%	95.5%	100%
Zone 4	1.2%	95.7%	100%
34.5 MeV	After 43 krad Irradiation	After Exercising	After 6 Month RTA
Zone 1	1.6%	∗	79.72%
Zone 2	5.8%	∗	80.2%
Zone 3	6.6%	∗	90.4%
Zone 4	5.2%	∗	96.0%
40.9 MeV	After 41 krad Irradiation	After Exercising	After 6 Month RTA
Zone 1	3.2%	3.2%	99.99%
Zone 2	3.1%	3.1%	100%
Zone 3	3.7%	3.7%	100%
Zone 4	2.7%	2.7%	100%
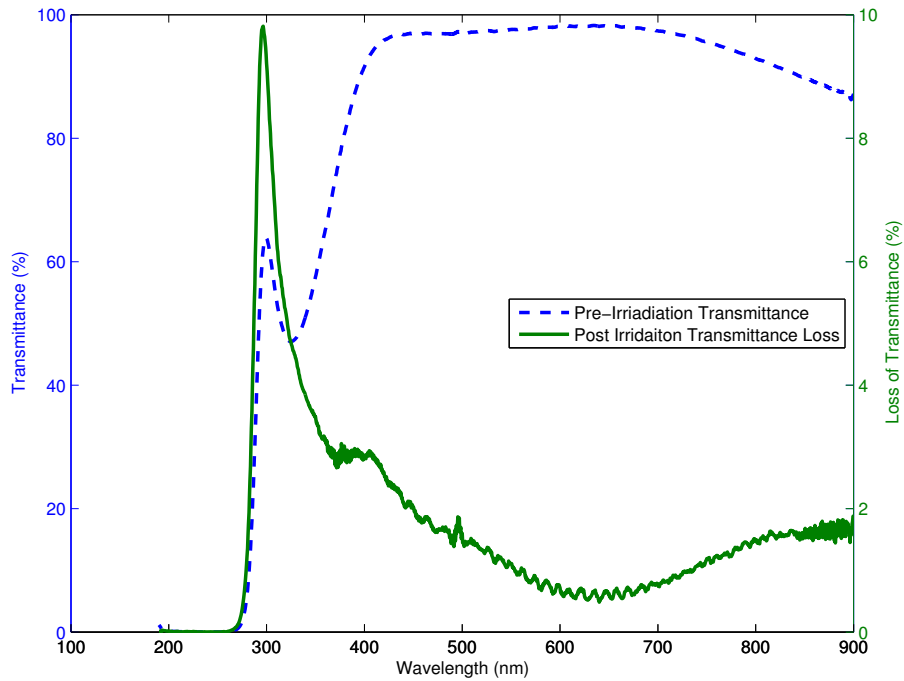
Figure 4.14: (Left y-axis) Average pre-irradiation transmittance of the DMD windows. (Right y-axis). Average post-irradiation transmittance loss for a 20 krad dose. These values are for a single-pass measurement through the window.

4.4.2 Duty-Cycle Effects

As discussed previously the DMD was divided into four different duty-cycle regions. The region on the left in Figure 4.7 failed first in all of the four cases. Figure 4.15 shows the duty-cycle dependence of the mirrors. As TID increased, the non-symmetric duty cycle mirrors began to fail (i.e. regions 2, 3 and 4). This was the case at all 3 energies. To characterize this dependence more thoroughly, smaller dose increments would be required. Also in a space deployed MOS system there may be system operational modes that could minimize the effects of radiation. For example in such a space mission, a majority of the time the mirrors are in one state, away from the spectrometer side of the instrument. However, space telescopes often have multiple instruments, so when the MOS instrument is not being utilized, the mirrors could be either returned to their flat state, or biased in the opposite state so that the mirrors have a more uniform duty-cycle under irradiation.

The underlying cause for this duty-cycle effect is unknown, but may be mechanical in nature. Since the failure appears to be incremental, it is likely that it is either something mechanical, or due to trapped charge buildup in the device. Possibly, when the mirror is latched in one state and the torsional hinge is irradiated, new defects are created in the hinge. These defects reduce the stress in the latched hinge, and once bias is removed from this mirror, the mirror no longer returns to its flat state. A related effect, seen when DMDs are used in projectors operated at elevated temperatures is called "hinge memory" [90]. Duty-cycle effects may also be less of an issue at low temperatures, because there is less thermal energy present to anneal out stress when the DMDs are landed. The two higher energies that used even larger dose increment began exhibiting performance issues at slightly lower TID levels. This indicates that the DMD has an apparent dose-rate effect, and that both the irradiation rate and TID are important in assessing the effect of protons on DMD performance.

The exercising and duty-cycle effects were observed with the testing conditions that were harsh and unrealistic for several reasons. A minimum increment 2 krad was used during our testing. This 2 krad dose corresponds to the radiation dose the DMD would obtain after several months on orbit. On orbit, it may be beneficial to optimize DMD operation to extend their life. Operationally, one can envision to exercise the DMD during idle mode, switching them at high frequency (10 KHz or more, as designed) between their on/off positions, each time an observation is not being carried out, such as during telescope moves.

Trapped Oxide charge (Dielectric Charging)

Another possible cause of sticking mirrors is trapped charge in DMD oxides. MOS transistors are very sensitive to trapped charge in insulating oxide layers [92]. The types of trapped charge affect NMOS and PMOS devices differently. As a charged particle passes through the oxide layer, the radiation creates electron hole pairs. On average one charge pair is produced for each 18 eV of energy absorbed by the material [93]. The only trapped charge that is important for the MEMS portion of the mirrors is unshielded trapped charge. Meaning there are regions of the DMD that have oxide without overlapping metal that can cause the mirror actuation voltage to change. Without being able to directly test the CMOS memory, it is difficult to determine if the trapped charge is present in the DMD's CMOS transistors, or if the trapped charge occurs in its MEMS spacer oxide layers in the super-structure. Trapped charge in either of these locations could cause mirrors to no longer function as designed.
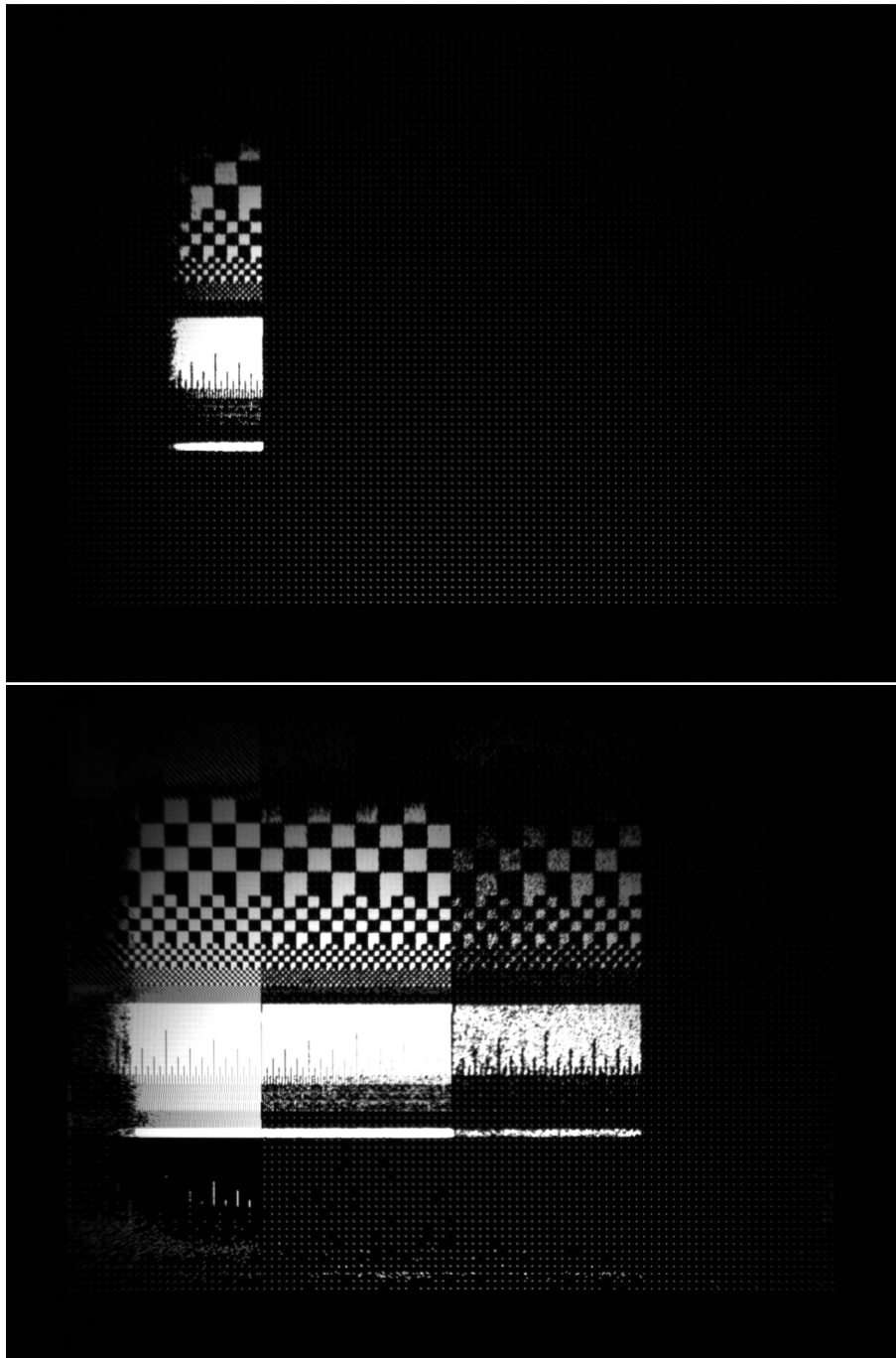
Figure 4.15: Images from the CCD are shown for the 35 MeV trial. Images from exposure #11 (top) and #12 (bottom) are shown here. At 25 krad (35 krad at the active region), the left most columns are starting to become stuck to the device. At 42 krad (at the active region) the majority of the array is beginning to stick with the exception of the final column of mirrors. These appear to be mirrors that can only stay latched in one position.
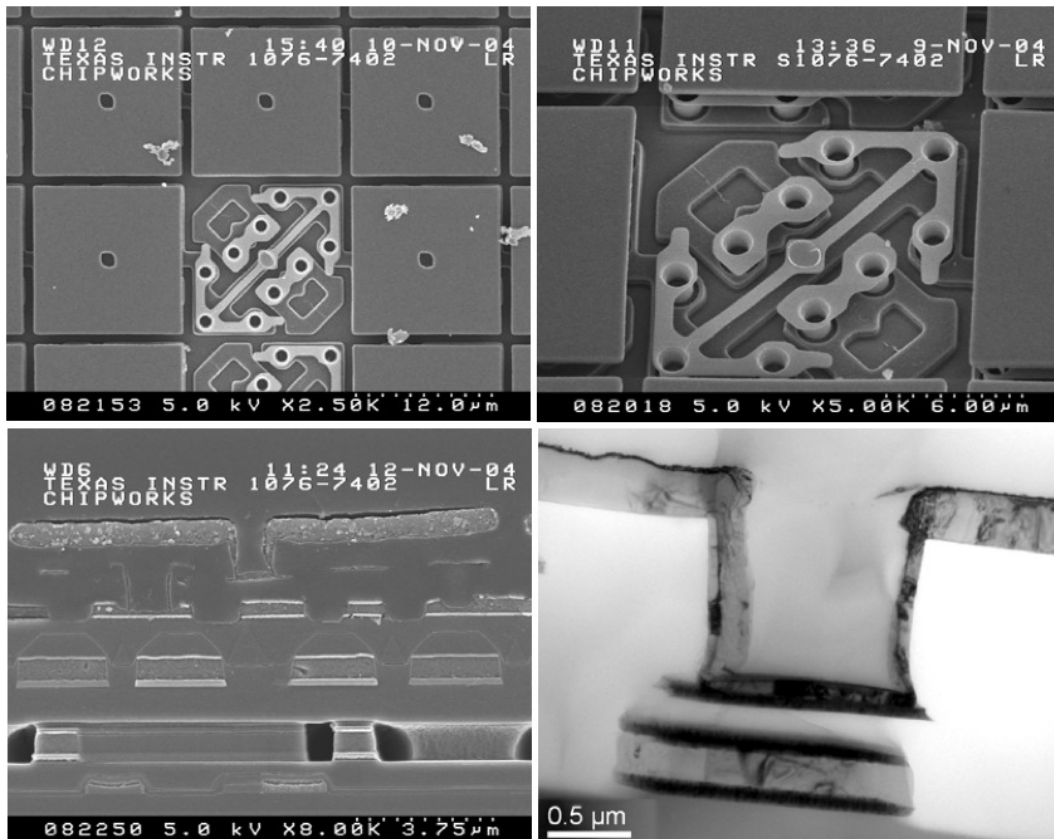
Figure 4.16: These images show the cross-section of an indivual DMD mirror. The images are of a XGA 13.68 μm fast track DMD. Several sample images from Chipwork's report are shown above [91].
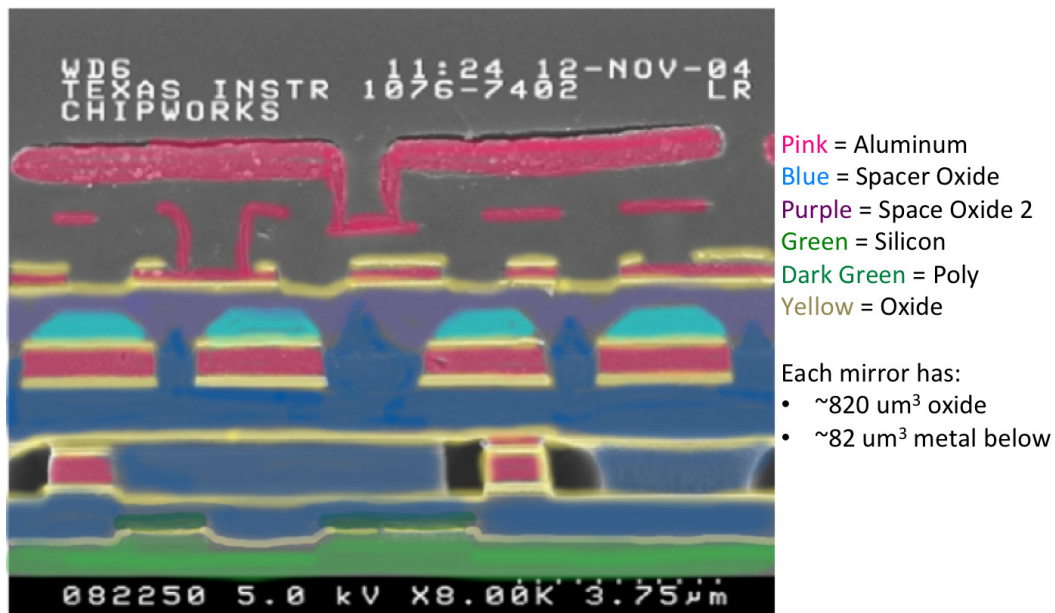
Figure 4.17: Chipworks TEM was colored (by the author) to illustrate the locations trapped charge can occur in a 13.68 μm XGA fast track DMD [91].

Figure 4.16 shows a TEM cross-section of the chip. It can be seen that the transistor level is on the lowest portion of the chip. There are oxides in-between each of the layers. Metal 1 and metal 2 are above. Metal 3 is the first MEMs layer. It appears the Transistors are capped with a nitride layer as well. There is on the order of 5 μm of oxide in the stack where trapped charge can reside. The localized position of this charge will greatly effect the MEMs mirror operation in the areas near the electrodes and edges of the pixel that are not shielded by a metal layer. Figure 4.17 shows a pseudo colored image of the DMD's super structure. The DMD (due to the open oxide regions) does not lend itself well to make it possible to shield charge everywhere in the device. If the trapped charge is localized near the transistors, this could affect the SRAM operation, but if the trapped charge is closer to the mirror surface, then it could potentially affect the operation of the drive capacitors themselves.

It is also important to minimize the amount of hydrogen that exists in the MEMs hermetically sealed packages. Exposure of devices to hydrogen after fabrication has been shown to increase interface inducted charge buildup in MOSFETS [94]. Even hydrogen amounts as small as 0.5% can be significant in increasing interface charges, resulting in decreased radiation tolerances. For DMDs the dark rough oxide plays a crital role in reducing the scattered light below the mirrors, because also reduces the radiation tolerance. It is not feasible to remove this oxide in this design of micromirror, because it would decrease the optical contrast.

Heating Effects (Thermal Analysis of Kinetic Energy Transfer)

Previous research has shown that under high temperatures, the DMD can fail prematurely [95]. This is especially important when the DMDs are used in projectors. A worst-case heating scenario due to proton kinetic energy transfer is examined as follows. The basic assumption here is that all of the kinetic energy from the protons during an irradiation step is converted into thermal energy. Table 4.3 shows the results of this simple example. The highest kinetic energy possible at the Berkley Cyclotron is 55 MeV. This example assumes that all of this kinetic energy is transferred to thermal energy when it is absorbed by the target

Table 4.3: Worst-Case Heat Transfer

Description	Value	Units
Kinetic Energy of Proton	55	MeV
Conversion Factor	1.60E-13	$\frac{J}{MeV}$
Energy Per Proton	8.81E-12	J
Aperture Size Diameter	5.08	cm
Aperture Area	20.27	cm^2
Average Flux	5.00E+07	$\frac{p+}{cm^2 s}$
Energy Flux	8.93E-03	$\frac{J}{sec}$
Time	500	s
Heat Energy	4.47	J
Target Width	2	cm
Target Height	2	cm
Target Depth	2.54	cm
Target Volume	10.16	cm^3
Aluminum Density	2.7	$\frac{g}{cm^3}$
Weight	27.43	g
Specific Heat	0.9	$\frac{J}{gK}$
δT	0.18	K

material. In previous SRIM analysis it was shown that a 0.5" aluminum would stop all 55 MeV protons. The first portion of the table converts the energy of the particle to Joules. These are relativistic particles, and the complete 55 MeV was assumed to be transferred, meaning that the rest mass was not taken out of the kinetic energy. After the energy in Joules per particle is known, the size of the beam-line aperture must be calculated. A 2" aperture was used for the irradiations, which corresponds to an area of 20.27 cm^2. The flux obtained was on average $5 \times 10^7 \frac{p+}{cm^2 s}$. Since the energy per particle and area of the particles are known, the energy flux can be calculated. The exposure time used was approximately 500 s for most exposures. From this the energy can be calculated per irradiation. Next assuming all of this energy is absorbed in a target of the given size the volume and mass can be calculated assuming the complete target material is aluminum. Around 27 grams of aluminum are assumed for the target. The change in temperature can be calculated from the specific heat, mass previously calculated, and thermal energy. A δT of much less than 1°C was obtained. This is not a significantly large amount of thermal energy to do any harm to the DMD. When the DMD is being used in a high power projector, a much greater thermal load ($\delta T > 10$ °C) is placed on the DMD by the light source than is present in the proton testing.

4.4.3 (Mirror Upsets During Irradiation) Single Event Upsets

The single event effects were relatively easy to detect by simply subtracting two different frames. During the test procedure a pattern was loaded into the DMD. Subsequently the DMD was irradiated. The reloaded frame and the frame immediately following the exposure were subtracted and the differences on the two frames were the hits. These interaction events were present at all of proton energies tested. These upsets were in each case completely recoverable meaning that the upset was not permanent. The same pattern was uploaded to the DMDs again and all of the mirrors returned to their pre-irradiated state.

During proton irradiation, some mirrors flipped from their programmed position to the opposite position (from $\pm 12°$ to $\mp 12°$). Figure 4.18 shows the number of such upsets as a function of dose. This is likely
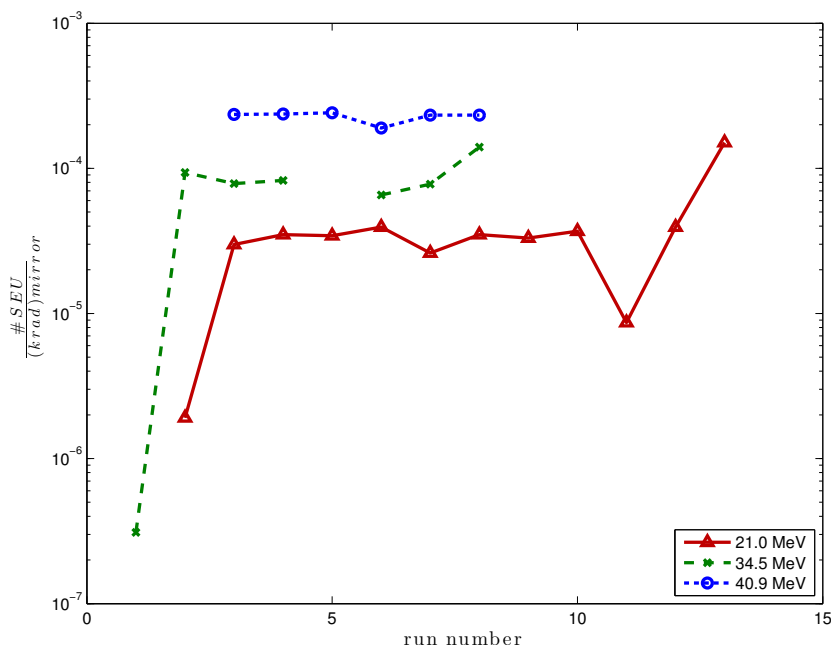
Figure 4.18: Number of upsets per mirror versus run number at each proton energy. For example, 10^{-4} $\frac{\#SEU}{(krad)mirror} \times (1024 \times 768 mirrors) \times 6.6krad = 519\frac{SEU}{5-years} = 103.8\frac{SEU}{year} = 0.28\frac{SEU}{Day}$. This DMD would have one upset mirror every four days of operation during a 5-year mission at L2.

caused by upsets in the CMOS memory. The upset was non-destructive and was correctable by reloading the DMD memory. These types of upsets are well characterized in SRAM and are often called a single event upset (SEU). These upsets were present in all proton energies tested. As the proton energy increased, the number of upsets per dose increment was more frequent. At each energy and dose, when the DMD memory was reloaded, all of the flipped mirrors returned to their programmed state. The upset rate is approximately 10^{-4} $\frac{\#SEU}{(krad)mirror}$. Since there are 1024×768 mirrors and the dose for five years is 6.6 krad, 519 $\frac{SEU}{5-years}$ upsets would occur during the 5-year mission. On average at L2, this DMD would have one mirror upset every four days.

The cumulative number of upsets was calculated for all of the irradiation steps. The number of upsets per mirror is shown as a function of fluence (# of protons) in Figure 4.19. The last irradiation increment resulted in an increased number of upsets at each of the energies. This point was believed to be a critical TID (Total Ionizing Dose) level in which the DMD started to malefaction. A line was fit to each of the datasets corresponding to the three energies. The point from the last irradiation increment was not included in the regression because the nature of the SEU phenomenon changes. The slopes of this line, proportional to the SEU cross-section, are tabulated in Table 4.4. With this information, the probability of a mirror flipping on orbit during a spectrometer integration time can be calculated. The number of upsets and cross-sections are comparable to other SRAM memory devices [96].

Table 4.4: SEU cross-section values are presented here for each proton energy.

Energy (MeV)	Cross-section $\left(\frac{cm^2}{mirror}\right)$
21.0	6.525×10^{-15}
34.5	1.346×10^{-14}
40.9	3.755×10^{-14}
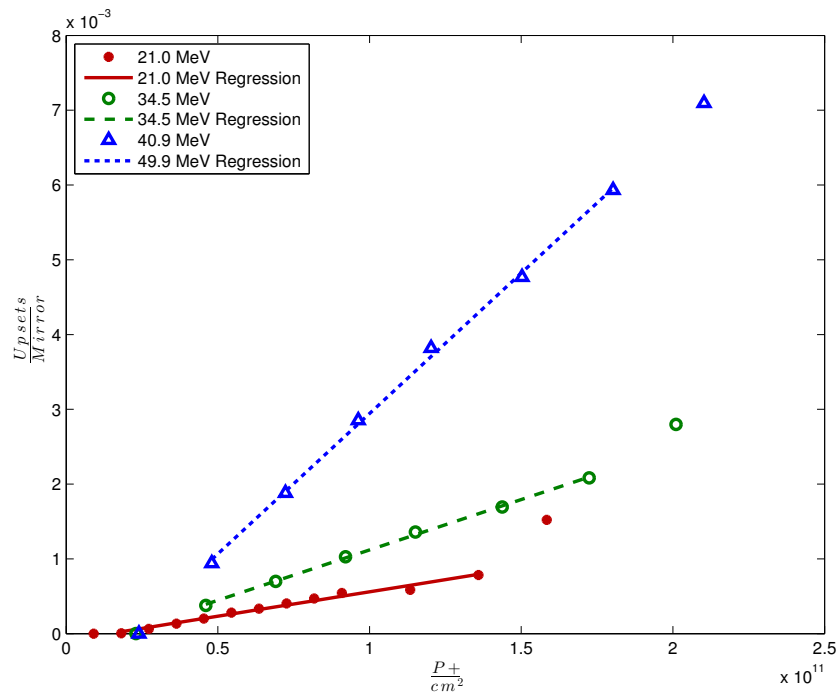
Figure 4.19: This plot shows the number of upsets for a single DMD mirror as a function of proton fluence. The slope represents the SEU cross section.

4.5 Summary

A test procedure was developed to characterize proton irradiated DMDs at three different proton energies. During irradiation two effects were observed that affected the performance of the device. The DMDs were 100% functional to a TID of 30 krad. For higher doses, it appears that the duty-cycle of the mirrors (i.e the ratio of time the mirror is latched in one state versus the opposite latched position) during the irradiation is important. Additionally, the proton flux rate also appears to be a significant factor in determining DMD performance above 30 krad. The two higher energy test DMDs were irradiated at larger dose increments and failed sooner. The DMD failures are believed to be caused by trapped charges in oxide layers, either in the CMOS memory transistors, or in the MEMs super-structure itself. Future work should test additional electrical parameters to determine if the failure mechanisms are within the CMOS memory or in the MEMS super-structure. Operationally, there were benefits from exercising the mirrors to avoid duty-cycle effects, and thermal annealing cured most of the damage not recovered by exercising the mirrors. Some mirrors flipped from their programmed position to their opposite position during proton irradiation. This is a type of SEU caused by CMOS memory upsets. The calculated SEU rates and corresponding upset cross-sections agreed with those quoted for other SRAM devices fabricated with similar design rules. A DMD with the shielding from its package can withstand a 5-year mission with a 2× margin of safety and a 4.5× margin of safety if 100 mil of spacecraft shielding is assumed. Overall, DMDs appear to function well in a proton radiation environment to be a candidate for a MOS slit mask on a future space mission.

4.6   Future Work and Lessons Learned

All of the radiation analysis in this chapter just considered the interactions of protons, (the primary species) in these tests. Future work could investigate modeling some of the other secondary particles generated when the protons interact with the materials in the DMD package. Further radiation tests with gamma and heavy-ion species are important for understanding the tolerance in the different sets of tests conditions. However to perform gamma testing simplified drive electronics, rather than those provided by TI, must be fabricated to control the DMDs. To accomplish this task the DMD protocol, clocks, and voltages must be reverse engineered. The testing of biased versus additional unbiased DMDs would have allowed us to examine the influence of different recombination carrier lifetimes within the device to be examined. A limited number of test DMD available to us restricted the testing to only biased DMDs.

   The ability to read-out the DMD SRAM memory would be very useful to more accurately analyze the SEU. The SRAM memory can be read-out serially through a pin on the package at TI's factory to determine which memory elements are operating within the desired specifications. Due to the proprietary nature of TI's DMD, knowledge of how to do this is not available outside Texas Instruments. Another important testing aspect would be a way to monitor the power consumption on different regions of the DMD. This was not possible to do because TI's drive electronics board was used during the testing. Understand which electrical characteristics of the DMD of the DMD (e.g. low voltage SRAM or high voltage MEMS) change would enable better knowledge of where the trapped charge is being deposited. The ability to measure the flat position of the mirrors on site would also help monitor the mechanical hinge effects.

CHAPTER 5

LOW TEMPERATURE DMD TESTING

The operation characteristics of a DMD at lower temper is important to know since these TI DMDs are proposed to be used in an IR spectrograph. Given the reduce temperature. Various performance metrics dependent on temperature were evaluated including flatness deformation and operation.

5.1 Background

5.1.1 Thermal Emission

To utilize a DMD in an infrared instrument, the DMD and its corresponding package must be cooled to minimize the thermal emission added to the signal being gathered from the field under view. The electrical power required to operate the DMD causes the DMD to warm, which generates more thermal photons. The relationship between a blackbody radiator and emitted thermal radiation is shown in Equation 5.1 (Plank's Law). The variables consist of: h is planks constant, c the speed of light, λ is the wavelength of light, k is the Boltzmann constant, and finally T is the temperature of the source. Several different temperature blackbody radiators are shown in Figure 5.1. In order to build spectrometers that operate further into the infrared, all the optics, the detectors and mirrors must be kept cold enough to minimize emission at the wavelengths of interest. For example, if a spectrometer with a cutoff wavelength of 1.8 μm is built, the instrument can operate at a higher temperature than a spectrometer with a cutoff wavelength of 2.5 μm. An astronomical infrared spectrometer should not be limited by the emission of the optics, but rather limited by the zodiacal light background. To build a spectrometer operating in the near infrared (< 2 μm, the components must be kept below 173 K or $-100\,°$C. Generally, silicon electronics are designed and tested to operate from $-40\,°$C to $100\,°$C. Outside of this range, especially at the low end, it becomes difficult to test devices. Silicon electronics can operate at very low temperatures, and in devices such as CCDs some parameters such as dark current, become more optimal when cooled.

$$B(T) = \frac{2hc^2}{\lambda^5(e^{\frac{hc}{\lambda kT}} - 1)} \tag{5.1}$$
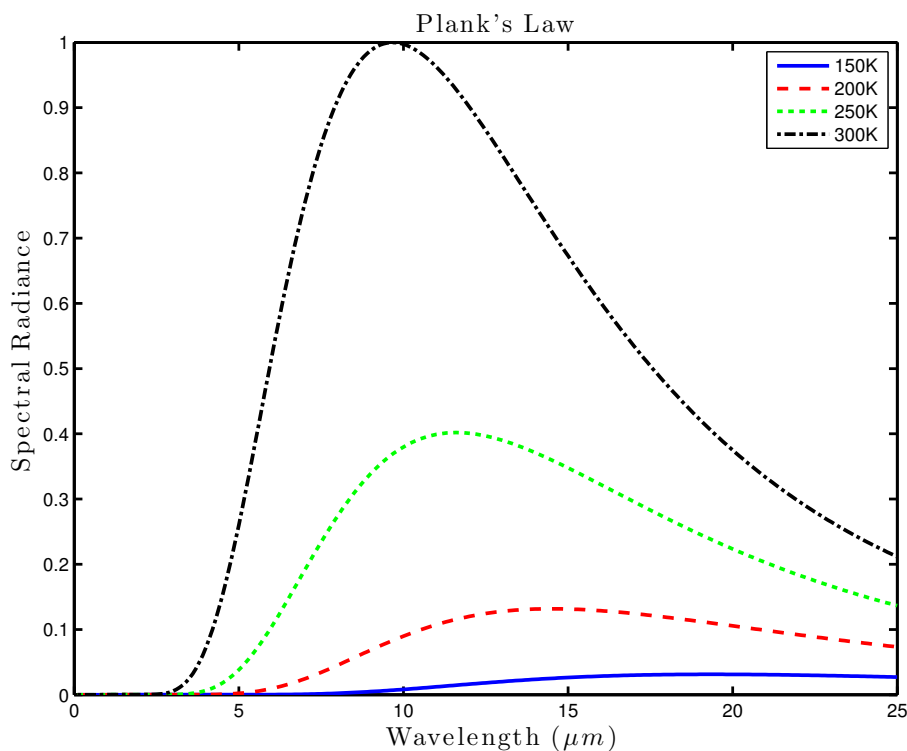
Figure 5.1: Plank's Law is shown for several blackbody radiators. Peak normalized spectral radiance is shown as a function of wavelength.

5.1.2   DMD Hermetic Packaging

The packaging design for any MEMs device is tremendously important for overall system reliability. Hermetic (impervious to air or moisture) sealing packages for MEMs and other electronic devices are commonly used [98]. Keeping moisture and dust from entering the device is imperative to to ensure long-term reliable operation. The DMD super-structure (the back-end MEMS portion of the Device) must be kept particle free to maximize device yield. Because the mirrors are sensitive to particle contamination, all of the packaging and testing needs to be completed in a class 10 or cleaner clean room ($< 0.3\,\mu\mathrm{m}$ particle size). In this Chapter, the DMD package will be examined further to determine the effects associated with cooling the DMD below ambient temperature.

The DMD package design is integral to protecting the device from harsh environmental conditions, such as dust and moisture. The "Type A" DMD package is composed of several different materials and is illustrated in Figure 5.11. To start the packaging process, the wafers are partially sawed with the device surface down to minimize particle contamination on in the active area of the DMD. A special collet is used to mount the silicon DMDs to a ceramic substrate. Once this is done, a plasma etch is done to remove the sacrificial layers in the DMD superstructure, releasing the individual mirrors. Then it is placed vertically and the dies are removed from the wafer from the bottom to top to minimize particulate contamination. The DMD is mounted on a land grid array (LGA) ceramic substrate. A LGA is a ceramic packaging element with pins on the outside and bond pads on the inside to wire bond the silicon DMD substrate. This packaging LGA enables the DMD to connect to external circuitry and mount to a PCB. The silicon is mounted to the ceramic LGA, and gold wire-bonds are used to connect the silicon chip to the LGAs pads. Notable
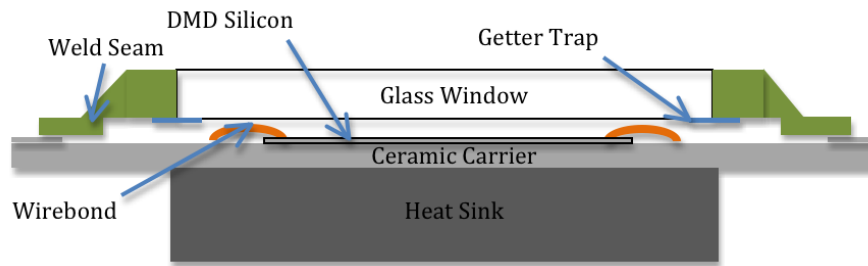
Figure 5.2: The illustration shows the DMD package. The DMD is usually connected to an aluminum heat sync. The silicon is mounted to a ceramic carrier. A borosilicate window is held above the DMD by a kovar metal frame. The device is wire-bonded to interconnects which terminate at the bottom of the ceramic carrier. .

attention was given to utilize adhesives with minimal outgassing and high thermal conductivity. Adhesive outgassing was an early cause of permanent mirror stiction in DMDs [99]. Stiction is when a mirror becomes stuck to the substrate because Van-der-Waals forces overcome the restoring electrostatic force between the aluminum mirror and drive electrodes. A cleaning step is then completed with dry chemistry to remove the particles without damaging the mirrors. After this a proprietary anti-stiction chemical vapor deposition process is completed. The surfactant used in this is perfiuordecanoic acid (PFDA) [100]. This is similar to many fluorinated Teflon based materials. This surfactant reduces the probability that the electrode and contact point on the mirror will become permanently attracted by Van der Waals forces. Next a Kovar metal frame is mounted to the ceramic carrier. A second Kovar metal frame has a piece of alkali-borosilicate glass sealed to the frame in a $1000°C$ belt furnace. The glass is an alkali borosilicate glass (manufactured by Corning type 7056). Kovar is a nickel metal alloy that its Coefficient of Thermal Expansion (CTE) matched to the borosilicate sealing glass. After the metal is fused to the glass, a double-sided polish is performed on the glass and then the frame is also electroplated with Nickel and Gold. The kovar metal is electroplated in $8\,\mu m$ of nickel and then $2\,\mu m$ of gold. A low reflectance coating is coated on the inside of the glass. This layer will become the black aperture which blocks light reaching the gold wire bonds and other reflective non-active portions of the outside of the mirrors themselves [101]. After the aperture layer is etched a MgF_2 antireflective coating is applied to both sides of the glass, so that the average single pass transmission is greater than 98% and the single pass reflectance loss is 0.5% in the visible. Also two getter strips are attached just inside the aperture to draw moisture away from the active MEMs portion of the DMD [102]. Next in a Dry Nitrogen environment, a the window frame is welded to the metal frame previously attached to the substrate. A small amount of helium is added to the inert environment to aid in the leak detection process of the package. In addition, the packing procedure was designed to minimize the amount of heat reaching the DMDs, because high temperature processing can cause a change in the mirrors' mechanical properties. A metal stud is heat-synced to the back of the DMD chip by metal passthroughs the ceramic chip. This allows thermal energy absorbed by the DMD to be dissipated by an external heat sync. The package has very strict optical, mechanical, chemical, and electrical requirements and it is one of the main reasons for the DMD's success.
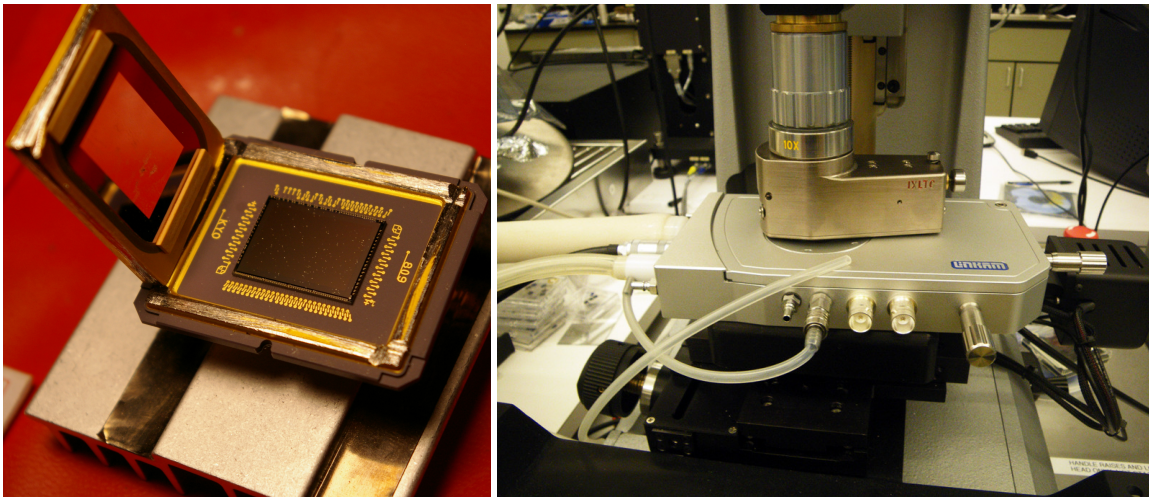
Figure 5.3: (left) A DMD with the kovar frame and window remove frome the mirrors and substrate. Getter strips are seen attached to the underside of the window. In addition, wire bonds are shown above and below the DMD silicon. (Right) DMD was placed inside this small dewar. A piece of the dewar's window was placed in the optical path of the Wyko interferometer. Wyko's Through Transmissive Media Module (TTMM) was used so that the DMD could be viewed through the dewar window. Tube on top blew air across the dewar window to prevent moisture from building up. Liquid nitrogen and a heater controlled the internal temperature of the DMD chuck inside the dewar.

5.2   Cooling an Unpackaged DMD

A 848×600 17 μm DMD was unpackaged and cooled to determine if the shape of individual mirrors changed. The window was removed from a DMD by carefully sing a saw around the weld seam. This was done while the DMD was device side down to minimize the amount of particle contamination that would land in the superstructure of the DMD. The un-packaged DMD is shown in Figure 5.3. An unpackaged DMD was placed in a small dewar. The dewar was purged with dry nitrogen for a period of one hour and then subsequently cooled. During the cooling process, the DMD was inspected with a WYKO white light dynamic interferometer. The dewar and WYKO are shown in Figure 5.3. A time-lapse series of photos as the DMD was cooled is shown in Figure 5.4. At ambient temperature all of the mirrors were flat. As the temperature was reached water condensed out of the ambient atmosphere and landed both on the mirrors and below the mirrors reflecting surface, the individual mirrors became stressed. Once the water froze it caused the hinges and other super structure parts to break and fail. This effect can be seen as multiple interference fringes on individual mirrors. As the device cooled the water condensation caused the mirrors to tilt far outside the collection aperture of the interferometer (these mirrors are dark). In order to avoid this from happening on a unpackaged device, the mirror should have been baked to remove the water prior to cooling. The DMD package is very proficient at keeping moisture out of the package. All subsequent testing of DMDs was done with a packaged device to eliminate the possibility of contamination. If DMDs are unpackaged in the future, a water removal step should be done to prevent this type of damage when cooling the mirrors.
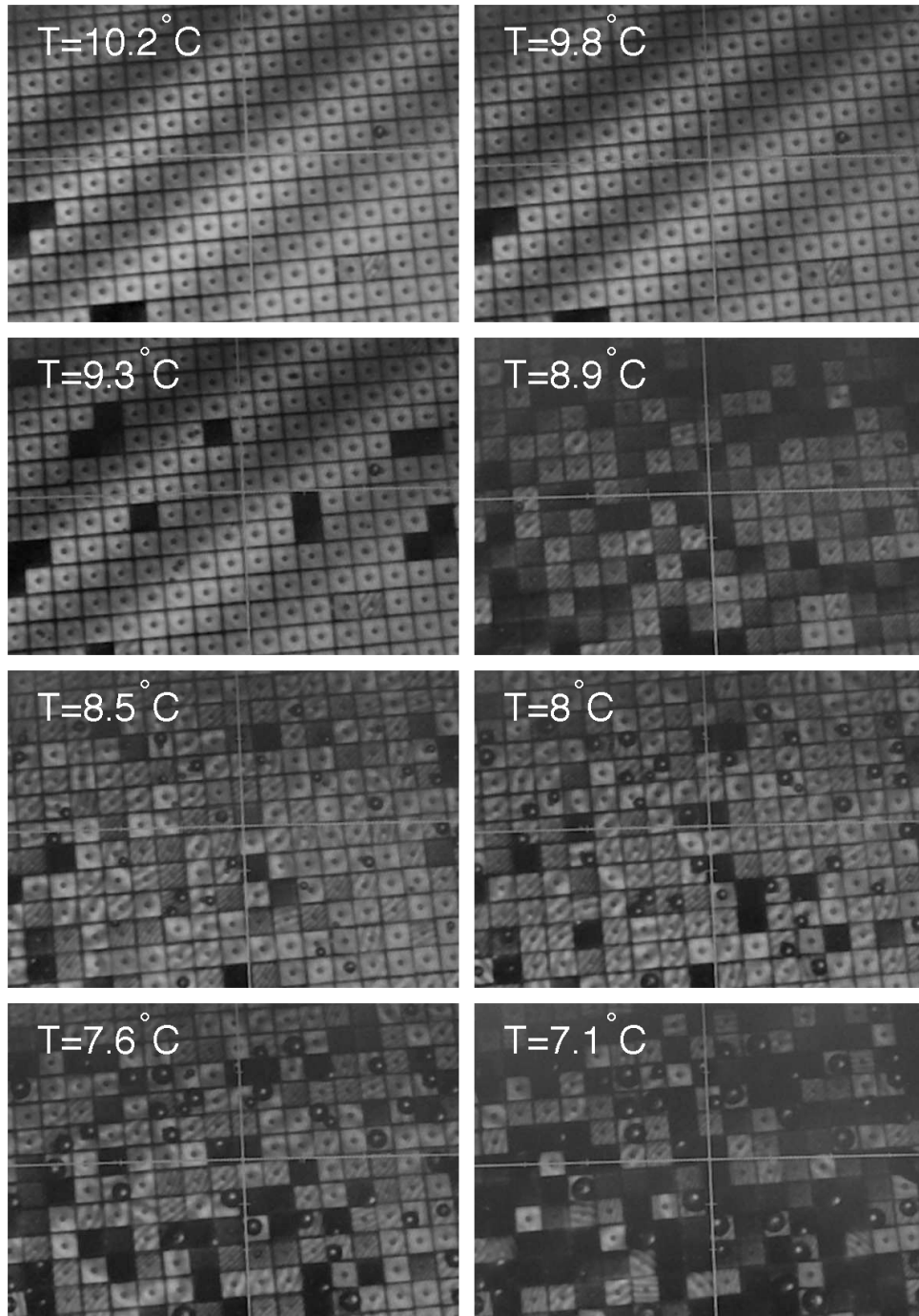
Figure 5.4: A time sequence showing the DMD mirrors as the temperature was lowered. Fringes were aligned along the mirror diagonal. This fringe orientation was chosen because the Wyko and most interferometers have fewer issues doing phase unwrapping when the fringes are not along a straight line or harsh discontinuity such as mirror edges. Eight different temperatures are shown as the device cools down.

5.3   Cooling a Packaged DMD

During a 10 week residency at Goddard Space Flight Center (GSFC) by the author, low temperature testing of DMDs was initiated. A packaged DMD was placed into a dewar (see Figure 5.5). The DMD could not be run inside the dewar at this time, because the XGA DMD chips require 196 electrical connections to operate. Additionally 64 of these data lines require high throughput and specialized wiring because they operate at 400 MHz. This would have required expensive custom dewar feed-through. The primary purpose of this unbiased test was to determine if there were any mechanical failures of the package and also to monitor the optical surface. The dewar was pumped down and the flatness across the array was monitored as the device cooled to 173 K. A high quality fused silica window was used for the dewar window. It was polished to $\frac{1}{10}\lambda$ ($\lambda = 0.5\,\mu m$) A functionality test was performed both prior and after the cooling procedure to ensure all mirrors function properly. The surface deformation was measured using a Zygo Interferometer at a range of temperatures as the device cooled. The mirrors tip about the diagonal, but for these experiments they were left in their unbiased state. Prior to cooling the DMD, measurements were taken of just the DMD device, the DMD device with the dewar window, and the dewar window so that these effects could be subtracted from the interferometry measurements. It took approximately 6 hours for the DMD to cool from room temperature to its operational temperature. Temperature was verified using a calibrated Lakeshore diode and the associated controller. The diode was placed at the back of the DMD in place of the aluminum heat sink. Figure 5.6 shows the room temperature and 173 K deformation. There is a significant deviation from flatness, on the order of half a micron peak to valley at room temperature. This is simply due to manufacturing variations of the glass, DMD and complete package. Because a packaged DMD would likely be flown without modifications, it was important to characterize the package as a whole, not just the mirror surface. There was a shift in the power on the DMD surface. Power is defend as a first order curvature, and is usually the $z = 4$ term in a set of Zernike polynomials. The results from the interferometer were subtracted to get the difference between the devices. Zygo MetroPro software was used to post process the interferometer data. Zernike Polynomials were fit to the surface as is shown in Appendix Table D.1. These are amplitude normalized fringe Zernike polynomials. Sixth order polynomials were fit to the surface normal. The dewar window was subtracted from the deformed results. The cooling showed that the DMD did change shape, but the effects were quite small (less than 1 μm center to edge).

5.4   Opto-Mechanical Modeling of DMD Package

The next step in the evaluation of a DMD for space was to model the mechanical characteristics of the package as the device was cooled. If the materials have well matched CTE's, then there should be minimal stress and deformation of the optical surface. This type of modeling is extremely important for modern infrared detectors, hybridized detectors, and even other 3-d semiconductor chips. HgCdTe detectors are prone to breaking when grown on silicon, and correspondingly many methods of incorporating buffer layers between a silicon substrate and the detector HgCdTe material have been developed to this end [103]. Modern 3-d semiconductor chips utilize Through Silicon Vias (TSV) which are copper filled interconnects. Computer chips heat up dramatically under use and the difference in CTE between silicon and the copper TSV's can cause chips to shatter due to stress [104].

Figure 5.5: Dewar containing an un-biased DMD was setup on a Zygo HeNe interferometer.
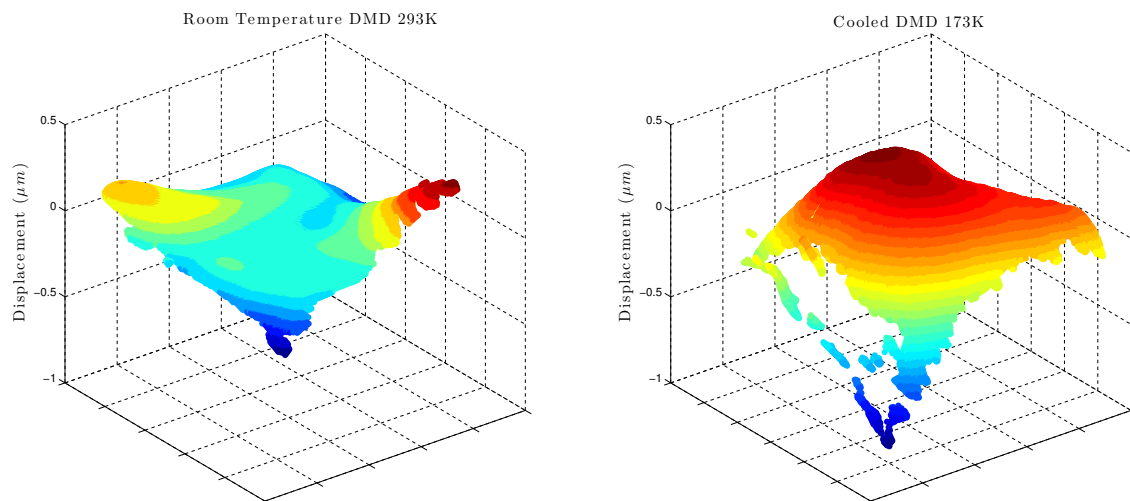
Figure 5.6: Zygo surface plots showing the flatness of the DMD at room temperature (Left) and at $-100°C$ (Right).
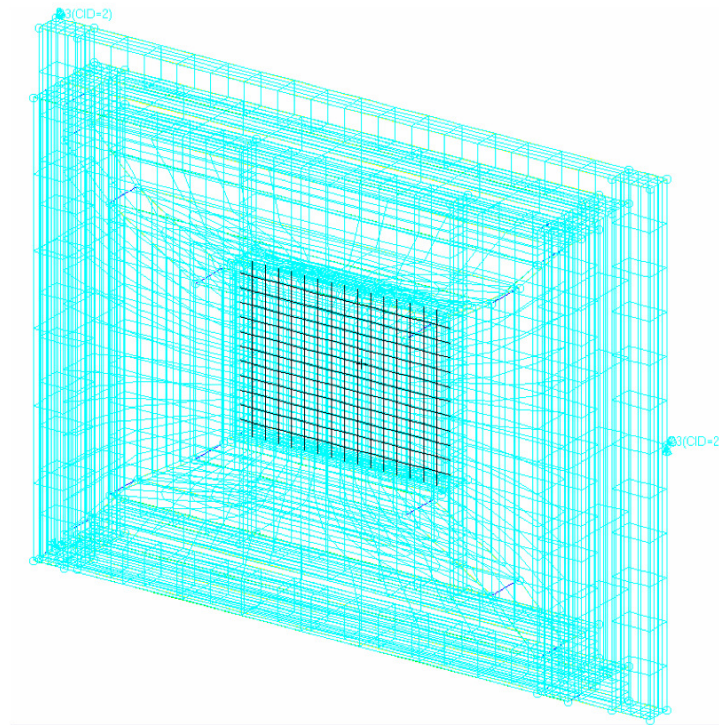
Figure 5.7: Complete DMD was modeled in PATRAN. Plot illustrates the mesh used for this FEM.

After the DMD measurements were completed at GSFC, an opto-mechanical model was built for the DMD package to examine the optical effects on the device. MD NASTRAN 2010 was used to build this model [105]. Zernike polynomials were fit to the deformed surface after a thermal load of $-100°C$ was placed on each node of the mechanical model. This simple mechanical model of the DMD package was built in PATRAN, (the graphical front end for NASTRAN). The goal of this Finite Element Model (FEM) model was not to create individual mirror level structures, but to look at global deformations across the whole array. The software package NASTRAN was used to simulate the Finite Element Model (FEM) constructed with PATRAN. The first part of the model built was the silicon DMD device. The silicon was meshed into 16 parts along the horizontal direction and 12 parts along the vertical direction. This resulted in one FEM node per 64×64 micromirrors. This is shown in Figure 5.7. The ceramic carrier was broken up into several parts so that it would be possible to mesh the silicon to the ceramic. In the future, an epoxy could be added to the interface, to simulate the CTE difference between the ceramic and epoxy. The device modeled is a 13.68 μm pixel pitch DMD, which has a $\pm12°$ tilt angle. The remaining FEM Figures are located in Appendix D. Next, the ceramic carrier was meshed to the silicon DMD. The remainder of the ceramic was modeled with a more coarse mesh to minimize computer simulation memory requirements. Common nodes were placed in the ceramic carrier that matched the mesh-points for the kovar mechanical frame. Next the metal frame was built upon the ceramic carrier. The remainder of the ceramic carrier was modeled, and nodes were positioned so that they would align to the metal frame's nodes. Three displacement constraints were placed at the model's edges to constrain all the degrees of freedom, with the exception of the radial direction. The lower metal frame was then added on top of the ceramic carrier. The metal frame was made of kovar and the FEM used kovar's mechanical properties. Finally, a second metal

Table 5.1: Summary of Optical Displacement and Stress.

	Simple	Intermediate	Borosilicate	Fused Silica
Disp. Range Silicon (μm)	0.3	0.2	0.11	0.22
Max Disp. Surf. 1 (μm)	-	-	1	0.26
Max Disp. Surf. 2 (μm)	-	-	1	0.25
		n	1.52	1.46
		Total Path	0.22	0.42
Max Stress Silicon (MPa)	0.8	3.25	2.29	16.1
Max Stress Surf 1 (Bottom) (MPa)	-	-	9.04	16.7
Max Stress Surf 2 (Top) (MPa)	-	-	5.16	14.8

frame was added that contained the borosilicate window. By planning ahead and designing the geometry mesh points, so that the model could be simply meshed, made it much simpler is the subsequent optical analysis. If auto-meshing was used instead, then a non-regular grid would have been formed, and a lot more memory would be required to obtain the same amount of information.

This mechanical model was built in several steps to validate the model building process. The first simple model contained just a piece of ceramic and a piece of silicon with an aluminum coating. The maximum deformation was examined with a temperature load of $-100°C$. Table 5.1 shows the results of this model. A displacement of 0.3 µm was obtained for this simple model as shown in Figure D.1. An intermediate model was built that had the full ceramic carrier, and the first metal frame. The displacement for this complete model is shown in Figure D.2. The displacement is not symmetric between the row and column axes, because there is a difference in stiffness along these two directions. The maximum stress occurs along where the silicon is bonded to the LGA ceramic carrier and is shown in Figure D.3. Then a complete model was built with a borosilicate window and a fused silica window (Figure 5.7). Two different window materials were shown in the device. The max deformations were different in both the fused silica and borosilicate window models. The displacement was lower in the fused silica model for the window. However the stress was much greater in the fused silica window. Figure D.4 shows the displacement results for the silicon surface with both window types, and Figure D.5 shows the difference in shape of the two window types. The fused silcia window under stress has a much different shape than the borosilicate, because its CTE is much lower than that of the other package materials. The primary aberration created by cooling the model is power, due to small differences between the CTE of the different materials in the model.

5.4.1 Stressed Optic Analysis Optical Modeling

Now that a mechanical model was generated, and a cooling load (at each node the temperature was set to $-100°C$ below ambient) had been placed on the model, it was of interest to see how these changes result in changing the optical properties of the DMD. To accomplish this goal, a software package called SIGFIT [106] was used to translate the mechanical deformation into surfaces an optical modeling program could read in. A MTF analysis was then completed with the optical system. SIGFIT was used to fit Zernike polynomials to the deformed optical surfaces. Table D.2 shows the Zernike fit to each optical surface in the DMD. Note that these are single pass fits, and when a DMD is used in an optical system the resulting wavefront error would be doubled. The largest deformations occurred on the window bottom, with the significant terms
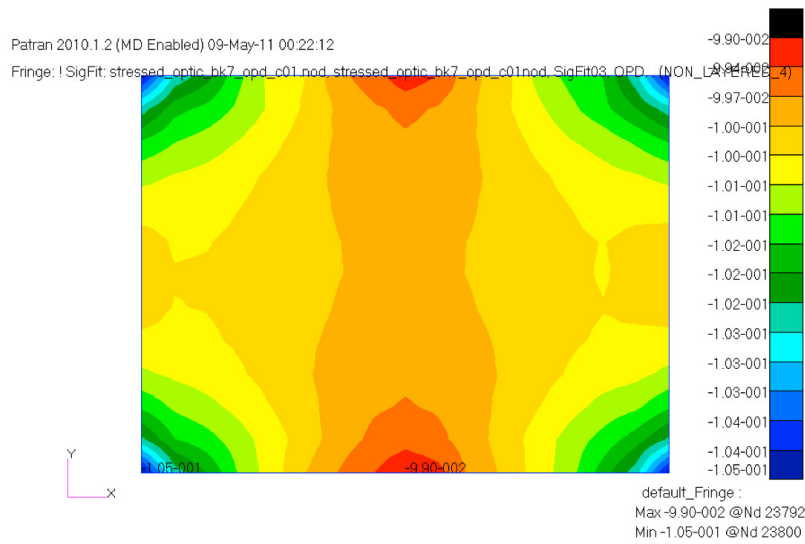
Figure 5.8: The OPD as a result of performing a stressed optic analysis. The OPD was plotted here assuming a wavelength of $1\mu m$ as a result of the stress induced change in index.

being power, spherical and astigmatism. The astigmatism occurs, because the window is non-square and therefore the stress is different in the row and column directions.

SIGFIT [107] was also used to do a stressed optic analysis. This is a general term referring to when a mechanical load (temperature, gravity, pressure ect) is placed on an optical element. Two different effects occur. The first is simple deformation of the optic due to thermal expansion, or deformation due to distinct material types. This is more straight forward in terms of understand the OPD that occurs as a result of the deformation. The second effect is a stressed induced change in refractive index. This effect can be very significant for transmissive optics such as lenses or windows. Fringe Zernike were fit to the $\frac{dn}{ds}$ to simulate the optical path difference (OPD) from the stress in the optic. It was a small effect on the optics at a temperature of $-100^{\circ}C$, but overall the larger optical effect. Figure 5.8 shows the stress of the window in the final borosilicate window.

A simple optical Model with a lens imaging onto the DMD glass was setup using the OSLO software package (Figure 5.9). This model was built to determine which optical surface has the largest deformation. An $f/6$ lens images onto the DMD. The MTF was used as an analysis metric. Figure 5.10 shows the MTF for various scenarios. The blue line shows the diffraction-limited curve. The deformations from both an ideal window (black line) and deformed glass window (red line) are shown here as well. The stressed optic ($\frac{dn}{ds}$)is by far and by large the largest effect on MTF and image quality (green line).

Modeling this DMD package interactively and checking the results with only parts of the package was a very useful exercise to determine what each package element does to the optical surfaces in the package. In order to make the results more accurate, more detailed information needs to be known about each material type. Measurements on another DMD device could also be completed to understand the manufacturing defects in greater detail. The consequence of the hermetic package results in some optical degradation. The stress in the glass package is the limiting factor on image quality If an alternative window type such as fused silica is used, then the stressed optical analysis must be completed for the different window type to understand the optical effects associated with the new window material. Overall this was a useful exercise
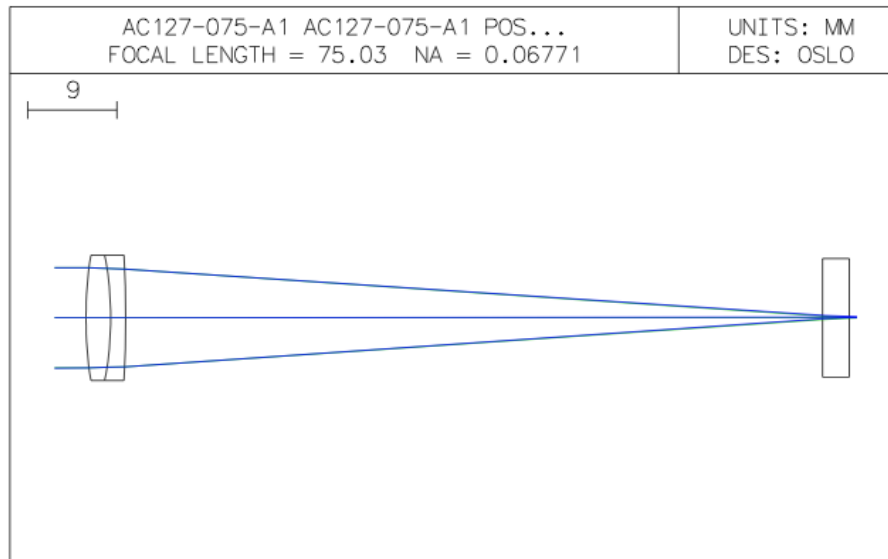
Figure 5.9: Optical set-up in OSLO for testing deformation and stressed optic. A diffraction limited $f/6$ lens projects a spot onto the DMD package window.
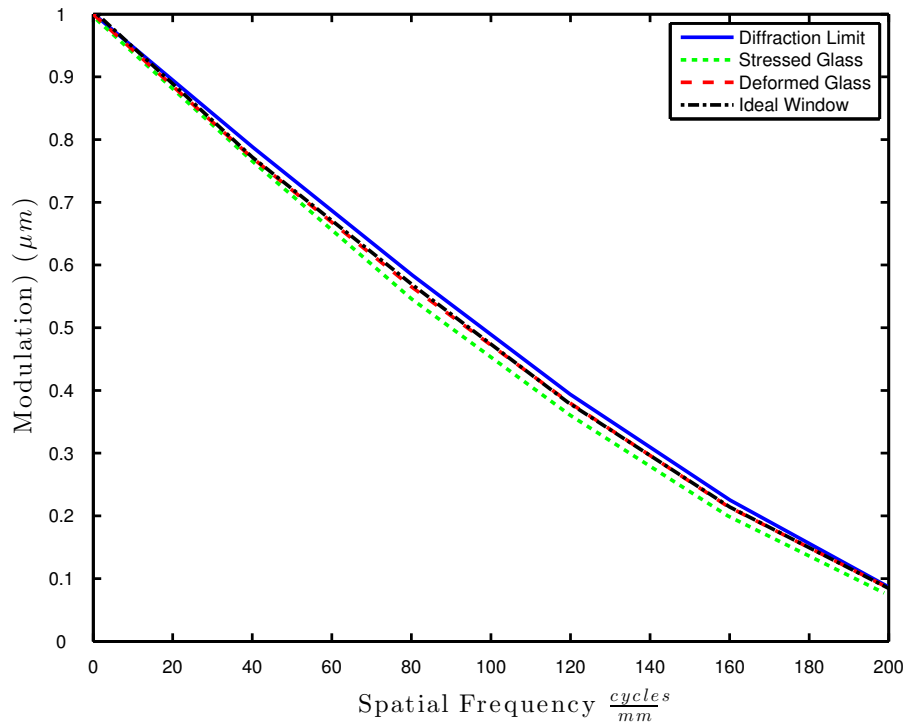
Figure 5.10: (Blue curve) Diffraction limited MTF is shown here. (Green curve) Stressed glass MTF. (Red curve) Deformed glass with distortions from FEM model. (Black curve) Ideal glass with a non-deformed perfectly flat glass window. Slight degradation is from the additional spherical aberration induced by the window in the optical path.
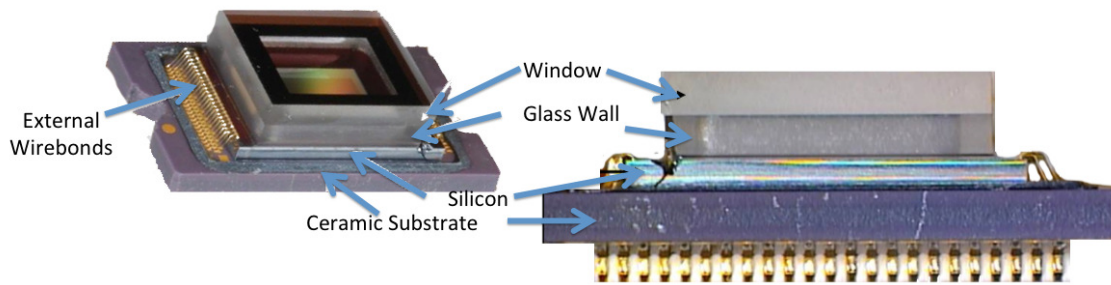
Figure 5.11: New DMD package is shown here. it is notable that the package is sealed directly to the silicon wafer probably to reduce packaging costs and minimize the number of seals in the package [108].

to understand how to model the mechanical effects in a DMD package, and how they affect the optical performance of the device when it is cooled. Alternate cheaper DMD package types have been developed since the "type-A" package design. One such design is shown in Figure 5.11.

5.5   DMD Operation at Low Temperatures

While it was important to test unbiased DMD's at lower temperatures, an important question is to determine the temperature at which a DMD no longer functions properly. The low temperature tests were undertaken to determine if a 0.7" 13.6 μm XGA DMD could operate at the temperatures required by a near-infrared spectrometer. Testing the operation of the XGA DMD at low temperatures required constructing a dewar that allowed the DMD to be operated under vacuum, connected electrically to an external control computer and with a temperature control loop. Since the DMD requires a large number of electrical interconnects (200 for an XGA DMD), the DMD control board (Discovery 4100 KIT) was positioned within the liquid nitrogen dewar. With this method, it drastically simplifies the dewar feed-through requirements to operate the DMD. This approach required only two DC power feed-throughs and one 4-pin hermetic USB feed-through into the dewar wall to operate the DMD. A special hermetic high speed USB feed-through to perform this task was purchased from SRI Hermetics. Four additional electrical feed-throughs were also required for the heater and temperature monitoring. The DMD control board was heat-sinked to the dewar wall, so that the DMD control electronics remained warm (i.e. at approximately room temperature). The DMD itself was mounted directly to the cold work surface, which allowed it to be cooled by the liquid nitrogen. Figure 5.12 shows the dewar design with the electronics control board. A Lakeshore DT-470 temperature diode was affixed directed to the DMD package, and this proximity to the active area ensured accurate temperature measurement. Additionally, a resistive heater element was placed below the DMD mount (Figure 5.12) to permit our dewar's push-pull temperature control system.

An external experimental testing apparatus also had to be assembled. A liquid nitrogen tank and electrically actuated solenoid valve supplied the liquid nitrogen cryogen to the dewar. A light source was placed outside the dewar to illuminate the DMD. The dewar window was sized appropriately so that the DMD could be illuminated at 24° off-axis relative to the DMD normal with minimal vignetting. A Lakeshore temperature proportional-integral-derivative (PID) controller was used to set and monitor the temperature. A CCD camera located outside the dewar was used to image the illuminated DMD through the dewar window. This apparatus is shown in Figure 5.13. Two experiments were conducted while the DMD was held
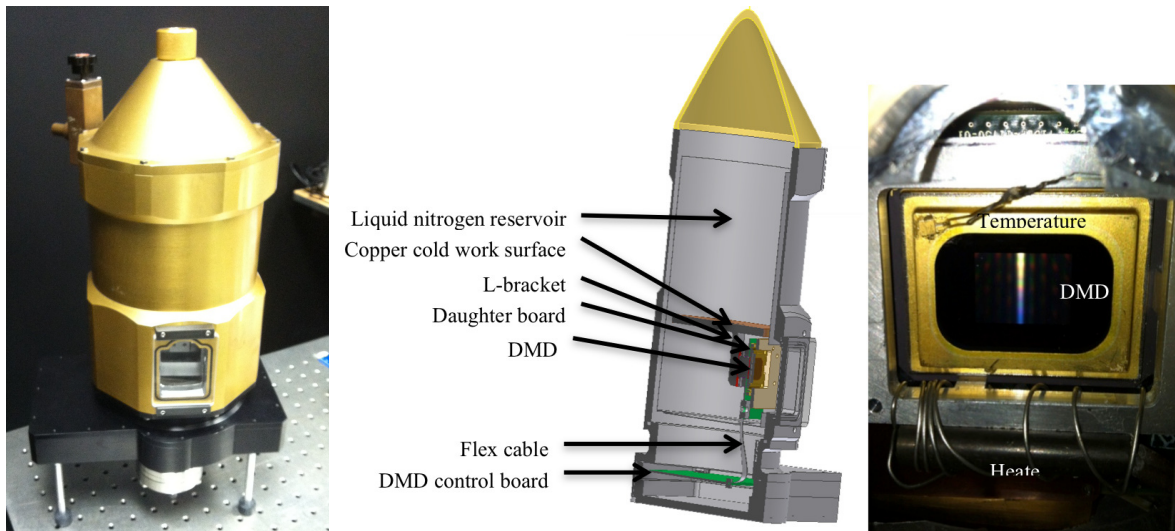
Figure 5.12: (Left) The assembled dewar and electronics board extension chamber. (Middle) Dewar design is shown here. A vacuum USB feed-through was placed below the control board (not shown). An additional six-pin feed-through was placed on the side of the dewar (not shown). (Right) DMD package mounted inside the dewar.

at low temperature. The first experiment was designed to determine the minimum temperature of DMD operation. The second experiment was performed to examine the long-term stability of the DMD.

The dewar (Infrared Labs Model HD5) was pumped down to remove air and moisture from the enclosure. A base pressure of approximately 1×10^{-5} torr was obtained using a turbo vacuum pump. This level of vacuum was sufficient to prevent frost from forming on the DMD as it cooled. Liquid nitrogen was then added to the dewar to start the cooling process. The cool-down rate was initially rapid, (2 K per minute), but slowed once lower temperatures were reached. The target temperatures (273 K, 263 K, 253 K, etcetera.) were set using the Lakeshore controller. The controller modulates the power to the resistive heater element to keep the temperatures at a set point to balance out the cooling power of the Liquid nitrogen. Test patterns were uploaded, and images were captured at each temperature. After the DMD had cooled to 150 K, the DMD was then warmed back up, and test images were collected again. The same series of test patterns was used as described in Section 4.3.4. Below a temperature of 150 K, the heat load from the control board and parasitic heat from the DMD flex cable was larger than the cooling power of the nitrogen cryogen. At maximum heater power, a stable temperature of 215 K was maintained, and stable temperatures between 150 K and 215 K could be maintained.

Typically, the electronic control board was powered up and operating during cool down. In one of the subsequent trials, the DMD electronics were powered off until the DMD reached its coolest temperature (130 K). This was lower than the 150 K reached when the board was powered on during cool down. Once this lower temperature was reached, the DMD electronics were switched on and corresponding test images from the CCD were captured immediately. Even at this low temperature, no indications of stuck DMD mirrors were observed. A stuck mirror would present it self as always either "on" or "off" in each of the test patterns used. This experiment showed that the DMD mirrors did not need to be continuously re-landed during the cool down process to remain functional at low temperature.

To ensure that hinge memory or warping effects were not a problem at low temperatures, which would cause distortion in the reflected images, a second test was performed. The DMD was cooled to 173 K, and
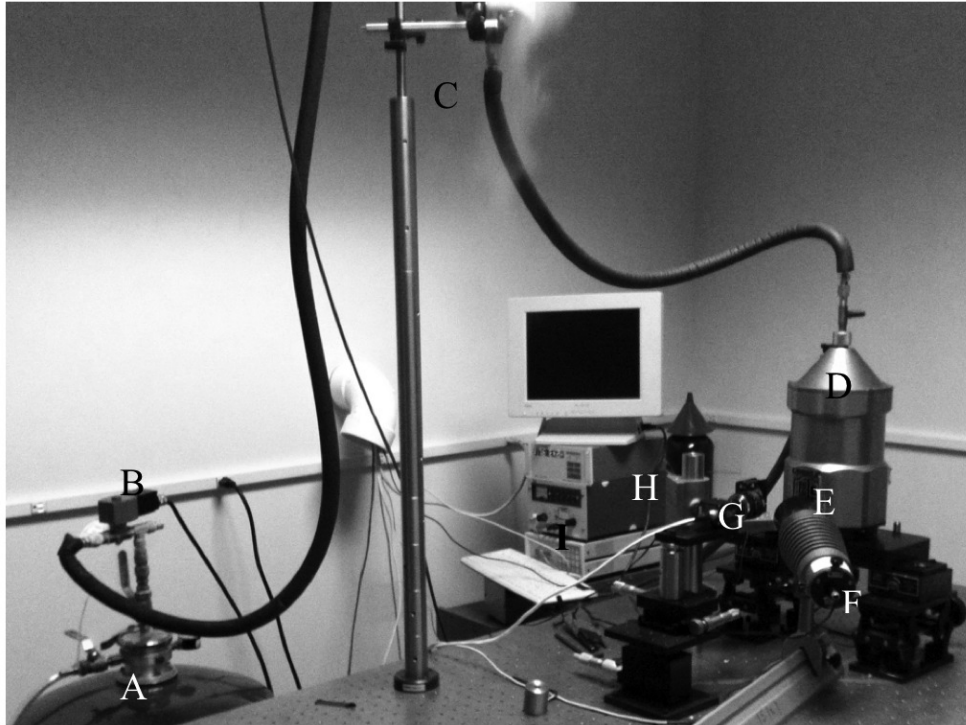
Figure 5.13: Low temperature testing apparatus: (A) liquid nitrogen tank, (B) solenoid valve, (C) gravity feed, (D) dewar, (E) DMD (F) light source, (G) camera, (H) power supplies and (I) temperature controller The reflection of light from the DMD to the CCD camera turn out to be highly sensitive to the tilt and positions of the DMD within the dewar. Accurate measurements require high spatial stability. This experiment was limited by the design of our dewar. As the liquid nitrogen was consumed, the mechanical structure of the dewar changed. The cold work surface within the dewar must be thermally isolated from the outside walls of the dewar. This was accomplished by suspending the cold work surface by the filler neck at the top, held in place by two plastic tabs at the bottom. When the neck cooled down, the cold work surface moved, and the alignment between the source and camera (aligned to be at the specular angle of the DMD mirrors) was no longer optimal. In addition, when liquid nitrogen was added to the dewar, the vibrations also caused small shifts in the DMD position relative to the position of the light source and CCD camera. These factors limited the accuracy of these stability measurements.

the temperature control loop was optimized to keep it within $\pm 1\,$K. A DMD pattern was then uploaded and the mirrors were landed for 30 minutes. This time was chosen, because it is a practical exposure time for a space-based spectrograph, and ideally the mirrors would not move during this integration time, otherwise stray light from unselected sources would be present in the spectrograph. At the end of the 30 minutes, a set of test patterns with all of the mirrors facing the CCD camera was uploaded to the DMD, and the corresponding test images were taken. This cycle of the mirrors landed and tested was repeated for approximately 24 hours. The test image brightness was normalized using the periphery of the DMD package to remove light source variation. The normalized irradiance of the light reflected from the DMD onto the CCD was then measured using these test patterns. We selected a region centered on the active DMDs, taking the mean of 700×400 image pixels. Any fraction of the mirrors not turning towards the camera would affect the measured irradiance.

5.5.1 Low Temperature Operation Results

The upper curve in Figure 5.14 shows the DMD temperature as measured by the DT-470 diode. The middle curve shows the shift of the DMD array relative to the CCD camera, in both the row and column directions. The shifts were measured by monitoring the positions of all four corners of the active DMD region in the CCD images. The lowest plot in Figure 5.14 shows the measured irradiance when all mirror are turned towards the CCD camera. At image numbers 3 and 7 in Figure 5.14, there are discontinuities in both the position curves (Middle) and irradiance curves (Bottom) during cool down. These points correspond to times at which liquid nitrogen was added to the dewar. At points 1, 5 and 21, the DMD is imaged at nearly the same position on the CCD (i.e. implying that the DMD is at the same spatial position inside the dewar), and the measured irradiances are within 1%. This indicates that the DMD's reflectivity was stable within 1%. During these tests, every mirror flipped to its programmed state at each temperature and there was no indication, even at temperatures of 130 K, of any sticking mirrors. This was verified by running the same optical "test" patterns that were completed after each irradiation step, except here it was done at each temperature step.

The second operational experiment involved performing a long-term test. An image with all the mirrors flipped towards the CCD camera was used to calculate the normalized irradiance in Figure 5.15 (Bottom). The same periphery region on the gold-coated metal package was used to factor out light source variations in each image. Additionally, an image of the DMD was taken when the mirrors were unbiased (in their flat position) at each time increment. The mirrors went back to their nominal flat state at each test point. No hinge memory or warping effects were present when the DMD was in unbiased state. This was verified by releasing the mirrors and looking for a line between the two different test sections. Apparently, there is insufficient thermal energy at the tested temperatures to permanently warp the hinge, even when the mirrors are landed in one position for an extended period of time. Between hours 8 and 9, liquid nitrogen refills were needed over this time, and this resulted in a shift in the DMD position. After 20 hours, the DMD warmed up because all the liquid nitrogen was consumed. This caused the array to shift, which produced a change in the measured DMD irradiance. After nitrogen is added, the irradiance curve displays an artificial downward irradiance trend. This can be attributed to the liquid nitrogen being consumed and causing the position of the DMD to change. In future experiments, an improved iso-thermal mount would be required
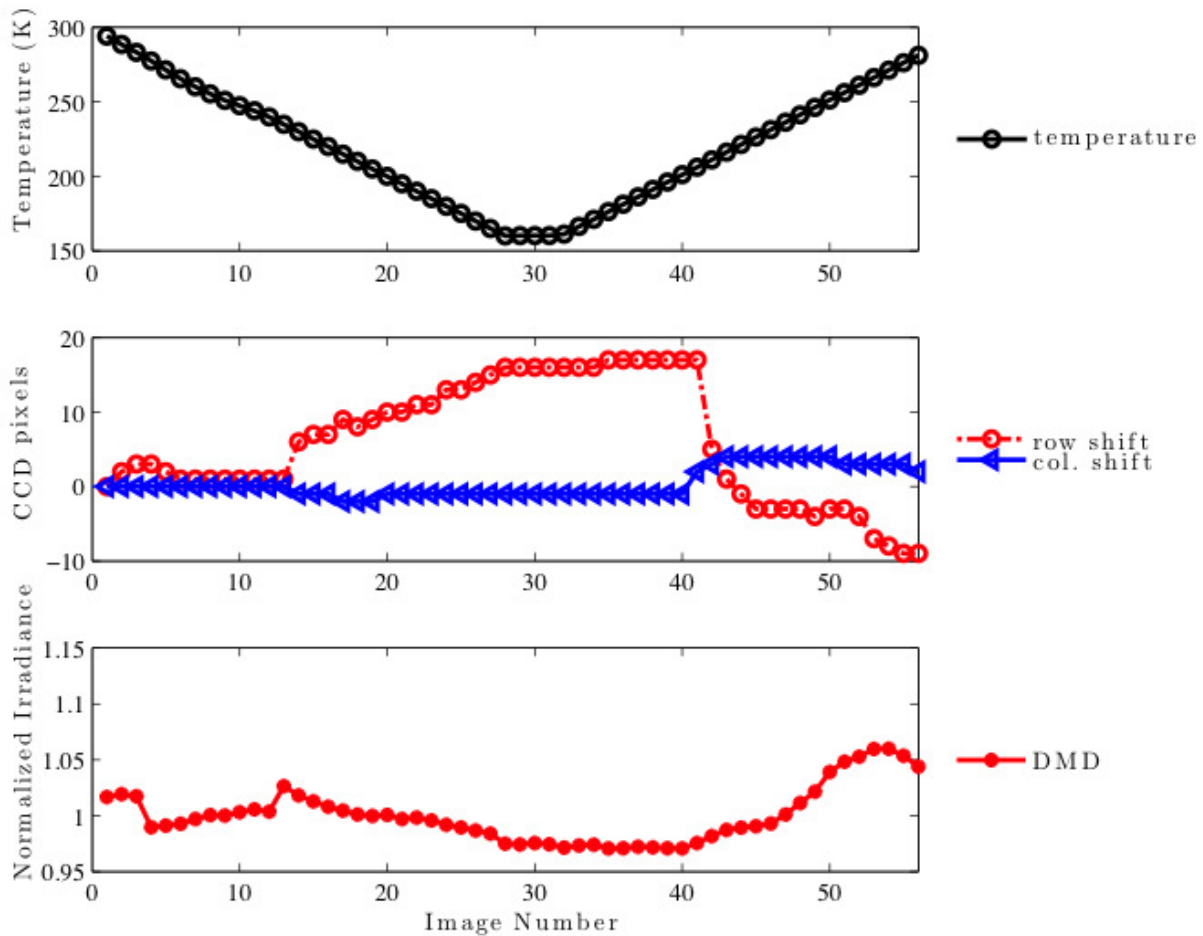
Figure 5.14: (Top) DMD temperature as it cooled after nitrogen fill. (Middle) Shift of the DMD image on the CCD camera in number of pixels. (Middle) Row shift was large due to the vertical motion of the cold plate relative to the camera/light source outside. (Bottom) Normalized irradiance from the DMD is shown as a function of image number. Variations in spatial position of the DMD array result in variations in the measured irradiance (counts).

to obtain more stable irradiance measurements. Within the limitation of our setup, during the entire low temperature test procedure, none of the test patterns showed any sign of stuck mirrors.

5.6   Summary

After removing the window from the DMD it became apparent that a great deal of care is required to prevent them from becoming contaminated. A water removing bake should be performed prior to cooling an unpackaged DMD. An opto-mechanical model was built to model the mechanical characteristics. The DMD model followed elasticity (meaning when the temperature load was applied, the DMD optical properties changed, but these properties returned to their former state after it went back to room temperature), and the largest surface deformation was "power" due to the slight mismatch between material CTE's. Also the critical parameter when cooling a DMD is the stress induced change in refractive index of the protective
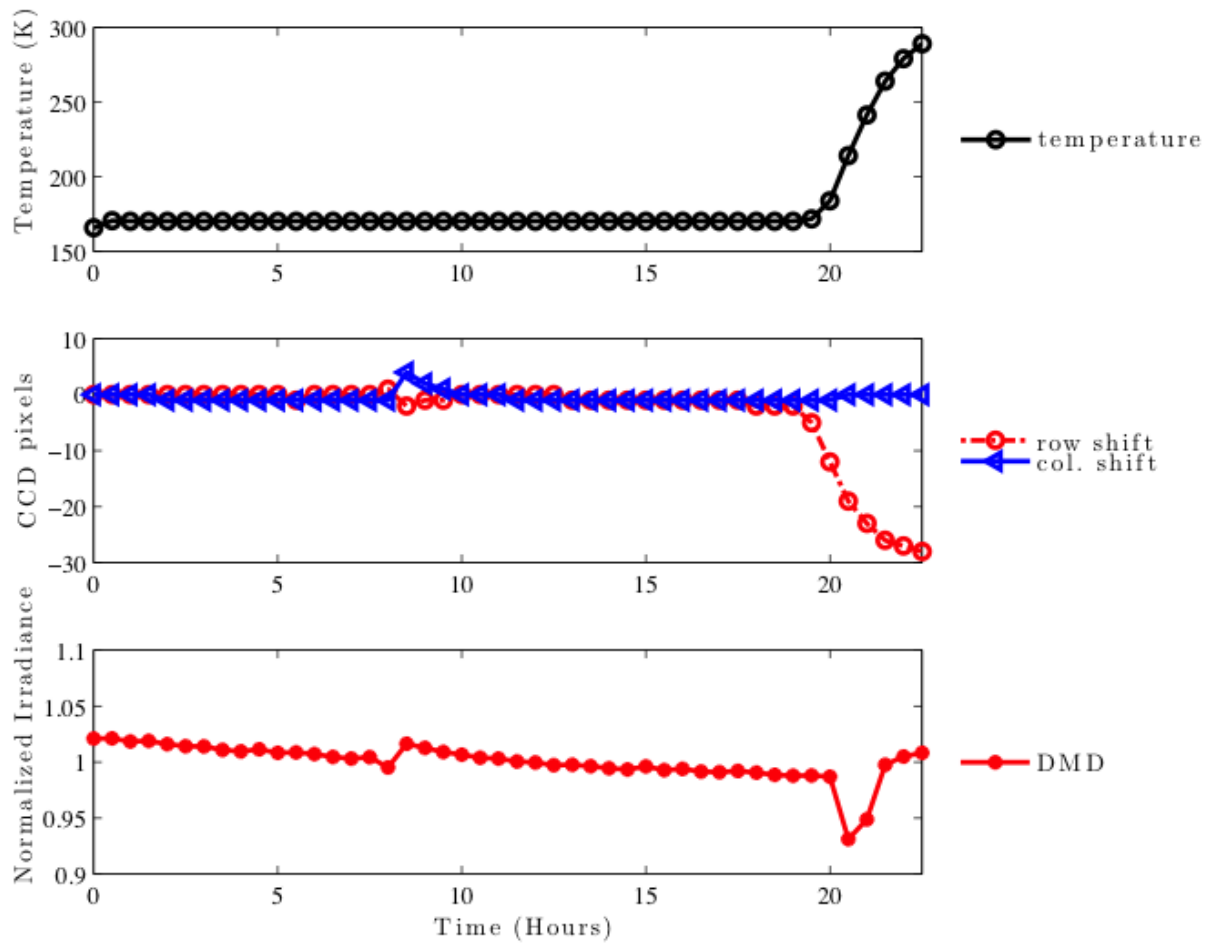
Figure 5.15: (Top) Temperature recorded over 24 hours. One measurement is taken every 30 minutes. Target test temperature was 173 K. Over this time the temperature was stable within 1C. (Middle) Plot shows the motion of the DMD relative to the CCD camera. (Bottom) Curve shows the normalized irradiance as a function of time.

glass, not the glass surface deformations. Cooling the packaged DMD showed that the main aberration created was an increase in "power".

The low temperature results were very promising. All of the DMD mirrors latched in their programmed state down to temperatures as low as 130 K. There was no indication that mirrors were sticking to the substrate in either of the two DMD positions. These measurements were limited by the mechanical stability of the dewar during cool down. To better than a few percent, there is no indication that the optical tilt angle varied or that any optical properties of the DMD changed with temperature. Further testing will be required to examine stability over longer periods of time. Also due to the limited number of DMDs tested, the experiment should be repeated on other DMDs to reaffirm these results. Overall, the tests confirm the viability of DMDs for the next generation of space-based MOS.

CHAPTER 6

CONCLUSION AND FUTURE WORK

This dissertation investigated the ability of a DMD to operate in a space environment. Prior to this thesis, there were very few publications available to determine if it was possible to consider utilizing a DMD in a space mission.

An appropriate method was developed to measure scattered light in DMDs. The 848×600 17 µm $10°$ DMD optical spot scans showed that there is more scattered light when the spot illuminates the edge or central via within an individual DMD mirror. These scans also enabled a contrast measurement, which indicated this DMD has a contrast of 270-320:1 in the visible. After these spot scans were completed, a shift-variant reflectivity and scatter model was produced for the characterized wavelengths.The limitation to the optical performance of the DMD appears to be the protective window. The window does not transmit light over the complete spectral range of interest for a UV-VIS-Near-IR spectrograph and are not optimal with regard to minimizing stray light. These mirrors were found to have a small amount of curvature, verified by two independent methods (interferometry and centroiding), which further decreased their throughput. Additional losses such as duty-cycle, fill factor, and diffraction efficiency were discussed, but were determined to no be the limiting factors for a 17 µm or 13.68 µm DMD with regard to total DMD optical efficiency. Finally, a model was presented to calculate the total optical throughput for a DMD and window.

The proton radiation experiments on 3 13.68 µm $12°$ DMDs yielded very positive results at each proton energy level tested (21.0 MeV, 34.5 MeV, and 40.9 MeV). The DMDs remained fully operational for a total dose of greater than 30 krad ($4.5\times$ the total dose expected for a 5-year mission). A method was developed to count SEU's without reading out the DMD memory. Additionally single event upsets were found in which mirrors flipped from their programmed state while being exposed to protons. Cross-sections were calculated for these SEUs, and on average one upset would occur every 4 days in an L2 Orbit. Our test conditions were quite harsh due to the large dose increments used for the test, so these results are likely representative of a worst-case scenario for the relevant space mission. The failures seen are likely related to trapped charge in the DMDs. Exercising the mirrors and annealing them proved to bring the DMDs back to normal operation. The borosilicate windows were found to yellow significantly (up to 10% transmission loss in the far UV) for a 20 krad proton exposure.

101

A DMD was unpackaged and cooled. Moisture caused the mirrors to change shape, and extreme caution should be taken when unpackaging DMDs. A packaged DMD was cooled to determine the change in shape, and a FEM model was created to model this temperature load on the DMD package. An optical model took the deformations from the FEM model and showed that there are minimal optical effects associated with the MTF change as the mirrors cool. The operational low temperature experiments illustrated that the 1024×768 XGA 13.68 μm XGA 12° DMD tested could be ran at 130 K. The DMD long-term cold test kept the DMD cool for 24 hours at 173 K and the mirrors were held landed in one position for 30 minutes. Several temperature cycles were completed, and throughout the low temperature testing, there was no indication of stuck mirrors or mirrors that did not tip their complete 12°. The mechanical stability of the dewar set the upper bound for the stability measurements, not the DMD. There was minimal change the DMD's optical performance as it cooled, meaning that its package was well designed and has a well matched CTE.

6.1 Future Work

Two potential instruments that utilize a DMD are discussed in Appendix E. A clever instrument concept utilizing a DMD as a time delay integration slit-mask for an airborne or low earth orbit (LEO) high signal-to-noise ratio spectrometer is described in Appendix E. The second instrument describes the DMD's utility as a radial velocity scanning spectrograph.

A potential MIDEX mission utilizing DMDs is being considered at NASA Goddard. Such a project would further increase confidence that real science can be completed with DMDs. The science case for this mission involves performing UV astronomy to wavelengths as short as 200 nm. The borosilicate window cuts off at approximately 360 nm so a UV transmissive window needs to be integrated to the DMD package. Borosilicate is not the optimal window material to use on a DMD with regard to its optical characteristics. Borosilicate is very similar to Pyrex glass, which was developed by Schott to resist high temperatures. If TI would provide alternative window materials, it would open up many more scientific applications for the DMD, in the UV and Near Infrared. However, TI will not provide their devices either un-packaged or without a window. TI backfills the DMD package with some proprietary anti-stiction materials such as floro-polymers (Teflon like materials) [109]. Over 50 different types of lubricants have been tested for DMDs with the most successful one being a perfluorinated n-alkanoic acid. These lubricating materials have the advantage of making the DMDs self-healing. This means that new material can be deposited from the vapor as it becomes worn away. In short, it would be ideal to get packaged devices directly from TI with the window material required for the mission directly bonded to the kovar frame.

6.2 Summary

Based on these results it is apparent that the DMD is both very well designed and robust to proton radiation, and low temperature tests. It makes sense to propose the DMD for future space missions based on the initial results presented in the present work. Proton testing was the only form of radiation testing completed. No gamma or heavy ion testing was completed on these devices in the current work. The low temperature results were very promising, but the test was only completed on a single DMD. However, now that some

of the fundamental questions have been answered, it is be possible to propose to fly a DMD in a future mission.

Included in Appendix F is an overview of Micro-grid Polarizer Arrays (MGPAs). The MGPA opens the possibility to build compact, lightweight simple polarimeters ideal for space applications. Together a new class of scientific spectrographs (FITTSUMA - Appendix E , MORVS, PSMOS ect) could be proposed utilizing the DMD as a slit mask and the MGPA as the polarizing filter to collect simultaneous spectral and polarization information.

APPENDIX A

POWER SUPPLY NOISE IN CCD MEASUREMENTS

A low level of unknown noise was present in the CCD images of some of the scatter measurements. The noise source was persistent, but worse on some days. After many weeks of attempting to perform measurements when the noise was not significant, an investigation into the root cause of the noise source was performed. The noise pattern was present in dark frames, and varied from 0 to ± 10 ADU (1 ADU $= 5e^-$). Grounding points were checked on the camera and corresponding electronics boards. The ground was examined in the wall current. The read out of the camera was 40 kHz. The noise period was approximately 6 pixels, so given the read out speed this means that the noise source operated on the order of 7 kHz. This didn't appear to be a harmonic of 60 Hz AC noise. After a great deal of work it was determined that the power supply on the light source was noisy enough to couple into the CCD, by means of the CCD cooling fluid. The CCD was liquid cooled, and when the coolant lines were in proximity of the light source power lines, noise was observed. An experiment was run to determine the magnitude of this effect. The coolant fluid is a glycol water mixture. Figure A.1 shows that as the current to the light source was increased, the noise pattern magnitude increased. The shape of the image histograms also changes: they become multi-peaked. Additionally, to check for noise a radon transform was performed on the data's dark frames. The noise always presenting itself with lines orientated around 135° in the images acquired. This transform was very sensitive to the noise, much more so than just using standard deviations or variance to detect the noise in the measurements. The noise pattern's magnitude increases as current increases in the filament. The spot scans are composed of a large number of images, so it was important to have a method to quickly determine if the noise pattern changed during the spot scan experiment. The noise was insignificant after the light source and cooling lines were separated, and a metal shield was additionally placed between the two items.
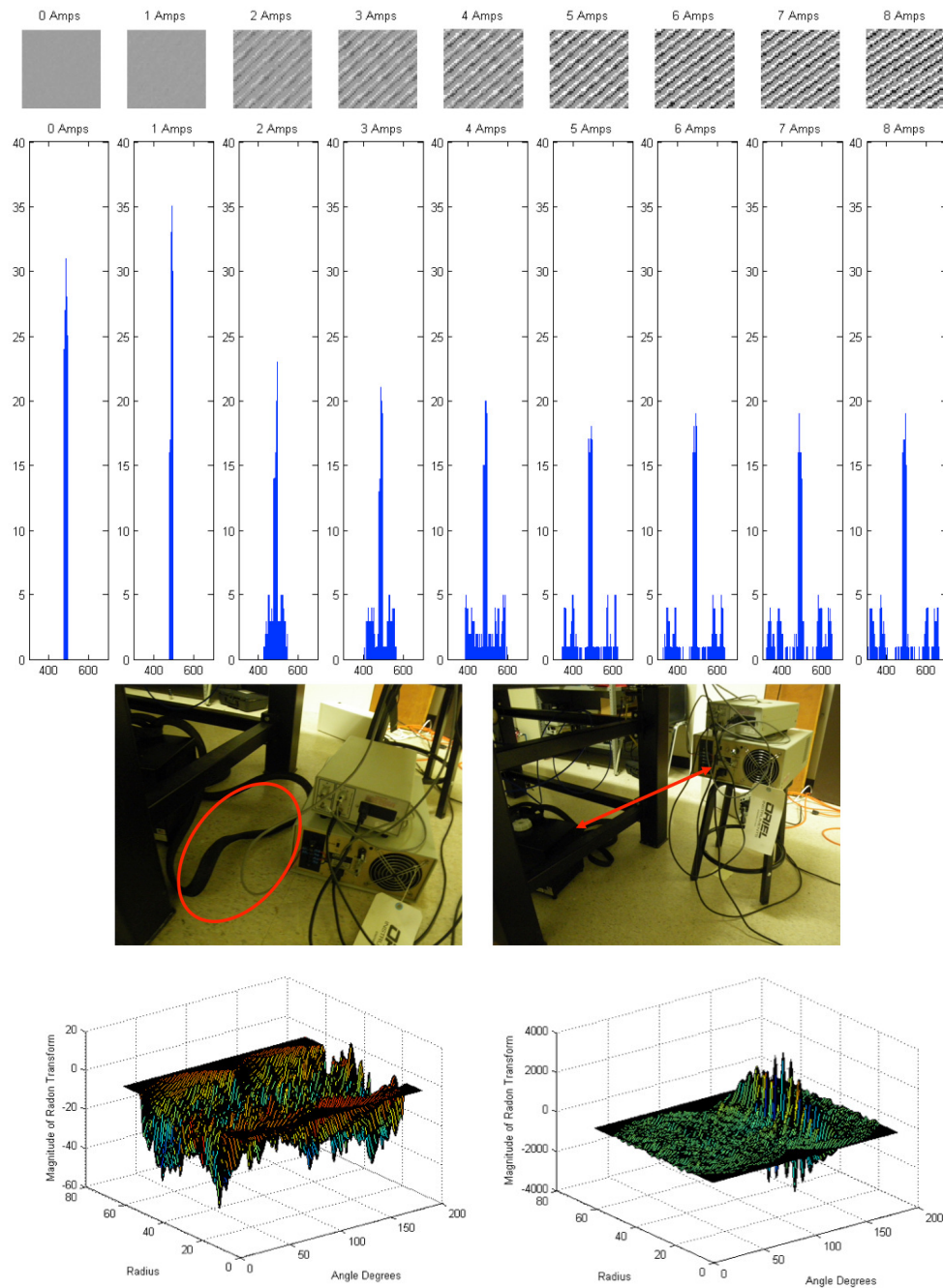
Figure A.1: (Top) CCD images as current was increased to the light source. Image histograms as a function of power supply current. (Middle) Two images show that when the CCD cooling lines were in proximity to the lines for the light source supply, the electric field could couple into the water. (Bottom Left) Surface plot shows the radon transform on the mean subtracted data without the noise source present. (Bottom Right) Plot shows the magnitude of the mean subtracted data with the noise source present.

APPENDIX B

DMD ELECTRICAL OPERATION

B.1 DMD Clocking and Electrical Operation

Two electrodes are used to actuate an individual DMD mirror. Below these two electrodes, a CMOS SRAM cell is used to determine the corresponding charge placed on each electrode. Each SRAM Cell is composed of 5 transistors. Figure B.1 shows the DMD electrical architecture. The DMD has a SRAM cells below the DMD for each mirror. Above the SRAM is the column data driver. This location temporary holds a row of data that is read into the DMD (sometimes this is referred to as a D-Latch). The row select circuit is connected to the lines that send the row number to the DMD. Once data is read into the column data driver, the row select determines which portion of the micromirror memory array will be updated. The consequences of this input scheme means that an individual DMD mirror cannot be randomly addressed. A complete row of the DMD SRAM memory array must be updated. After the SRAM memory is read into the DMD the pixels can then be reset with a reset pulse. The following section discusses a reset pulse generator.

B.1.1 Design of a Reset Pulse Generator

A reset pulse generator is one of the fundamental parts in the DMD drive electronics. A simple reset pulse generator was designed for a custom set of electronics. The purpose for the rest pulse generator is to latch the mirrors in one of their stable states. As data is read into a row of mirrors, the mirrors do not change position. It is not until a reset pulse is applied that the mirrors reset move to the new position. The XGA DMD is broken up into 16 reset zones. There are 16 electrical pins on the DMD (called MBRST $0 - 15$) that are connected to the mirrors directly. Each MBRST zone can reset 48 rows of mirrors. All of these mirrors are connected in parallel along these lines. Figure B.2 shows the five different steps it takes to rest a mirror. In zone 1, the data is read into the mirror. The bias voltage for the mirror electrodes is set by the power supply on the chip denoted VCC2 (7.5 V). The MBRST voltage is $+24$ V. Next (Zone) the MBRST voltage goes to -26 V and the address voltage increases to 7.5 V. This is called the "stepped address" voltage. In the stay transition the mirror has a minimal amount of torque applied to it during this step. However in
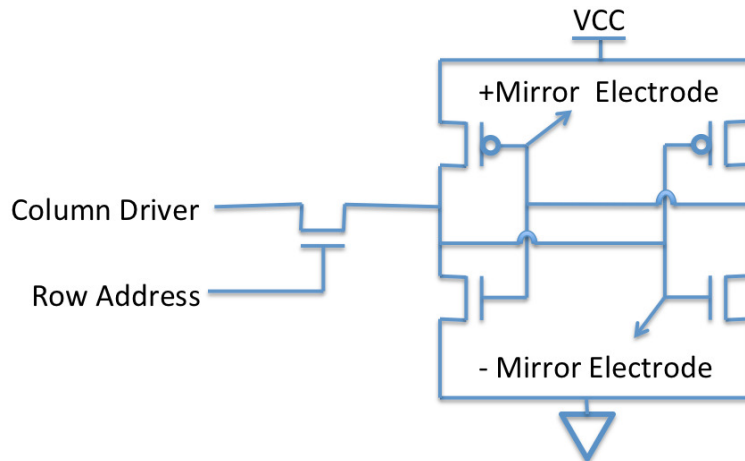
107

Figure B.1: Unit cell is shown here for each mirror. There are five transistors in this SRAM cell. A sixth transistor is not required, because the cell doesn't need to be read out quickly. Usually a 6th access cell is placed on another column line. The two transistors at the top are PMOS, and the two at the bottom are NMOS transistors.

the crossover transition, the spring tips are compressed and the mirror stores energy for a "launch." This potential launch energy allows the mirror to easily break away from the adhesive Van der Waals forces holding the mirror in place. The width of this pulse is extremely critical for efficient mirror to ensure all of the mirrors release properly. During zone 3, the MBRST voltage is set to 7.5 V, the same charge as the right electrode. There is no potential voltage difference on the right side electrode in the stay transition and none on the left side of the cross over transition. The duration of this pulse width is critical for landing the mirror properly. If it is too long the mirror in a cross over trajectory can bounce back and be landed on the wrong side. If this pulse width is too short the cross over mirrors will be recaptured rather than going to the new side. For zone 4, the MBRST voltage is returned to +24 V and the mirror is either returned to its previous state (left) or in the crossover transition landed on its new side. The stepped address voltage in this zone decrease the amount of torque applied to the mirror, so that it can land softly in this step. Finally in zone 5, the address voltage is returned to its nominal 5 V. This is a very simple reset voltage procedure, because the portions of the array can be globally reset, which minimizes the number of control lines required to re-latch a complete DMD array.

The design for the simple discrete resent pulse generator is shown in Figure B.3. A 5 Volt supply powers the two 4123's The pulse width is set by an external resistor and capacitor. The larger capacitances create wider the pulse widths. Conversely, with a large resistor, the pulse width is decreased. Both 4123's are triggered simultaneously by the FPGA in the design. The Trigger is an active high, in this case a 5 volt triggered pulse (As shown by the Vpulse source). Both of the Q bar outputs are connected to a voltage divider circuit. Since a single DIP houses two of these circuits, it is possible to generate multi-level outputs. The top 4123 is set to have 450 ns pulse width, and the second one is set to have a 550 ns pulse width. C3 is added to act as a small charge buffer needed after adding the diodes to the circuit. Diodes that respond very quickly are needed otherwise the rise and fall time of the circuit become very long. Diodes are placed in the circuit so that there is not a conflict by connecting the output of two 4123's to the same node. In essence, this is a output buffering method, with the drawback being that there is a voltage drop across each of the diodes. One note of caution is that 4123's are very sensitive to temperature variations. The RC constant
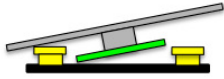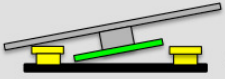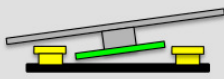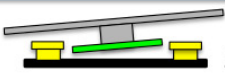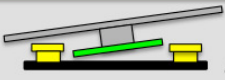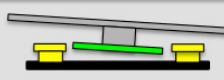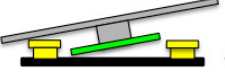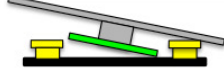
	Stay Transition	Crossover Transition
Zone 1	$\Delta V_1=24V$ $\Delta V_2=19V$ $V_L=0$ $V_b=24$ $V_R=5$	$\Delta V_1=19V$ $\Delta V_2=24V$ $V_L=5$ $V_b=24$ $V_R=0$
Zone 2	$\Delta V_1=26V$ $\Delta V_2=33.5V$ $V_L=0$ $V_b=-26$ $V_R=7.5$	$\Delta V_1=33.5V$ $\Delta V_2=26V$ $V_L=7.5$ $V_b=-26$ $V_R=0$
Zone 3	$\Delta V_1=7.5V$ $\Delta V_2=0V$ $V_L=0$ $V_b=7.5$ $V_R=7.5$	$\Delta V_1=0V$ $\Delta V_2=7.5V$ $V_L=7.5$ $V_b=7.5$ $V_R=0$
Zone 4	$\Delta V_1=24V$ $\Delta V_2=16.5V$ $V_L=0$ $V_b=24$ $V_R=7.5$	$\Delta V_1=16.5V$ $\Delta V_2=24V$ $V_L=7.5$ $V_b=24$ $V_R=0$
Zone 5	$\Delta V_1=24V$ $\Delta V_2=19V$ $V_L=0$ $V_b=24$ $V_R=5$	$\Delta V_1=19V$ $\Delta V_2=24V$ $V_L=5$ $V_b=24$ $V_R=0$

Figure B.2: Five different steps to reset a DMD mirror are shown here. Left side shows the stay trajectory and the right side shows a crossover trajectory

should be designed for the operational temperature of the electronics, so that the appropriate pulse widths are selected for the DMD.

The DMD is represented by the 300 pF load (taken directly from a TI datasheet). This is representative of the capacitive load of a complete 1024×768 XGA DMD. Next a standard non-inverting rail-to-rail op-amp is used to amplify the signal. A voltage offset is applied to the negative terminal at $R15$. This voltage is set from the 5 V supply by the resistors $R12$ and $R13$. This centers the output so that the resulting signal going to the DMD is from $\pm 26V$ rather than a single ended output like the signal generation side of the circuit. $R10$ is a current limiting resistor. $R9$ is the feedback resistor, which determines the gain of the op-amp stage. In the real design a high-speed high-voltage op-amp will be used, a MSK131. MS Kennedy, based in Liverpool, NY, manufactures the MSK131 They are a manufacturer of many radiation-hardened parts. The MSK131 is a very specialized high voltage op-amp. It has a slew rate of $500 \ \frac{V}{\mu s}$ and can have up to $400V$ supply with an output swing of ± 90 V. This is a one of a kind op-amp and to get comparable performance, a desecrate design would have to be implemented. The MSK131 was not simulated directly, because the Spice model was not available for this part. Instead another op-amp was placed in the circuit to validate the design, with the issue of slightly lower performance (slower slew rates than the MSK131). The outputs are shown in figure B.4 for this spice simulation.

In order to fully radiation test the DMD's, a custom set of radiation hard drive electronics would have to be built. However due to time restrictions, a Discovery 4000 electronics was used to perform the initial proton testing. Prior to performing the testing a new set of simple low speed drive electronics were investigated. The DMD is an elctro-static MEMs device that operates on the principle of electro-static force. The
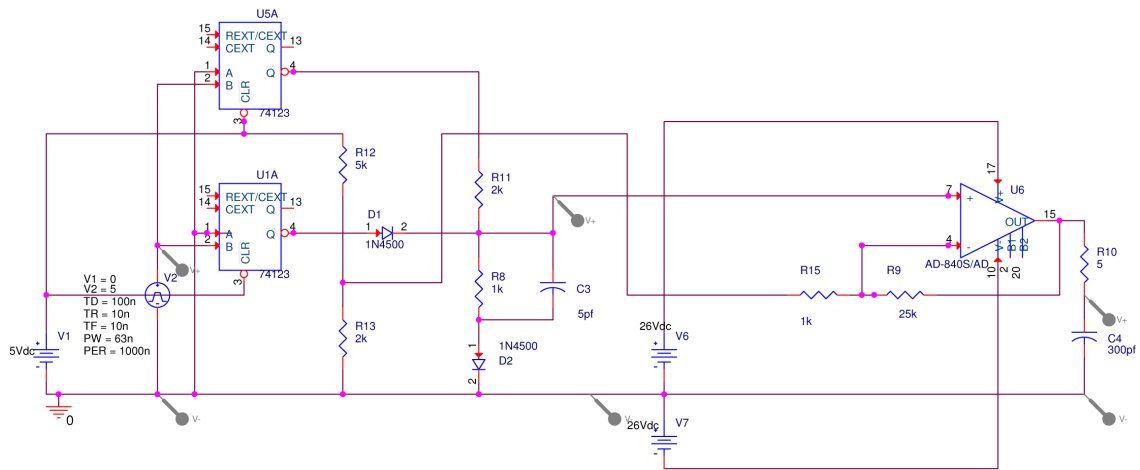
Figure B.3: This circuit contains two main components. The two (74123) and inverter/ resistor network generate the analogue pulse shape required to reset the DMD. Then amplifier on the right amplifies the signal to the higher voltage required for the MEMs.
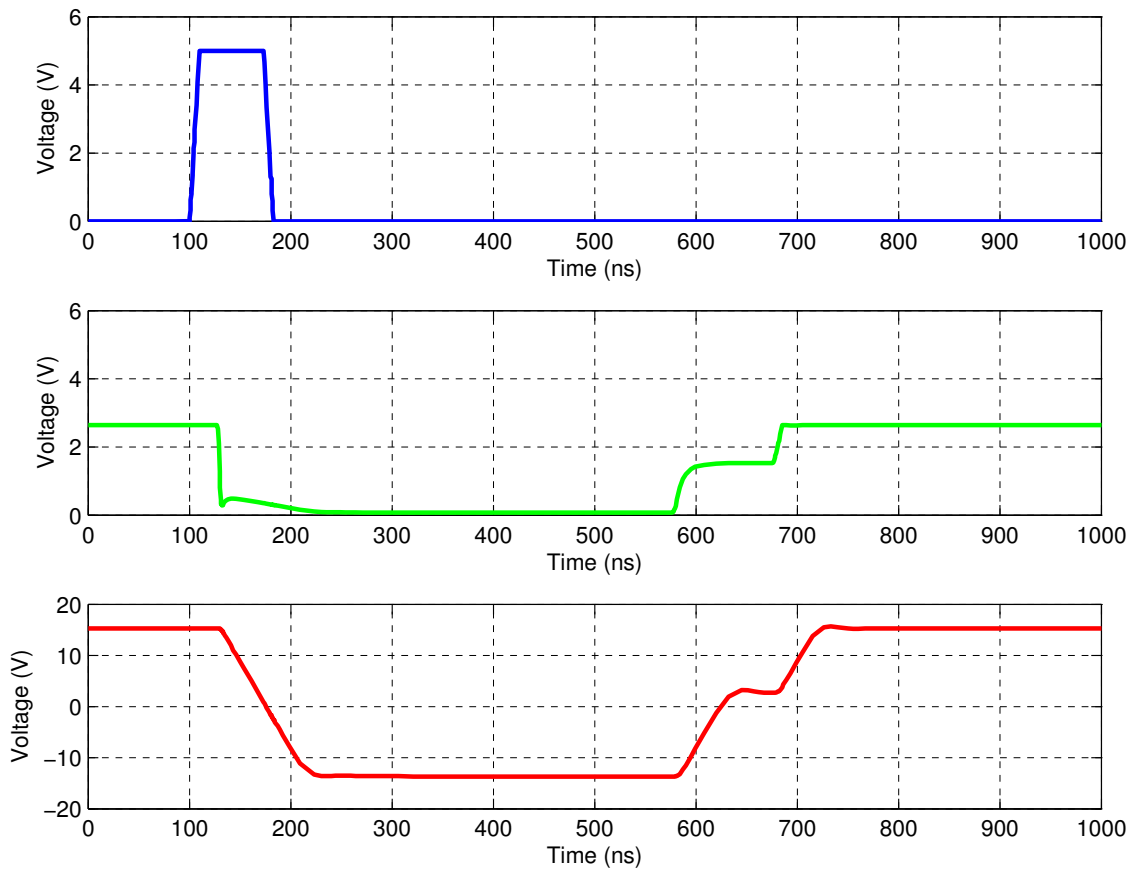
Figure B.4: This shows the temporal form of the DMD reset pulse. The top plot shows the generation of a trigger pulse from the FPGA circuit. The middle plot shows the low voltage reset pulse. Finally the high voltage output is shown on the bottom in red. The generation is with 2 4123's and the output is double ended. Note the actual output will be higher, because a specialized high voltage op-amp will be used in the circuit.

electric field within a parallel plate capacitor is shown by Equation B.1 where V is the voltage difference between the plates, d is the distance separating the plates, σ is charge density, A is the area of the plate, and ϵ is the permittivity. In the case of the DMD, the dielectric material is simply air in between the plates, so ϵ becomes ϵ_0. It is simplest to think of a single DMD pixel as 2 capacitors in parallel: one electrode on the first address electrode and one on the second address electrode. An electrode size was used as the size of the parallel plate capacitor. The capacitance for a single capacitor is a function of voltage, charge, and distance between the parallel plates (Equation B.2). In the case of the DMD, $k = 1$. Equation B.3 describes charge across a capacitor. To determine the energy stored in the capacitor, it can be calculated by integrating over the charged stored in the capacitor (Equation B.4). Performing this integral and using equation B.3 to substituted in the value for Q, equation B.5 for energy stored is derived. The electrical force can then be related by equation B.6. Now this is a radial force or torque a distance away from the center of rotation (the torsional spring). It can be seen that the force required to move the mirror is non-linear with respect to both distance and the applied voltage. Figures B.6 and B.7 show the electric force generated for $2\,\mu m \times 2\,\mu m$ electrodes for distances and voltages appropriate for this micromirror.

$$E = \frac{V}{d} = \frac{\sigma}{\epsilon} = \frac{Q}{A\epsilon} \tag{B.1}$$

$$C = \frac{\epsilon A}{d} = \frac{k\epsilon_0 A}{d} = \frac{Q}{V} \tag{B.2}$$

$$Q = CV \tag{B.3}$$

$$dU = \int_0^Q \frac{q}{c} dq \tag{B.4}$$

$$U = \frac{CV^2}{2} = \frac{\epsilon_0 A V^2}{2d} \tag{B.5}$$

$$F = -\frac{U}{d} = \frac{\epsilon_0 A V^2}{2d^2} \tag{B.6}$$

Understanding the electrostatic nature of addressing mirror electrodes is key to understanding how electro-statically actuated MEMs like the DMD operate. Figure B.5 illustrates the electrode and structural formation. The energy stored in a micromirror can be related by equation B.7. Equation B.7 assumes that the electrode is small, d the mirror height is small and also the deflection angle ϕ is small. A is the area of the mirror and V is the voltage difference applied to the electrode. The torque applied to the mirror is shown in equation B.8. The mirror torque is found by differentiating the change in energy as a function of change in
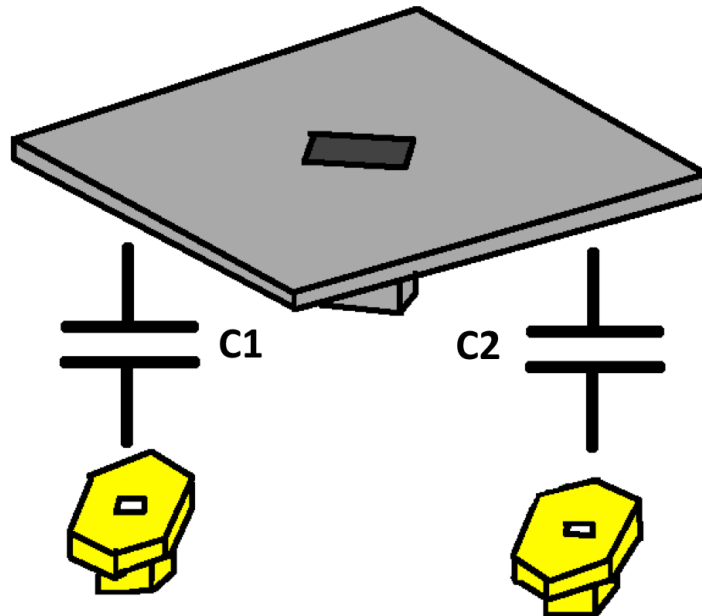
Figure B.5: Capacitor model for a DMD is shown above. DMD pixel can be modeled by capacitors in a single DMD pixel, one C_1 shown on the left, and C_2 shown on the right for the second address electrode.
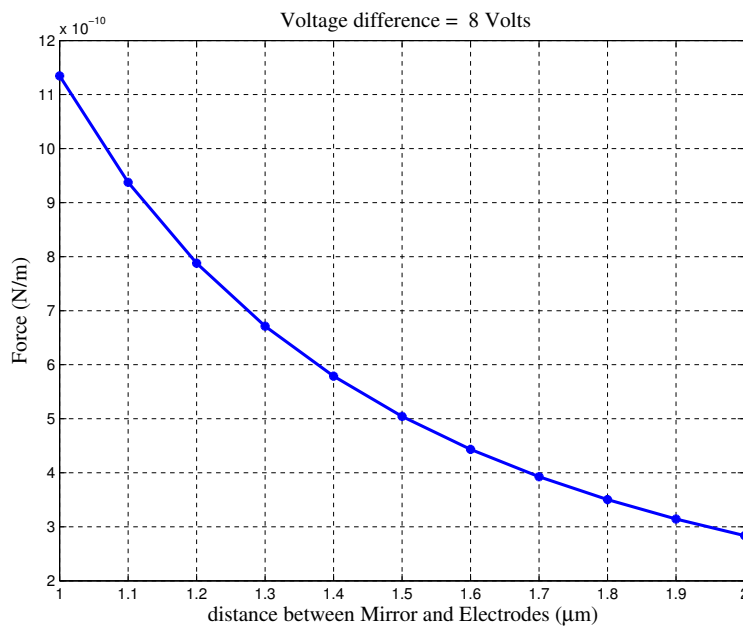
Figure B.6: Equation B.6 shows the electric force a voltage difference across a capacitor creates as a function of distance. The voltage in this case is fixed at 8 V.
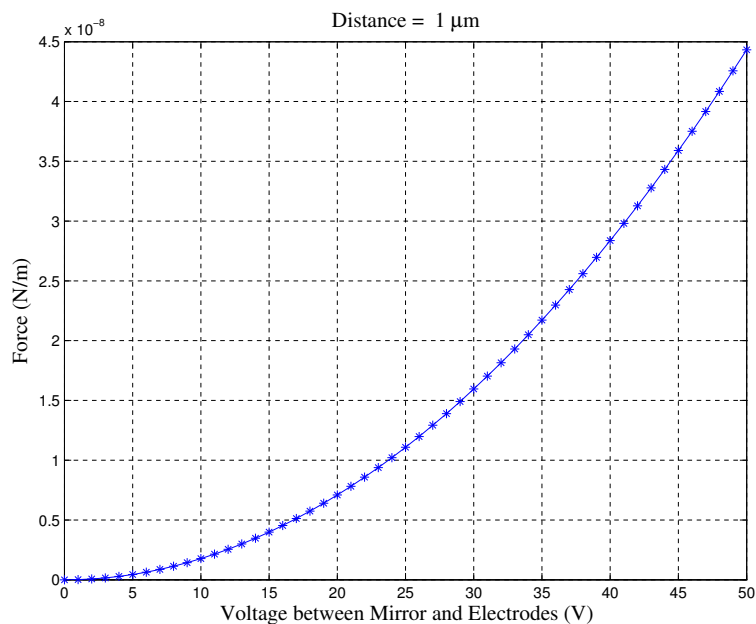
Figure B.7: Equation B.6 shows the electric force a that voltage difference across a capacitor creates as a function of voltage. The distance in this case is fixed at 1 μm.

tilt angle. However an additional term, the mirror elastic restoring torque must be added to the equation. The spring constant k is added as a term that resists the torque and is a function of many parameters such as mirror material type and thickness. It can be seen that the voltage required to drive the mirror to a specific deflection angle is highly non-linear. This becomes important if one wants to operate move the mirror to an analogue position. This is why DMDs are designed to operate digitally (either "on" or "off"). In addition, operating an array of these mirrors in an analogue mode becomes increasingly difficult due to device manufacturing variation and positional feedback requirements.

$$E = \frac{CV^2}{2} = \frac{A\epsilon_0 V^2}{2(d - r\phi)} \tag{B.7}$$

$$T_e = \frac{dE}{d\phi} = \frac{Ar\epsilon_0 V^2}{2(d - r\phi)^2} \tag{B.8}$$

$$T = \frac{dE}{d\phi} = \frac{Ar\epsilon_0 V^2}{2(d - r\phi)^2} - k\phi \tag{B.9}$$

B.1.2 Reverse Engineering the DMD Protocol

The DMD uses a LVDS (low voltage data interface). The DMD has selectable throughput, through two different pins which enable 32 LVDS pairs, 16 LVDS pairs, or 8 LVDS pairs. The Discovery 4000 kit operates at $400 MHz$. The chips is broken up into two parallel data channels, an "A" data channel and a "B" data channel. There are 2 LVDS clock signals for the DMD, one for each data channel. Additionally there are two
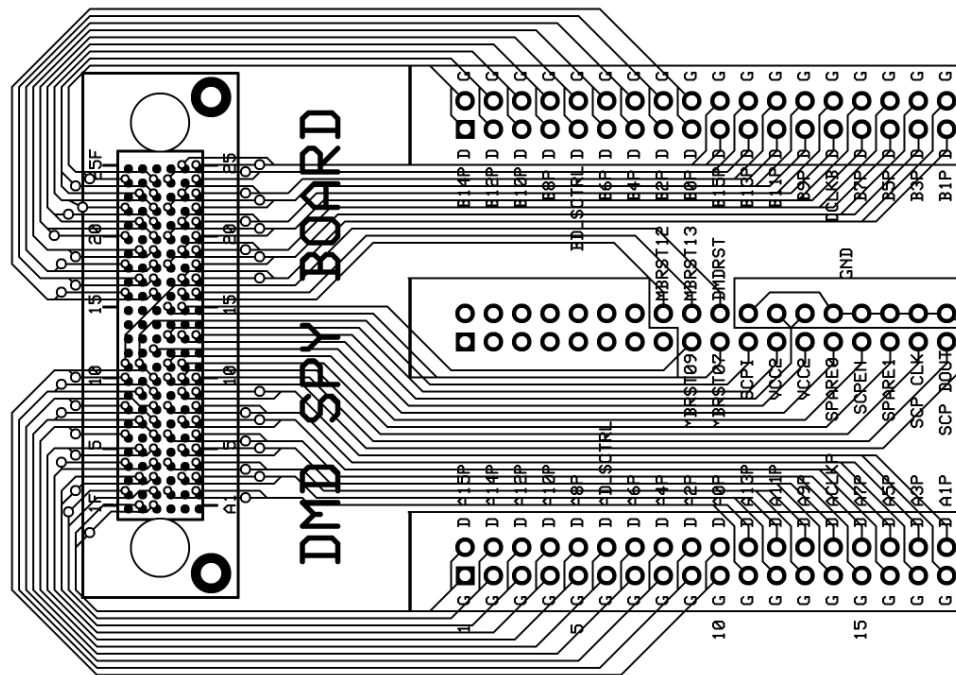
Figure B.8: The break out board layout that was built to examine the protocol for the Discovery electronics use to communicate with the DMD. An axially conducting tape was placed on the board to intercept the signals from the Discovery 4000 board.

"SERLCNT" (serial control lines) for each data channel. One of these lines "SERLCNTA" is used to send the row address for the DMD. It is simply the row address in binary for the DMD. The second line appears to be an additional sync line. A spy board was created to reside in-between the DMD control electronics board, and the cable that ran to the DMD. It is shown in Figure B.8. Additionally there are several low-speed serial lines that are used for DMD initialization (The protocol for these has yet to be determined.) In order to build custom DMD electronics a FPGA with enough outputs must be found and programmed. Minimally 8 data LVDS pairs, 2 clock pairs, 2 serial control lines, serial interface lines, and one four the MBRST (if the DMD is globally reset.) A company called Chipworks has taken apart the DMD. Figure 4.16 shows how thin the hinge material actually is (70*nm*)

APPENDIX C

PROTON RUN LOGS

Table C.1: 34 MeV run log For DMD serial number 140508. The energy at the DMD silicon is 21.0 MeV. *Started to see sticking mirrors in Zone 1. **Started to see additional sticking and non-functional mirrors in other zones. *** Effects continued across all four zones.

#	Average Flux $\frac{p+}{cm^2 s}$	Fluence $\frac{p+}{cm^2}$	Integrated Fluence $\frac{p+}{cm^2}$	Incremental Dose (krad)	Integrated Dose (krad)	Time (s)
1	5.3×10^7	9.07×10^9	9.1×10^{09}	2.0	2.0	172
2	5.4×10^7	9.07×10^9	1.8×10^{10}	2.0	4.0	169
3	5.3×10^7	9.08×10^9	2.7×10^{10}	2.0	6.0	173
4	5.5×10^7	9.08×10^9	3.6×10^{10}	2.0	8.0	166
5	5.6×10^7	9.08×10^9	4.5×10^{10}	2.0	10.0	163
6	5.8×10^7	9.08×10^9	5.4×10^{10}	2.0	12.0	157
7	5.5×10^7	9.09×10^9	6.4×10^{10}	2.0	14.0	164
8	5.4×10^7	9.08×10^9	7.3×10^{10}	2.0	16.0	168
9	5.1×10^7	9.11×10^9	8.2×10^{10}	2.0	18.0	179
10	4.8×10^7	9.10×10^9	9.1×10^{10}	2.0	20.0	189
11*	5.1×10^7	2.25×10^{10}	1.1×10^{11}	5.0	25.0	445
12**	4.6×10^7	2.25×10^{10}	1.4×10^{11}	5.0	30.0	493
13***	4.7×10^7	2.25×10^{10}	1.6×10^{11}	5.0	34.9	476

Table C.2: 44.2 MeV run log For DMD serial number 140507. The energy at the DMD silicon is 34.5 MeV. *Started to see effects in Zone 1 After dose increment 8, this DMD received an extra unknown dose due to beam-line control malfunction

#	Average Flux $\frac{p+}{cm^2s}$	Fluence $\frac{p+}{cm^2}$	Integrated Fluence $\frac{p+}{cm^2}$	Incremental Dose (krad)	Integrated Dose (krad)	Time (s)
1	8.5×10^7	2.30×10^{10}	2.3×10^{10}	4.1	4.1	271
2	7.5×10^7	2.30×10^{10}	4.6×10^{10}	4.1	8.1	305
3	8.4×10^7	2.30×10^{10}	6.9×10^{10}	4.1	12.2	273
4	8.6×10^7	2.30×10^{10}	9.2×10^{10}	4.1	16.2	269
5	8.4×10^7	2.30×10^{10}	1.2×10^{11}	4.1	20.3	274
6	7.3×10^7	2.87×10^{10}	1.4×10^{11}	5.1	25.4	391
7*	7.3×10^7	2.87×10^{10}	1.7×10^{11}	5.1	30.4	392
8	7.1×10^7	2.86×10^{10}	2.0×10^{11}	5.1	35.5	404

Table C.3: 49.3 MeV run log For DMD serial number 140106. The energy at the DMD silicon is 40.9 MeV. *Started to see effects in Zone 1 **Global effects continue, and some mirrors recover by the end of optical characterization. ***Most of array is non-functional.

#	Average Flux $\frac{p+}{cm^2s}$	Fluence $\frac{p+}{cm^2}$	Integrated Fluence $\frac{p+}{cm^2}$	Incremental Dose (krad)	Integrated Dose (krad)	Time (s)
1	5.0×10^7	2.40×10^{10}	2.4×10^{10}	4.0	4.0	479
2	4.5×10^7	2.40×10^{10}	4.8×10^{10}	4.0	8.0	537
3	4.1×10^7	2.43×10^{10}	7.2×10^{10}	4.0	12.0	597
4	3.9×10^7	2.40×10^{10}	9.6×10^{10}	4.0	16.1	611
5	3.6×10^7	2.40×10^{10}	1.2×10^{11}	4.0	20.1	672
6*	3.4×10^7	3.00×10^{10}	1.5×10^{11}	5.0	25.1	890
7**	3.3×10^7	3.00×10^{10}	1.8×10^{11}	5.0	30.1	902
8***	3.0×10^7	3.00×10^{10}	2.1×10^{11}	5.0	35.1	995
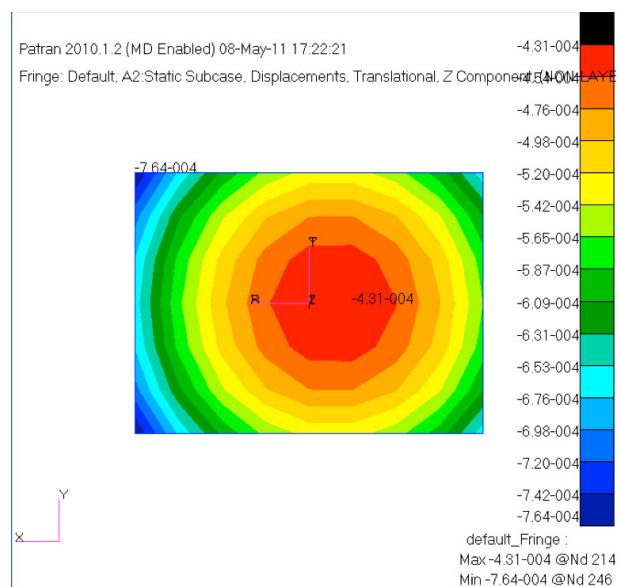
Figure D.1: Z component of the displacement is shown here. Mounts for the DMD were simulated as being free in the radial direction, but constrained in the z and theta direction. Three mounts were used for the simulation above, one on the right side and two on the left. Note the asymmetry in the position of the maximum displacement. At the edges of the chip, the DMD was 3 µm lower than in the center. Displacement units are in mm.
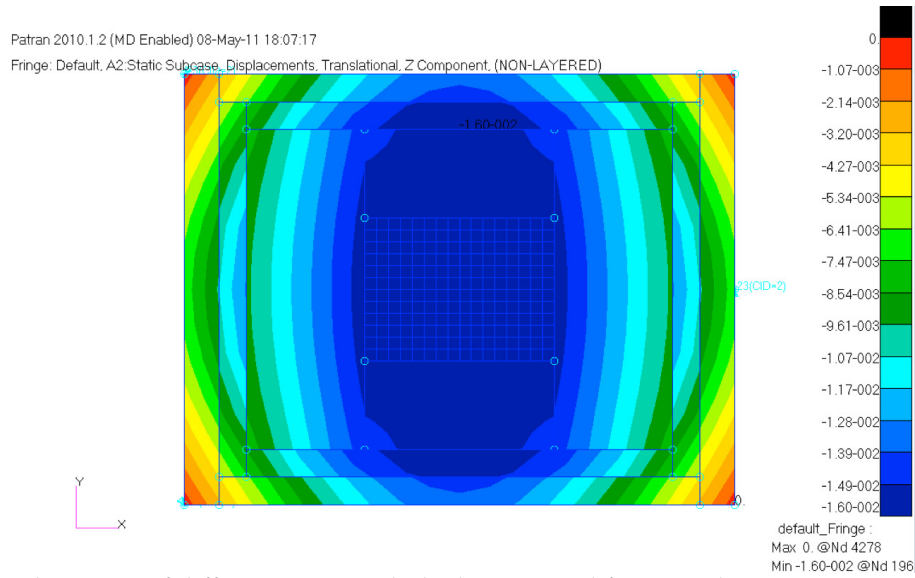
Figure D.2: Displacement of different parts with the lower metal frame and LGA ceramic carrier. It can be seen that there is now an asymmetry, due to the stiffness different in the x and y axes on the lower portion of the DMD package. Displacement units are in mm.

Table D.1: Sixth Order Fringe Zernike fit for Interferometer results. The units are in waves where 1 Wave = 632.8nm The first column is the room temperature DMD, The second column is the cooled DMD. The third column is the room temperature DMD without the dewar window.

Z number	$-100°C$ DMD+DW	RM DMD+DW	Just DMD	Delta	Aberration
1	-3.410	0.720	0.798	-4.928	Bias
2	3.053	0.064	2.800	0.189	Tip
3	2.253	0.336	1.693	0.224	Tilt
4	-0.912	0.071	-0.161	-0.822	Power
5	0.041	-0.071	-0.217	0.329	Astig X
6	1.143	0.537	0.350	0.256	Astig Y
7	-0.304	0.980	-0.200	-1.084	Primary Coma X
8	-0.226	0.210	0.005	-0.441	Primary Coma Y
9	0.403	-0.240	-0.010	0.653	Primary Spherical
10	-0.400	-0.134	-0.221	-0.045	Tri-foil X
11	0.120	0.055	0.106	-0.041	Tri-foil Y
12	0.486	0.033	0.014	0.439	Secondary Astig X
13	0.199	0.036	-0.054	0.217	Secondary Astig Y
14	-0.216	0.006	-0.097	-0.125	Secondary Coma X
15	-0.241	-0.103	-0.058	-0.08	Secondary Coma Y
16	0.013	0.006	0.038	-0.031	Secondary Spherical

Table D.2: The fit for the modeled borosilicate window DMD. Only the magnitude for each optical surface is shown where 1 Wave = 632.8*nm*.

K	N	M	Aberration	Window Bottom	Window Top	Silicon
1	0	0	Bias	1.978	0.282	-0.082
2	1	1	Tilt	0.330	0.000	0.000
3	2	0	Power (Defocus)	5.908	0.809	-0.184
4	2	2	Primary Astigmatism	3.323	0.196	0.171
5	3	1	Primary Coma	0.229	0.001	0.000
6	4	0	Primary Spherical	-0.613	-0.007	-0.039
7	3	3	Primary Tetra-foil	0.364	0.000	0.000
8	4	2	Secondary Astigmatism	4.580	0.020	0.040
9	5	1	Secondary Coma	0.045	0.000	0.000
10	6	0	Secondary Spherical	-1.549	0.000	-0.010
11	4	4	Primary Tetra-foil	1.363	0.034	0.171
12	5	3	Secondary Trefoil	0.044	0.000	0.000
13	6	2	Ternary Astigmatism	5.583	0.007	0.004
14	7	1	Ternary Coma	0.095	0.000	0.000
15	8	0	Ternary Spherical	-0.679	0.000	0.000
16	5	5	Primary Penta-foil	0.154	0.000	0.000
17	6	4	Secondary Tetra-foil	0.342	0.006	0.027
18	7	3	Ternary Trefoil	0.068	0.000	0.000
19	8	2	Quadra-Astigmatism	2.231	0.001	0.005
20	10	0	Quadra-Spherical	-0.079	0.000	-0.001
21	11	1		0.025	0.000	0.000
22	12	0	Quinta-Spherical	0.660	0.000	-0.001
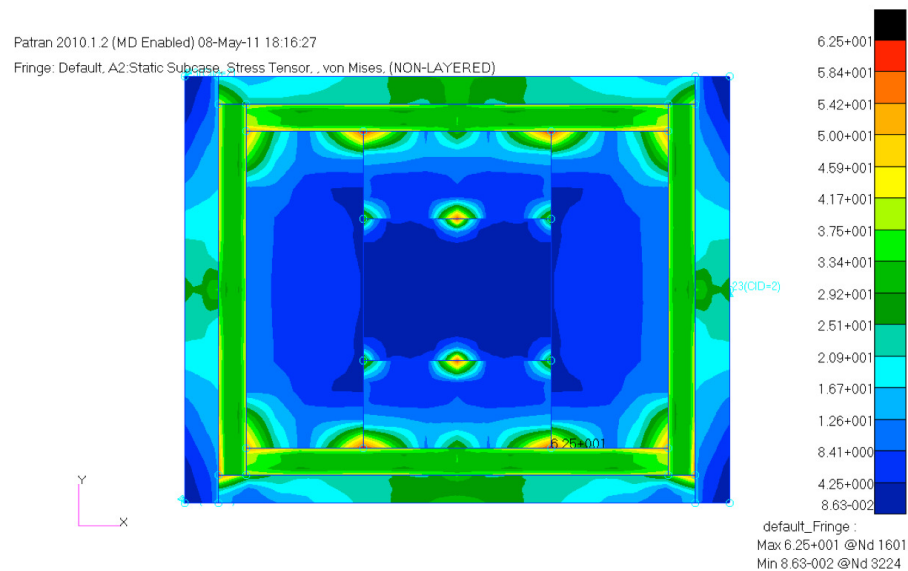
Figure D.3: Plot shows the stress locations on the package (units MPa). Maximum stress is located at the intersections of the kovar and ceramic carrier. Von Mises Component is shown. For more accurate stress results, a finer mesh is required.
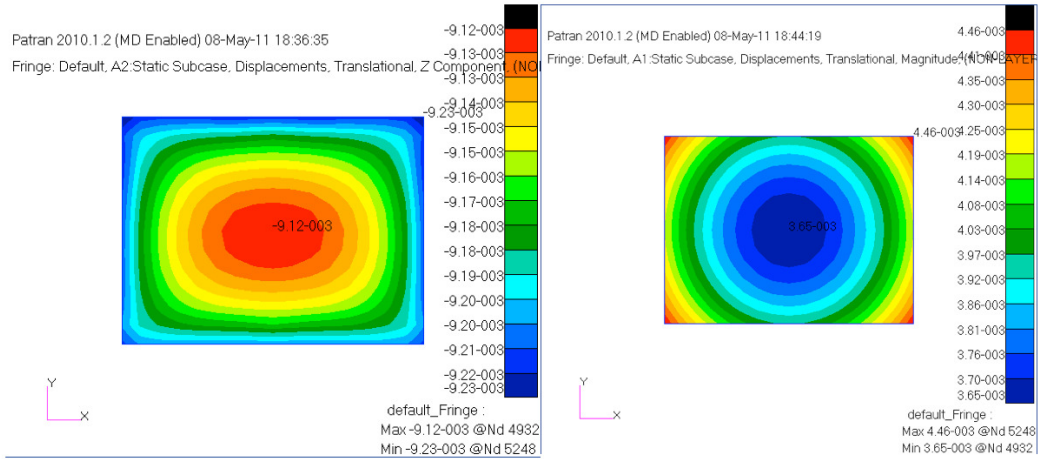
Figure D.4: Shape of the silicon in the final model. (Left) Model uses the borosilicate window and (Right) is for the fused silica. The z displacement is less than $< 1\,\mu m$. Displacement units are in mm.
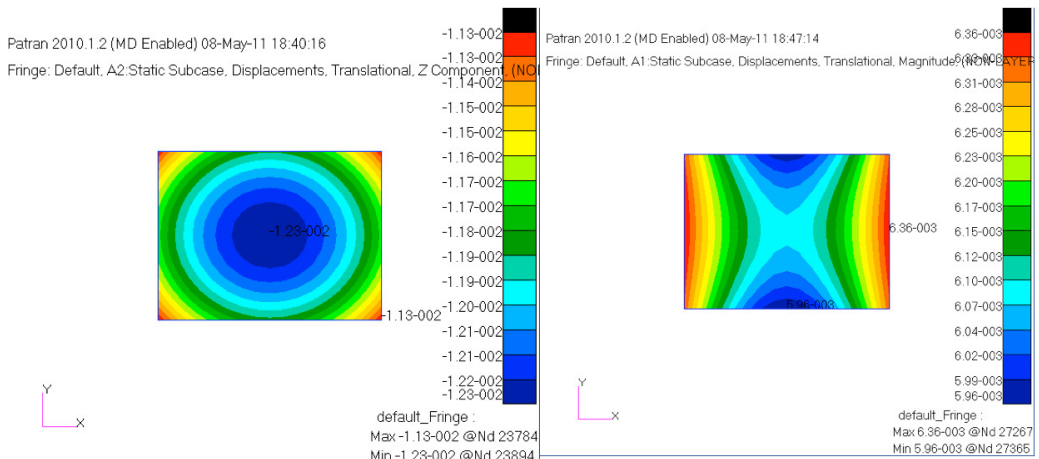
Figure D.5: Shape of the top surface of the glass is illustrated here. In the final model, the z displacement is less than $< 1\,\mu m$ for both the borosilicate glass left and the fused silica right. Displacement units are in mm.

E.1   A Flexible TDI Spectrometer Utilizing Micromirror Arrays (FIT-SUMMA)

A proposal was written for the NASA Early Stage Innovations program encompassing this new method of collecting spectral data with a DMD. The following sections illustrate the instrument concepts for a new type of flexible spectrometer

E.1.1   Time Delay Integration (TDI)

Time Delay Integration (TDI) is a technique commonly used in two different scenarios. The first situation is when the platform is moving (commonly an aircraft or spacecraft) and the earth is imaged below. Typically there are 10 to 100 CCD pixel stages for the signal to be integrated over. These systems utilize individual filters on separate CCD arrays to collect light at several wavelengths to generate multi-spectral data. Conventional spectrometers such as AVIRIS [110] have low signal to noise ratios (SNR) because they are photon starved. In such spectrometers, it is very important to increase dwell time to maximize SNR. The other scenario involves a fixed platform and a moving scene. In astronomy, a technique known as drift scan imaging utilizes a TDI CCD. The telescope and camera system are located at a single fixed look angle while the image of the celestial sky moves across the focal plane array. The CCD is set up to transfer electrons to the adjacent pixels at the same rate as the stars in the field move across the frame. Once the integrated charge reaches the end of the CCD, it is read out. Such techniques are, for example, used on liquid mirror telescopes that have been utilized for faint galaxies searches [111] and for tracking space debris [112].

E.1.2   Remote Sensing Low Light Imager

This chapter seeks to evaluate the DMD in a TDI imaging spectrometer. One of the common problems in remote sensing is capturing hyperspectral data with high SNR for a given FOV. The proposed instrument utilizes a lens to image light onto the DMD. The light then passes through a TIR (total internal reflection)
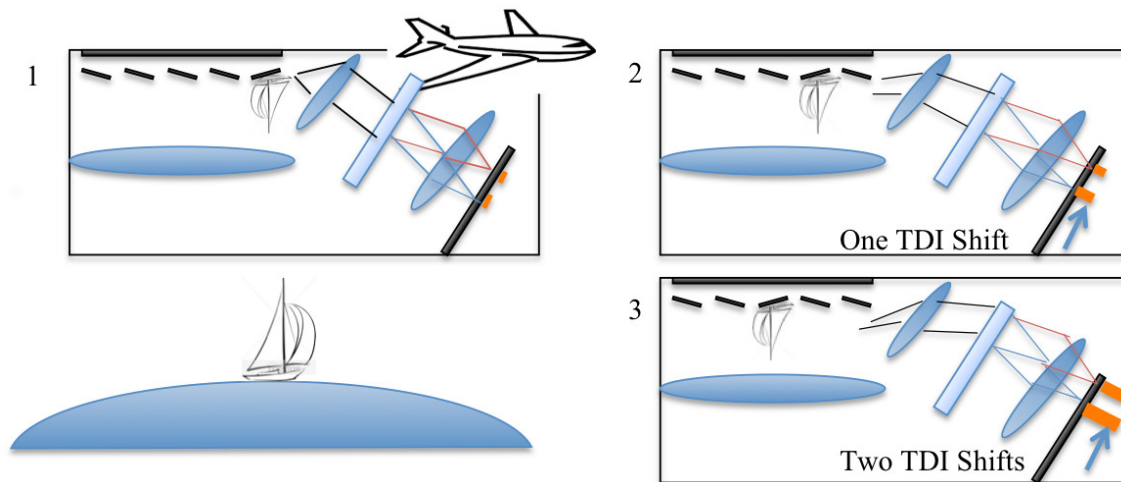
Figure E.1: The optical configuration of the FITSUMMA Spectrometer. One mirror is pointing towards the spectrometer. The light passes through a collimator and then grating. The dispersed spectrum is then re-imaged onto a CCD operating in TDI mode. Part 1 shows the complete spectrometer. Part 2 shows the platform has moved forward. The next mirror in the TDI zone has been moved towards the spectrometer. The charge is shifted in the direction shown by the arrow. Part 3 shows the next mirror and a greater signal on the CCD as the platform has moved forward another step. This graphic only shows one TDI zone. Multiple zones will be acquiring spectra of different ground point locations simultaneously. Note the drawing is not to scale.

prism to be imaged onto the DMD. A DMD acts as a spatial light modulator to generate a slit pattern that compensates for the spacecraft or aircraft motion. As the imaging platform moves relative to the scene, this slit (formed by the mirrors) moves across the DMD. The reflected light is collimated and then sent through a grating or dispersive prism element. The light is then re-imaged onto a TDI CCD where the spectra are shifted across the CCD at a rate that matches the movement of the slit formed by the micromirrors. After a sufficient number of photons have been collected (enough stages of integration), all of the mirrors are turned away from the spectrometer and the CCD is read out. Figure E.1 shows the simplified optical configuration of the FITSUMMA spectrometer.

An alternative configuration involves imaging onto the DMD at 24° off axis (twice the tip angle of the DMD mirrors) and the spectrometer being built nadir at zero degrees to the optical axis. This drastically simplifies the spectrometer design. The imaging lens is then placed at an angle to satisfy the Scheimpflug principle [113], which relates a tipped subject plane to a tilted image plane. Another important consideration in using an imaging lens is that it be optimized for the additional optical path length of going through the TIR prism and protective DMD window. The TIR prism reduces overall system size and makes the spectrometer much more compact. This compact spectrometer is also a very good candidate for a UAV (unmanned air vehicle). If the TDI CCD was replaced with an orthogonal transfer CCD (OTCCD), the spectrum could be shifted and the residual roll of the aircraft could be compensated. An OTCCD allows the charge to tip along both rows and columns to compensate for tip tilt errors. A large OTCCD camera is currently being built for the PannStars telescope to correct for atmospheric perturbations rather than conventional adaptive optics in Hawaii [114].

A TDI zone is a subset of adjacent mirrors on the DMD. The DMD is configured as adjacent sets of TDI zones. A TDI zone contains a line of n individual mirrors along the cross-track direction. This entrance slit corresponds to a line of points on the ground. If there are N TDI zones and n mirrors within a TDI zone, the

total number of mirrors that can be used in the along track direction are (TATM) as shown in Equation E.1 and Equation E.2. The number of columns in a DMD limits the TATM. Equation E.3 relates along track GSD along to the number of mirrors. The GSD (ground sample distance) of this spectrometer is a single DMD mirror in the cross track direction. The current state of the art DMD has 1920 columns and 1080 rows of pixels. If the DMD was positioned as shown in Figure E.2, this device would have a swath width of 1.08 km and an across-track *GSD* of 1 meter. Figure E.2 shows the DMD broken up into 5 TDI zones. If the device were broken up into 5 TDI zones, there would be 384 mirrors for each integration period. In comparison to a conventional spectrometer, this is two orders of magnitude improvement in dwell time. The along track GSD and the number of mirrors in a TDI zone are tradeoffs. The instrument could be reconfigured to give higher SNR (more mirrors per TDI zone) if the aircraft flew slower. If the aircraft flies faster, more TDI zones are required to capture the same number of along track ground pixels. Multiple DMDs can be located on the instrument focal plane in series to enable both longer dwell times or greater along track GSD. The most efficient method to resample the pixels in the along track direction will be examined.

$$\sum_{u=1}^{N}(n+u) = (N+1) \times \frac{N}{2} \times n = TATM \tag{E.1}$$

$$n = floor(\frac{2 \times TATM}{N^2 + N}) \tag{E.2}$$

$$GSD_{AlongTrack} = \frac{Velocity \times T_{int}}{N} \tag{E.3}$$

With regard to a low light hyperspectral imager, fewer mirrors in a TDI zone could be used when imaging a well-lit area on different pixels across the swath. A very high dynamic range image is required for nighttime imaging. If a pixel was saturated in a TDI zone, the spectra could be re-measured with a proper exposure as the object passes over another TDI zone by simply not using all n mirrors within the TDI zone.

When the ground is moving relative to the micromirror array, the ground pixels march across the DMD. As part of optimizing such a system, the most efficient time to transfer both the mirror and the TDI CCD charge must be determined. The DMD mirrors can be refreshed very quickly ($22000Hz$), and the pixels could be dithered over this transition. An alternative approach is to leave the strip of mirrors latched until a percentage of the ground pixel transitions to the next mirror. DMDs also have a finite settle time, so there is a point at which running them semi-statically may be beneficial for scattered light into the spectrometer. Also each time a new frame pattern is sent to the DMD, the mirrors return to their flat state and then are re-latched. This is a mechanism to extend the lifetime of the mirrors by preventing sticky mirrors and counteracting electrical memory when leaving the mirrors in one position. The DMD orientation on the focal plane is also important to investigate with regard to scatted light into the entrance pupil of the spectrometer. The rows of the DMD are broken up into 16 separate blocks. These blocks are electrically isolated and there may be advantages to driving them separately. In order for the instrument to operate correctly, the grating pitch must be matched to the TDI CCD charge transfer rate. Shown in Figure E.2, the
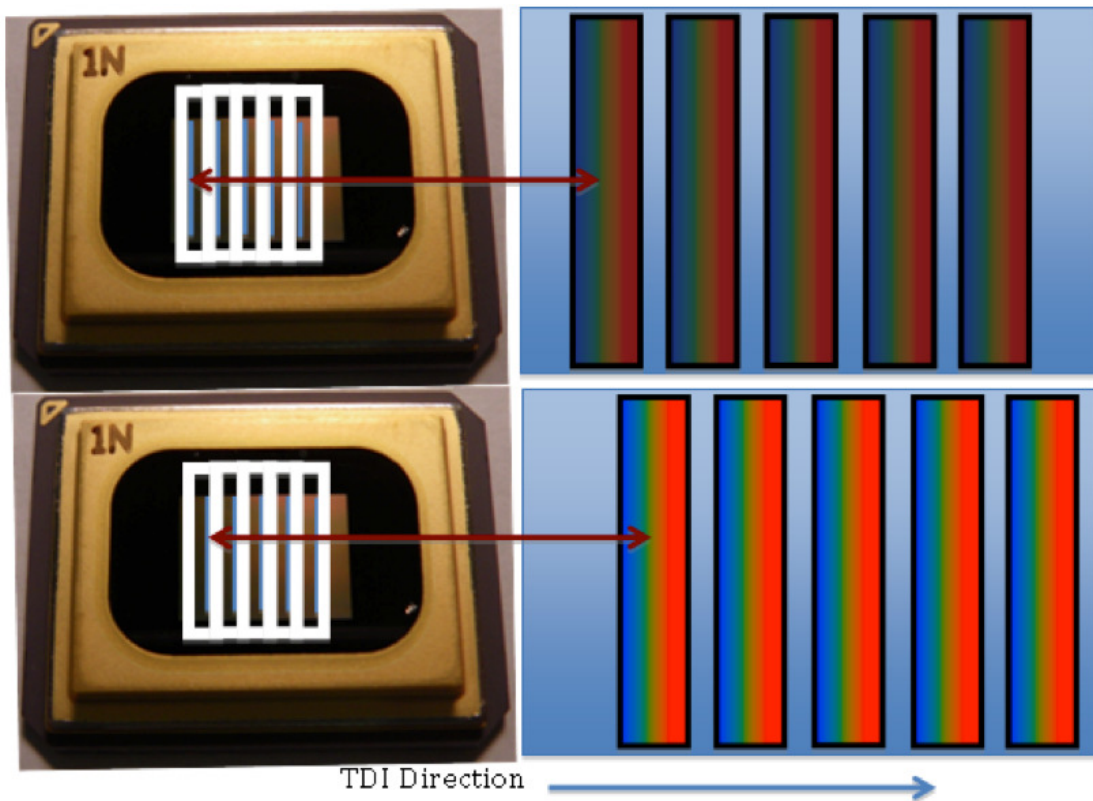
Figure E.2: For the illustration shown the DMD (left) is shown divided into 5 TDI Zones. The DMD is packed in a hermetic sealed package. The pictured DMD is a 0.7" diagonal XGA 1024 × 768 DMD. The top two portions of the figure represent the DMD slit mask. The 5 TDI zones are outlined on the DMD. The mirrors pointing towards the spectrometer are shown in blue on the DMD. On the right, the TDI CCD shifts the spectrum parallel to the dispersion direction to compensate for the motion of the mirrors at the appropriate rate. The bottom illustration shows that the mirrors have moved to the end of the TDI zone and the spectrum on the right CCD is now brighter because the CCD has integrated over the complete TDI zone. Next all of the mirrors are turned away from the spectrometer and the TDI CCD is read-out. In the cross-track direction, the spectrometer records a spectrum for each spatial location

TDI CCD will contain a spectrum for each pixel across the swath at each TDI zone. The linear dispersion of the spectrometer must be matched to the slit with and slit separation (both determined by the DMD) to prevent overlapping spectra. As the slits move on the DMD they spectrum moves on the TDI CCD.

E.1.3 Liquid Mirror Telescope

Liquid mirror telescopes such as Large Zenith Telescope (LZT) [115] are used for classifying galaxies and require specialized instrumentation. LZT is a large rotating mirror filled with liquid mercury. A perfect parabolic shape forms due to the inertial motion and the mercury's surface tension. The telescope is limited to a fixed vertical pointing, but is still very useful for large-scale galaxy surveys. TDI cameras are common on these types of telescopes. However, there is no available MOS configuration that can measure spectra on all stars in the telescopes FOV. The bright stars limit the classification of nearby galaxies, because the CCD will be saturated. The present spectrometer has the ability to reject light from these stars by turning the mirror away from the spectrometer as the star moves across the FOV. This would be easily implemented by

a lookup of star positions to block out stars before they are re-imaged on to the CCD. Previous Instruments Using DMDs

E.1.4 Spectrometer Configuration

There are two main methods for separating white light into its components: a grating or a dispersing prism. A grating is commonly employed in astronomical instruments where high dispersion is required to measure the spectral position of chemical absorption or emission lines of interest. Gratings diffract light into multiple diffraction orders and a spectrometer can generally only use the light from a single diffraction order. This is why gratings are blazed for a specific wavelength or order, to maximize the light in a particular direction. There has to be suitable order sorting filtering when using diffraction grating based spectrometers to eliminate multiple overlapping orders being imaged onto the CCD.

It is becoming common, in many spectrometer designs to use a dispersing prism. In the remote sensing application, it would be much simpler to use a prism because a much lower spectral resolution and higher-spectral coverage are acceptable to reach the scientific goals. A well-designed prism with proper AR (anti-reflective) can be designed to have very little light loss. A prism design would eliminate the problem of overlapping grating orders. Regardless of the approach selected, a low distortion optical design will be even more important than in a conventional spectrometer, because the charges are moved across large areas of the TDI CCD. If there are optical distortions, the TDI CCD would need to be clocked asymmetrically to correct for these distortions, but this drastically complicates the camera CCD clocking.

A color-separating prism similar to the ones used in $3 - CCD$ cameras could be used to break the light into red, green and blue to increase the spectral coverage and increase spectral resolution. Phillips style high throughput prisms have been developed for cinema projectors and 3-CCD camera systems. By placing a DMD at each color channel of the 3 channel focal plane, different grating pitch could be optimized for each narrower spectral channel. In a 3-channel device, each grating would have a different number of lines/mm and therefore each TDI CCD would have to be clocked at different rates. Having three DMDs allows a different slit size for each channel simultaneously.

The flexibility of FITSUMMA would change the way hyperspectral remote sensing is currently conducted, by enabling data collection in low-light or nighttime urban areas for remote sensing and planetary sciences. A highly reliable commercial built part is the key enabler for this new type of long dwell time imaging spectrometer. The instrument has a flexible dwell time, flexible hyperspectral resolution, and enables full spatial resolution both in the in-track and cross-track directions.

E.2 Radial Velocity Scanner

The first Radial Velocity Scanner (RVS) was developed by R. F. Griffin in 1967 [116]. Several radial velocity scanners followed, with the most utilized being CORAVEL [117]. The CORAVEL scanner worked by having a mask with transparent slots located at the stellar absorption lines placed at the focus of a spectrograph. The light passing through the slots was then focused onto a photo-multiplier tube and a measurement was obtained. The slots were then translated and this was repeated until the slots were positioned aligned to the absorption lines of the object of interest. At this point the light passing thought the slots is a minimum, and the Doppler shift can be found by measuring the translation of the slots. In a DMD based RVS, the

limit to the slot translation size would be the pitch of a single mirror. This has the advantage that only the position or radial velocity needs to be returned to the ground from the instrument. This is relevant to the Kepler Mission [118]. A similar mission could be proposed, to perform radial velocity measurements from space rather than just photometry. Kepler has been very successful at finding planets by using the transit technique. The Kepler mission finds objects by looking at the light curve as a function of time. When the planets passes in front of the star a dip is seen in the light curve, which is proportional to the area of the planet. This process only works when the planet transits a star along our line of sight to the star. When planetary bodies, orbit a star, this causes the star to wobble. Rather than trying to measure this wobble directly using astrometry, the radial velocity can be measured. One of the main advantages of a radial velocity type scanner is that it utilizes the principles of compressive sensing. Rather than collecting the complete spectrum, it collects the convolution of the spectrum over a range. Optimization could be done on the slit mask based on a reference spectrum of the star, and with this type of instrument the reference spectrum could be measured by scanning through each wavelength bin. The advantage of this instrument is that it could easily be done with a single HgCdTe detector elements. A complete spectrum is not required, because all of the light from the slots is focused onto the single detector element. Since the DMD is an array, a series of slot masks could be generated for multiple objects simultaneously. Using cylindrical optics this light could be then focused down to a linear array of HeCdTe detectors to create a Multi-Object Radial Velocity Scanner (MORVS).

APPENDIX F

MIGRO-GRID POLARIZER ARRAYS (MGPA)

Polarization is a fundamental property of electromagnetic radiation. Polarization enables additional information to be extracted from a scene. In astronomy, polarization is very useful for direct imaging of extra solar objects [119] [120]. In remote sensing applications, polarization can be used to look for man-made objects [121] in a forest such as metals, tarps or additionally to track vehicles [122]. The Earths sky dome light is polarized. Various animals and insects use this as a navigational aid [123]. There are several neutral points in this sky where the sky is unpolarized. The arago point is 20° above the anti-solar point [124]. The Babinet point 20° above the sun and the Brewster point which is 20° below the sun. The key piece of equipment to image these points has been a Savart polarimeter, which involves a piece of calcite [125]. A sophisticated electronic wide field of view instrument to replace this type of polarimeter has great utility in the field of polarimetry. A MGPA is a suitable candidate to replace this type of system.

Measuring polarization using a single image is a challenge. The conventional approach requires capturing several frames, while rotating a polarizing filter at the front of a camera system. The scene being imaged can change during sequential frames and polarization artifacts (e.g. a tree moving in the wind) are present when utilizing this approach. An alternative method is to divide the focal plane into regions with a wire-grid polarizer located above each detector pixel. A wire-grid polarizer is a series of metal lines fabricated on a transparent substrate. The structure and size of the lines determine the optical performance of the polarizer. The pitch relative to the wavelength of light determines the ratio of Transverse Electric (TE) versus Transverse Magnetic (TM) light transmitted. In a MGPA, each individual polarizer has many wire-grid lines.

The MGPA under test here at RIT is a commercial device obtained from Moxtek Incorporated [126]. Figure F.1 shows a schematic of the MGPA to be tested. These devices have aluminum lines deposited on a glass substrate. The MGPA has 7.4 μm pitch between adjacent polarizers. The four polarization orientations on the MGPA are vertical (V), 45° ($D2$) and 135° as shown in Figure F.2. These four orientations comprise a super-pixel. A super-pixel contains all of the information required to calculate the linear stokes parameters (S_0, S_1, and S_2). It is not possible to calculate circular polarization (S_3) with this configuration. Rather than utilizing the device directly on top of a CCD, it is possible to re-image the polarizer filter onto the CCD. A laboratory apparatus was assembled to measure the pixel cross talk and MGPA efficiency using
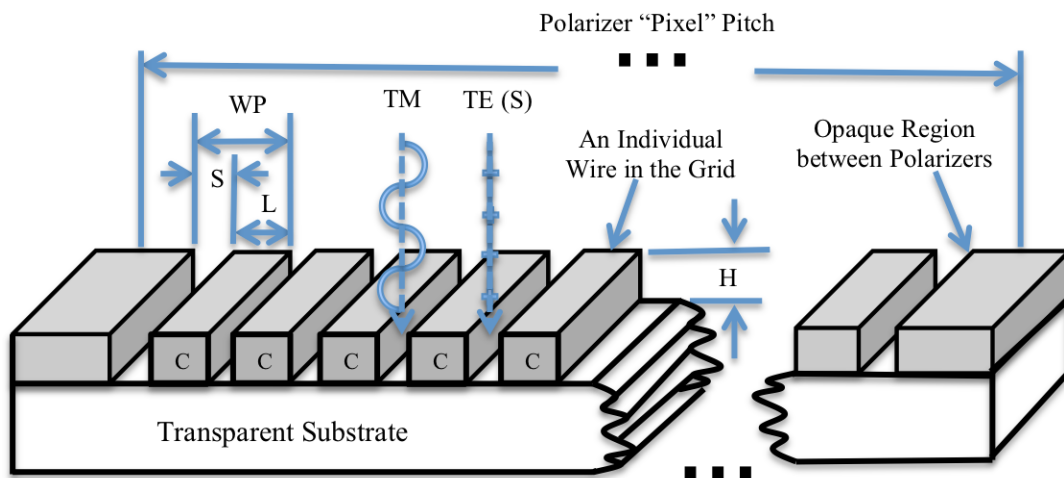
Figure F.1: Wire-grid polarizer is composed of metal lines or conductors (C) fabricated on a transparent substrate. H is the height of the metal lines. *S* is the width of the space, *L* is the line width, and WP is the repeating wire pitch. All of these parameters determine the optical performance of the polarizer. Note there is a break in the illustration (many lines are not shown).

this reimaging technique. By reimaging a MGPA, it is possible to change the optical magnification to match the detector pixel pitch to the MGPA or oversample the MGPA as needed.

F.1   Optical Performance

There is interest in aligning a MGPA directly to a detector, but several key optical parameters must be determined before this alignment is done. A laboratory experiment was designed to characterize the individual MGPA pixels without convolving detector level effects. Figure F.3 shows the optical setup. A white light source illuminates a wavelength selection filter. A Melles Griot Glan-Thompson Prism (part #03PTO005) polarizer was placed in the beam. This prism was uncoated, laser grade glass with an extinction ratio of 5×10^{-6} transverse electric (TE) to (TM) polarization. The stop was placed before this prism, so that it would have a circularly symmetric field of view, and to also prevent light from overfilling the prism. After the prism, the light is approximately linearly polarized. A Mitutoyo 5× infinity corrected microscope objective was used to image the MGPA onto a detector. The total system magnification was 12×. This gave us information about the MGPA without convolving the information with the sub-pixel response of the CCD. Alignment was not critical in this experiment due to sufficient oversampling of the MGPA. The analyzer polarizer was also used without the MGPA to determine the instrument polarization. For the second part of the experiment an additional 100mm Gradium (gradient index) $f/2.8$ lens was placed in front of the MGPA to re-image a laser spot onto the MGPA.

   The MGPA pixels were oversampled by re-imaging them with a long working distance microscope objective. The sampling was 12×12 detector pixels for each MGPA polarizer. The analyzer was set to 0° at the start of the experiment. A science image was captured and the analyzer was rotated 5°. Then a second science image frame was taken. This process was completed for 36 steps with increments of 5° increments. All 36 frames were averaged together to determine the MGPA locations on the detector as described in Figure F.4. The edges of the MGPA pixels were found by looking at the mean of the pixels across all CCD
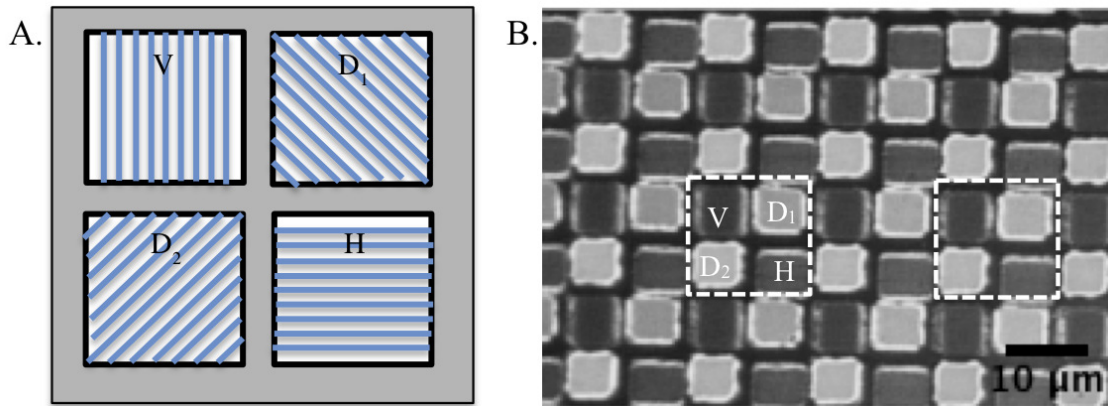
Figure F.2: A. super-pixel illustration shows the four micro-grid polarizer orientations (Vertical (V), Diagonal (D_1 and D_2) and horizontal (H)). The region between the individual pixels is opaque. B. The MGPA is shown illuminated with polarized light under an optical microscope (in reflection mode). The individual polarizer pixels appear bright or dark because of the difference in the polarization of the illumining beam and the polarizer orientation. Regions between the pixels are opaque to minimize the pixel-to-pixel cross talk. Note the difference in the gap spacing between pixels. Two super pixels are highlighted and labeled accordingly using the dashed boxes.
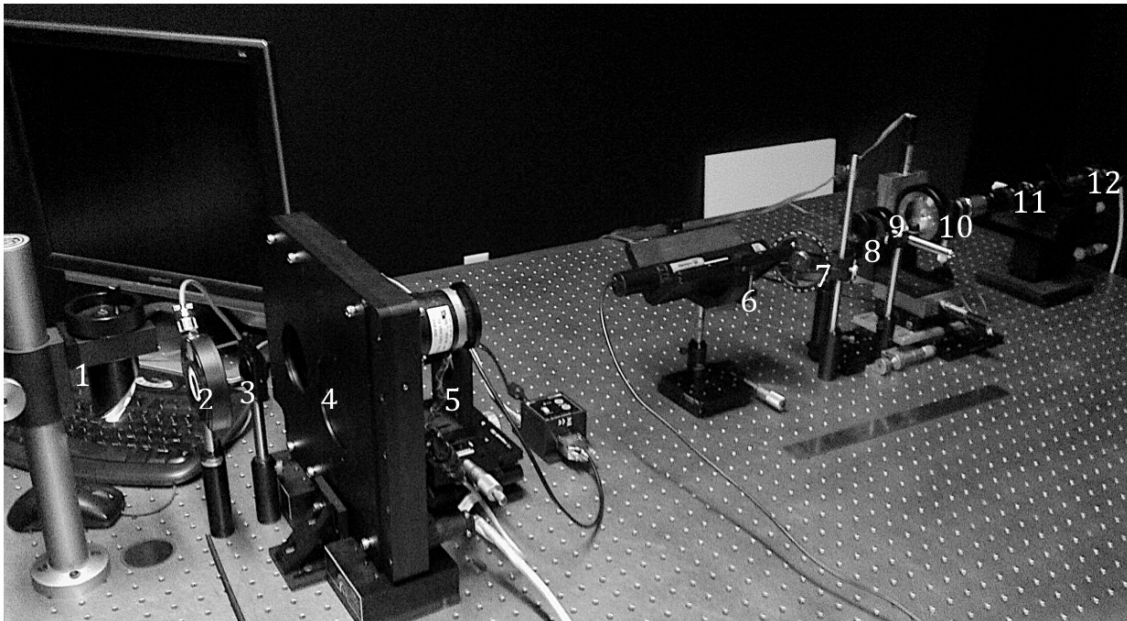

Figure F.3: Apparatus for characterizing the MGPA is shown here. A collimated tungsten filament light source is below the table (not shown). A fold mirror below the table directs the light to the upper table surface. (1) A second fold mirror is used to direct the light horizontal to the table. (2) A shutter is positioned here to block the light for acquisition of dark frames. (The CCD has an electronic shutter, so a physical shutter is required to acquire dark frames). (3) A stop is added here. (4) A filter wheel houses a Bessel filter set (B,V,R, and I) [69]. (5). A Glan-Thompson Prism with a 1" aperture is placed here. (6) A HeNe Laser is placed in the path as a polarization target. (7) A neutral density filter is added to the beam path to attenuate the laser. (8) A stop is added here so that the $f/\#$ of the imaging lens can be changed. (9) An imaging lens is placed here to image the laser spot onto the MGPA. (10) The MGPA is placed in a filter holder and stage. (11) A microscope is used to reimage the MGPA onto the CCD (12). Note the laser (6) and neutral density filter (7) are not present in the system for the calibration procedure or analysis of the MGPA.
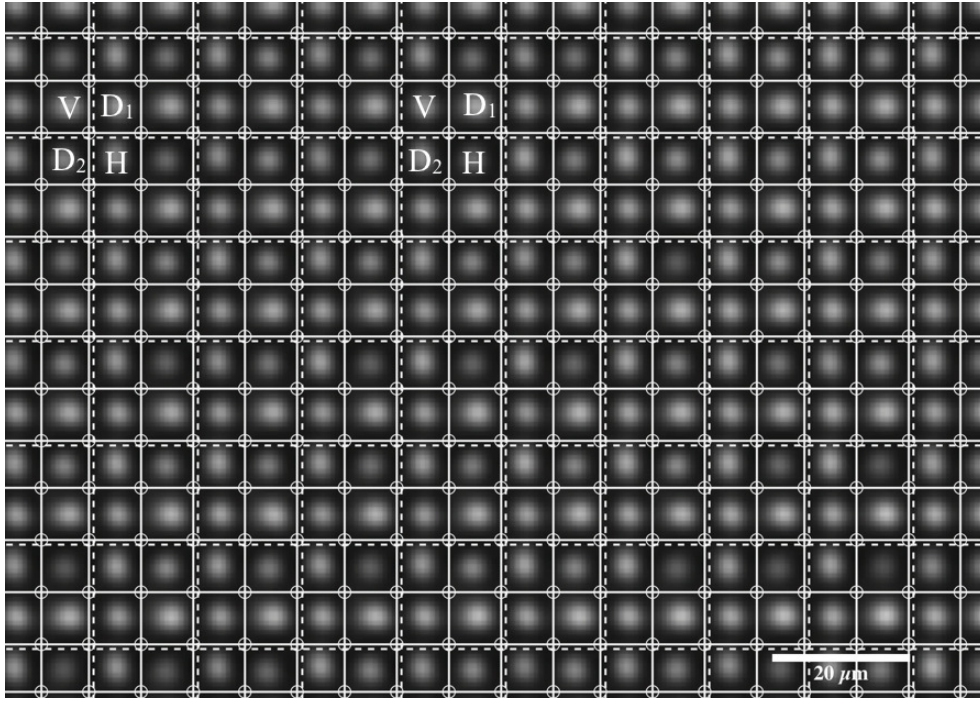
Figure F.4: This is an image of the over sampled MGPA illuminated by the tungsten filament source. By locating the minimum values along the image rows and columns, the MGPA corners (shown as circles) were found. The solid white lines indicate the borders of individual polarizers. These polarizers were then separated into super pixels (shown with the offset dotted line). The letters on top of the super pixels designate the polarizer orientation.

rows and columns (for this to work properly the rotational alignment of the CCD to MGPA had to be very precise). All of the values within the corners of the pixel were summed to get a throughput for the individual MGPA pixel. The pixels were then sorted into the four polarizer orientations. The results (Figure F.5) for all of the same polarizers in the frame were averaged together to obtain an accurate representation of all the polarizer pixels in the array. Each science image was divided by a flat-field image to remove detector pixel-to-pixel sensitivity variations. The flat image was acquired with the MGPA removed from the optical apparatus so the source illuminating the detector directly. The V pixel with maximum at $0°$ had the greatest modulation of the four pixel orientations. Modulation in the following results is defined as the maximum throughput minus the minimum throughput. The D_1 pixel had the lowest modulation. The difference in modulation between V and D_1 was almost 50%

The stokes parameters were calculated using Equations F.1, F.2, F.3. These measurements enabled the calculation of DOLP (Equation F.4) and AOP (equation F.5).

$$S_0 = \frac{F_V + F_{D1} + F_{D2} + F_H}{2} \tag{F.1}$$

$$S_1 = \frac{F_V - F_H}{2} \tag{F.2}$$
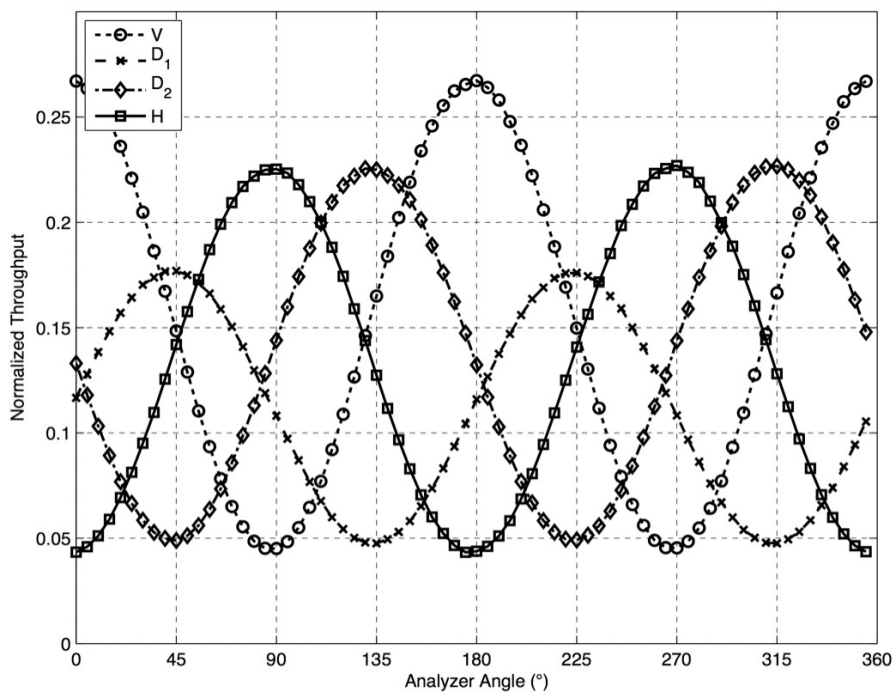
Figure F.5: The rotation of an analyzer illustrates the differences in modulation for the four polarizer orientations.

$$S_2 = \frac{F_{D1} - F_{D2}}{2} \tag{F.3}$$

$$DOLP = \frac{\sqrt{S_1^2 - S_2^2}}{S_0} \tag{F.4}$$

$$AOP = \frac{tan^{-1}\left(\frac{S_1}{S2}\right)}{S_0} \tag{F.5}$$

F.2 Illumination $f/\#$ and Modulation

An optical experiment was run that varied the illumination $f/\#$ illuminating the MGPA. A aperture stop was used to control the cone angle illuminating the MGPA. Figure F.6 shows the results of this experiment for each of the four polarizer orientations on the MGPA. The faster (lower $f/\#$) resulted in lower polarizer modulation. As the imaging lens was stopped down, the modulation increased.

Figure F.6: Modulation was plotted for various illumination $f/\#$.

F.2.1 Surface Height Differences in MGPA's

While setting up the optical experiment it was apparent that the individual polarizers appeared to be focused at different axial positions. Upon investigating the device structur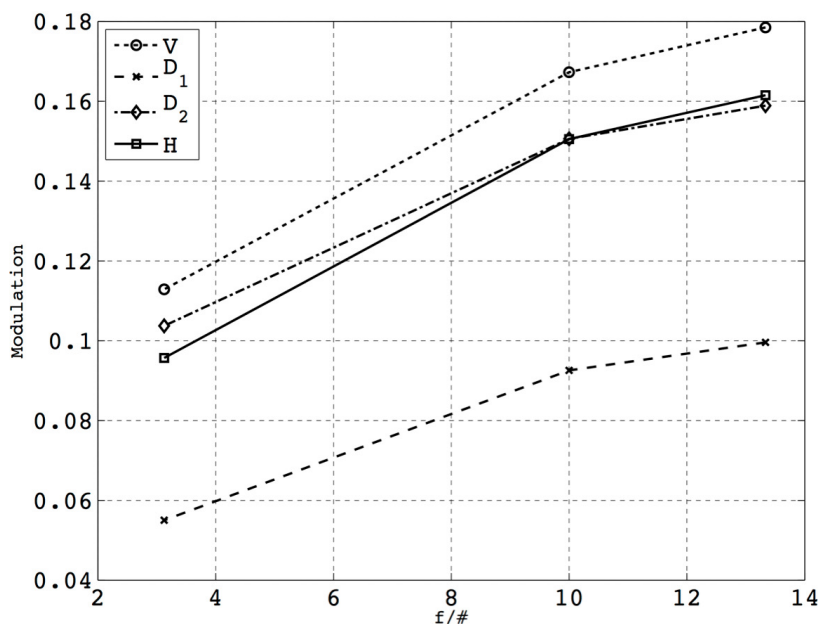e further, it was determined that each polarizer pixel was fabricated with a separate lithography patterning process. When using this device in a reimaging mode at high magnification, these defocus errors were examined for all 4 polarizer orientations (V, D_1, D_2, and H). Two methods were used to perform this characterization: interferometry measurements (Figure F.7) and an optical scan (Figure F.8).

Table F.1: SEM Measurement Values

Pixel	AREA (μm^2)	Line Width (μm)	Space Width (μm)	Pitch (μm)	$f/13$ modulation
V	40.5	0.104	0.040	0.144	0.18
D1	25.4	0.111	0.026	0.137	0.10
D2	26.1	0.098	0.037	0.141	0.16
H	31.3	0.112	0.029	0.141	0.16

To determine the magnitude of the defocus effect, an optical experiment was conducted. The same experiment ($5°$ incremental rotations from $0° - 360°$) was run, but it was repeated as the MGPA was translated along the optical axis. The modulation was plotted for each polarizer orientation at each focal position. Figure F.8 shows the plane of best focus for each polarizer orientation. This small defocus may manifest itself as a near field effect when the device is aligned and mounted to a detector.

F.3 FE SEM Characterization of MGPA

A Zeiss model 40VP (Variable Pressure) Field Emission Scanning Electron Microscope (FESEM) was used to examine the individual polarizer pixels. Figure F.9 (A) shows the four different MGPA pixels. The differences in pixel area are immediately apparent in these high-resolution images. Two super-pixels are
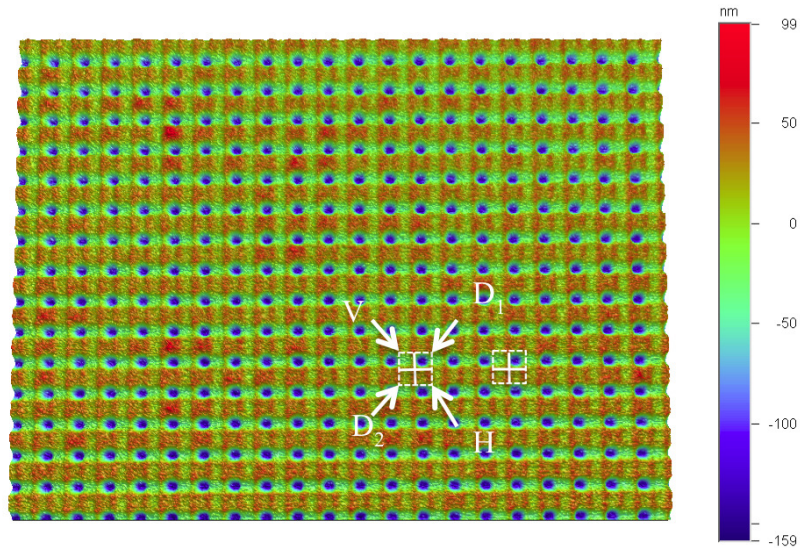
Figure F.7: A Wyko interferometer shows the surface topology on the MGPA. The color indicates the surface height relative to an arbitrary mean level. Two adjacent super pixels are shown above.
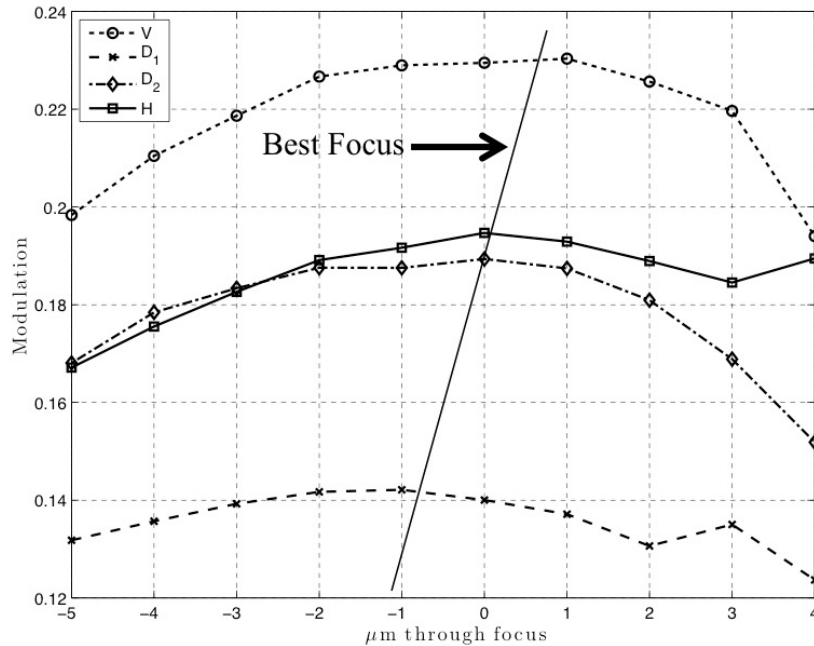
Figure F.8: When the device is being re-imaged onto a CCD, only one set of polarizers were at their optimum focus. This decreases the modulation of the out-of-focus polarizers. The MGPA was scanned axially through focus to examine the change in modulation. As the MGPA moves out of focus additional cross-polarized light enters adjacent detector pixels. These measurements were completed with a Bessel R filter at $f/13.5$. These results correlate well with the interferometry measurements. The V pixel is slightly higher and than the D_1 pixel, which is the lowest in the surface height interferometry image.

Figure F.9: (A) Four different polarizer orientations are shown in the upper left FESEM image. There multiple defects in the each polarizer. *V* has the largest area, but has several pull out defects. D_1 die has the smallest area and is shifted up and to the right. D_2 has the next largest area, but also there is a rim around where the aluminum lines have not cleared completely. Horizontal lines appear well formed, but the regions at the top and bottom are not completely cleared and therefore this reduces the effective polarizer throughput. Area differences can also be seen in 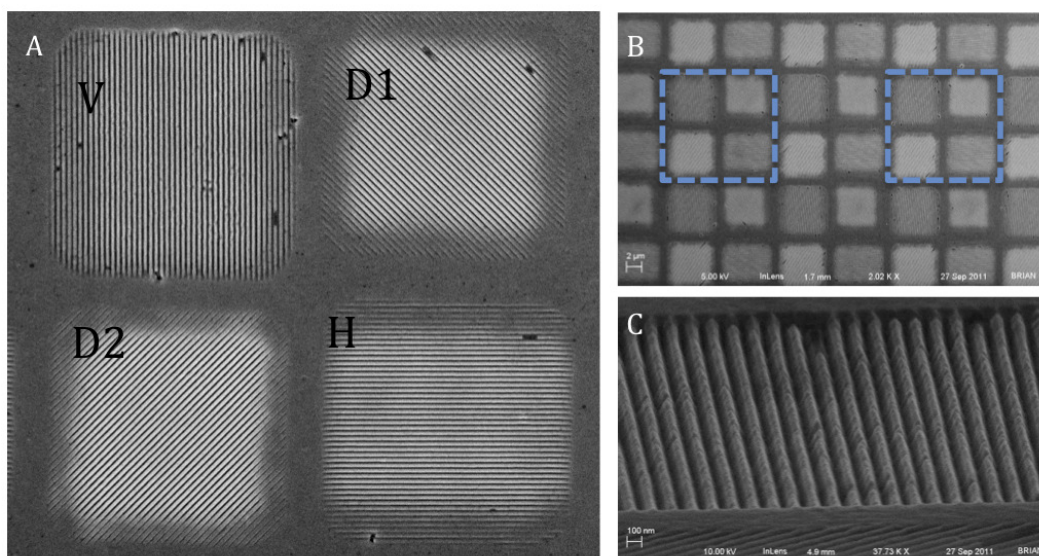the optical microscope image shown in Figure F.2. (B) Dotted lines illustrate the size of a super-pixel. (C) Shows the profile of the aluminum lines.

outlined in Figure F.9 (B). The metal lines are also "house shaped" with a triangular top structure as seen in the edge-on image as shown in Figure F.9 (C). Table F.1 shows the estimated areas for each pixel orientation. The modulation values are shown in the last column of Table F.1 to confirm that the largest area pixel (V) also had the highest modulation. Conversely D1 had the lowest modulation and smallest area.

F.4   Calibration and Demonstration

A laser spot was imaged onto the MGPA. To account for differences in area of the individual polarizers, a correction factor was applied to the signal obtained for each super-pixel. The modulation from each pixel in the previous experiment was used to provide the correction factor for each super-pixel in the image. In addition, the detector has a finite well depth and the larger area polarizers caused the detector to reach saturation before the smaller polarizer pixels. This effectively reduces usable dynamic range of the camera system, but still allows for DOLP and AOP to be correctly calculated for an image after calibration. A laser source was placed in the optical setup and re-imaged onto the detector. Since the polarizer locations on the CCD pixels were measured the previous experiment, a polarization image could be generated for the data at hand (Figure F.10).
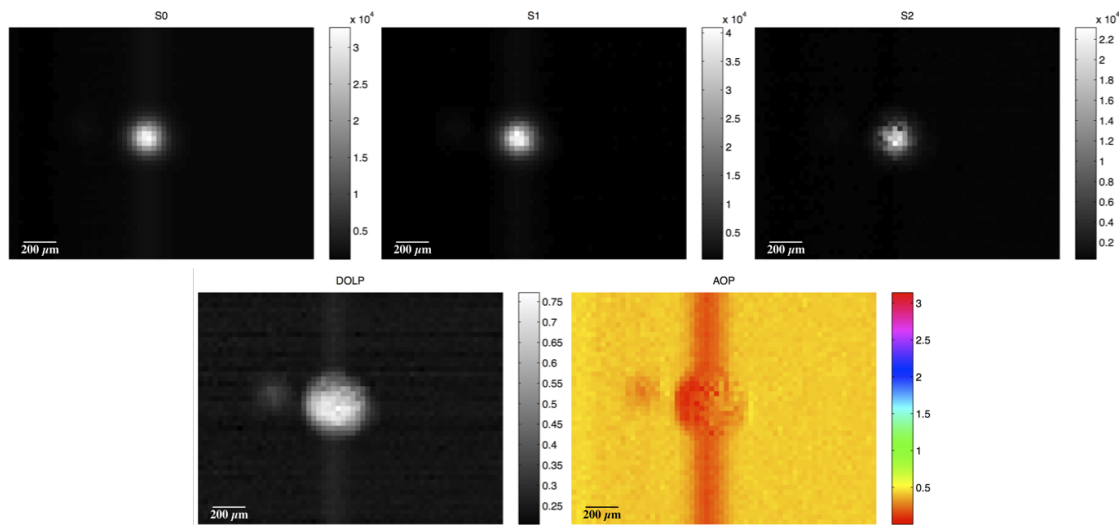
Figure F.10: The laser was imaged onto the detector. The Top 3 plots show S_0 (the intensity image), S_1 and S_2. The bottom two plots show the calculated degree of linear polarization (DOLP) and angle of polarization (AOP). In the DOLP plot a secondary reflection spot is present which cannot be seen in the normal intensity image. The vertical line is an artifact of the CCD smear.

F.5 Simulation Results (Alignment Sensitivity)

The next step in building a compact portable imaging polarimeter is to directly bond the MGPA to the detector array rather than using a much more cumbersome re-imaging system. A simulation was run in preparation for aligning this MGPA directly to a detector. Photon Engineering's FRED, a non-sequential optical ray-tracing package, was used to simulate a MGPA filter. FRED an non-sequential optical ray tracing package was used to trace rays through a MGPA aperture. A series of shifts in X and Y were done in X and Y to determine how accurately the MGPA must be aligned to the detector pixel elements. The irradiance is measured in each pixel. Light that doesn't make it through was considered a loss in throughput; however light that enters an adjacent pixel is cross talk or cross polarized light. Figure F.11 shows the geometry of the MGPA constructed for the simulation. An $f/\#$ of 13.5 was simulated because the telescope for this instrument operates at $f/13.5$. Micro-lenses were placed above the detector. Figure F.12 shows the results of the simulations. The ratio of polarized light to cross-polarized light was taken, and this is analogous to a signal to noise ratio. It is seen that the MGPA must be very close to the array $< 10\,\mu m$ and have an overlay alignment error of less than $0.5\,\mu m$ in both X and Y in order to minimize cross polarized light at $f/13.5$.

F.6 Alignment

A method to perform the alignment of a MGPA to a CCD was developed without the requirement of alignment marks. A camera is placed in proximity to the array. The array is illuminated with polarized light. The array is illuminated and the MGPA is stepped around in X and Y until a maximum in throughput is found. A FFT is computed for each image. The image, which has the highest peak at the Nyquist frequency in both directions is the optimum alignment location. However MGPA rotation must be accounted for. To achieve this goal, a high precision rotation stage is required. Images are taken at multiple rotation points.
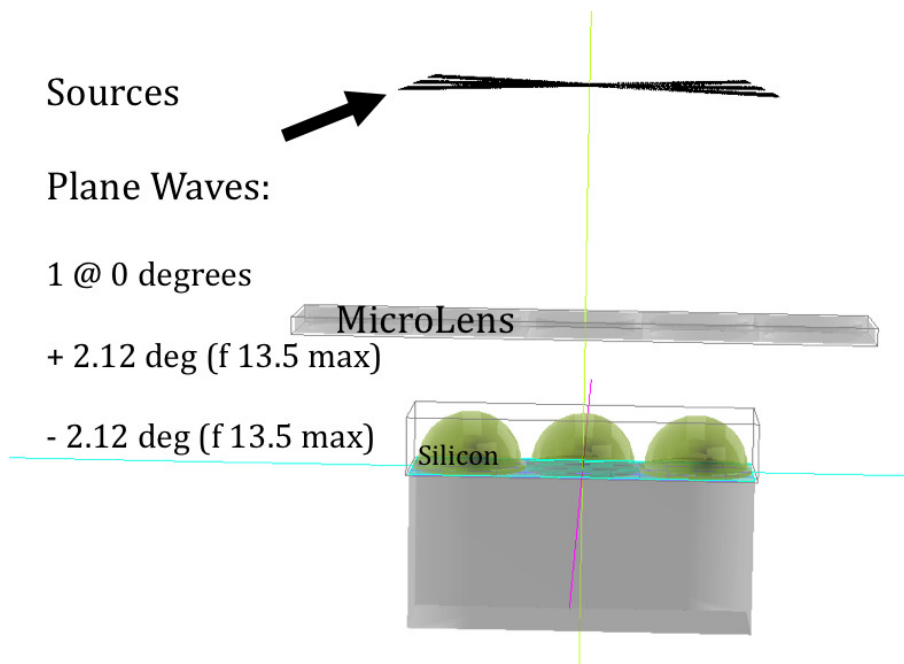
Figure F.11: The simulation the simulation layout is shown here. Polarizer array acts as apertures. As the polarizer array is shifted in *X* and *Y*, a ray trace is performed to measure the light falling in the center pixel and the adjacent pixels.
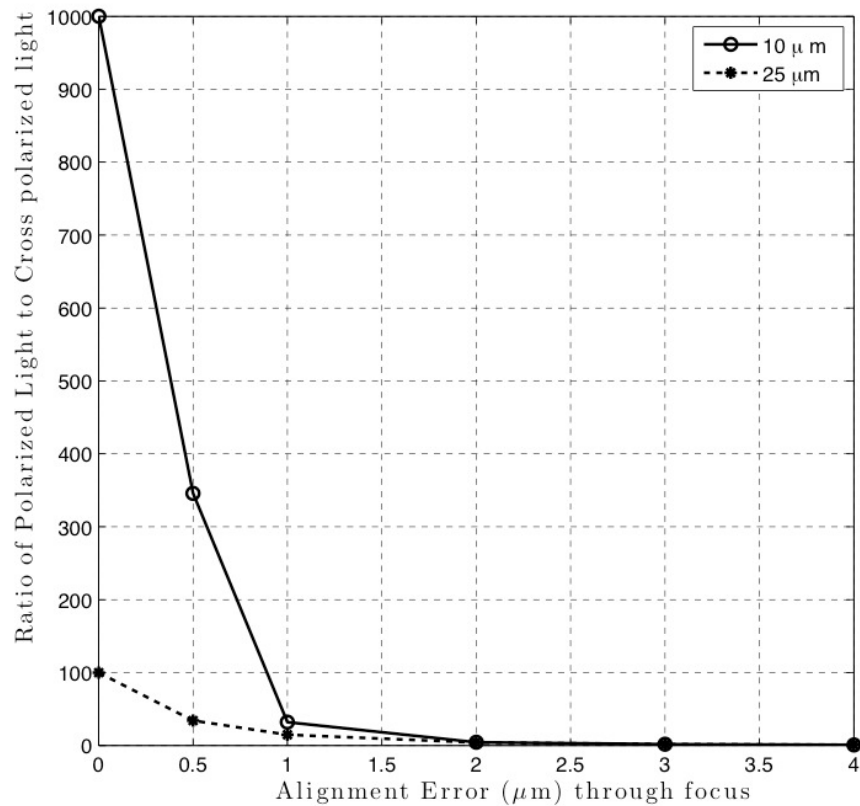
Figure F.12: The plot above shows the alignment error as a function of MGPA array height above the detector. The dashed curve shows when the MGPA array is 25 µm above the detector and the solid line shows when the MGPA is 10 µm above the detector. As the alignment error decreases, the cross talk decreases. Alignment than 0.5 µm or better must be obtained at 10 µm above the device to create a useful polarimeter. A $f/13.5$ 600 nm source was used for this simulation.

A radon transform is performed at each image. The slice from the radon transform is examined and when a maximum value is obtained the device is at its optimum alignment. After a series of iterations of aligning the shifts and rotations a convergence will be met. A trivial way to perform this alignment would be to add alignment marks (box in box structures used for semiconductor lithography overlay)

A potentially simpler way to do the crosstalk and leakage measurements would be to take two MGPA's and align a micro-grid polarizer to itself, shifted by 1 pixel in the X direction and 1 pixel in the y direction. The two wire-grids would have to be placed in proximity; aluminum lines to aluminum lines. This would require flipping the sample and rotating it $90°$, so that the V and H pixels could overlap. This would enable a simple way to obtain a measurement of the bulk leakage, because the V and H polarizers would be aligned.

F.6.1 Alternative configuration

An alternative MGPA pixel orientated is shown in Figure F.13. One of the largest issues with the current MGPA relate to unequal polarizer areas.
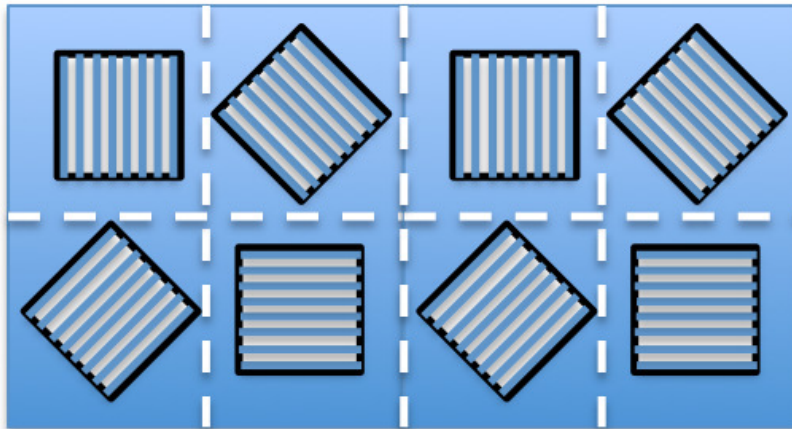
Figure F.13: An alternative configuration of the micro-grid polarizer. Two super-pixels are shown above. When this type of micro-grid polarizer pattern is placed above a CCD it would have the benefit of each polarizer being the same area. This assumes that the CCD sub-pixel response of is spatially uniform.

F.7 Conclusion

A division of focal plane (DoFP) micro grid polarizer array (MGPA) has been characterized. The MGPA under test is a commercial device available from Moxtek Inc. These wire grid style polarizers use aluminum lines fabricated on a glass substrate and have opaque regions surrounding individual pixels. The approach to testing the MGPA was to reimage them onto a detector by placing the MGPA at an intermediate focal plane. For the purposes of characterizing the MGPA, a high magnification reimaging optical system was assembled. The oversampled MGPA pixels were examined by using an adjustable analyzing polarizer. The effects of pixel throughput and cross talk are examined as a function of both wavelength and illumination $f/\#$. A calibration procedure has been determined for the use of such devices. The MGPA array was also examined using a scanning electron microscope (SEM). From these SEM measurements, the pitch, fill

factor, and aluminum thickness were measured. In preparation for attaching the MGPA directly to a CCD, an alignment tolerance analysis was completed. The results indicate that 0.5 µm alignment of MGPA pixel center to image sensor is required to get a system with significantly low crosstalk for useful polarization imaging.

F.8   Polarization Sensitive MOS (PSMOS)

With the work presented thus far it would be conceivable to build a MOS capable of collecting polarization and spectral information simultaneously. To this end, the question becomes how can one build a system that can perform this task. Previous papers spoke about having 3 polarizer pixels and one micro-mirror super-structure per super-pixel. This special micromirror pixel would actually be a Fabri-Perrot interferometer. This idea is only appropriate if the funds exist to build a MEMS imager from scratch, however a more feasible approach is to have a modular instrument with a spectral channel and a polarization channel. The main concern with this type of instrument is to design all of the coatings on the optics to reflect/transmit TE/TM polarization. There are several instrument designs, which could exist. The simplest would be to place a MGPA on the spectrometer's detector. The pattern of MGPA pixels may be different than the 2×2 super pixel design utilized in the Moxtek device. For this configuration to work, a 1×3 or 1×4 design would be preferable. In this case the length of the spectrum defines the polarizer size. This way each detector pixel along the dispersion direction would have the same polarization. As long as the slit was tall enough to cover the super pixel region, the spectrometer can detect different polarizations. Future work will investigate advanced instrument concepts.

BIBLIOGRAPHY

[1] Neil Gehrels. "The Joint Dark Energy Mission (JDEM) Omega." In: *Arxiv preprint arXiv:1008.4936* (Aug. 2010). arXiv:1008.4936.

[2] D.C. Martin et al. "The Galaxy Evolution Explorer: A Space Ultraviolet Survey Mission." In: *Arxiv preprint astro-ph/0411302* (2004).

[3] H.J. Seo and D.J. Eisenstein. "Probing dark energy with baryonic acoustic oscillations from future large galaxy redshift surveys." In: *The Astrophysical Journal* 598 (2003), p. 720.

[4] Committee for a Decadal Survey of Astronomy. *New Worlds, New Horizons in Astronomy and Astrophysics*. Natl Academy Pr, 2011.

[5] J.C. Mankins. "Technology readiness levels." In: *White Paper, April* 6 (1995).

[6] A.S. Kutyrev et al. "Programmable microshutter arrays for the JWST NIRSpec: optical performance." In: *Selected Topics in Quantum Electronics, IEEE Journal of* 10.3 (2004), pp. 652–661.

[7] James Green et al. "Wide-Field InfraRed Survey Telescope (WFIRST) Interim Report." In: *Arxiv preprint arXiv:* (Aug. 2011), p. 71. arXiv:1108.1374. URL: http://arxiv.org/abs/1108.1374.

[8] S.C. Barden and Taft Armandroff. "Performance of the WIYN fiber-fed MOS system: Hydra." In: *Proceedings of SPIE*. Vol. 2476. 1995, p. 56. URL: http://link.aip.org/link/?PSISDG/2476/56/1.

[9] Roger L. Davies et al. "GMOS: the GEMINI Multiple Object Spectrographs." In: ed. by Arne L. Ardeberg. Vol. 2871. 1. Landskrona/Hven, Sweden: SPIE, 1997, pp. 1099–1106. DOI: 10.1117/12.268996. URL: http://link.aip.org/link/?PSI/2871/1099/1.

[10] Reed D. Meyer. "RITMOS: a micromirror-based multi-object spectrometer." In: *Proceedings of SPIE* 5492 (2004), pp. 200–219. ISSN: 0277786X. DOI: 10.1117/12.549897. URL: http://link.aip.org/link/?PSI/5492/200/1\&Agg=doi.

[11] John W. MacKenty. "IRMOS: an infrared multi-object spectrometer using a MEMS micro-mirror array." In: *Proceedings of SPIE* 4841.2 (2003), pp. 953–961. ISSN: 0277786X. DOI: 10.1117/12.461484. URL: http://link.aip.org/link/?PSI/4841/953/1\&Agg=doi.

[12] JW MacKenty and M. Stiavelli. "A multi-object spectrometer using micro mirror arrays." In: *Imaging the Universe in Three Dimensions*. Vol. 195. 2000, p. 443.

[13] EJ Garcia et al. "Surface Micromachined Micromirror Arrays for the Next Generation Space Telescope." In: *Bulletin of the American Astronomical Society*. Vol. 31. 1999, p. 984.

[14] J. Gal-Edd and CC Fatig. "L2-James Webb Space Telescope operationally friendly environment?" In: *Aerospace Conference, 2004. Proceedings. 2004 IEEE*. Vol. 1. IEEE. 2004.

[15] F. Zamkotsian et al. "Space evaluation of 2048× 1080 mirrors DMD chip for ESA's EUCLID Mission." In: *Proceedings of SPIE*. Vol. 7731. 2010, p. 773130.

[16] JP Beaulieu et al. "EUCLID: Dark Universe Probe and Microlensing planet Hunter." In: *Arxiv preprint arXiv:1001.3349* (2010).

[17] *Archimedes and the burning mirrors*. URL: http://www.daviddarling.info/encyclopedia/A/Archimedes_and_the_burning_mirrors.html.

[18] Eugene Hecht. *Optics 4th Edition*. 4th ed. Addison Wesley, 2001. ISBN: 0805385665.

[19] Gordon E. Moore. "Cramming more components onto integrated circuits, Reprinted from Electronics, volume 38, number 8, April 19, 1965, pp.114 ff." In: *IEEE Solid-State Circuits Newsletter* 20.3 (Sept. 1965), pp. 33–35. ISSN: 1098-4232. DOI: 10.1109/N-SSC.2006.4785860. URL: http://ieeexplore.ieee.org/lpdocs/epic03/wrapper.htm?arnumber=4785860.

[20] David Armitage. *Introduction to Microdisplays*. New York: Wiley, 2006. ISBN: 9780470852811.

[21] T. Hudson et al. "Real time optical correlator architectures using a deformable mirror spatial light modulator." In: *Applied Optics* 28.22 (1989), pp. 4853–4860.

[22] R. Davies and M. Kasper. "Adaptive optics in astronomy." In: *Annual Review of Astronomy and Astrophysics* 50 (2012), pp. 1–47. arXiv:arXiv:1201.5741v1. URL: http://books.google.com/books?hl=en\&lr=\&id=4n5tBN21LRsC\&oi=fnd\&pg=PP1\&dq=Adaptive+Optics+for+Astronomy\&ots=7FV8ETZB4A\&sig=iq9aCWghHxdCJzypB5UepdPDxmghttp://books.google.com/books?hl=en\&lr=\&id=4n5tBN21LRsC\&oi=fnd\&pg=PP1\&dq=Adaptive+optics+in+astronomy\&ots=7FV8ETZB6y\&sig=7vbb9_SeCU8Scg8_sshU7vfsw5A.

[23] D. Dudley, W. Duncan, and J. Slaughter. "Emerging digital micromirror device (DMD) applications." In: *Proc. SPIE*. Vol. 4985. 2003, pp. 14–25.

[24] L.J. Hornbeck. "Current status of the digital micromirror device (DMD) for projection television applications." In: *Electron Devices Meeting, 1993. IEDM'93. Technical Digest., International*. IEEE. 1993, pp. 381–384.

[25] L.J. Hornbeck. "Digital light processingTM for high-brightness, high-resolution applications." In: *Proc. SPIE*. Vol. 3013. 1997, pp. 27–40.

[26] C.J. Van Den Branden Lambrecht. "A working spatio-temporal model of the human visual system for image restoration and quality assessment applications." In: *Acoustics, Speech, and Signal Processing, 1996. ICASSP-96. Conference Proceedings., 1996 IEEE International Conference on*. Vol. 4. Ieee. 1996, pp. 2291–2294.

[27] R.L. Heckaman and M.D. Fairchild. "Effect of DLP projector white channel on perceptual gamut." In: *Journal of the SID* 14.9 (2006), pp. 755–761.

[28] G. Pettitt and B. Walker. "DLP Cinema Color Management." In: *SMPTE Conferences* 2002.5 (2002), pp. 1–11.

[29] S. Nascimento and O. Masuda. "Psychophysical optimization of lighting spectra for naturalness, preference, and chromatic diversity." In: *JOSA A* 29.2 (2012), A144–A152.

[30] MR Douglass. "DMD reliability: a MEMS success story." In: *Proceedings of SPIE* 4980 (2003). URL: http://www.engineering.ucsb.edu/~sumita/courses/Courses/ME141B/DMD_reliability.pdf.

[31] A. Sullivan. "58. 3: A Solid-state Multi-planar Volumetric Display." In: *SID Symposium Digest of Technical Papers*. Vol. 34. 1. 2003, p. 1531.

[32] Jeffrey B. Sampsell. "An Overview of the Performance Envelope of Digital Micromirror Device (DMD) Based Projection Display Systems." In: *Society for Information Display International Symposium* (1994), pp. 669–672.

[33] L.J. Hornbeck. *Multi-level deformable mirror device*. US Patent 5,083,857. 1992.

[34] L.J. Hornbeck. *Active yoke hidden hinge digital micromirror device*. US Patent 5,535,047. 1996.

[35] N.B. MacKinnon, C.E. MacAulay, and U. Stange. *Apparatus and methods relating to wavelength conditioning of illumination*. US Patent 6,781,691. 2004.

[36] *DLP Cinema Delievers Enhanced 4k Chip to Light up the Biggest Screens*. 2010. URL: http://www.dlp.com/technology/dlp-press-releases/press-release.aspx?id=1396.

[37] L.J. Hornbeck. "Projection displays and MEMS: timely convergence for a bright future." In: *Proceedings of SPIE*. Vol. 2639. SPIE. 1995, p. 2.

[38] D. Brett Beasley. "Dynamic IR scene projector based upon the digital micromirror device." In: *Proceedings of SPIE* (2001), pp. 96–102. ISSN: 0277786X. DOI: 10.1117/12.438061. URL: http://link.aip.org/link/?PSI/4366/96/1\&Agg=doi.

[39] M.F. Duarte et al. "Single-Pixel Imaging via Compressive Sampling." In: *IEEE Signal Processing Magazine* 25.2 (Mar. 2008), pp. 83–91. ISSN: 1053-5888. DOI: 10.1109/MSP.2007.914730. URL: http://ieeexplore.ieee.org/lpdocs/epic03/wrapper.htm?arnumber=4472247.

[40] Dana Dudley. "Emerging digital micromirror device (DMD) applications." In: *Proceedings of SPIE* 4985.Dmd (2003), pp. 14–25. ISSN: 0277786X. DOI: 10.1117/12.480761. URL: http://link.aip.org/link/?PSI/4985/14/1\&Agg=doi.

[41] Nabeel A. Riza and Sarun Sumriddetchkajorn. "Fault-Tolerant Dense Multiwavelength Add-Drop Filter With a Two-Dimensional Digital Micromirror Device." In: *Appl. Opt.* 37.27 (1998), pp. 6355–6361. URL: http://ao.osa.org/abstract.cfm?URI=ao-37-27-6355.

[42] T.M. Spudich et al. "Potential for Using a Digital Micromirror Device as a Signal Multiplexer in Visible Spectroscopy." In: *Applied Spectroscopy* 57.7 (2003), pp. 733–736.

[43] Aaron T. Ohta, Pei Yu Chiou, and Ming C. Wu. "Dynamic DMD-driven optoelectronics tweezers for microscopic particle manipulation." In: *Conference on Lasers and Electro-Optics/International Quantum Electronics Conference and Photonic Applications Systems Technologies*. Optical Society of America, 2004, CWS5. URL: http://www.opticsinfobase.org/abstract.cfm?URI=URI=CLEO-2004-CWS5.

[44] S. Lee et al. "2-Dimensional Optical Trap and Lattices Generated by DMD–ALP." In: *Frontiers in Optics* ().

[45] Chuan-Cheng Hung et al. "Confocal microscopy scanned by digital micromirror device with stray light filters." In: *Proceedings of SPIE* 6884.2008 (2008), 68840T–68840T–11. ISSN: 0277786X. DOI: 10. 1117/12.758830. URL: http://link.aip.org/link/PSISDG/v6884/i1/p68840T/s1\&Agg=doi.

[46] R.M. Pasternack et al. "Measurement of subcellular texture by optical Gabor-like filtering with a digital micromirror device." In: *Optics Letters* 33.19 (2008), pp. 2209–2211.

[47] Shih hui Chao et al. "Phosphorescence lifetime based oxygen micro-sensing using a digital micromirror device." In: *Opt. Express* 15.17 (2007), pp. 10681–10689. URL: http://www.opticsexpress. org/abstract.cfm?URI=oe-15-17-10681.

[48] S.C. Barden, D.G. Sawyer, and R.K. Honeycutt. "Integral field spectroscopy on the WIYN telescopes using a fiber array." In: *Proc. SPIE*. Vol. 3355. 1998, pp. 892–899. URL: http://www.noao.edu/noao/ meetings/spie98/densepak.ps.

[49] M.A. Bershady et al. "SparsePak: a formatted fiber field unit for the WIYN telescope Bench Spectrograph. I. Design, construction, and calibration." In: *Arxiv preprint astro-ph/0403456* June (2004), pp. 1–33. arXiv:0403456v1 [arXiv:astro-ph]. URL: http://arxiv.org/abs/astro-ph/0403456.

[50] JR Haynes et al. "Square core jacketed air-clad fiber." In: *Optical Fiber Communication Conference, 2006 and the 2006 National Fiber Optic Engineers Conference. OFC 2006*. IEEE. 2006, 3–pp.

[51] *hydra*. http://www.noao.edu/image_gallery/html/im0460.html. 1992. URL: http://www.noao. edu/image_gallery/html/im0460.html.

[52] K. Szeto et al. "Fabrication of narrow-slit masks for the Gemini Multiobject Spectrograph." In: *Society of Photo-Optical Instrumentation Engineers (SPIE) Conference Series*. Ed. by A. L. Ardeberg. Vol. 2871. Society of Photo-Optical Instrumentation Engineers (SPIE) Conference Series. Mar. 1997, pp. 1262– 1271.

[53] AC Phillips et al. "DEIMOS: A Powerful New Spectrograph at Keck II." In: *Bulletin of the American Astronomical Society*. Vol. 34. 2002, p. 1320.

[54] I.S. McLean et al. "Design and development of MOSFIRE: the multi-object spectrometer for infrared exploration at the Keck Observatory." In: *Proc. SPIE*. 2010, pp. 7735–49.

[55] SH Moseley et al. "Microshutters arrays for the JWST near infrared spectrograph." In: *Proc. SPIE*. Vol. 5487. 2004, pp. 645–652.

[56] E.P. Wagner et al. "Construction and evaluation of a visible spectrometer using digital micromirror spatial light modulation." In: *Applied spectroscopy* 49.11 (1995), pp. 1715–1719. URL: http://www. opticsinfobase.org/abstract.cfm?id=123620.

[57] K.J. Kearney and Zoran Ninkov. "Characterization of a digital micromirror device for use as an optical mask in imaging and spectroscopy." In: *Proceedings of SPIE*. Vol. 3292. 1998, p. 81. URL: http: //link.aip.org/link/?PSISDG/3292/81/1.

[58] A. Cimatti et al. "SPACE: the spectroscopic all-sky cosmic explorer." In: *Experimental astronomy* 23.1 (2009), pp. 39–66.

[59] Frederic Zamkotsian et al. "Space evaluation of 20481080 mirrors DMD chip for ESA's EUCLID Mission." In: *Millimeter* 7731 (2010), pp. 773130–773130–12. DOI: 10.1117/12.861969. URL: http://link.aip.org/link/PSISDG/v7731/i1/p773130/s1\&Agg=doi.

[60] F. Zamkotsian et al. "DMD-based MOS demonstrator on Galileo Telescope." In: *Proc. of SPIE Vol*. Vol. 7735. 2010, 77356E–1.

[61] Frederic Zamkotsian et al. "Demonstrator of a Multi-Object Spectrograph based on the 2048x1080 DMD." In: *Proc. of SPIE Vol*. Vol. 8254. 2012, 82540Q–1.

[62] Frdric Zamkotsian et al. "BATMAN: a DMD-based MOS demonstrator on Galileo Telescope." In: (2012), 84464U–84464U–14. DOI: 10.1117/12.926330. URL: +http://dx.doi.org/10.1117/12.926330.

[63] John P. Kerekes et al. "Sensor modeling and demonstration of a multi-object spectrometer for performance-driven sensing." In: ed. by Sylvia S. Shen and Paul E. Lewis. Vol. 7334. 1. Orlando, FL, USA: SPIE, 2009, 73340J. DOI: 10.1117/12.819265. URL: http://link.aip.org/link/?PSI/7334/73340J/1.

[64] *DIRSIG*. http://www.dirsig.org/.

[65] *FRED*. http://www.photonengr.com/.

[66] T. SCHEIMPFLUG. *-SCHEIMPFLUG*. US Patent 751,347. 1904.

[67] G. Mie. "Beiträge zur Optik trüber Medien, speziell kolloidaler Metallösungen." In: *Annalen der Physik* 330.3 (1908), pp. 377–445.

[68] L. Rayleigh. "On the scattering of light by small particles." In: *Philosophical Magazine* 41 (1871), pp. 447–451.

[69] MS Bessell. "UBVRI photometry II: The cousins VRI system, Its temperature and absolute flux calibration, and relevance for two-dimensional photometry." In: *Publications of the Astronomical Society of the Pacific* 91.543 (1979), pp. 589–607.

[70] *OSLO*. http://www.lambdares.com/softwareproducts/oslo/.

[71] *Rhinoceros*. http://www.rhino3d.com/.

[72] JB Schutt et al. "Highly reflecting stable white paint for the detection of ultraviolet and visible radiations." In: *Applied Optics* 13.10 (1974), pp. 2218–2221.

[73] Data Sheet. "DLP Discovery . 7 XGA LVDS 12 0 Type A Customer Datasheet." In: May (2010).

[74] Lance Barron. "High-reflectance, sputter-deposited aluminum alloy thin thin films for micro-electro-mechanical systems." In: (2005).

[75] Jason M Neidrich and Lance W Barron. *Spatial light modulator mirror metal having enhanced reflectivity*. US Patent 7,576,902. 2009.

[76] Toshiyuki Kaeriyama. *Improvements in and relating to micro-mechanical devices*. EP Patent 0,694,801. 1999.

[77] Christian Boit. "Fundamentals of photon emission (PEM) in silicon–electroluminescence for analysis of electronic circuit and device functionality." In: *Microelectronics failure analysis desk reference,* (2004), pp. 356–68.

[78] Bertram Schwarzschild. "WMAP Spacecraft maps the entire cosmic microwave sky with unprecedented precision." In: *Physics Today* 56 (2003), p. 21.

[79] Yves Toulemont et al. "The 3.5-m all-SiC telescope for HERSCHEL." In: *Astronomical Telescopes and Instrumentation*. International Society for Optics and Photonics. 2004, pp. 1119–1128.

[80] M. Robberto et al. "Applications of DMDs for astrophysical research." In: *arXiv preprint arXiv:0902.2775* (2009).

[81] Frederic Zamkotsian et al. "DMD chip space evaluation for ESA's EUCLID mission." In: *Library* 7596 (2010), 75960E–75960E–12. DOI: 10.1117/12.845690. URL: http://link.aip.org/link/PSISDG/v7596/i1/p75960E/s1\&Agg=doi.

[82] H.R. Shea. "Effects of Radiation on MEMS." In: *Proc. of SPIE Vol*. Vol. 7928. 2011, 79280E–1.

[83] D. Heynderickx et al. "ESAs SPace ENVironment Information System (SPENVIS): A WWW Interface to Models of the Space Enviroment and its Effects." In: *Proc. AIAA* 371 (2000).

[84] M.A. Xapsos et al. "Space Environment Effects: Model for Emission of Solar Protons (ESP): Cumulative and Worst Case Event Fluences." In: *NASA STI/Recon Technical Report N* (1999), p. 21507.

[85] J.L. Barth, J.C. Isaacs, and C. Poivey. "The radiation environment for the next generation space telescope." In: *NGST Project, internal document* (1999).

[86] *James Ziegler - SRIM & TRIM*. URL: http://www.srim.org/.

[87] *Gafchromic RTQA2*. http://www.gafchromic.com/.

[88] Bernhard Gross. "Irradiation effects in borosilicate glass." In: *Physical Review* 107.2 (1957), p. 368.

[89] SF Pellicori, EE Russell, and LA Watts. "Radiation induced transmission loss in optical materials." In: *Applied Optics* 18.15 (1979), pp. 2618–2621.

[90] M.R. Douglass. "Lifetime estimates and unique failure mechanisms of the digital micromirror device (DMD)." In: *Reliability Physics Symposium Proceedings, 1998. 36th Annual. 1998 IEEE International*. IEEE. 1998, pp. 9–16.

[91] *Chipworks inside TI's DLP chip*. URL: http://www.eetasia.com/articleLogin.do?artId=8800416404\&fromWhere=/ART_8800416404_1034362_NT_a5fd45ee.HTM\&catId=1034362\&newsType=NT\&pageNo=null\&encode=a5fd45ee.

[92] P.J. McWhorter and PS Winokur. "Simple technique for separating the effects of interface traps and trapped-oxide charge in metal-oxide-semiconductor transistors." In: *Applied physics letters* 48.2 (1986), pp. 133–135.

[93] GA Ausman and FB McLean. "Electron-hole pair creation energy in SiO2." In: *Applied Physics Letters* 26 (1975), p. 173.

[94] R.A. Kohler, R.A. Kushner, and K.H. Lee. "Total dose radiation hardness of MOS devices in hermetic ceramic packages." In: *Nuclear Science, IEEE Transactions on* 35.6 (1988), pp. 1492–1496.

[95] A.B. Sontheimer. "Digital micromirror device (DMD) hinge memory lifetime reliability modeling." In: *Reliability Physics Symposium Proceedings, 2002. 40th Annual*. IEEE. 2002, pp. 118–121.

[96] EL Petersen. "The SEU figure of merit and proton upset rate calculations." In: *Nuclear Science, IEEE Transactions on* 45.6 (1998), pp. 2550–2562.

[97] Hideki Satake and Toshihiko Hamasaki. "Low-temperature (77 K) BJT model with temperature dependences on the injected condition and base resistance." In: *Electron Devices, IEEE Transactions on* 37.7 (1990), pp. 1688–1697. URL: http://ieeexplore.ieee.org/xpls/abs_all.jsp?arnumber= 55756.

[98] R. Darveaux and L. Munukutla. "Critical challenges in packaging MEMS devices." In: *Advanced Semiconductor Manufacturing Conference and Workshop, 2005 IEEE/SEMI*. Ieee. 2005, pp. 210–216.

[99] M.A. Mignardi. "Digital micromirror array for projection TV." In: *Solid State Technology* 37.7 (1994), p. 4.

[100] L.J. Hornbeck. *Low reset voltage process for DMD*. US Patent 5,331,454. 1994.

[101] P. Rai-Choudhury. *MEMS and MOEMS Technology and Applications*. Vol. 85. Society of Photo Optical, 2000.

[102] K. Gilleo and S. Corbett. *Getters molecular scavengers for packaging*. 2001.

[103] TD Golding et al. "HgCdTe on Si: Present status and novel buffer layer concepts." In: *Journal of electronic materials* 32.8 (2003), pp. 882–889.

[104] X. Liu et al. "Failure mechanisms and optimum design for electroplated copper through-silicon vias (TSV)." In: *Electronic Components and Technology Conference, 2009. ECTC 2009. 59th*. IEEE. 2009, pp. 624–629.

[105] *MSC Nastran for Finite Element Analysis*. URL: http://www.mscsoftware.com/products/cae-tools/msc-nastran.aspx.

[106] *Sigfit*. http://www.sigmadyne.com/sigweb/sigfit.htm.

[107] V. Genberg and G. Michels. "Integrating MD Nastran with Optical Performance Analysis." In: ().

[108] *MEMs Reverse Costing Report Texas Instruments SystemPlus Consulting*. http://www.i-micronews. com/upload/Rapports/Yole_TI_DLP_Teardown_analysis_sample.pdf. URL: http://www.i-micronews.com/upload/Rapports/Yole_TI_DLP_Teardown_analysis_sample.pdf.

[109] W Robert Ashurst, C Carraro, and Roya Maboudian. "Vapor phase anti-stiction coatings for MEMS." In: *Device and Materials Reliability, IEEE Transactions on* 3.4 (2003), pp. 173–178.

[110] R.O. Green et al. "Imaging spectroscopy and the airborne visible/infrared imaging spectrometer (AVIRIS)." In: *Remote Sensing of Environment* 65.3 (1998), pp. 227–248.

[111] R.A. Cabanac, E.F. Borra, and M. Beauchemin. "A Search for Peculiar Objects with the NASA Orbital Debris Observatory 3 Meter Liquid Mirror Telescope." In: *The Astrophysical Journal* 509 (1998), p. 309.

[112] FJ Montojo et al. "TRANSFORMATION OF THE BAKER-NUNN CAMERA OF SAN FERNANDO." In: ().

[113] N. Brown. "An advanced slit-image camera." In: *British Journal of Ophthalmology* 56.8 (1972), pp. 624–631.

[114] B.E. Burke et al. "The orthogonal-transfer array: a new CCD architecture for astronomy." In: *Proc. SPIE*. Vol. 5499. 2004, pp. 185–192.

[115] E.F. Borra, P. Hickson, and J. Surdej. "The International Liquid Mirror Telescope." In: *Optics and Photonics News* 20.4 (2009), pp. 28–33.

[116]   RF Griffin. "A photoelectric radial-velocity spectrometer." In: *The Astrophysical Journal* 148 (1967), p. 465.

[117]   M. Mayor. "Metal abundances of F and G dwarfs determined by the radial velocity scanner CORAVEL." In: *Astronomy and Astrophysics* 87 (1980), p. L1.

[118]   G. Basri, W.J. Borucki, and D. Koch. "The Kepler Mission: A wide-field transit search for terrestrial planets." In: *New Astronomy Reviews* 49.7 (2005), pp. 478–485.

[119]   SV Berdyugina et al. "Polarized reflected light from the exoplanet HD189733b: First multicolor observations and confirmation of detection." In: *The Astrophysical Journal Letters* 728 (2011), p. L6.

[120]   N. Baba and N. Murakami. "A method to image extrasolar planets with polarized light." In: *Publications of the Astronomical Society of the Pacific* 115.814 (2003), pp. 1363–1366.

[121]   B.J. DeBoo, J.M. Sasian, and R.A. Chipman. "Depolarization of diffusely reflecting man-made objects." In: *Applied optics* 44.26 (2005), pp. 5434–5445.

[122]   A.D. Raisanen et al. "Simulation of practical single-pixel wire-grid polarizers for superpixel stokes vector imaging arrays." In: *Optical Engineering* 51 (2012), p. 016201.

[123]   M.L. Brines and J.L. Gould. "Skylight polarization patterns and animal orientation." In: *Journal of Experimental Biology* 96.1 (1982), p. 69.

[124]   G. Horváth et al. "Polarization portrait of the Arago point: video-polarimetric imaging of the neutral points of skylight polarization." In: *Naturwissenschaften* 85.7 (1998), pp. 333–339.

[125]   C. Zhang et al. "Birefringent laterally sheared beam splitter-Savart polariscope." In: *Proceedings of SPIE*. Vol. 6150. 2006, p. 615001.

[126]   D. Hansen et al. "18. 3: Invited Paper: The Display Applications and Physics of the ProFlux Wire Grid Polarizer." In: *SID Symposium Digest of Technical Papers*. Vol. 33. 1. 2002, p. 730.